NORTHWESTERN UNIVERSITY

Linking Properties to Microstructure through Multiresolution Mechanics

A DISSERTATION

SUBMITTED TO THE GRADUATE SCHOOL IN PARTIAL FULFILLMENT OF THE REQUIREMENTS

for the degree

DOCTOR OF PHILOSOPHY

Field of Mechanical Engineering

By

Cahal James McVeigh

EVANSTON, ILLINOIS

December 2007

ABSTRACT

Linking Properties to Microstructure through Multiresolution Mechanics

Cahal McVeigh

The macroscale mechanical and physical properties of materials are inherently linked to the underlying microstructure. Traditional continuum mechanics theories have focused on approximating the heterogeneous microstructure as a continuum, which is conducive to a partial differential equation mathematical description. Although this makes large scale simulation of material much more efficient than modeling the detailed microstructure, the relationship between microstructure and macroscale properties becomes unclear. In order to perform computational materials design, material models must clearly relate the key underlying microstructural parameters (cause) to macroscale properties (effect).

In this thesis, microstructure evolution and instability events are related to macroscale mechanical properties through a new *multiresolution* continuum analysis approach. The multiresolution nature of this theory allows prediction of the evolving magnitude *and* scale of deformation as a direct function of the changing microstructure. This is achieved via a two-pronged approach: (a) Constitutive models which track evolving microstructure are developed and calibrated to direct numerical simulations (DNS) of the microstructure. (b) The conventional homogenized continuum equations of motion are extended via a virtual power approach to include extra coupled microscale stresses and stress couples which are active at each characteristic length scale within the microstructure.

The multiresolution approach is applied to model the fracture toughness of a cemented carbide, failure of a steel alloy under quasi-static loading conditions and the initiation and velocity of adiabatic shear bands under high speed dynamic loading. In each case the multiresolution analysis predicts the important scale effects which control the macroscale material response. The strain fields predicted in the multiresolution continuum analyses compare well to those observed in direct numerical simulations of the microstructure. However much less computational effort is required because the detailed microstructure does not have to be modeled (unlike the direct numerical simulations). Furthermore the characteristic length scale of inhomogeneous deformation is predicted to change as a function of the evolving microstructure. As such the predicted scale of inhomogeneous deformation which controls the macroscale response is a function of the underlying microstructural instability events. This provides an important link between macroscale properties and microstructure which is useful for materials design.

Acknowledgements

I wish to express my gratitude to my advisor, Professor Wing Kam Liu for his guidance, advice and suggestions during my graduate studies and research. I would also like to acknowledge my committee; Professor Brian Moran, Professor Ted Belytschko and Professor Gregory Olson.

I would like to thank Professor Sean Fulton and the Northern Ireland Fund for Reconciliation for providing me the opportunity to study at Northwestern University.

The financial support for this research has been provided by the Office of Naval Research under the D3D Digital Structure consortium program.

Table of Contents

List of Figures

List of Tables

1 Introduction

In materials science, rather than randomly discovering materials and exploiting their properties, the goal is to develop a comprehensive understanding of microstructure-properties relationships in order to systematically design materials with specific desired properties.

(Figure 1.1) illustrates the key product design relationships from a materials science perspective. Processing conditions determine the microstructure, which in turn control the material properties and subsequent performance. Extensive empirical data is available relating material microstructure to the raw material processing conditions (such as temperature and deformation rate). This relationship is well defined for traditional processing techniques such as extrusion (Borrego et al. 2002; Sellars and Zhu 2000) and rolling (Brand et al. 1996; Karhausen and Roters 2002; Wang et al. 2003) and increasingly well understood for new large deformation techniques such as friction stir welding (Sutton et al. 2002). At the other end of the design chain, the link between material properties and performance is well established; data is available which relates properties (e.g. strength, toughness, density, chemical resistance) to desired performance requirements. The middle link between structure and properties is now discussed in Section 1.1.

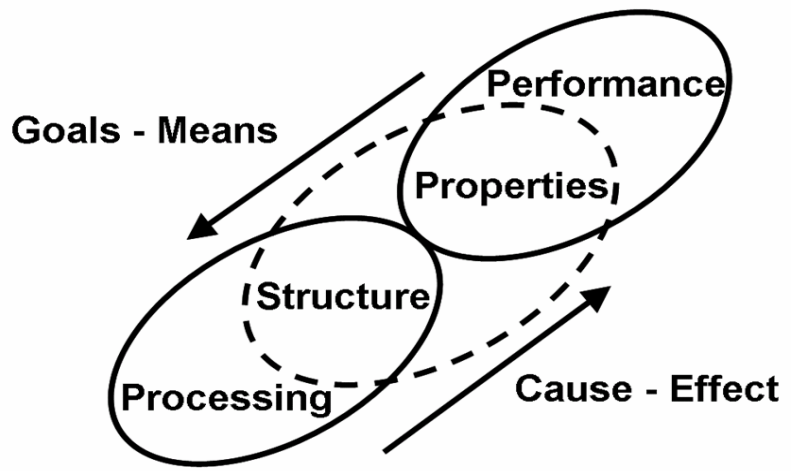

Figure 1.1. Important relationships from processing to performance (Olson)

1.1 Microstructure – Property Relationship

The relationship between macroscale properties and the underlying microstructure is often the most difficult to define as microstructure is often in an evolving state during the lifetime of a component. Microscale imaging techniques such as light microscopy, Scanning Electron Microscopy (SEM), Transmission Electron Microscopy (TEM) and Local Electrode Atom Probe (LEAP) can be used to accurately characterize the microstructure at a snapshot in time. The material properties, determined from physical experiments, can then be related to the observed microstructure.

In the engineering materials of interest in this thesis, we are interested in how microstructure evolves spatially and temporally, and relating the evolving microstructure to the macroscale properties and performance. Microstructural evolution occurs during raw material processing (e.g. heat treatments) or within a final component under normal operating conditions (e.g. fatigue crack growth). The ability to predict the evolving microstructure-property relationships all the

way from raw material processing right throughout the component lifetime is the key successfully predicting and designing material performance.

Recent advances in computational power and computational materials science have enabled direct numerical modeling of thermal-mechanical microstructure evolution as a means of predicting macroscale properties. The ultimate goal of computational materials science is to design optimized materials without an expensive and time consuming iterative empirical design process.

The goal of this work is to develop a computational modeling framework which can affordably predict material properties and component performance directly in terms of the evolving microstructure. This is the first step in solving the reverse problem i.e. to design a microstructure based on the desired properties and performance requirements.

The traditional continuum approach to materials modeling is described in Section 1.2. The different types of constitutive relationships are described in Section 1.3. Deficiencies of the conventional continuum approach are discussed in Section 1.4 and some techniques for combating these deficiencies are discussed in Section 1.5. The goals of this thesis are expanded upon in Section 1.6.

1.2 Review of Continuum Material Modeling

The most efficient approach to materials modeling is to approximate a heterogeneous body as a homogeneous continuum, which is then described mathematically by a set of continuum partial differential governing equations (i.e. the momentum equation, energy equation, charge equation and diffusion equation) (Belytschko et al. 2000).

1.2.1 Characteristic Length Scales of a Heterogeneous Body

Two criteria must be satisfied in order for the conventional continuum approach to be feasible. To describe these criteria, we first introduce three characteristic lengths (Figure 1.2):

- L: the typical dimension of the body to be approximated as a continuum. For example, a bridge will have an L value on the order of meters.
- λ: the wavelength or variation of the state s about its average $\overline{s}$. In terms of mechanical deformation, the state s is a strain field and hence λ is the characteristic wavelength of this strain field within the structure of size L.
- a: the distance over which the material's underlying properties undergo considerable variation about their mean value. This represents the microstructure's spatial variation; in terms of homogenization theory it is related to the size of a representative volume element (RVE) which is described later.

The criteria are now defined in terms of these length scales.

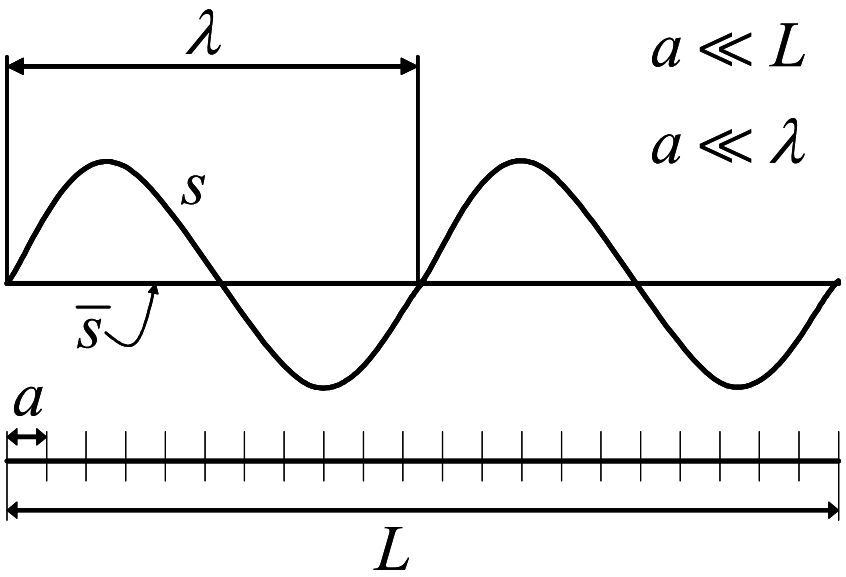

Figure 1.2. The RVE is much smaller than the component size and deformation variation

1.2.2 Criteria for Continuum Modeling

Criterion (i): L and λ are large compared to a.

Explanation: This is the separation of scales principle (Auriault 1991); the body L is much larger than the microstructure scale a and the strain occurs homogeneously over a large scale λ compared to the microstructure a.

Criterion (ii): the nature of the microstructure in a volume element a^3 in one region is the same as in another region.

Explanation: This ensures that the microstructure is similar throughout the body i.e. there are no interfaces between different materials or strong variations in microstructure e.g. grain size, porosity etc.

If the material satisfies both criteria it is said to be a statistically homogeneous body (Beran 1968). It follows from criterion (ii) that a volume element a^3 can be identified whose mechanical behaviour is statistically representative of the heterogeneous medium as a whole i.e. a representative volume element (RVE). In the continuum approximation, any material point can be represented by the average behavior of a corresponding RVE.

1.2.3 Hill-Mandel Lemma: Work Conjugacy of Stress and Strain Measures

The relationship between a continuum point and a RVE is based on the Hill-Mandel relation (Hill 1963). The variation of work rate δp at a material point $\mathbf{x}$ is equivalent to the average variation of work rate within a superimposed RVE V_0:

$$\delta p(\mathbf{x}) = \frac{1}{V_0}\int_{V_0} \boldsymbol{\sigma}_m : \delta \mathbf{L}_m dV_0 \tag{1.1}$$

where V_0 is the volume of the RVE, $\boldsymbol{\sigma}_m$ is the *microscale* Cauchy stress and $\mathbf{L}_m$ is the *microscale* velocity gradient field. The microscale measures are the actual fields within the heterogeneous RVE as shown in (Figure 1.3).

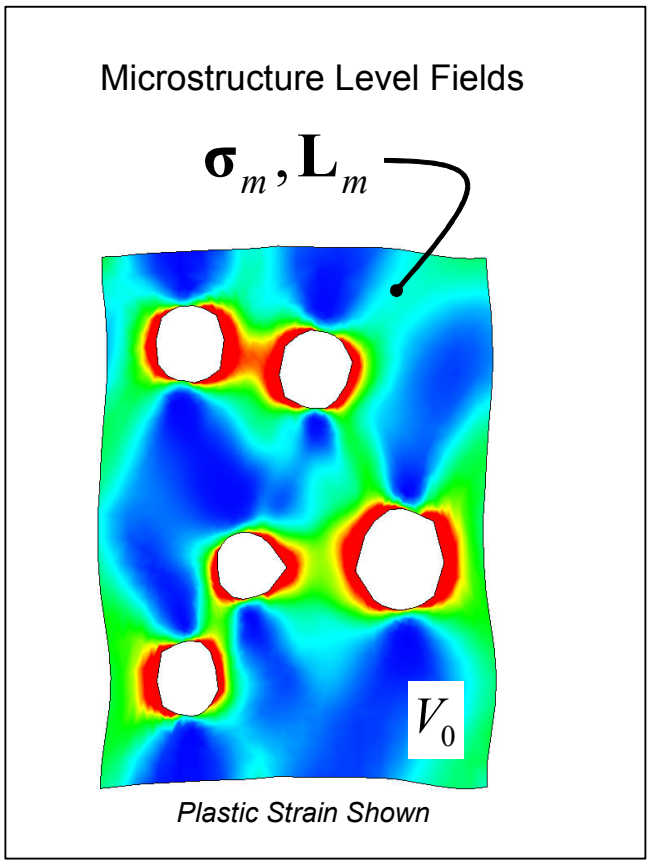

Figure 1.3. Plastic Strain contour in RVE showing the local plastic strain contour $\mathbf{L}_m$. The local stress $\boldsymbol{\sigma}_m$ could also be plotted in the same manner.

The virtual internal power can be rewritten in terms of the Hill-Mandel lemma

$$\delta p = \frac{1}{V_0}\int_{V_0} \boldsymbol{\sigma}_m : \delta \mathbf{L}_m dV_0 = \boldsymbol{\sigma} : \delta \mathbf{L} \tag{1.2}$$

where the continuum velocity gradient $\mathbf{L}$ is written as a volume average of the local velocity gradient over the RVE:

$$\mathbf{L} = \frac{1}{V_0}\int_{V_0} \mathbf{L}_m dV_0 \tag{1.3}$$

where the *continuum* stress $\boldsymbol{\sigma}$ is also a volume average over the RVE:

$$\boldsymbol{\sigma} = \frac{1}{V_0}\int_{V_0} \boldsymbol{\sigma}_m dV_0 \tag{1.4}$$

Continuum expressions can also be derived for the virtual external and kinetic power density. By integrating these virtual power density expressions over the entire body, applying the principle of virtual power and using divergence theorem, a set of partial differential governing equations and boundary conditions can be derived for the continuum – more details are found in (Belytschko et al. 2000):

$$\begin{aligned} \nabla \bullet \boldsymbol{\sigma} + \mathbf{b} &= 0 \quad \text{in} \quad \Omega \\ \mathbf{n} \bullet \boldsymbol{\sigma} &= \bar{\mathbf{t}} \quad \text{on} \quad \Gamma_t \\ \mathbf{u} &= \bar{\mathbf{u}} \quad \text{on} \quad \Gamma_u \end{aligned} \tag{1.5}$$

where $\mathbf{b}$ is a body force, $\bar{\mathbf{t}}$ is an applied traction on the surface Γ_t (with unit normal $\mathbf{n}$) and $\bar{\mathbf{u}}$ is a prescribed displacement on the surface Γ_u.

1.3 Continuum Constitutive Relationships

A constitutive relationship is required to solve the governing equation i.e. the relationship between the continuum stress and deformation must be computable at every continuum point. The most computationally intensive way is to perform a global-local analysis. This involves concurrently simulating an RVE at each continuum point (Ghosh et al. 2001; Kouznetsova et al. 2002; Michel et al. 1999). The known continuum strain is applied as an average strain over the RVE, equation (1.2), and the continuum stress is computed via equation (1.4). Due to the expense of such an approach, pre-formulated mathematical models are used as affordable surrogates of the RVE. Different types of constitutive models have been developed in the

literature depending on the nature of the microstructure being replicated. In general constitutive relationships fall into two categories: empirical or physically based.

Empirical constitutive models, such as a J2 flow model with a simple power-law hardening relation or the rate and temperature dependent Johnson-Cook Model (Johnson and Cook 1985; Li. et al. 2002; Medyanik et al. 2005) are often favored in industry for large scale simulations (ABAQUS 2004). These offer an efficient way to implicitly describe the *effects* of the underlying physical processes within the microstructure; these are usually calibrated using experimental data. These models are reliable only within the range of experimental validation and are unable to capture history effects. As such they are not useful for materials design purposes.

Physically based constitutive models (micromechanical models), conversely, are based directly on the underlying microscale mechanisms e.g. dislocation movement, damage nucleation, grain boundary formation etc. A large number of *analytical* micromechanical techniques have been proposed and a comprehensive overview is given in the literature (Mura 1987; Nemat-Nasser and Hori 1993).

Parameterized microstructural variable such as grain size and damage are used as numerical representations of the physical microstructure. Evolution equations describe the rate of change of the microstructure (parameters) in terms of the loading conditions and current microstructure and environmental conditions. The stress state is then directly related to the microstructural parameters. In the BCJ (Bammann-Chiesa-Johnson) internal state variable (ISV) constitutive model (Bammann et al. 1996; Bammann et al. 1990), variables represent the evolving

microstructure (e.g. dislocation climb, glide, annihilation and damage accumulation). It is also possible to directly track the dislocation density (Domkin 2005) and model its effect on plastic flow. The highly anisotropic nature of plasticity at small scales can be captured using crystal plasticity models which explicitly account for the dislocation behavior on individual slip planes (Asaro 1983a; Asaro 1983b).

Physically based constitutive relations are often derived through a computational hierarchical technique (Hao et al. 2004; Hao et al. 2003; Liu et al. 2004) (also known as serial coupling or parameter passing). The average constitutive behavior at the smallest scale is used to determine the behavior at the next largest scale, and so on until the macroscale behavior is defined.

1.4 Deficiencies of Continuum Theory

Although the conventional continuum approach, coupled with a micromechanically based constitutive relation is useful for material prediction and design proposes, in many engineering materials a conventional homogenized continuum is insufficient. In general, two situations can negate the fundamental assumptions of homogenization.

1.4.1 Micro-components

The first situation is when the component's characteristic length, L, and hence the deformation wavelength λ approaches the RVE size, a, which may occur in micro or nano devices (Figure 1.4). In this case the only option is to model the discrete microstructural features directly.

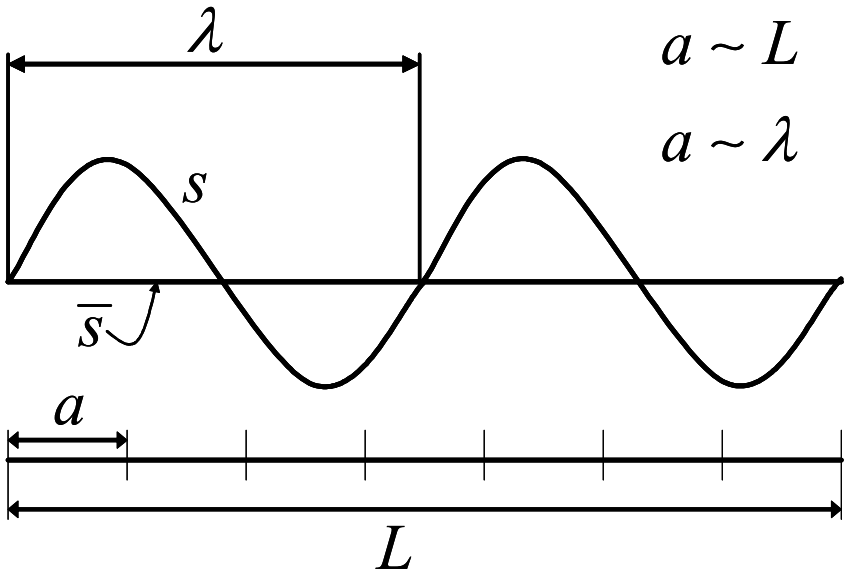

Figure 1.4. Homogenization is invalid when the RVE size a approaches L, the characteristic length scale of the component/body; this may occur in micro/nano scale devices.

1.4.2 Inhomogeneous Deformation

The second situation arises when the wavelength of the deformation, λ, approaches the RVE size a (Figure 1.5). This highly ***inhomogeneous*** deformation may occur for several reasons:

- Ahead of a sharp crack tip strong strain gradients mean that λ may be on the order of the microstructural size a
- Strain localizes due to a micromechanical process such as void coalescence.
- In multi-material bodies, strong strain gradients occur at the material interfaces.

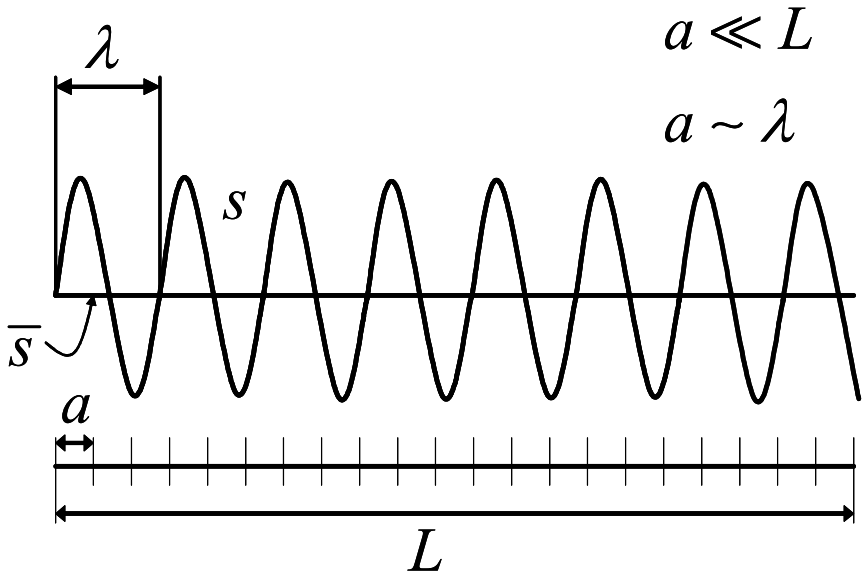

Figure 1.5. Conventional homogenization is invalid when the characteristic length scale of the deformation approaches the RVE size a

A continuum approach is still feasible even when inhomogeneous deformation arises i.e. an RVE may still be associated with each continuum point. However it is insufficient to represent a continuum point as a first order average of an RVE, equation (1.1). Furthermore in many materials which exhibit inhomogeneous deformation localization, the associated continuum governing equations suffer a local loss of ellipticity upon material softening, resulting in an illposed mathematical description; numerical results do not converge to a physically meaningful solution (De Borst and Muhlhaus 1991; Tvergaard and Needleman 1995; Vosbeek 1994).

1.5 Modeling Inhomogeneous Deformation

Two approaches are generally taken to overcome the problems associated with inhomogeneous deformation; one involves improving the conventional continuum approach by making it non-local. Practically speaking this involves introducing higher order terms in the continuum formulation as described in Section 1.5.1-1.5.2. The second, and more computationally intensive approach, is to couple the continuum simulation with direct microstructure scale simulations in regions where deformation is known to be inhomogeneous (Section 1.5.4).

1.5.1 Non-local Continua

The simplest way to introduce non-local terms in the continuum formulation is to define the constitutive behavior in terms of a non-local averaged quantity (Bazant and Belytschko 1987; De Borst et al. 1993; Pijaudier-Cabot and Bazant 1987). A good overview of these methods is given in (Rolshoven and Jirasek 2002). For example the macroscale damage f may be averaged about a continuum point as follows:

$$\bar{f}(\mathbf{x}) = \frac{1}{V_{nl}} \int_{V_{nl}} k(\mathbf{y}) f(\mathbf{y}) dV \tag{1.6}$$

where V_{nl} is a non-local averaging volume centered on the continuum point $\mathbf{x}$, $\mathbf{y}$ is the position relative to $\mathbf{x}$ and $k(\mathbf{y})$ is a kernel function which weights or biases the averaging operation. The constitutive behavior is then computed as a function of the non-local damage $\bar{f}$. This results in a smoothing of the local inhomogeneous deformation field over a length scale associated with the non-local averaging volume V_{nl}. Hence it is necessary to calibrate the averaging volume size to the microstructural length scale of inhomogeneous deformation (Brekelmans 1993).

Another non-local approach involves extending the virtual power expression, which relates a continuum point to the microstructure (RVE), to include a strain gradient and power conjugate couple stress measure. This requires an extension of the Hill-Mandel relation, equation (1.1), to higher order:

$$\delta p = \frac{1}{V_0}\int_{V_0} \boldsymbol{\sigma}_m : \delta \mathbf{L}_m dV_0 = \boldsymbol{\sigma} : \delta \mathbf{L} + \overline{\boldsymbol{\sigma}} \vdots \delta \mathbf{L} \overleftarrow{\nabla} \tag{1.7}$$

where the variation of internal work rate is now represented by a velocity gradient $\mathbf{L}$ and its gradient $\mathbf{L}\overleftarrow{\nabla}$. The work conjugate measure of $\mathbf{L}\overleftarrow{\nabla}$ is a higher order stress $\overline{\boldsymbol{\sigma}}$. This is sometimes known as a gradient enhanced model (Aifantis 1992; Fleck and Hutchinson 1997; Peerlings and Fleck 2001; Triantafyllidis and Bardenhagen 1996). Under certain circumstances the non-local averaging and gradient enhanced approaches are equivalent e.g. when a linearly varying non-local strain is considered.

It is important to note that the constitutive relation must now also describe the relationship between the higher order stress $\overline{\boldsymbol{\sigma}}$ and the second gradient $\mathbf{L}\overleftarrow{\nabla}$; defining this relationship is not trivial. Kouznetsova (2002) went so far as to simulate an individual RVE boundary value problem for each material integration point in a gradient enhanced continuum in order to compute the complicated higher order constitutive relationship 'on the fly' during a quasi-static simulation.

Gao et al. (1999) realized that gradient term was useful for describing the extra hardening effect arising from geometrically necessary dislocations (GNDs) when local inhomogeneous

deformation occurs at very small scales. In effect, the magnitude of the strain gradient indicates the scale at which strain is occurring; large strain gradients indicate small scale deformation and the level of work hardening increases accordingly.

Another variation on this higher order approach is a Cosserat continua; extra rotational degrees of freedom are introduced in addition to the conventional translational degrees of freedom (Cosserat and Cosserat 1909; De Borst et al. 1993; Kadowaki and Liu 2004; Kadowaki and Liu 2005; Toupin 1962). Coupled thermal-mechanical models (with extra temperature degrees of freedom) have also been successful in capturing the scale of inhomogeneous deformation in dynamic adiabatic shear bands (Medyanik et al. 2005; Needleman 1988; Sluys and De Borst 1992; Wang et al. 1996).

One of the main contributions of this theory is the development and application of a multiresolution continuum theory. The higher order gradient enhanced models described above are a particular case of this theory. This general theory supplements the conventional work rate conjugacy description of a continuum point with multiple extra strain and strain gradient measures. Each pair of strain and strain gradients describes the deformation at a particular scale. This allows inhomogeneous deformation to be resolved to multiple discrete length scales. A continuously variable length scale model is also proposed which simplifies the implementation while replicating the multiscale nature of the original model.

1.5.2 Discussion of Non-Local Models

The key to non-local models is that they introduce a physical length scale into the continuum model either through the constitutive response or directly within the governing equations. Material behavior is then a function of the *scale* at which deformation is occurring. The introduction of a length scale acts to reduce strong gradients and inhomogeneous deformation is smoothed over a more physical length scale.

Hence important material behavior can be captured physically, such as the length scale dependence of plastic deformation, plastic flow localization in shear bands and the effect of crack size and geometry on fracture behavior. These phenomena control important mechanical behavior such as fracture toughness and strength. However the higher order models have crucial weaknesses, which limit them in terms of materials prediction and design.

- The constitutive parameters remain empirically based.
- Neither approach can model the variation in material behavior if the scale of inhomogeneous deformation evolves with microstructure and time.

1.5.3 Numerical Implementation Approach

A simple numerical approach to capture the physical length scale of localization is to use a discretisation which coincides with the physical scale of localization. For example if strain is known to localize at a scale of a micron, the numerical solution mesh is discretized to a micron. Hence, localizing deformation is forced to localize at the scale of the numerical discretisation used, which has been pre-calibrated to a physical length scale. This approach has been proposed

by (Busso et al. 1998) to model fracture in several metallic materials which exhibit a clear length scale of localization at failure. This approach can only capture strain localization at a single length scale. The region in which failure will occur must be known a-priori in order to mesh that region down to the appropriate scale.

1.5.4 Continuum - Discrete Microstructure Concurrent Coupling

Other research has focused on developing frameworks in which a continuum or 'coarse grain' approach is improved upon by performing a fine scale direct numerical simulation (DNS) of the microstructure in a region where homogenization is invalid or insufficient e.g. at a crack tip, material interface, surface behavior. Several models have been proposed which vary mainly in the way they relate information between the coarse and fine scale simulations.

The Quasi-continuum Method (QM) (Knap and Ortiz 2001) and the Bridging Scale Method (BSM) (Tang et al. 2006; Wagner and Liu 2001; 2003) are particular examples where the direct numerical simulation (DNS) is usually performed using molecular dynamics (MD). Currently, the atomic region which can be examined efficiently remains extremely small and the technique has been limited to the simulation of nanoscale applications such as Carbon Nanotubes (CNT) and atomic scale phenomena such as dislocation formation (Liu et al. 2004; Park et al. 2005; Qian and Gondhalekar 2004; Qian et al. 2002).

The BSM has also been used to couple a continuum simulation with a highly resolved Cosserat type continuum (Kadowaki and Liu 2004; Kadowaki and Liu 2005). (Liu and McVeigh 2007)

have performed a two-scale simulation in which a DNS is performed using continuum mechanics (i.e. individual microstructural features are explicitly modeled and spatially discretized) and coupled to a continuum simulation. They have outlined a hierarchical and a concurrent coupling technique in which the approach can be extended to N scales of analysis (Liu and McVeigh 2007).

The disadvantages of a direct DNS coupling approach are as follows:

- The issue of boundary conditions between the scales is problematic as the disparity in spatial resolution may cause spurious wave reflection at the interface (Karpov et al. 2005; Wagner and Liu 2001).
- This reflection can be reduced by using complicated (and expensive) boundary conditions, although this issue has still to be fully resolved particularly for three dimensional cases (Liu et al. 2004; Park et al. 2004; Wagner et al. 2004).
- The expense associated with direct numerical simulation (DNS) of the microstructure, makes it prohibitively expensive to use for component scale simulations.

1.6 Goals and Approach

The goals of the current work are to develop an affordable material modeling framework for materials design; the proposed multiresolution theory overcomes the limitations of a conventional continuum approach, higher order/gradient models and direct coupling schemes. In key features of the proposed framework are:

- Allows macroscale properties (e.g. strength and toughness) and performance to be predicted directly in terms of the key microstructure design parameters including length scales of inhomogeneous deformation.
- Is general enough to incorporate a statistical description of the microstructure
- Provide a foundation for microstructure level computational materials design

In particular the proposed theory works as follows:

- Predicts the evolving scale and magnitude of inhomogeneous deformation directly in terms of the evolving microstructural parameters and length scales (including rate and temperature dependence)
- Employs a set of continuum microstresses which describe the resistance to inhomogeneous deformation at each characteristic length scale in the evolving microstructure. These microstresses are directly coupled to the conventional macroscale stress through a set of multiresolution continuum governing equations.
- The multiresolution continuum governing equations can be discretized and solved using a conventional finite element analysis (FEA) approach with a single mesh.
- Does not require complicated inter-scale boundary conditions (only a single FEA mesh is used)
- Does not require *large scale* direct numerical simulation of microscale features (however limited microstructure scale modeling can be used to determine constitutive relations)

The proposed theory is a multi-resolution extension of conventional homogenization. The continuum governing equations are developed by averaging over the RVE scale as before, equations (1.1)-(1.4), *and* also at several scales within the RVE microstructure associated with

inhomogeneous deformation. The result is a set of multiresolution continuum partial differential governing equations which are an extension of the conventional governing equations involving extra *inhomogeneous microstresses*; these microstresses arise naturally from the extra small scale averaging operations within the RVE. Conveniently, a traditional finite element solution procedure can be used to discretize and solve the weak form of the multiresolution governing equations; special finite element interpolants are *not* required. In terms of constitutive model development, average constitutive relationships are now required at each scale of interest within the RVE to describe the extra *inhomogeneous* microstresses in the extended multiresolution governing equations. The constitutive relationships are derived by averaging the stress and strain at each scale within computational RVE models.

To demonstrate the proposed theory, a cemented carbide, high strength steel and dynamic shear band problem are chosen. Each exhibits inhomogeneous deformation at multiple scales, leading to material failure. In all cases the scale at which deformation occurs is crucial to the macroscale toughness and strength.

1.7 Thesis Outline

This thesis is structured as follows:

Chapter Two: An overview of multiscale material behavior is given in terms of a cemented carbide composite, high strength steel, and adiabatic void assisted shear banding; each exhibits failure involving inhomogeneous deformation at progressively smaller length scales related to the microstructural features.

Chapter Three: The macroscale continuum plasticity and damage constitutive models which are used in this thesis are discussed; in particular the rate, temperature and damage dependent model of Bammann, Chiesa and Johnson (Bammann et al. 1993; Bammann et al. 1990) and the crystal plasticity model of Asaro (Asaro 1983a; Asaro 1983b).

Chapter Four: A hierarchical micromechanical constitutive model is developed for a tungsten-carbide-cobalt cemented carbide and numerical fracture toughness predictions are made.

Chapter Five: From the standpoint of microstructure homogenization and gradient enhanced theories, a general Multiresolution Continuum Theory (MRCT) is derived for modeling materials which undergo inhomogeneous deformation at several scales.

Chapter Six: An approach for deriving microscale constitutive relations (required to solve the MRCT governing equations) is proposed and illustrated for a steel alloy.

Chapter Seven: The MRCT is applied to make numerical fracture toughness predictions for a cemented carbide with various microstructural design parameters. Numerical fracture toughness simulations are performed.

Chapter Eight: The MRCT is coupled with a thermal analysis to examine void assisted adiabatic shear bands in high strength steel.

Chapter Nine: Conclusions and future directions are outlined.

2 Multiscale Material Systems

In many engineering materials, permanent deformation is accompanied by energy dissipation at several distinct scales. Cemented carbides and high strength steels are two such materials systems; both undergo inhomogeneous deformation at more than one length scale during damage initiation, growth and final failure. Furthermore, during dynamic loading of high strength steels, thermal diffusion also affects the scale of the resulting *adiabatic* shear band. These materials are focused on in this thesis; they illustrate the shortcomings of a conventional continuum approach to material modeling and motivate the proposed multiresolution continuum theory (MRCT), developed in Chapter 5. The MRCT remains within the context of continuum mechanics while attempting to capture the important characteristic length scales of inhomogeneous deformation. A brief overview of cemented carbides, its applications and properties is given in Section 2.1. An overview of multiscale failure in high strength steel is given in Section 2.2 and adiabatic shear failure of a steel alloy is discussed in Section 2.3.

2.1 Cemented Carbides

A brief overview of the development, properties and applications of cemented carbides are given in Section 2.1.1 to familiarize the reader with this material. This is developed further in Section 2.1.2 where the key microstructure-properties relationships are described. The multiscale nature of failure is described in Section 2.1.3. The nature of ductile rupture within the composite is described in terms of vacancy clustering in Section 2.1.4. A direct numerical simulation of a

WC-Co microstructure is illustrated in Section 2.1.5. Some notable empirical and modeling work from the literature is described in Section 2.1.6.

2.1.1 Development, Properties and Applications

Tungsten Carbide-Cobalt (also known as WC-Co, cemented carbide, hardmetal or cermetal) is an example of a metal matrix composite which can also be described as ductile reinforced brittle composite. Very hard and brittle tungsten monocarbide (WC) grains (hexagonal crystal structure) are 'cemented' together by a tough cobalt alloy binder matrix (FCC structure) by liquid phase sintering. The combination of a WC phase with a metallic cobalt binder tends to be a favorable combination for the sintering process. The ceramic WC is highly soluble in the metal cobalt at high temperatures and sufficient wetting of WC by the liquid cobalt binder gives good densification during the liquid phase sintering resulting in a very low porosity (itia.org.uk 2006). Cemented carbides have excellent hardness, toughness, compressive strength, transverse rupture strength (resistance to bending failure), and wear resistance. Applications range from aerospace, munitions, sports, automobile to home appliances, and it is particularly well known for its use in cutting tools, metal forming tools, mining tools, and wear resistance surfaces. The first patents on WC-Co were issued in 1923 and produced in 1926 under the name of 'Widia' (Inframat.com Dec 4th 2006). Since then there has been a continuous expansion in the consumption of cemented carbide from an annual world total of 10 tons in 1930; to 100 tons around 1935; 1,000 tons in the early 1940's; through 10,000 tons in the early 1960's and up to nearly 30,000 tons at present (itia.org.uk 2006), largely due to the introductions of ultra fine submicron WC grains in the late 70s and early 80s. This greatly extended the application of cemented carbides into new

emerging applications in the area of micromachining of microelectronics and telecommunications components (itia.org.uk 2006).

The drive toward reducing grain size stems from experimental observations of increased toughness, hardness and wear resistance of WC-Co. Grain sizes of WC powders used in cemented carbides range from 0.15 μm to 150 μm allowing a wide choice of hardness and toughness properties. These relationships are described in Section 2.1.2.

2.1.2 Key Microstructure - Properties Relationships

Microstructure

The key microstructural parameters which characterize the cemented carbide are:

(i) Cobalt volume fraction f : the ratio of cobalt phase to the total volume.

(ii) Cobalt grain size d : this is interpreted here as the average distance a dislocation can travel in the cobalt before hitting a carbide grain i.e. the size of a cobalt pool. It is closely related to the carbide grain size.

(iii) Contiguity C_{WC} of the carbide phase is defined as the ratio of the carbide/carbide interface area (carbide grain boundary) to the total interface area. Contiguity usually increases with carbide volume fraction.

These parameters are often inter-related making it difficult to isolate microstructure-property relationships experimentally (Kim 2004). For example conflicting reports have been made about the relationship between carbide contiguity and carbide grain size. Gurland (1988) reports that

increasing carbide grain size leads to decreased contiguity, while German (1985) suggests that the contiguity is independent of grain size. Here we are focused on the effects of cobalt volume fraction and grain size; contiguity is not considered in this thesis as it is generally the least important (and most difficult to investigate) of the three material parameters. Cobalt volume fraction f is simply given by:

$$f = \frac{V_{Co}}{V} \tag{2.1}$$

where V_{Co} is the volume of cobalt and V is the total volume of the sample. The cobalt/carbide volume fraction ratio can be related to the cobalt/carbide grain size ratio via the following linear-intercept equations derived from stereological principles by (Kim 2004; Underwood 1970):

$$\frac{d}{d_{WC}} = \frac{f}{f_{WC}\left(1 - C_{WC-Co}\right)} \tag{2.2}$$

where C_{WC-Co} is the contiguity.

Properties

The two crucial performance indicators of cemented carbides are:

- Hardness which is a measure of resistance to penetration and is closely related to ultimate strength and
- Fracture toughness which is a measure of the energy absorbed during fracture

	Density $\left(kgm^{-3}\right)$	Young's Modulus $\left(GPa\right)$	Hardness $\left(GPa\right)$
WC	15800	700	19.61
Co	8900	209	0.7
WC-Co	~1500	~600	~16
Stainless Steel	7900	200	5.84

Table 2.1 Comparison of density, Young's modulus and hardness for cemented carbide components

The high hardness and strength of cemented carbides is due to the high carbide volume fraction; WC (density $15800kgm^{-3}$) has a Young's modulus of 700GPa and hardness of 19.61GPa, compared to for example stainless steel (density $7900kgm^{-3}$) with a Young's modulus of 200GPa and hardness of around 5.84GPa (memsnet.org 2006a). The high fracture toughness of cemented carbides on the other hand is mainly due to the highly ductile cobalt (density $8900kgm^{-3}$) binder. These are summarized in Table 2.1.

Toughness is directly related to the *amount* (volume fraction) of ductile cobalt f, which absorbs energy via plastic deformation. However a larger cobalt fraction f is accommodated by a decreased fraction of the much harder carbide, resulting in a reduction in strength.

A large cobalt grain size d also increases the toughness as the plastic deformation dissipates over a larger area. However larger cobalt grains d are weaker according to the Hall-Petch effect. In general, larger grain size d and more cobalt f results in a tougher behavior but less strength. Hence fracture toughness exhibits an inverse relation to hardness. The effects of cobalt volume

fraction f and grain size d on hardness and toughness are shown schematically in (Figure 2.1). These relationships must be captured in a WC-Co constitutive relationship.

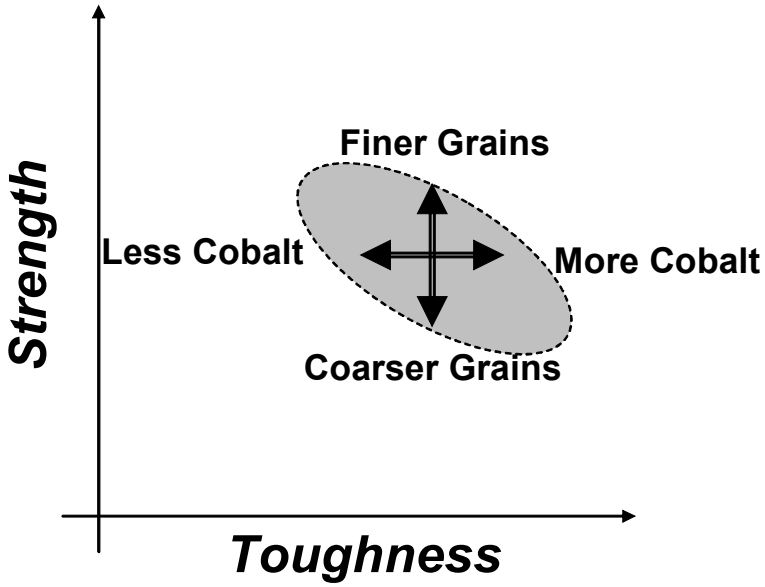

Figure 2.1. Strength versus Toughness for cemented carbide; coarse grains and more cobalt increase toughness to the detriment of strength and vice versa.

2.1.3 Physics of Failure in Cemented Carbides

Failure involves combined brittle fracture of the WC phase and ductile fracture of the cobalt binder as shown schematically in (Figure 2.2). Five stages are involved in failure:

- Stage 1: Initial deformation is relatively homogeneous over the sample
- Stage 2: Brittle fracture occurs in the carbide grains but is resisted by the formation of crack bridging cobalt ligaments at several positions near the crack tip. This is known as

the multi ligament zone (MLZ) (McHugh and Connolly 2003). Plastic strain in the work hardening ligaments is fairly homogeneous over the entire ligament. The ligament is composed of a single cobalt grain of size d . This length scale is also called l^1 here.

- Stage 3: Stress within the cobalt ligament approaches a saturation level as dislocation hardening and recovery cancel each other out (dislocation recovery describes dislocations overcoming obstacle, reducing the work hardening) . This first occurs in the ligament just ahead of the brittle crack tip where deformation is naturally highest. Deformation subsequently localizes to the scale of the opening brittle crack l^2 .
- Stage 4: The stress, deformation and triaxiality are sufficient for microvoids to nucleate and grow in the cobalt ligaments. Microvoid nucleation is a vacancy diffusion based process here (not particle debonding). Plastic strain localizes between neighboring microvoids at scale l^3 .
- Stage 5: As the microvoids coalesce, the *micro*-ligaments between the voids neck and final failure occurs.

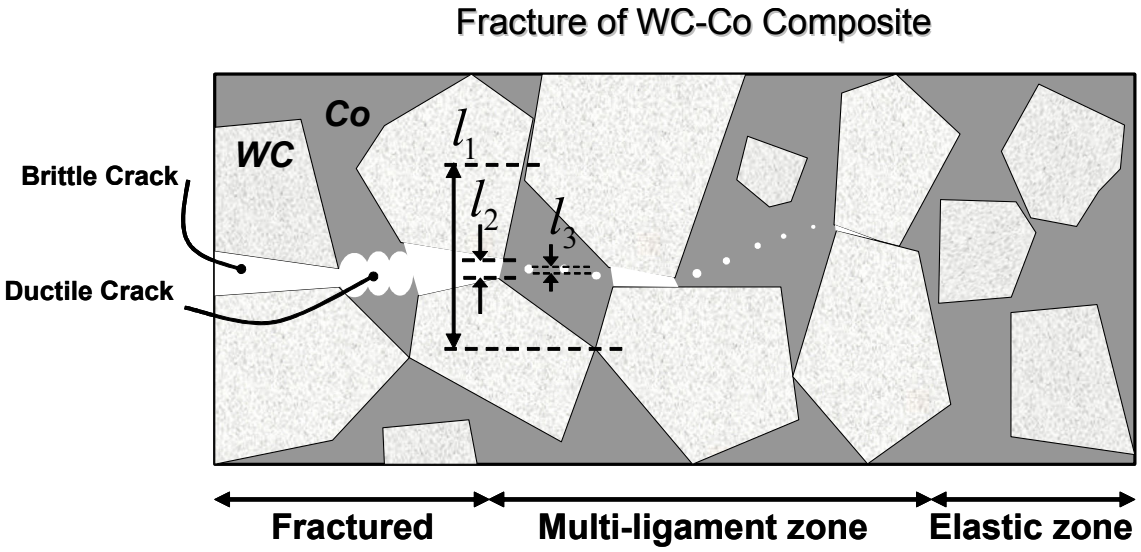

Figure 2.2. In the multiligament zone (MLZ) inhomogeneous deformation arises at three scales related to the cobalt grain size, the brittle crack opening and finally the microvoids

The energy dissipated in stretching the cobalt ligaments strongly contributes to the fracture toughness. The manner in which the cobalt ligaments fail (i.e. ductile rupture) is controlled by microvoid nucleation (from vacancy clustering). As there no embedded particles in the cobalt alloy, it is not immediately obvious how microvoids nucleate. This is discussed further in Section 2.1.4.

2.1.4 Nucleation of Microvoids in Cobalt

No evidence for heterogeneous nucleation at embedded particles has been observed in the cobalt binder in cemented carbides; precipitates are not generally found in the cobalt binder and have not been observed in the dimples on a fracture surface (Sigl and Exner 1987). However (Ranjan 1983) showed that the formation of stacking fault intersections can be achieved easily in materials with low stacking fault energies such as cobalt. Using geometric considerations,

(Ashbee 1967) postulated that when two stacking faults intersect, a volumetric dilation equivalent to a row of vacancies occurs along the line of intersection. This mechanism is very likely to be responsible for producing huge numbers of vacancies in the highly deformed cobalt within the multiligament zone (crack tip). (Cuitino and Ortiz 1996) described another mechanism which may be responsible for vacancy production during plastic slip - the motion of jogged screw segments. Jogged screw segments are formed mainly by dislocation intersection and by double cross slip as illustrated in (Figure 2.3). (Cuitino and Ortiz 1996) have furthermore described a 'vacancy condensation' void nucleation mechanism in FCC metals by which vacancies can diffuse towards each other by "pipe diffusion" along dislocations which are also present in huge numbers in the MLZ. To a lesser extent vacancies may diffuse by lattice diffusion at higher temperatures. The vacancies are therefore mobile and can cluster together to form microvoids within time frames relevant to quasi-static fracture.

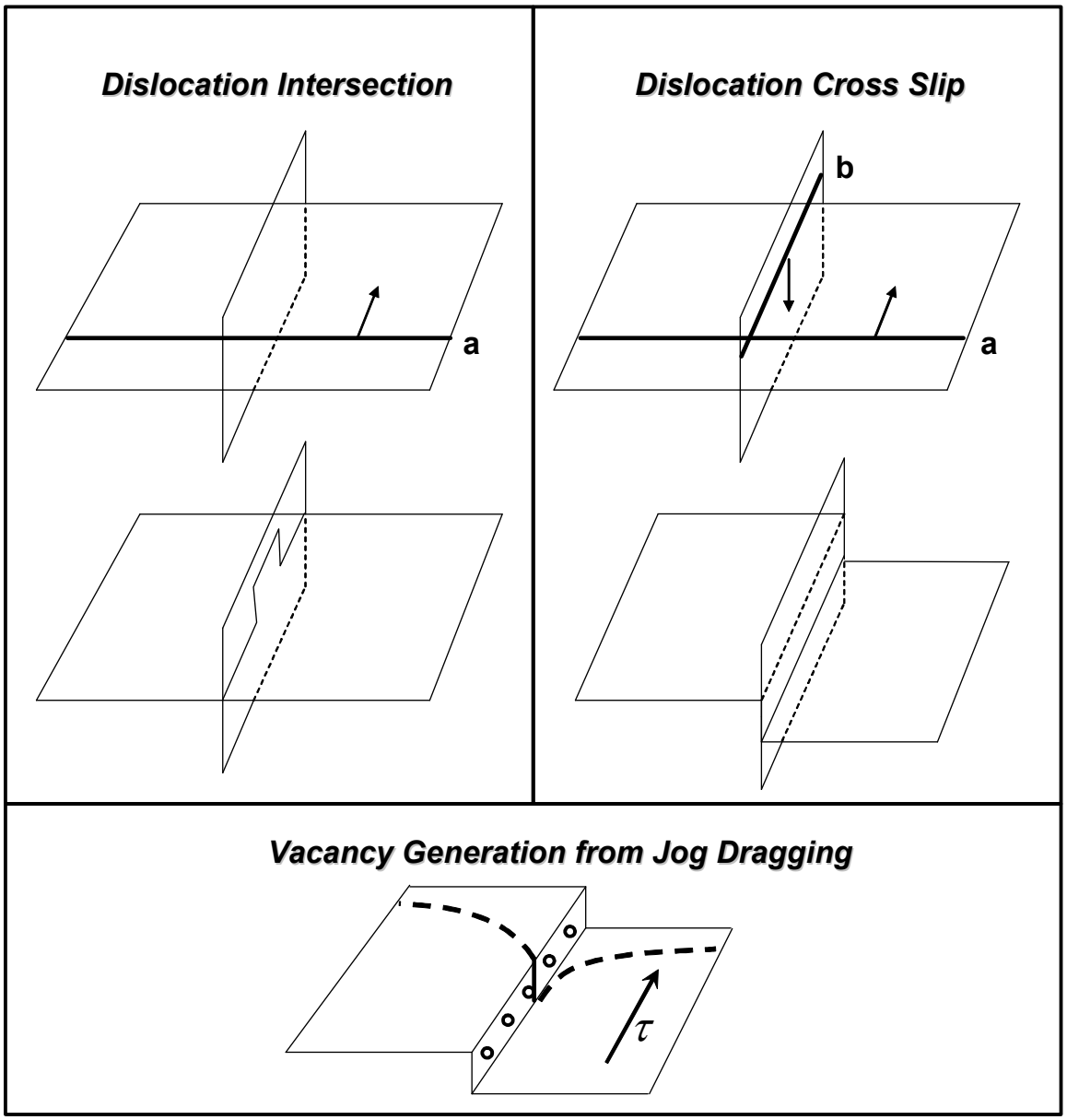

Figure 2.3. Dislocation intersection and dislocation cross slip combined with subsequent jog dragging are sources of vacancies in alloys

(Vijayaraju et al. 1986) confirmed this microvoid nucleation mechanism occurs experimentally, observing that *vacancies play a significant role in the initial stages of ductile fracture through micro-void nucleation*. Specifically related to WC-Co composites, (Murray and Smith 1973)

determined that *cobalt vacancy diffusion is thought to be a dominant deformation mechanism in tensile testing of Co-bonded WC composites*. As the formation of stacking faults occurs relatively homogeneously in the cobalt binder, the nucleated micro-voids are also expected to be dispersed homogeneously. This is in contrast to other alloys in which microvoid nucleation happens quite heterogeneously due to cracking or debonding of embedded precipitates.

Here we assume that a microvoid forms when a vacancy cluster reaches approximately the size of the mean distance between dislocations; this is consistent with the work of (Cuitino and Ortiz 1996) who reasoned that beyond this size, the voids could grow via macroscopic plasticity according to Rice and Johnson's theory (Rice and Johnson 1970). As a deformed FCC crystal can exhibit dislocation area densities approaching $10^{15} - 10^{16} m^{-2}$ (2D) the mean dislocation separation is approximately $20nm$ in 2D. This is taken as the initial radius of a void in the present study.

Macroscopically speaking, 'vacancy condensation' based microvoid nucleation is a stress and strain controlled process. Stress produces the stacking fault intersection where the vacancies are created. Plastic flow strain makes the vacancies mobile enough to cluster together via pipe diffusion.

2.1.5 Direct Numerical Simulation: Multiscale Failure of WC-Co

A direct numerical simulation of a typical microstructure is performed using finite element analysis (ABAQUS) as shown in (Figure 2.4). A large elastic homogenized WC-Co domain is

modeled i.e. material 1 in (Figure 2.4). Near the center of the model an embedded direct numerical simulation (DNS) of the WC-Co composite is modeled using approximately 22000 elements. Within the DNS region several carbide grains are modeled. These grains are perfectly bonded to the surrounding cobalt matrix. The carbide is modeled using a simple elastic-brittle smeared crack relation i.e. material 3 in (Figure 2.4). The cobalt regions are represented through an elastic-plastic constitutive relationship i.e. material 2 in (Figure 2.4). A pre-crack is modeled in the homogenized zone; the pre-crack tip ends directly at the interface between the homogenized and DNS regions. Quasi-static Mode I loading is applied to the system.

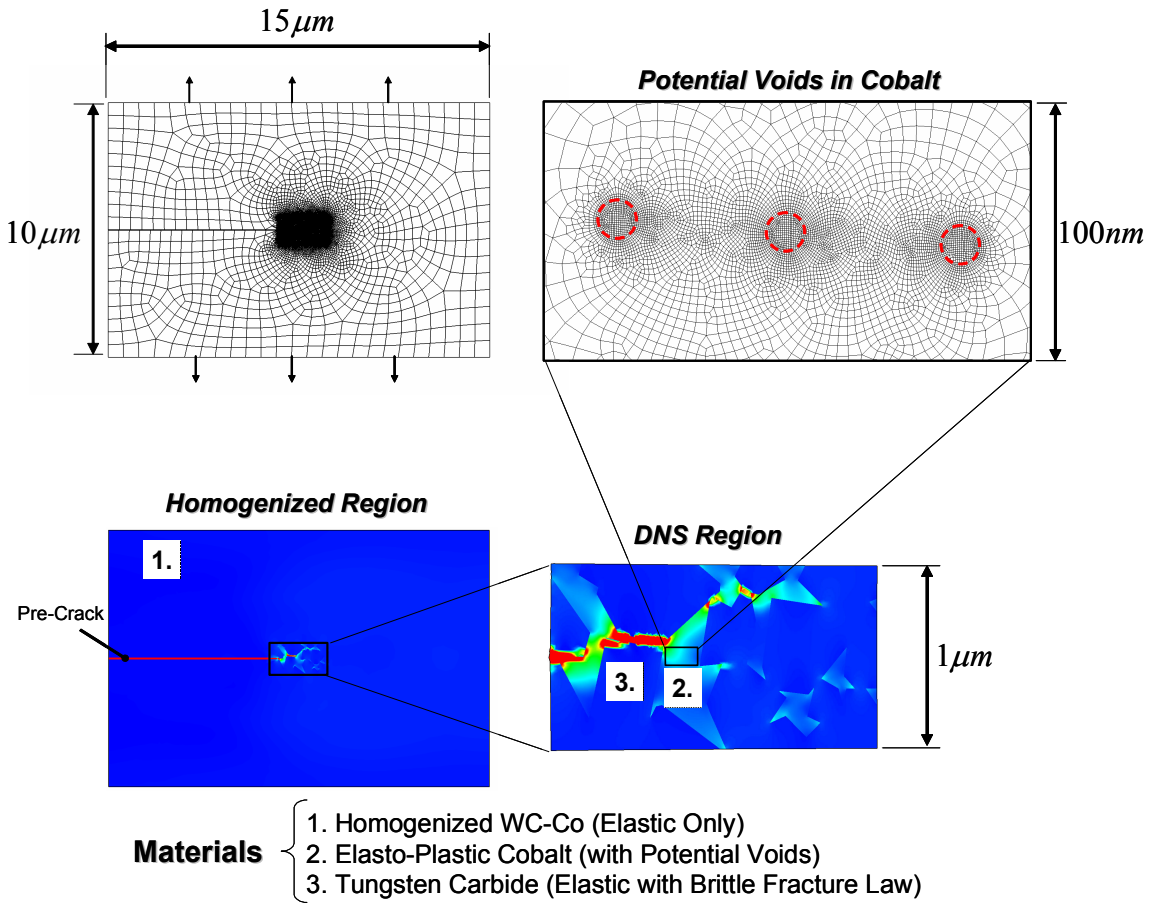

Figure 2.4. A finite element model of the WC-Co composite highlights the failure mechanism involving both brittle and ductile fracture. The cobalt region is shown in more detail in Figure 2.5

Nucleation of microvoids plays a key role in the subsequent composite failure and is modeled in the direct numerical simulation shown in (Figure 2.4). Within the cobalt zone, pre-defined sets of elements are given the following property: when any element in a group satisfies a void nucleation criterion, all of the elements in that group are deleted (stress is set to zero), instantly creating a void. The void nucleation criterion is given in terms of stress and strain and is described in Chapter 4, equation (4.3). This allows us to model void nucleation without explicitly creating a new void surface and remeshing. These element regions represent 'potential' void sites. Three of these potential voids are shown in (Figure 2.4).

2.1.6 Discussion of Multiscale Failure Mechanism: WC-Co

The resulting strain in the loading direction is plotted in (Figure 2.5); a single cobalt ligament is extracted for clarity and the strain contour is plotted on the undeformed configuration. The five stages in composite deformation and failure are observed:

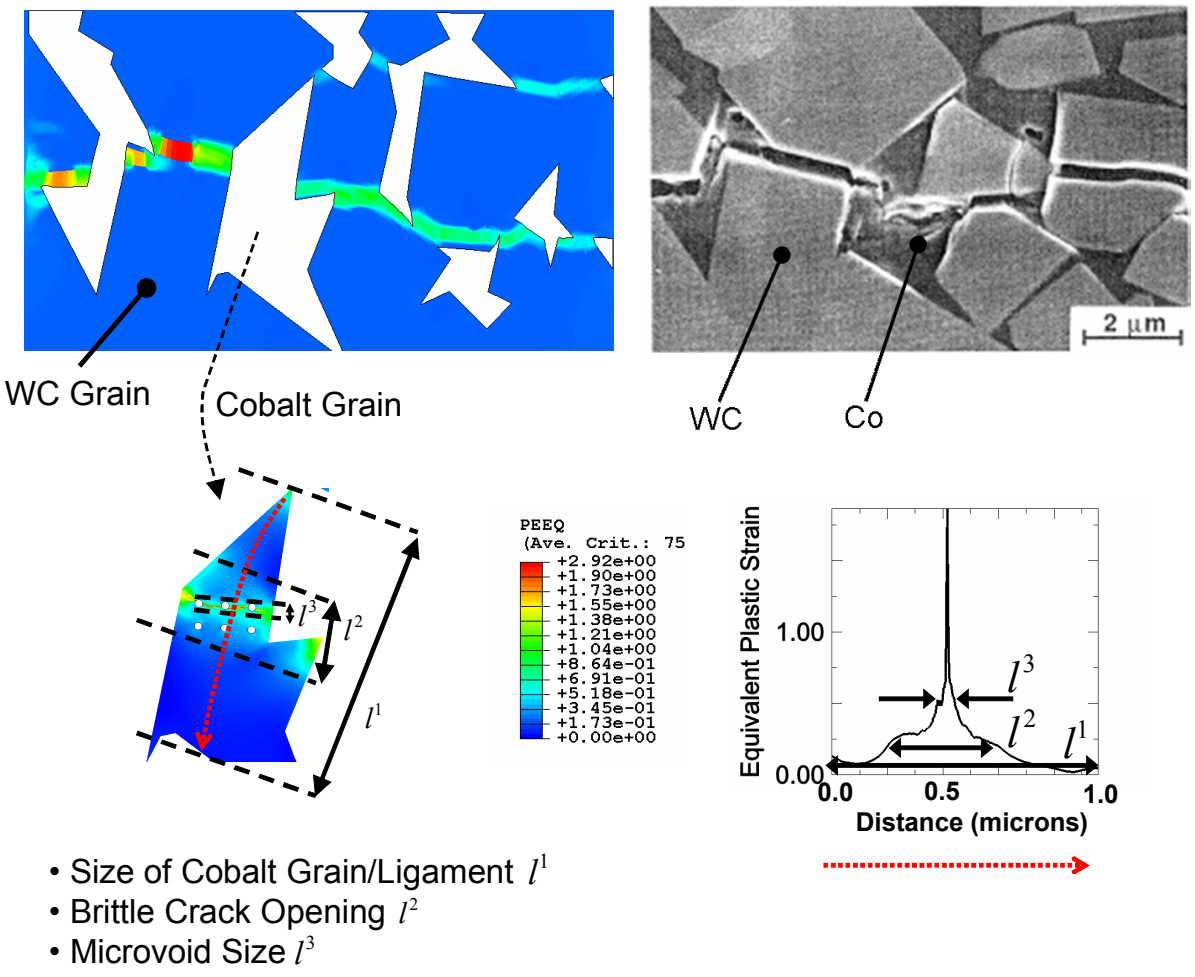

Figure 2.5. The characteristic length scales of inhomogeneous deformation within the cobalt are closely related to the microstructure

- The composite initially deforms homogeneously as the carbide and cobalt phases deform elastically.
- After brittle fracture occurs in the carbide grains, the resulting cobalt ligaments undergo significant plastic deformation and work hardening occurs across the entire ligament l^1 - the amount of work hardening is defined by the slope of the stress-plastic strain curve.

- As the stress within a ligament saturates the deformation localizes at the brittle crack tip l^2 - here the dimension of the brittle crack tip is given by the element size in the carbide.
- Vacancy driven void nucleation occurs (six voids reach the nucleation criteria as shown in Figure 2.5) in the cobalt ligament and deformation localizes between neighboring voids at scale l^3 equal to the void size.
- Strain then localizes within the micro-ligaments between voids; the micro-ligaments neck and rupture.

Each stage involves a transition of the inhomogeneous deformation to a smaller scale. Furthermore each stage is initiated by a particular *microstructural instability event* i.e. carbide fracture, cobalt stress saturation, cobalt microvoid nucleation, cobalt microvoid coalescence. The concept of microstructural instabilities is explained further in Section 5.4.3.

2.1.7 Previous Cemented Carbide Material Models

A number of attempts have been made to define the key microstructure-property relationships in tungsten carbide-cobalt composites. Most are semi-empirical models which rely on experimental coefficients from measured microstructural level data. These are summarized in Appendix A7.

Numerical Modeling

Several attempts have been made to model the microstructural deformation within a cemented carbide directly through numerical (finite element) analysis. Sigl (1988) showed that the ductile cobalt crack bridging mechanism dominates the toughening mechanism. Ljungberg (1986)

performed a fairly coarse finite element simulation in which several pre-fractured carbide grains were modeled directly. A very large plastic zone was observed which was several times larger than the characteristic size of the grain size in the region of the crack. This has been proven to be inaccurate by subsequent, more finely discretized finite element simulations, particularly those performed by Fischmeister et al. (1988). Qualitatively at least it was shown that upon brittle fracture of the WC phase the plastic zone size extends through the binder regions directly intersected by the crack i.e. over a distance related to the cobalt grain size.

Quinn et al. (1997) examined the behavior of the cobalt binder phase usual a crystal plasticity material model to describe the cobalt binder, while directly modeling the growth of periodically arranged voids within the binder. It was shown that initial void shape has very little effect on the subsequent growth and that dislocation constraint in the binder layers has a significant effect on binder layer strength. Connolly et al. (1999) and McHugh et al. (2003) developed a simplified model of the multiligament zone in which a pre-crack in a carbide plate was bridged with cobalt ligaments. The cobalt ligaments were modeled using several material models including crystal plasticity. Although the model was useful for examining the micromechanics of the crack bridging mechanism, the computed fracture toughness values were much lower than those observed experimentally. The strain tended to localize spuriously within the cobalt ligaments as they softened due to damage.

2.1.8 Design Considerations

The key micromechanics of a WC-Co composite have been outlined in Section 2.1. The important design considerations for a WC-Co composite are investigated further in Chapter 4 and are summarized as follows:

- Composite toughness can be improved by (i) increasing the cobalt volume fraction f or increasing the cobalt grain size d
- Both of these options result in a decrease in composite strength
- Composite toughness increases when ductile rupture in the cobalt binder is delayed
- Composite strength increases when brittle fracture in the carbide is delayed

A hierarchical constitutive model is developed in Chapter 4 which contains each of these relationships. This model is used within a multiresolution continuum theory in Chapter 7 to numerically predict fracture toughness in terms of the key microstructural design parameters.

2.2 High Strength and Toughness Steel

An overview of high strength and toughness steels is given here. In Section 2.2.1 a direct numerical simulation is performed to illustrate the length scales associated with failure of such an alloy. A brief discussion of the failure mechanism follows in Section 2.2.2.

In this work we idealize steel as an alloy matrix containing a population of embedded inclusions on the order of a micron and a population of spherical precipitates on the order of tens of nanometers (Hao et al. 2004; Hao et al. 2003). In materials such as 4340 steel, the inclusions are titanium nitrides, introduced as an impurity by-product of the raw material processing. They

contribute nothing to the strength but adversely affect the toughness; the weak interface tends to separate from the surrounding alloy matrix at low nominal strains, introducing voids. Alternatively the inclusions may crack again nucleating a void.

The precipitates in 4340 steel are typically titanium carbides which form during heat treatment. In general, precipitates are introduced to strengthen the alloy response by either:

- Grain Refinement: Preventing grain coarsening by pinning migrating grain boundaries (thereby resulting in smaller, stronger grains)
- Precipitate Strengthening: Impeding dislocation movement which means greater resolved shear stresses are required to plastically deform the alloy.

Although the precipitate-matrix interface is relatively strong, decohesion with the surrounding matrix (or even precipitate cracking) occurs at large nominal strains leading to the formation of microvoids; these microvoids can cause ductile failure.

2.2.1 Direct Numerical Simulation of a Steel Alloy: Set Up

An idealized model of a steel alloy containing the particles described above is now examined in order to observe the defamation and failure mechanism. In (Figure 2.6) two large inclusions have been modeled directly along with several smaller precipitate particles, using ABAQUS (ABAQUS 2004) finite element software (21000 elements). Quasi-static fully periodic displacement boundary conditions (Appendix A1) are applied to the 2D plane strain volume element, such that an average shear strain ε_{12} is applied. The other strain components are left unconstrained in order to avoid pressure build ups in the model. This means that although a shear

strain is applied, these are not zero triaxiality boundary conditions. Debonding of the inclusions and precipitates is included through an interfacial cohesive relationship. The alloy matrix is modeled using an elastic-linear plastic J2 flow plasticity model. The material properties are:

- Titanium Nitrides: Area Fraction 1%, Elastic Modulus $600GPa$, Poisson's Ratio 0.3, Interfacial Strength $0.1GPa$, Diameter 1 micron
- Titanium Carbide Particles: Area Fraction 0.1%, Elastic Modulus $600GPa$, Poisson's Ratio 0.3, Interfacial Strength $1.0GPa$, Diameter 200 nm
- Steel Alloy Matrix: Elastic Modulus $200GPa$, Poisson's Ratio 0.28, Initial Yield Stress $1.6GPa$, Hardening Modulus $0.65GPa$ (McVeigh et al. 2006b).

During deformation the weakly bonded inclusions and strongly bonded precipitates can debond from the surrounding matrix, via interfacial cohesive relationships, creating voids and microvoids respectively.

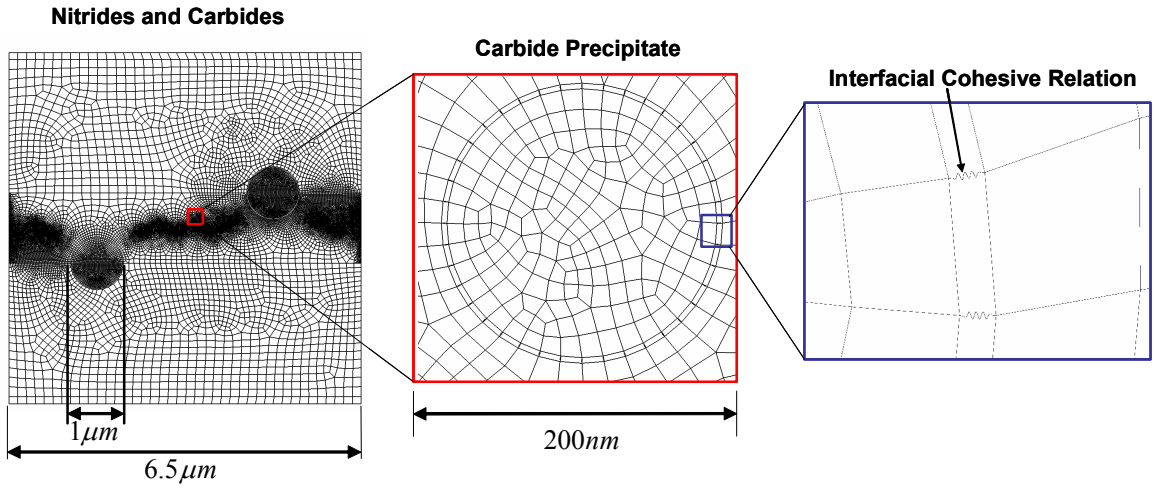

Figure 2.6. Nitride and Carbide particles are embedded in a steel alloy matrix; debonding is model through h an interfacial cohesive relation

The plastic shear strain contours are shown in (Figure 2.7) at nominal shear strains of 10%, 20% and 30%. The local true shear strain across a section is also plotted at each snapshot in time.

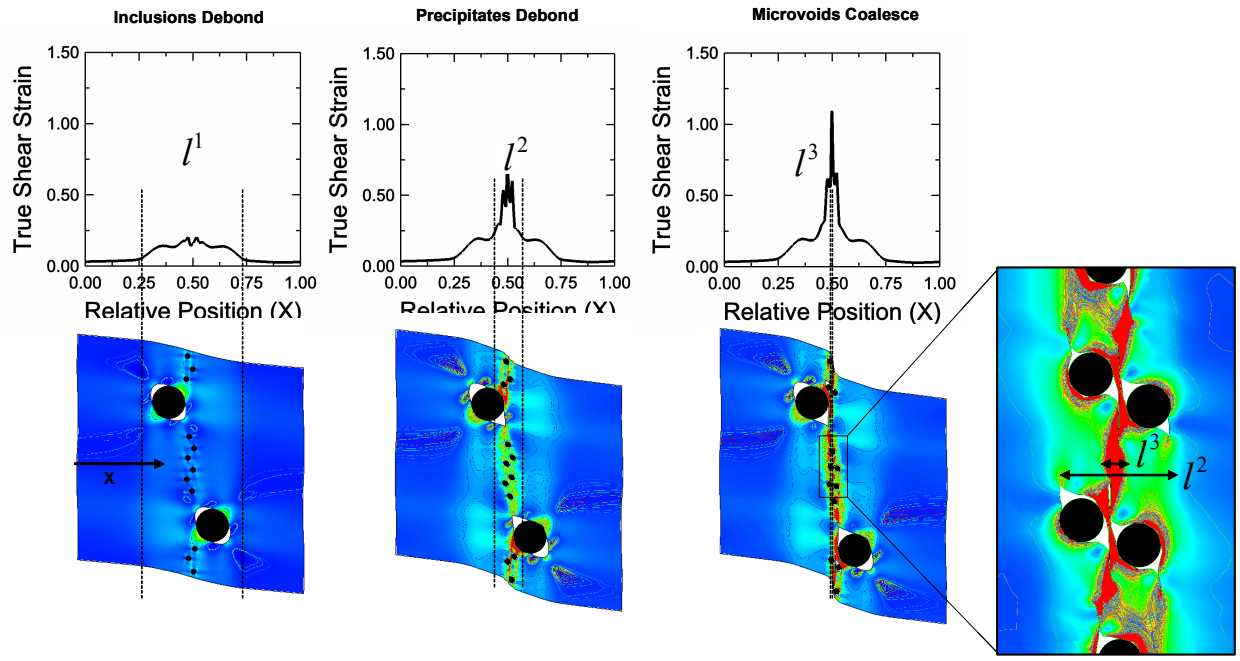

Figure 2.7. The characteristic length scales of inhomogeneous deformation are related to the underlying microstructure; primary inclusions, secondary precipitates and microvoid coalescence (X=1 corresponds to 6.5 microns).

2.2.2 Discussion of Multiscale Failure Mechanism: Steel Alloy

The alloy deformation and failure process illustrated in (Figure 2.7) can be described in four stages:

- Deformation is initially homogeneous as the matrix work hardens and the embedded particles deform elastically

- Inclusions debond at very low nominal strains < 2%; this is accompanied by very inhomogeneous deformation which localizes rapidly between the inclusion-nucleated voids at scale $l^1 \sim 3.5\mu m$ i.e. about three times the inclusion size.
- The local inhomogeneous strain field between these voids is large enough to drive interfacial decohesion of the strongly bonded precipitate particles, creating a population of microvoids between the inclusion-nucleated voids. Terminal strain localization occurs between the neighboring microvoids (McVeigh et al. 2006b) at a scale $l^2 \sim 0.7\mu m$ i.e. about three times the precipitate size. The material begins to rapidly lose load carrying capacity at this stage.
- The microvoids grow and coalesce, even under pure shear loading as shown on the far right in (Figure 2.7), encouraging further localization of deformation at scale $l^3 \sim 50nm$. In effect the coalescing microvoids link the larger inclusion level voids, allowing a ductile crack to propagate i.e. a void sheet mechanism occurs.

Each stage involves a transition of the inhomogeneous deformation to a smaller scale. Furthermore each stage is initiated by a particular *microstructural instability event* i.e. inclusion debonding, precipitate debonding, microvoid coalescence. The concept of microstructural instabilities is explained further in Section 5.4.3.

2.2.3 Design Considerations

In terms of materials design, the macroscale properties of a steel alloy are directly related to the underlying microstructure:

- Strength can be improved by increasing the number/volume fraction of precipitate particles (i.e. more grain refinement or precipitate strengthening)
- Toughness can be improved by reducing the volume fraction of inclusions (i.e. reducing the localized stress and strain concentration which drive microvoid nucleation between the inclusions)
- Toughness can be improved by increasing the interfacial strength of the precipitates (i.e. delaying microvoid nucleation and material instability)

Obviously it is impractical to model inclusions, precipitates and their debonding behavior directly within large scale numerical simulations. On the other hand, a homogenized continuum model which hopes to predict the correct macroscale response (e.g. fracture toughness) must capture the physical length scales of inhomogeneous deformation. A hierarchical constitutive model which contains each of the key design relationships is used in Section 6.4.2 within a multiresolution continuum framework. A similar model has been used by (Vernerey 2006) to predict the relationship between fracture toughness and the key microstructural parameters in a steel alloy.

A steel alloy with two scales of embedded particles is modeled in Section 6.3.3 using a multiresolution continuum theory which is outlined in Chapter 5. The key design relationships in a steel alloy have been explored by (Vernerey 2006) using the same theory.

2.3 Dynamic Adiabatic Shear Bands in High Strength Steel

The direct numerical simulation of high strength steel shown previously was performed under quasi-static loading conditions. As a result thermal effects arising from plastic dissipation is unimportant. However under dynamic loading temperature rise can be substantial, affecting the mechanical properties. Here we consider dynamic loading of an alloy containing a population of precipitates. Some background is given in Section 2.3.1. The instability mechanism associated with quasi-static loading is described in Section 2.3.2 and for dynamic loading in Section 2.3.3. Microvoid assisted shear banding is explained in Section 2.3.4. The length scales of shear banding are explained in Section 2.3.5.

2.3.1 Background

In various materials such as alloys, polymers and rocks, plastic instabilities may be explained by the formation of shear bands; narrow zones of material which undergo high levels of shearing relative to the surrounding material. As shown in (Figure 2.8) (Marchand and Duffy 1988) initial ‘stage 1’ deformation is quite uniform (regardless of loading rate) as the material work hardens. Under dynamic loading conditions a certain amount of strain rate hardening also occurs. Any temperature rise due to plastic dissipation is moderate due to the homogeneous nature of the deformation, even under dynamic loading conditions. Microvoid nucleation during the early stages of deformation is low.

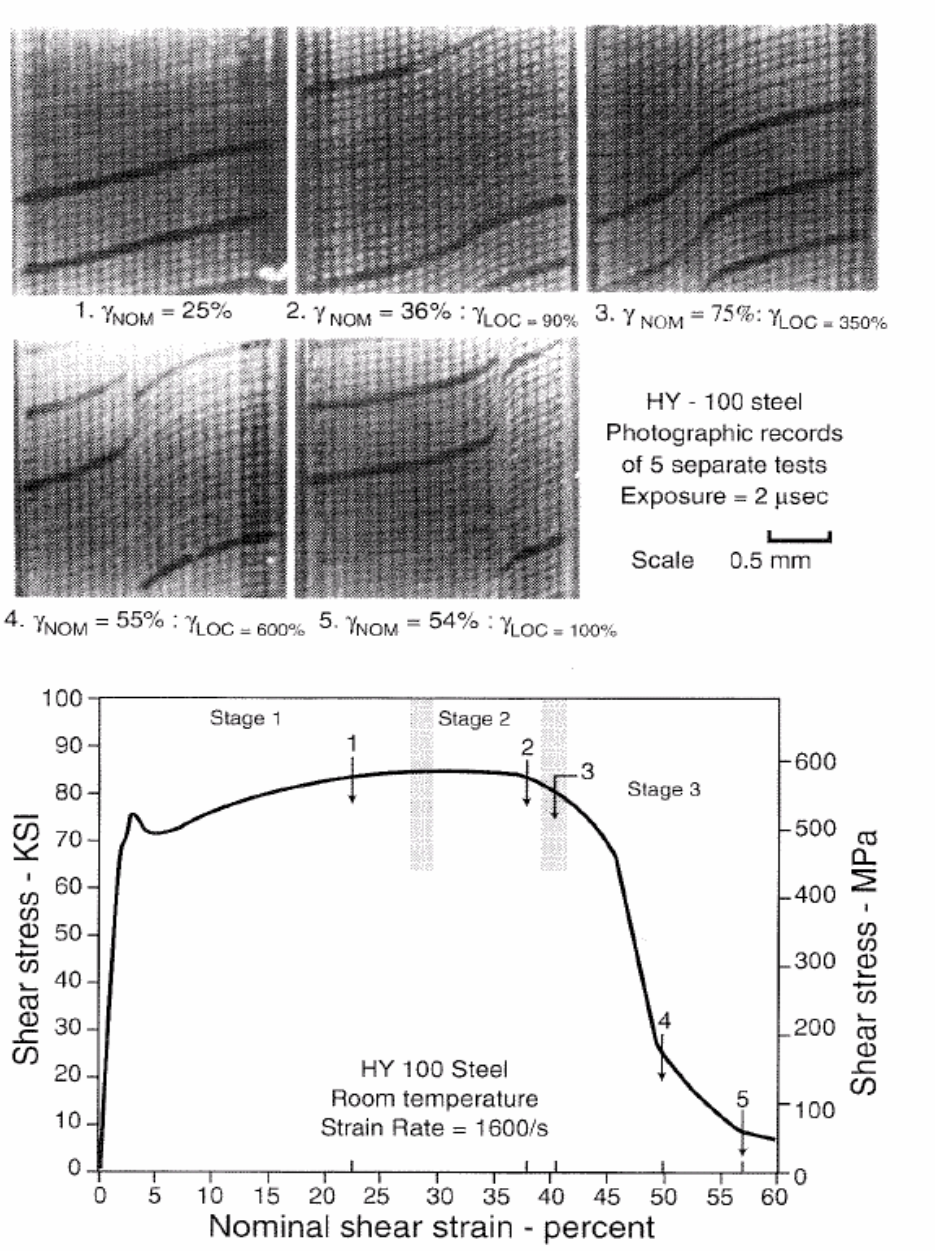

Figure 2.8. Adiabatic shear bands are bands of severe plastic strain localization which result in a nominal stress collapse. The inhomogeneous nature of the shear band is shown by comparing the local strain with the nominal strain; the resulting nominal stress is also shown: HY 100 Steel (Marchand and Duffy 1988)

The level of work hardening reduces during ‘stage 2’ either as a result of thermal softening, dynamic recovery, static recovery or even damage accumulation depending on the loading

conditions and material. As the stress passes through a maximum the first signs of shear band formation arise; deformation begins to occur non-uniformly. In (Figure 2.8) the nominal strain just after the material instability is $\gamma_{NOM} = 36\%$ while the local strain in the initiating shear band is $\gamma_{LOC} = 90\%$ indicating that deformation is already quite inhomogeneous (labeled number 2 at the top of Figure 2.8).

In 'stage 3' the material in the localizing region weakens further and the stress drops rapidly as a fully formed shear band develops. The phenomena which drive the material instability and the subsequent shear band deformation are discussed below for quasi-static and dynamic loading conditions.

2.3.2 Quasi-Static Loading: Microvoid Driven Shear Band

Under quasi-static loading conditions, deformation generally begins to localize due to microvoid nucleation, even under shear loading conditions (Cowie et al. 1989; McVeigh et al. 2006b). This process involves cracking or debonding of embedded particles as in the steel alloy shown in the previous section. Elastic energy stored in the surrounding material unloads into the weakened voided region resulting in localized deformation, further damage, degradation of the nominal flow stress and final material failure via a terminal microvoid driven shear localization band.

2.3.3 Dynamic Loading: Thermally Driven Adiabatic Shear Band

When loading is extremely rapid, such as during a high speed explosive impact or machining process, a significant temperature rise may occur due to plastic work dissipation. The actual softening mechanisms driven by temperature rise are

- increased thermal or dynamic dislocation recovery
- a reduction of the materials intrinsic resistance to dislocation glide
- grain recrystalization

It is generally believed that the instability of adiabatic flow alone can give rise to an adiabatic shear band (Wright 2002) without the assistance of microvoid nucleation. It should be noted that competing hardening mechanisms act to combat the thermal softening effect, stabilize the thermally softening material and delay the onset of adiabatic shear band formation as described in Appendix A5. Thermal conductance also delays the onset and severity of localization. However early studies into dynamic shear band formation tended to ignore the diffusive effects of conductance, giving rise to the misnomer '*adiabatic*' shear banding. Although the timescales involved are extremely small, so are the length scales and heat conductance is now accepted as being important in determining the post instability shear band behavior (Li et al. 2001; Li et al. 2002; Medyanik et al. 2005)

2.3.4 Dynamic Loading: Void Assisted Adiabatic Shear Bands

As explained by (Wright 2002), (Cowie et al. 1989) observed experimentally that microvoids nucleated along the sheared zone in double shear tests. In steel alloys these microvoids nucleate

due to precipitate (diameter $\sim 100nm$) debonding as described in Section 2.2. Shear localization was found to be delayed by performing the tests under an imposed compressive stress, presumably because this delayed the debonding process and hence delayed nucleation of microvoids. Microvoid nucleation was therefore determined to be the cause of terminal shear localization in high strength steels, under both quasi-static and dynamic loading conditions. (Anand et al. 1987) also included the effects of pressure in a perturbation analysis of adiabatic shear bands. Other authors have observed microvoid formation in torsion tests of alloys and metal matrix composites – see (Wright 2002).

To the author's knowledge, larger primary inclusion (diameter $\sim 1\mu m$) nucleated voids have not been discussed in the literature as a source of shear instability in alloys. It is noted that the role of the primary inclusions is discussed in the quasi-static analysis of steel, Section 2.2, and in Section 6.3.3. The goal of that work was to derive a constitutive model which worked over a range of triaxialities (McVeigh et al. 2006b). Primary inclusion debonding was considered as it was deemed to interact with the microvoids to cause a material instability (McVeigh et al. 2006b; Vernerey 2006). However in this thesis, the role of primary inclusions is not considered important in adiabatic shear bands, where almost zero triaxiality stress states occur.

Here we are interested in dynamic adiabatic shear bands in which the rate and strain hardening stabilizing effects are overcome by a combination of microvoid nucleation at the precipitate scale and thermal softening i.e. a void assisted adiabatic shear band. In Wright's wide ranging book on adiabatic shear bands (Wright 2002) he states that in personal communications, Weerasooriya has proposed that both void assisted shear and pure adiabatic shear must be considered in order

to fully understand adiabatic shear band formation in alloys but there is little work along this line in the literature.

2.3.5 Length Scales of Microvoid Assisted Adiabatic Shear Bands

The length scales which arise during the formation of an adiabatic shear band with damage are illustrated schematically in (Figure 2.9).

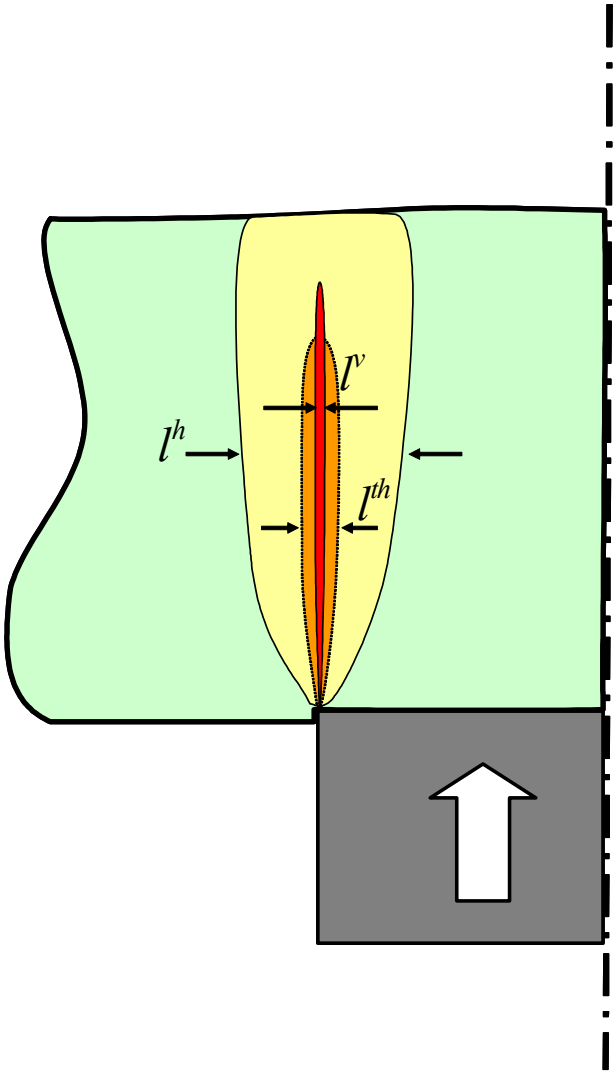

Figure 2.9. Microvoid assisted adiabatic sheer banding. Two characteristic length scales of inhomogeneous deformation are considered here; scale l^h corresponds to the diffuse (but high) external strain due to work hardening and scale l^v corresponds to the local post -instability strain in the shear band . Shear band widening also occurs due to thermal conductance. This is indicated by l^{th} .

Initial deformation is relatively homogeneous as the material hardens. The material deforms in a stable manner as rate and strain hardening dominate and thermal softening plays only a minor role. Deformation is quite diffuse, over a few hundred microns, l^h depending on the work hardening. As deformation increases, damage nucleates in the form of debonding precipitate particles. The thermal softening effect arising from plastic work dissipation (Section 3.3.4) and microvoid softening (Section 3.3.4) effects overcome the previously mentioned strain and rate hardening effects in the damaged region and deformation subsequently localizes at the scale of the microvoids l^v. Thermal conductance out of this region leads to a softening effect in the neighboring material and the shear band widens to a width l^{th}, related to the conductivity. It is noted that deformation may localize further to a smaller scale when the microvoids coalesce. Each of these events occurs over time scales on the order of a microsecond; the duration of time over which a material point undergoes homogeneous deformation is likely to be much longer than the time it takes for the stress to collapse once the material point becomes part of a shear band. In Chapter 8, these phenomena are modeled using a fully coupled thermal-multiresolution continuum model which is developed in Chapters 5 and 6.

2.3.6 Design Considerations

In terms of materials design, the shear band behavior in a steel alloy is directly related to the underlying microstructure. In terms of design, the ability of a shear band to penetrate a material is important. The key considerations are:

- Shear band velocity can be reduced by increasing the precipitates' interfacial strength or reducing the number of secondary precipitates (i.e. reducing the microvoid contribution to shear instability)
- Shear band velocity can be reduced by increasing the distance between precipitate particles, which acts to disperse the plastic deformation over a larger area
- Shear band velocity can be reduced by increasing the strain hardening, reducing the thermal softening, increasing the thermal conductivity.

Each of the key design relationships is explored in Chapter 8.

3 RVE Homogenization and Constitutive Modeling

As stated in the introduction, Chapter 1, a continuum material point represents the average behavior of a finite volume of the heterogeneous microstructure. The link between the continuum point and the microstructure is generally given through a constitutive relationship which in turn is usually calibrated to a mathematical constitutive model (the simplest case being the Young's modulus). The form of the mathematical model is chosen such that it can capture the character of the material behavior. In general a constitutive model involves several parameters (depending on the complexity of the material response) which can be calibrated to the specific material being modeled. This is achieved by correlating the mathematical constitutive model to either:

- the experimentally observed material behavior (tension, compression and torsion tests)
- the average response of a computational direct numerical simulation (DNS) of a volume of the microstructure which is large enough to be representative of the underlying inhomogeneities i.e. a representative volume element (RVE) as described in Chapter 1.

Should the latter approach be taken, there are several possibilities with respect to the type of boundary conditions that can be applied to the RVE. These boundary conditions are discussed in Section 3.1. An approach to extracting constitutive relationships from RVEs is described in Section 3.2. Section 3.3 and Section 3.4 describe two plasticity models used in the current thesis: the BCJ (Bammann-Chiesa-Johnson) model (Bammann et al. 1993) which is a rate, temperature and damage dependent model and a single crystal plasticity model (Asaro 1983b).

3.1 Computational RVE Boundary Conditions

In the RVE approach, a detailed microstructural configuration is modeled using a simulation technique such as finite element analysis; boundary conditions are applied to induce an evolving deformation. The average stress and strain over the RVE can be plotted against each other, in much the same way as the stress and strain are recorded during physical mechanical tests e.g. uniaxial, compression, shear tests. As in physical experiments, triaxiality, rate and temperature effects can also be examined by varying the applied boundary conditions. The extracted stress-strain behavior is then correlated to the chosen constitutive model via a set of material parameters or constants.

The types of boundary conditions which can be applied to a computational RVE are described in Section 3.1.1. A method for maintaining constant triaxiality is described in Section 3.1.2.

3.1.1 Boundary Conditions on an RVE Simulation

Several types of boundary conditions can be applied to the RVE. An average stress $\boldsymbol{\sigma}$ can be applied to the RVE through an applied traction $\mathbf{t}$ on the RVE surface S_0:

$$\mathbf{t} = \boldsymbol{\sigma} \bullet \mathbf{n} \quad \text{on} \quad S_0 \tag{3.1}$$

In practice, traction boundary conditions become unstable if the average stress decreases due to a material instability. For this reason, velocity based boundary conditions are often preferred.

An average deformation rate **D** can be applied to the RVE through the application of rigid velocity boundary conditions **v** on the RVE surface S_0:

$$\mathbf{v} = \mathbf{D}\bullet\mathbf{x} \quad \text{on} \quad S_0 \tag{3.2}$$

where **x** has an origin at the center of the RVE. In this case the boundaries remain flat and rigid, and the RVE tends to be over constrained, often leading to unphysical pressure build ups.

More general periodic boundary conditions can be applied by relating the displacements on opposite sides of the RVE. For a two-dimensional RVE with sides of length l and coordinate system (x_1, x_2) with an origin at the center of the RVE, an average deformation rate **D** may be imposed by requiring that the velocity **v** satisfies the conditions:

$$\begin{aligned} v_1\left(x_1, \frac{l}{2}\right) - v_1\left(x_1, -\frac{l}{2}\right) &= 2lD_{12} \qquad v_1\left(\frac{l}{2}, x_2\right) - v_1\left(-\frac{l}{2}, x_2\right) = lD_{11} \\ v_2\left(x_1, \frac{l}{2}\right) - v_2\left(x_1, -\frac{l}{2}\right) &= lD_{22} \qquad v_2\left(\frac{l}{2}, x_2\right) - v_2\left(-\frac{l}{2}, x_2\right) = 2lD_{21} \end{aligned} \tag{3.3}$$

(Figure 3.1) shows the different response when rigid and periodic velocity boundary conditions are used. In this example the matrix material is modeled as an isotropic elastic-plastic material with linear strain hardening. Several voids are modeled directly and a biaxial strain is applied. In both cases as the voids grow, strain localizes between them. When the periodic boundary conditions are used the localization bands extend physically into neighboring RVE's. When rigid boundary conditions are applied the localization bands terminate unphysically at the RVE boundary.

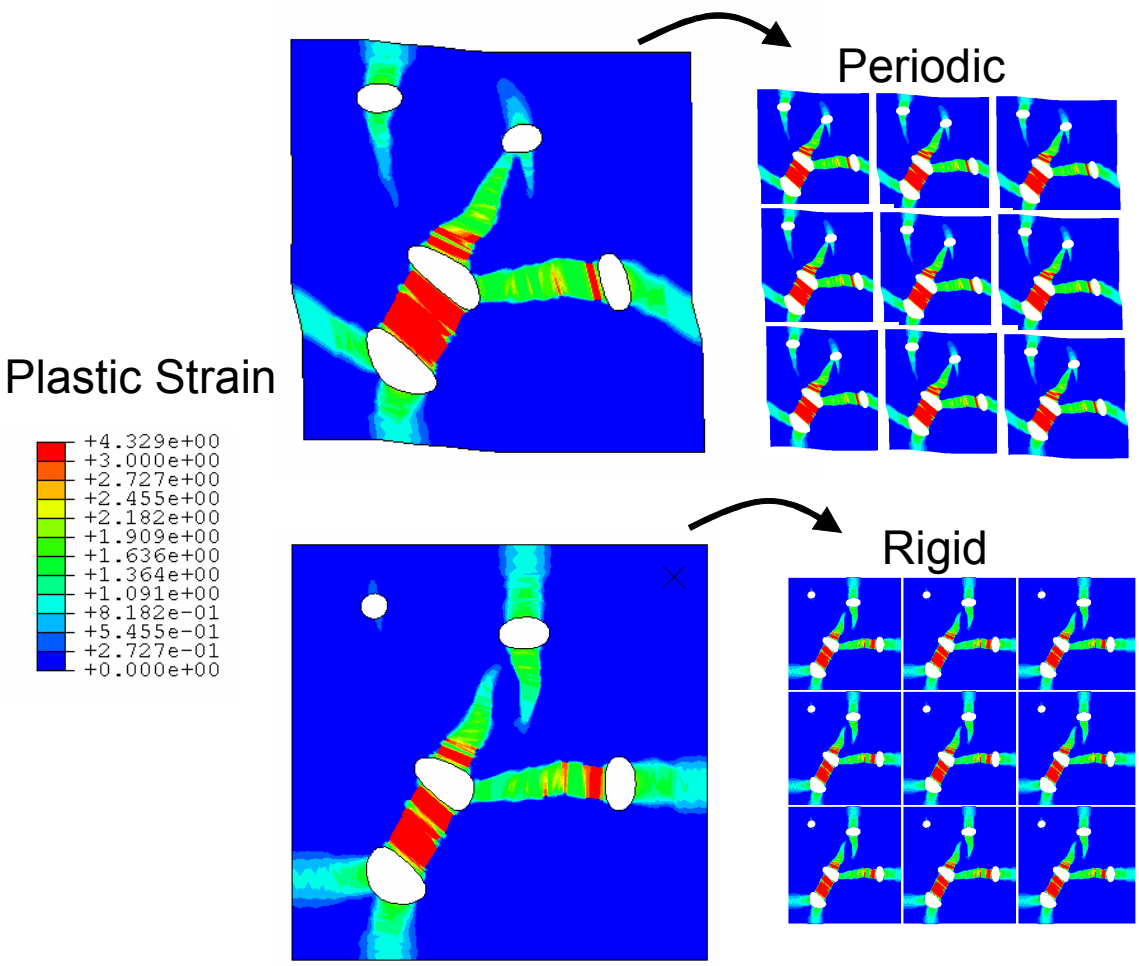

Figure 3.1. When rigid boundary conditions are used the deformation terminates at the interface.

Both approaches fail to capture the terminal behavior of localization i.e. a single localization path will always be favored over the others. The surrounding elastic energy then unloads into this path leading to terminal failure of the material. Although this failure event is not captured using the periodic boundary conditions, the general interaction between microstructural features is more naturally captured. These periodic boundary conditions are used throughout this thesis; application of periodic boundary conditions is explained further in Appendix A1. Research in the area of periodic boundary conditions is an ongoing topic e.g. (Mesarovic and Padbidri 2005).

3.1.2 Maintaining a Constant State of Triaxiality

In certain situations it is beneficial to study the deformation of an RVE while it is subjected to constant stress triaxiality. In this case the periodic boundary conditions, equation (3.3), may still be applied. A strain is applied in one direction only. At each increment in time the resulting stress state is computed and a corrector pressure is applied in the perpendicular direction to the applied strain to automatically bring the triaxiality back to the specified value (Socrate 1995) as shown in (Figure 3.2). This triaxiality corrector procedure is explained further in Appendix A2.

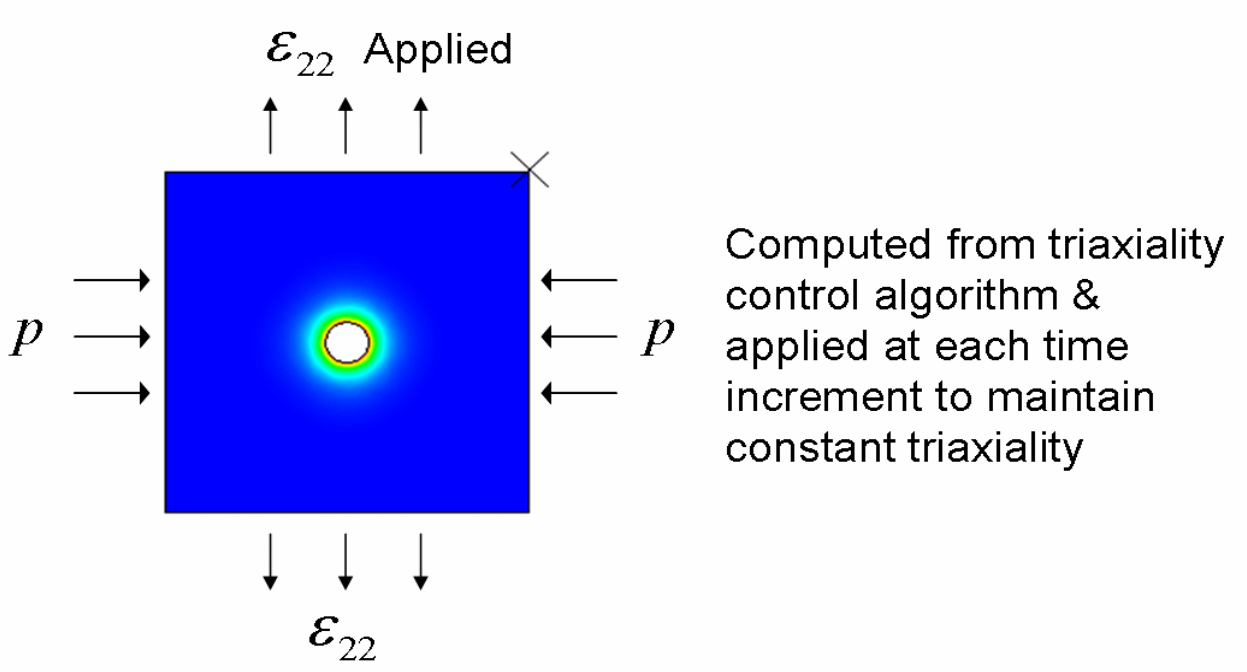

Figure 3.2. During simulation the triaxiality can be kept at a constant value by applying an evolving lateral pressure

3.2 Computational RVE Homogenization

(Figure 3.3) illustrates the approach taken to calibrate the macroscale constitutive model. The continuum stress $\boldsymbol{\sigma}$ is computed as a volume average of the local stress $\boldsymbol{\sigma}_m$ over the RVE V_0:

$$\boldsymbol{\sigma} = \frac{1}{V_0}\int_{V_0} \boldsymbol{\sigma}_m dV_0 = \frac{1}{S}\int_S \mathbf{t} \otimes \mathbf{x} dS$$
$$\sigma = \sqrt{\frac{3}{2}\boldsymbol{\sigma}^{dev} : \boldsymbol{\sigma}^{dev}} \tag{3.4}$$

where S is the current surface of the RVE. As shown, the divergence theorem is applied and the average stress is computed via the RVE surface traction $\mathbf{t}$. An equivalent stress measure σ has also been defined in terms of the deviatoric stress $\boldsymbol{\sigma}^{dev}$; this scalar quantity is often used in constitutive models.

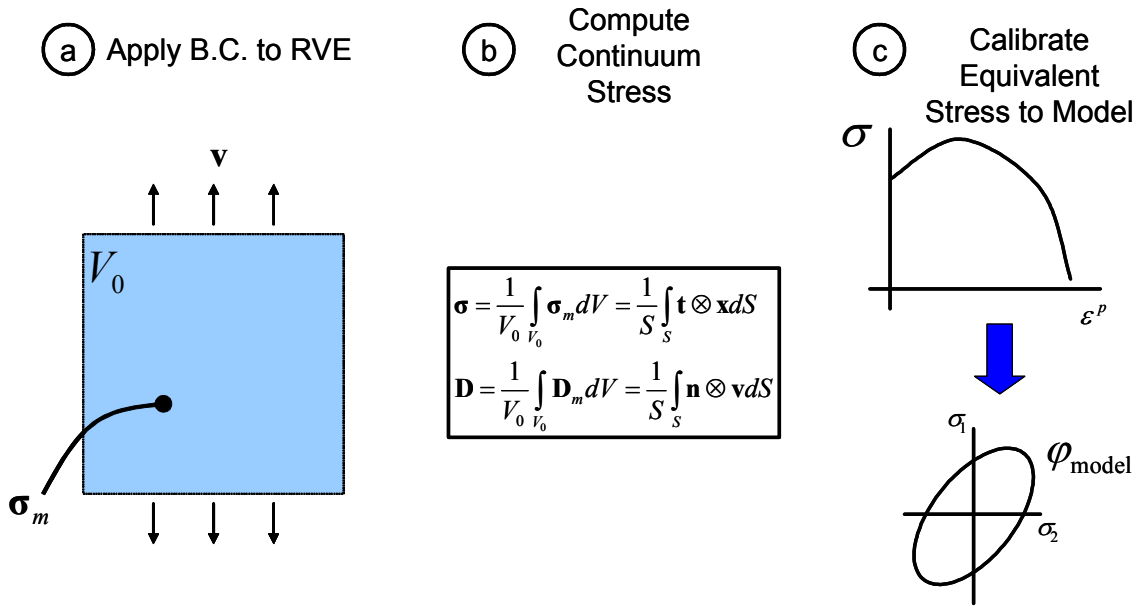

Figure 3.3. The average stress and strain over the RVE are averaged. The resulting stress-strain curve can be calibrated to a mathematical constitutive relation; effective stress and strain measures are often used.

The rate of deformation $\mathbf{D}$ can be computed as a volume average of the local deformation rate $\mathbf{D}_m$:

$$\mathbf{D} = \frac{1}{V_0}\int_{V_0} \mathbf{D}_m dV = \frac{1}{S}\int_S \mathbf{n} \otimes \mathbf{v} dS$$
$$\dot{\varepsilon}^p = \sqrt{\frac{2}{3}\mathbf{D}^p : \mathbf{D}^p} \tag{3.5}$$

where an effective plastic strain rate $\dot{\varepsilon}^p$ can also be defined in terms of the plastic part of the rate of deformation $\mathbf{D}^p$. This is often used in constitutive models.

3.3 Constitutive Models – BCJ Model

In this thesis, the BCJ (Bammann-Chiesa-Johnson) internal state variable constitutive model developed by (Bammann et al. 1990) is primarily used to model plasticity in alloys. This model has been tested extensively at Sandia National Labs and is used extensively in the literature (Horstemeyer et al. 2000a; Horstemeyer et al. 2000b; Horstemeyer et al. 2003). The elastic constitutive relationship and plastic flow equations are given in Section 3.3.1. The equations for the internal state variables relating to dislocation hardening and recovery are given in Section 3.3.2. The physics underlying these phenomenological equations are described in Section 3.3.3. The internal state variables relating to temperature and porosity are described in Section 3.3.4. A uniaxial simplification is given in Section 3.3.5 in order to describe the key relationships in the model. A comparison is made to the well known Gurson and Johnson-Cook models in Section 3.3.6. The uniaxial simplification is used in Section 3.3.7 to show the effect of temperature and damage on the stress state. A table with all of the BCJ equations is given in here.

Description	Relationship	Eqn.		Description
Rate Dependent Plastic Flow	$\mathbf{D}_p = \mathrm{f}\sinh\left[\frac{\left[\sqrt{\frac{3}{2}}\lVert\boldsymbol{\xi}\rVert - \left(Y(\vartheta)+\kappa\right)(1-\phi)\right]}{\mathrm{V}(1-\phi)}\right]\frac{\boldsymbol{\sigma}^{dev}}{\lVert\boldsymbol{\sigma}^{dev}\rVert}$	(3.9)	f	Reference Strain Rate
			V	Magnitude of Rate Effect
Rate Independent Yield Stress	$Y(\vartheta)=\mathrm{C}_1\left[1-\left(\frac{\vartheta-\vartheta_0}{\vartheta_m-\vartheta_0}\right)^t\right]+\mathrm{C}_2 d^{-1/2}$	(3.11)	d	Cobalt Grain Size
			t	Thermal Softening Exponent
			θ_0	Initial Temperature
			θ_m	Melt Temperature
			C_1	Initial Yield Stress
			C_2	Hall-Petch Effect
Isotropic Hardening & Recovery Moduli	$H(\vartheta)=\mathrm{C}_3\vartheta+\mathrm{C}_4$	(3.13)	C_3	Hardening Modulus Constants
			C_4	
	$R_d(\vartheta)=\mathrm{C}_5\exp\left(-\frac{\mathrm{C}_6}{\vartheta}\right)$		C_5	Dynamic Recovery
			C_6	
	$R_s(\vartheta)=\mathrm{C}_7\exp\left(-\frac{\mathrm{C}_8}{\vartheta}\right)$		C_7	Static Recovery
			C_8	
Kinematic Hardening & Recovery Moduli	$h(\vartheta)=\mathrm{C}_9\vartheta+\mathrm{C}_{10}$		C_9	Hardening Modulus
			C_{10}	
	$r_d(\vartheta)=\mathrm{C}_{11}\exp\left(-\frac{\mathrm{C}_{12}}{\vartheta}\right)$		C_{11}	Dynamic Recovery
			C_{12}	
	$r_s(\vartheta)=\mathrm{C}_{13}\exp\left(-\frac{\mathrm{C}_{14}}{\vartheta}\right)$		C_{13}	Static Recovery
			C_{14}	
Damage	$\dot{\eta} = \mathcal{N}\lVert\mathbf{D}_p\rVert$	(3.15)	$\mathcal{N}$	Nucleation
	$\dot{v} = \mathcal{G}\lVert\mathbf{D}_p\rVert$	(3.16)	$\mathcal{G}$	Growth
	$\phi_{coal} = \mathcal{C}\eta v$	(3.18)	$\mathcal{C}$	Coalescence
Adiabatic Temperature	$\dot{\vartheta} = \frac{h_c}{\rho c_{pt}}\boldsymbol{\sigma}:\mathbf{D}^p$	(3.21)	c_{pt}	Specific Heat
			ρ	Density
			h_c	Heat fraction

Table 3.1 Key Equations and Constants in BCJ model

3.3.1 Elastic and Plastic Equations

The BCJ (Bammann et al. 1990) model describes the stress state in terms of four internal state variables which in turn are representative of the microstructural evolution

- a scalar variable κ which represents an isotropic dislocation hardening/recovery effect, equation (3.12)
- a tensor variable $\boldsymbol{\alpha}$ which represents a kinematic dislocation hardening/recovery effect, equation (3.12)
- a scalar variable ϕ which represents the porosity, equation (3.17)
- the temperature ϑ, equation (3.21)

The porosity variable ϕ represents the void volume fraction and describes the average effect of nucleation, growth and coalescence of voids on the yielding behavior. The temperature rise is generally due to plastic work dissipation; both adiabatic temperature rise and conductance effects are considered in this thesis. Details on the implementation (integration) of the BCJ model can be found in (Horstemeyer et al. 2000b).

Elastic Constitutive Relationship

The BCJ model assumes an additive decomposition of the total deformation rate and spin tensor into elastic and plastic parts (Belytschko et al. 2000):

$$\begin{aligned} \mathbf{D} &= \mathbf{D}_e + \mathbf{D}_p \\ \mathbf{W} &= \mathbf{W}_e + \mathbf{W}_p \end{aligned} \tag{3.6}$$

The objective stress rate $\boldsymbol{\sigma}^{\nabla}$ is related to the Cauchy stress $\boldsymbol{\sigma}$ by

$$\boldsymbol{\sigma}^{\nabla} = \dot{\boldsymbol{\sigma}} - \mathbf{W}_e \bullet \boldsymbol{\sigma} + \boldsymbol{\sigma} \bullet \mathbf{W}_e \tag{3.7}$$

Furthermore, the elastic constitutive relationship involving the objective rate $\boldsymbol{\sigma}^{\nabla}$ may be written in terms of the elastic part of the deformation rate $\mathbf{D}_e$, the elastic bulk and shear moduli K_e and G_e and the damage ϕ (Bammann et al. 1993; Bammann et al. 1990):

$$\boldsymbol{\sigma}^{\nabla} = (1-\phi)\left[\left(K_e - \frac{2}{3}G\right) tr(\mathbf{D}_e)\mathbf{I} + 2G_e\mathbf{D}_e\right] - \frac{\dot{\phi}}{(1-\phi)}\boldsymbol{\sigma} \tag{3.8}$$

where $\mathbf{I}$ is the identity tensor. In order to determine the stress from this constitutive relationship, an expression for the rate of plastic deformation $\mathbf{D}_p$ is required.

Rate of Plastic Deformation $\mathbf{D}_p$

The plastic part of the deformation rate $\mathbf{D}_p$ is assumed to have a strongly non-linear dependence on the deviatoric stress through the deviatoric flow rule:

$$\mathbf{D}_p = \mathrm{f}\sinh\left[\frac{\left[\sqrt{\frac{3}{2}}\|\boldsymbol{\xi}\| - \left(Y(\vartheta) + \kappa\right)(1-\phi)\right]}{\mathrm{V}(1-\phi)}\right]\frac{\boldsymbol{\sigma}^{dev}}{\|\boldsymbol{\sigma}^{dev}\|} \tag{3.9}$$

where the net deviatoric stress $\boldsymbol{\xi}$ is given by:

$$\boldsymbol{\xi} = \boldsymbol{\sigma}^{dev} - \frac{2}{3}\boldsymbol{\alpha} \tag{3.10}$$

It remains only to describe expressions for the rate independent initial yield stress $Y(\vartheta)$, magnitude of rate effect V, reference strain rate f, porous damage ϕ, isotropic hardening, κ,

kinematic hardening $\boldsymbol{\alpha}$ and temperature ϑ. A comparison with the well known Gurson and Johnson Cook models is made in the one dimensional simplification which follows later in this section.

Initial Yield Stress $Y(\vartheta)$

The initial yield stress is temperature, rate and grain size dependent. The temperature ϑ is measured in Kelvin (K). Three separate temperature dependent parameters describe the initial yield stress; a rate independent yield stress $Y(\vartheta)$ and two rate parameters:

- f is the reference strain rate i.e. the strain rate at which the initial yield stress exhibits a transition from being rate independent (low rates) to being rate dependent (higher rates).
- V describes the magnitude of the rate dependency of initial yield.

An expression for the rate dependent yield stress Υ is given later in Section 3.3.5, equation (3.26). (Figure 3.4) gives an overview of the effect of the rate parameters f and V on the initial yield stress. Increasing V increases the amount of rate hardening. Increasing the reference strain rate f increases the strain rate at which rate hardening becomes significant.

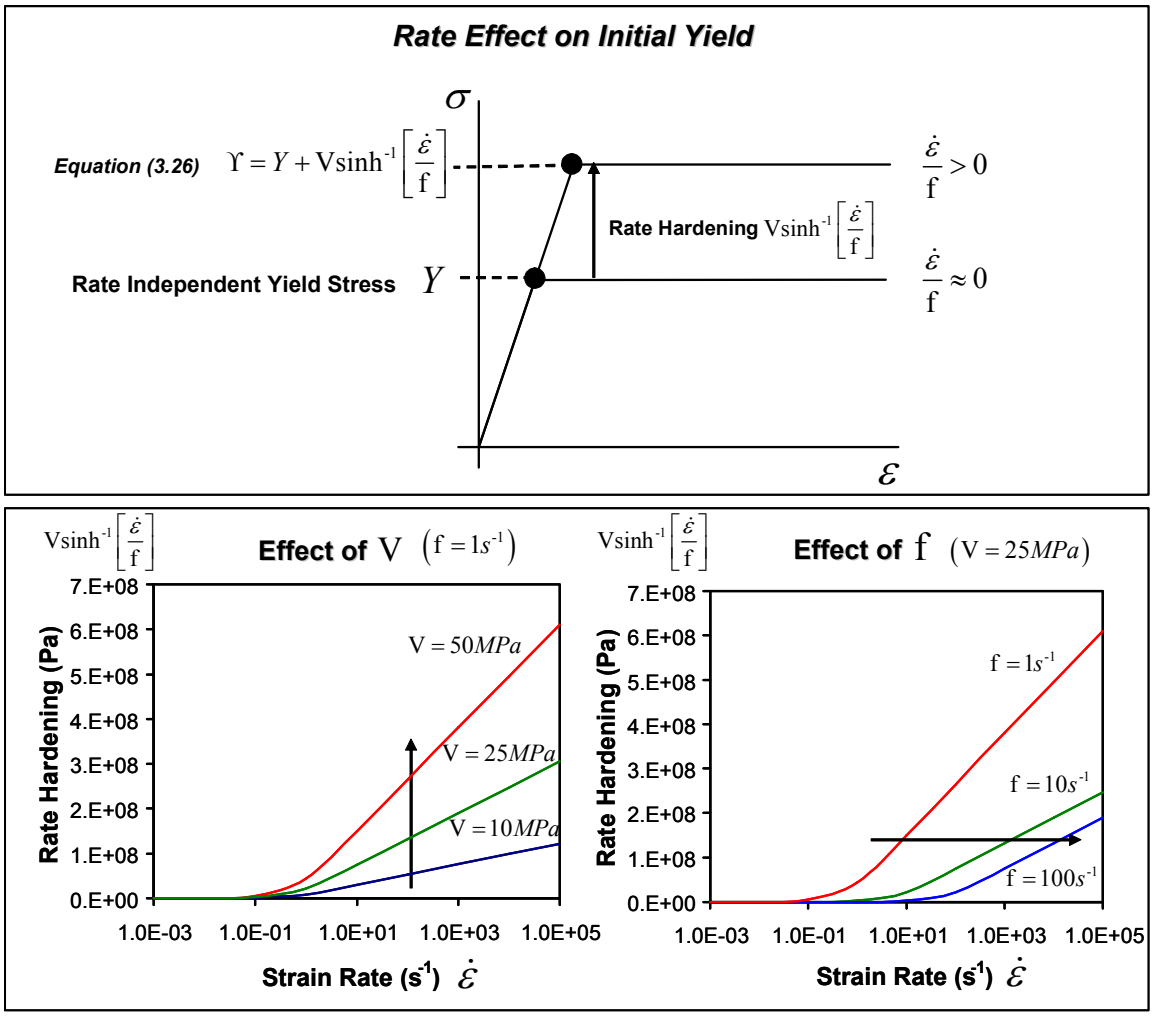

Figure 3.4. The rate dependency of initial yield is illustrated in the top graph. Increasing rate increases the initial yield stress. The magnitude of this increase is controlled by the parameter V. The rate at which the yield stress becomes rate dependent is controlled by parameter f.

The temperature dependence of the rate effects V and f are not considered here. In other words the rate dependency of initial yield is temperature independent. This may be untrue under extremely high temperatures. Furthermore, a general form for the rate independent yield stress is given in terms of the temperature ϑ and grain size d as follows:

$$Y(\vartheta) = C_1\left[1-\vartheta^*\right] + C_2 d^{-1/2}$$

where (3.11)

$$\vartheta^* = \left(\frac{\vartheta-\vartheta_0}{\vartheta_{mp}-\vartheta_0}\right)^t$$

where ϑ_0 and ϑ_m are the initial and melt temperatures and the thermal exponent t which is usually very close to 1 for alloys, introduces a slight non-linear character to the thermal softening. A similar grain size dependency has been introduced by many authors including (Quinn et al. 1997). The constant C_1 can be interpreted as the temperature and grain size independent yield stress and C_2 describes the magnitude of the Hall-Petch grain size effect i.e. as the grain size d decreases, the initial yield stress increases. This is usually explained in terms of grain boundary dislocation blocking. Smaller grains result in more grain boundary surface area. Grain boundaries impede dislocation motion resulting in a higher yield stress (Courtney 2000).

3.3.2 Internal State Variables: Hardening and Recovery (κ & α)

The internal state variables describe the state of the microstructure (e.g. dislocations, temperature, damage) and evolve with it. For example as dislocation density increases the isotropic hardening stress κ increases; the evolution equations for the internal state variables are written in terms of the strain, strain rate, temperature and stress triaxiality. The isotropic and kinematic stresses (κ

and $\boldsymbol{\alpha}$) are dealt with in this sub-section; a brief overview of the physics behind the resulting phenomenological equations is given in Section 3.3.3. The porosity ϕ and temperature ϑ are described in Section 3.3.4.

The evolution equations for the isotropic hardening stress κ and kinematic hardening stress $\boldsymbol{\alpha}$ used in the plastic flow relation, equation (3.9), are motivated by dislocation mechanics and are written in a phenomenological hardening-recovery format first developed at SNL by (Bammann et al. 1993). The result is a rate and temperature dependent isotropic hardening/recovery function:

$$\begin{aligned} \dot{\kappa} &= H(\vartheta)\left\|\mathbf{D}_p\right\| - \left[R_d(\vartheta)\sqrt{\frac{2}{3}}\left\|\mathbf{D}_p\right\| + R_s(\vartheta) \right]\kappa^2 \\ \boldsymbol{\alpha}^{\nabla} &= h(\vartheta)\mathbf{D}_p - \left[r_d(\vartheta)\sqrt{\frac{2}{3}}\left\|\mathbf{D}_p\right\| + r_s(\vartheta) \right]\sqrt{\frac{2}{3}}\|\boldsymbol{\alpha}\|\boldsymbol{\alpha} \end{aligned} \tag{3.12}$$

where $H(\vartheta)$ and $h(\vartheta)$ are temperature dependent hardening parameters, $R_d(\vartheta)$ and $r_d(\vartheta)$ describe the magnitude of dynamic recovery, and $R_s(\vartheta)$ and $r_s(\vartheta)$ describe the magnitude of static (sometimes called thermal) recovery. Together they are able to represent non-linear stress-strain response over a large strain regime. The hardening moduli simply describe a linear hardening response. However the recovery terms in each equation introduce a non-linear effect. These rate equations are of a form which reaches a saturation level i.e. they are not intended to reproduce a softening effect. Softening occurs due to thermal softening, equation (3.11) and porosity damage, equation (3.9) and (3.25).

Here, the hardening moduli are assumed to degrade with temperature in a linear manner for simplicity. The temperature dependency of the recovery moduli is given in terms of Arrhenius type non-linear functions (Bammann et al. 1993; Bammann et al. 1990) to capture the rapid increase in recovery with temperature:

$$\left.\begin{aligned} H(\vartheta) &= C_3\vartheta + C_4 \\ R_d(\vartheta) &= C_5 \exp\left(-\frac{C_6}{\vartheta}\right) \\ R_s(\vartheta) &= C_7 \exp\left(-\frac{C_8}{\vartheta}\right) \end{aligned}\right\} \textit{Isotropic}$$

$$\left.\begin{aligned} h(\vartheta) &= C_9\vartheta + C_{10} \\ r_d(\vartheta) &= C_{11} \exp\left(-\frac{C_{12}}{\vartheta}\right) \\ r_s(\vartheta) &= C_{13} \exp\left(-\frac{C_{14}}{\vartheta}\right) \end{aligned}\right\} \textit{Kinematic} \qquad (3.13)$$

A discussion on how to derive the various constants from physical experiments is given in (Bammann et al. 1993) and is outlined in Appendix A3 for cobalt.

3.3.3 Physical Basis of Dislocation Hardening/Recovery

A brief overview of the hardening and recovery mechanisms in alloys is now offered; these mechanisms are captured phenomenologically by the hardening and recovery stresses, equations (3.12). Of course these actual mechanisms are not simulated as such in the BCJ model; however their effect on the stress state is captured via equations (3.12) and (3.13). The following discussion is split into dislocation hardening, dynamic recovery and static recovery.

Dislocation Hardening Mechanisms (H, h)

The scalar isotropic stress κ describes an average of the grain boundary dislocation effects over many grains and hence has no direction. On the other hand, kinematic hardening $\boldsymbol{\alpha}$ arises from dislocations within the grains, and hence direction effects can be accounted for; the kinematic hardening is in tensor form. In both hardening/recovery measures, linear hardening is assumed to arise due to dislocation interactions. In (Figure 3.5) two dislocation hardening mechanisms are illustrated. The first is easy glide, followed by dislocation-dislocation interactions, and is described as a '*soft obstacle*'. (Courtney 2000). Dislocations have a non-local effect due to the atomic scale dilation and stress field they introduce in the surrounding atomic structure. An energy barrier exists which must be overcome in order to force dislocations on neighboring slip planes past each other i.e. energy must be supplied for a dislocation to travel through the stress field induced by a nearby dislocation.

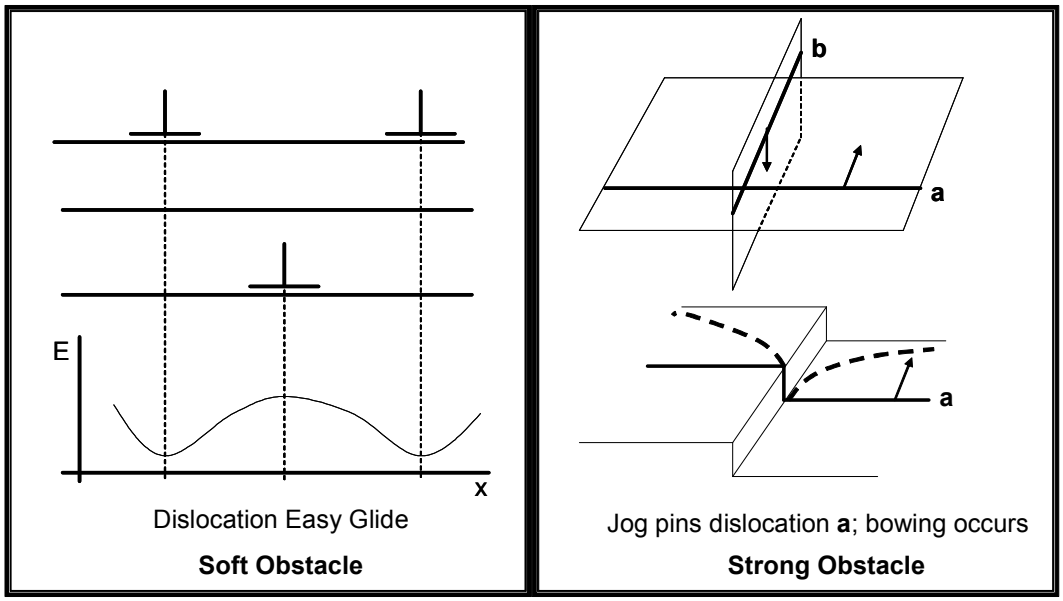

Figure 3.5. Dislocation hardening arises due to dislocation obstacles; these are generally classified as soft or strong (Courtney 2000)

Jog formation is known as a *strong* obstacle as dislocations are directly interacting with each other, often leading to dislocation bowing. Much more energy is required to overcome this type of interaction. During the initial stages of plastic deformation, large numbers of dislocations are produced creating networks of interacting dislocations which impede deformation either though direct or indirect dislocation interactions i.e. work hardening occurs. Other 'strong obstacle' dislocation hardening mechanisms include precipitation and grain boundary hardening (Courtney 2000).

Dynamic Dislocation Recovery Mechanisms $\left(R_d, r_d\right)$

Dislocation recovery mechanisms are also active in the material, competing with the hardening mechanisms. As shown in (Figure 3.6) the energy required for a dislocations to by-pass an impeding obstacle (e.g. another dislocation, an embedded precipitate) may be supplied either

through an applied stress or from thermal activation (i.e. heating the material). The dynamic recovery terms in equation (3.12) describe the recovery which occurs when the energy barrier is supplied mostly by an applied stress. The actual dislocation recovery process in this case is usually slip i.e. a dislocations by-passes an obstacle by traversing onto a neighboring slip plane. (Figure 3.7) illustrates how a dislocation can 'cross-slip' from a 111 plane onto a $1\bar{1}1$ plane in order to by-pass an obstacle. As this is a slip based mechanism, it occurs on the same time scale as regular dislocation glide – no additional rate dependence arises.

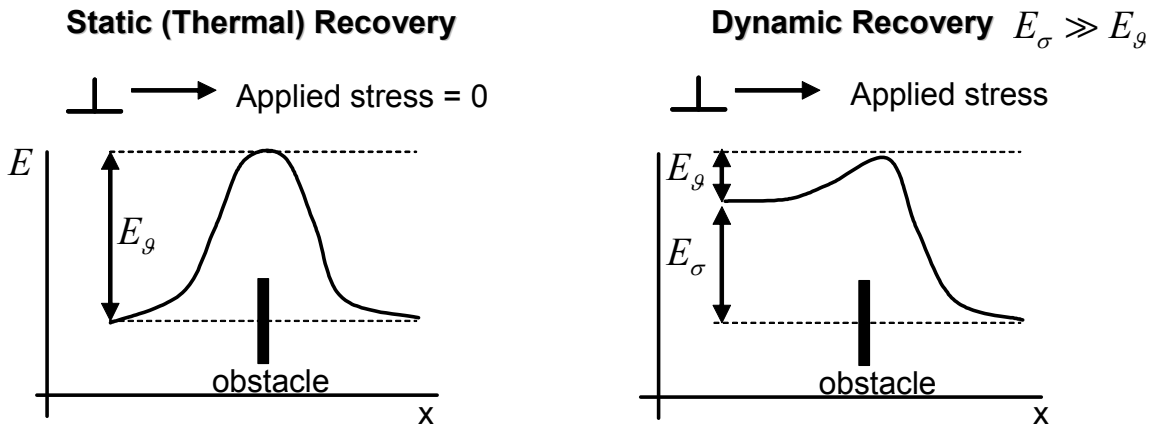

Figure 3.6. Obstacles can be overcome if enough energy is supplied. This energy can be thermal energy in the case of static recovery (left) or from an applied stress in the case of dynamic recovery (right(

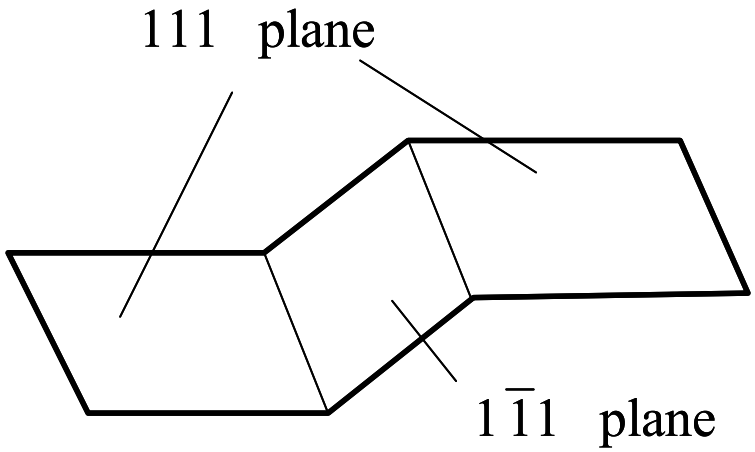

Figure 3.7. One mechanism of dynamic recovery is cross-slip. The dislocation by-passes an obstacle by crossing onto an unobstructed slip plane.

Static (Thermal) Dislocation Recovery Mechanisms $\left(R_s, r_s\right)$

The energy required to overcome an obstacle can also be supplied solely as thermal energy i.e. temperature rise as shown in (Figure 3.6). In this case an applied stress is not necessary to achieve dislocation recovery. Thermally driven or 'static' recovery is generally a diffusion based process and is associated with high temperature or long term material behavior and can often be observed in grain boundaries. Hence at low strain rates and high temperatures thermal recovery dominates, whereas at high strain rates dynamic recovery dominates in equation (3.12). In (Figure 3.8) a typical thermal recovery mechanism is illustrated in which thermal energy allows

dislocations to climb (through interaction with atomic vacancies). Dislocations then annihilate each other, reducing the dislocation density and easing subsequent deformation.

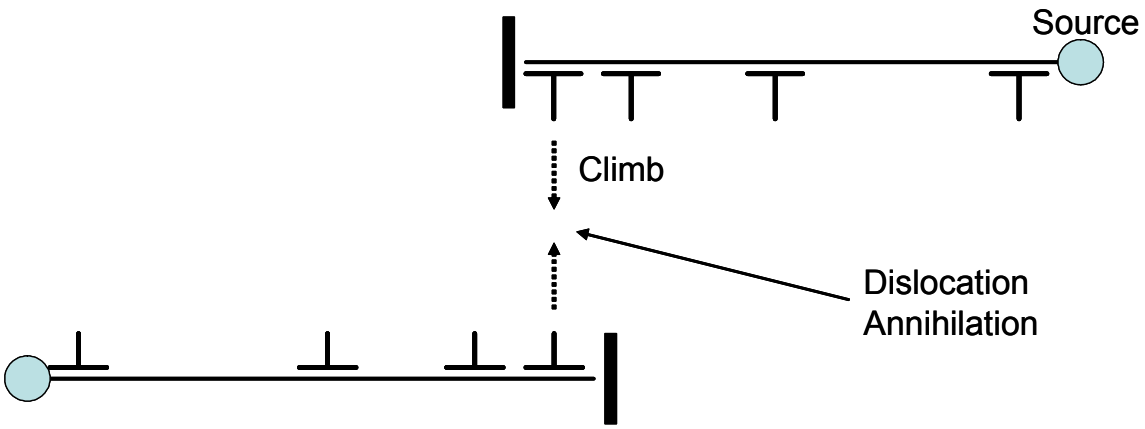

Figure 3.8. One mechanism of static (thermal) recovery is dislocation climb. This is s diffusion based process where dislocations of opposite signs can annihilate each other.

3.3.4 Internal State Variables - Porosity and Temperature (ϕ and ϑ)

The equations which describe the evolution of porosity ϕ and temperature ϑ are outlined in this Section. Porosity is considered in terms of microvoid nucleation, growth and coalescence. Temperature rise is considered to arise from plastic work dissipation. Both adiabatic temperature rise and heat conduction are described.

Porosity Damage Evolution ϕ

In the current thesis, porosity is considered to arise in the alloy due to microvoid nucleation and growth. In a continuum sense, the porosity at a point is the product of the average number of voids per unit volume η and the average volume of a void v:

$$\phi = \eta v \tag{3.14}$$

The rate of change of the number of nucleated voids per unit volume may be given as a simple rate equation, in terms of the plastic deformation rate $\mathbf{D}_p$:

$$\dot{\eta} = \mathcal{N} \left\| \mathbf{D}_p \right\| \tag{3.15}$$

Varying degrees of complexity and accuracy can be achieved depending on the form of the parameter $\mathcal{N}$. A simple expression for the evolution of the average volume of a void v can be described in terms of the plastic deformation rate $\mathbf{D}_p$:

$$\dot{v} = \mathcal{G} \left\| \mathbf{D}_p \right\| \tag{3.16}$$

where $\mathcal{G}$ is usually some function of triaxiality and temperature. The effects of void coalescence are usually included to model the rapid increase in void growth during the final stages of failure. Once a coalescence criterion is satisfied, the porosity function is modified to account for the coalescence effect and the post coalescence porosity expression becomes

$$\phi = \eta v + \phi_{coal} \tag{3.17}$$

where

$$\phi_{coal} = \mathcal{C} \eta v \tag{3.18}$$

The parameter $\mathcal{C}$ describes the magnitude of the coalescence effect in terms of the existing porosity ηv. It magnifies the porosity expression to replicate the effects of coalescence. Several attempts have been made to numerically quantify the effects of void coalescence. For example (Hom et al. 1989) investigated the growth of voids directly ahead of a crack tip and developed several void coalescence criteria which were used to predict fracture initiation. The effect of void configuration on both growth and coalescence has been modeled by (Horstemeyer et al. 2000a)

who discovered that coalescence effects can occur between voids as far apart as six void diameters.

General Damage Evolution

In the current work, only isotropic damage is considered. Here it is described in terms of void nucleation, growth and coalescence. Later, damage due to brittle fracture is also considered in an isotropic continuum manner. It is noted that in general the continuum damage equations provide a general framework for modeling the stress degradation due to damage. Microvoid nucleation may arise due to other phenomena such as radiation. In this case the nucleation equation will likely include terms which are determined by a separate mass diffusion simulation which takes account of radiation intensity and the type of radiation.

Temperature Evolution ϑ

The evolution of temperature at a material point is governed by (i) plastic work dissipation and (ii) heat conduction within the material. When conduction is considered, the full energy equation including heat conduction is solved:

$$\mathbf{q}\bullet\tilde{\nabla} + Q = \rho c_{pt}\dot{\theta} \quad \text{in} \quad \Omega \tag{3.19}$$

with boundary condition and constitutive relationship

$$\begin{aligned} &\mathbf{q}\bullet\mathbf{n} = \tilde{q} \quad \text{on} \quad \Gamma \\ &\mathbf{q} = -k\nabla\vartheta \end{aligned} \tag{3.20}$$

where $\mathbf{q}$ is the heat flux, k is thermal conductivity, Q is a heat source term related to the plastic work dissipation $Q = h_c\boldsymbol{\sigma} : \mathbf{D}^p$, h_c is the fraction of plastic work dissipated as temperature rise, ρ is the material density, c_{pt} is the specific heat, $\tilde{q}$ is an applied heat flux on the boundary Γ.

It is noted that a value of $h_c = 0.9$ is generally used in the literature for alloys and is used here. The thermal equation is coupled to the mechanical simulation through the heat source Q. The mechanical simulation is coupled to the thermal simulation through the temperature dependence of the mechanical constitutive relationship. Under adiabatic conditions, the conductance is ignored and the temperature rise can be computed within the constitutive model as:

$$\dot{\vartheta} = \frac{h_c}{\rho c_{pt}} \boldsymbol{\sigma} : \mathbf{D}^p \tag{3.21}$$

The constants required in the Internal State Variable Model (as described here) are summarized in Table 3.1.

3.3.5 Uniaxial Stress Simplification of the BCJ Flow Relation

A clearer understanding of the BCJ model can be developed by examining the one dimensional form; the material parameters used here are consistent with a cobalt alloy. This is intended to highlight the rate, temperature and damage dependent characteristics of the model.

One Dimensional Flow Rule

The BCJ constitutive model can be simplified for the case of uniaxial tension; the only stress component is σ and the plastic part of the deformation rate $\mathbf{D}_p$ can be replaced by the strain rate $\dot{\varepsilon}$. If only the isotropic hardening/recovery term κ is considered, the BCJ flow rule equation (3.9) can be rewritten as:

$$\dot{\varepsilon} = \mathrm{f}\sinh\left[\frac{\left[\sigma - \left(Y(\vartheta) + \kappa\right)(1-\phi)\right]}{\mathrm{V}(1-\phi)}\right] \tag{3.22}$$

Dividing across by f and taking the inverse hyperbolic sine ($\sinh^{-1}$) of each side:

$$\sinh^{-1}\frac{\dot{\varepsilon}}{\mathrm{f}} = \frac{\left[\sigma - \left(Y(\vartheta) + \kappa\right)(1-\phi)\right]}{\mathrm{V}(1-\phi)} \tag{3.23}$$

Multiplying across by $\mathrm{V}(1-\phi)$:

$$\mathrm{V}(1-\phi)\sinh^{-1}\frac{\dot{\varepsilon}}{\mathrm{f}} = \left[\sigma - \left(Y(\vartheta) + \kappa\right)(1-\phi)\right] \tag{3.24}$$

Rearranging this expression the BCJ flow rule can be written as a yield surface φ_{BCJ}:

$$\varphi_{BCJ} = \sigma - \left(\Upsilon + \kappa\right)(1-\phi) = 0 \tag{3.25}$$

where the rate dependent initial yield stress, Υ is introduced as:

$$\Upsilon = Y(\vartheta) + \mathrm{V}\sinh^{-1}\left[\frac{\dot{\varepsilon}}{\mathrm{f}}\right] \tag{3.26}$$

and the flow stress is given by the initial stress and the hardening stress, $\Upsilon + \kappa$. The experimentally observed non-linear relationship between strain rate $\dot{\varepsilon}$ and yield stress Υ is captured by the inverse hyperbolic sine function; the effect of the rate parameters V and f is shown in (Figure 3.4). This function also satisfies the criterion $\mathrm{V}\sinh^{-1}\left[\frac{\dot{\varepsilon}}{\mathrm{f}}\right] \Rightarrow 0$ when $\dot{\varepsilon} \Rightarrow 0$ i.e. the strain hardening approaches zero as strain rate decreases to zero. Note also that when damage is neglected $(\phi = 0)$, the flow stress σ is equal to the evolving initial yield stress Υ plus the hardening κ. Furthermore when the rate dependency is neglected, $\mathrm{V} = 0$, the model is identical to a conventional mises type yield surface model.

3.3.6 Comparison of BCJ to Gurson and Johnson Cook

The BCJ model combines the damage aspects of the Gurson model and the rate and thermal aspects of a Johnson-Cook model to form a rate and temperature dependent damage model. A comparison with each is given below.

Comparison to Gurson Model

The Gurson-Tvergaard-Needleman (Gurson 1977; Tvergaard and Needleman 1981) continuum damage model is an extension of conventional J2 flow theory to account for ductile rupture of metal alloys. In that model the yield surface is explicitly written in a pressure and porosity sensitive form:

$$\varphi_{GTN} = \left(\frac{\sigma}{\Upsilon + \kappa} \right)^2 + \phi \left(q_1 2 \cosh\left(q_2 \frac{\sigma_m}{\sigma} \right) - q_1^2 \phi \right) - 1 = 0 \qquad (3.27)$$

where q_1 and q_2 are material parameters and σ_m is the hydrostatic stress and σ is the von Mises (equivalent) stress. For comparison, the BCJ yield surface equation (3.25) can be rewritten as:

$$\varphi_{BCJ} = \left(\frac{\sigma}{\Upsilon + \kappa} \right)^2 + \phi\left(2 - \phi\right) - 1 = 0 \qquad (3.28)$$

The key difference is the inclusion of a hyperbolic cosine function in the Gurson model, equation (3.27), which captures the isotropic contraction of the yield surface as triaxiality increases (increasing hydrostatic stress). The magnitude of the contraction is governed by the constants q_1 and q_2, and the porosity ϕ. In the BCJ model, equation (3.28), there is no direct dependence of the plastic flow on pressure. However the yield surface is sensitive to pressure via the triaxiality dependency usually incorporated in the porosity ϕ. Comparing equations (3.27) and (3.28), both

models are equivalent when the Gurson pressure sensitivity parameters are set to $q_1 = 1$ and $q_1 = 0$. In both models rate and temperature effects can be introduced through the initial yield stress Υ function, equation (3.26), and the isotropic hardening stress κ, equation (3.12).

Comparison to Johnson Cook Model

The Johnson Cook model (Johnson and Cook 1985; Medyanik et al. 2005) is often used to extend J2 flow theory to the case of rate and temperature dependent plasticity. In the Johnson-Cook model the rate of plastic strain $\dot{\varepsilon}$ is written as:

$$\dot{\varepsilon} = \dot{\varepsilon}_0 \exp\left\{\frac{1}{C}\left(\frac{\sigma}{g} - 1\right)\right\}$$
$$\textit{where} \qquad (3.29)$$
$$g = \left(Y + \kappa\right)\left(1 - \vartheta^*\right)$$

Inverting the expression for strain rate, a yield surface φ_{JC} can be written as:

$$\varphi_{JC} = \sigma - \left(Y + \kappa\right)\left(1 + C\ln\left[\frac{\dot{\varepsilon}}{\dot{\varepsilon}_0}\right]\right)\left(1 - \vartheta^*\right) = 0 \qquad (3.30)$$

For comparison, the BCJ yield surface φ_{BCJ}, equation (3.25), can be rewritten as:

$$\varphi_{BCJ} = \sigma - \left(Y + \kappa\right)\left(1 + \frac{\mathrm{V}}{\left(Y + \kappa\right)}\ln\left[\frac{\dot{\varepsilon}}{\mathrm{f}} + \sqrt{\left(\frac{\dot{\varepsilon}}{\mathrm{f}}\right)^2 + 1}\right]\right)\left(1 - \phi\right) = 0 \qquad (3.31)$$

where the inverse hyperbolic sine function has been replaced by the equivalent logarithmic expression. It is clear that these expressions are similar in form. Both include a hardening term κ and each incorporates a non-linear dependency on the strain rate $\dot{\varepsilon}$ (normalized in both cases

by a referential strain rate $\dot{\varepsilon}_0$ and f). In the Johnson Cook model a natural logarithm function is used whereas in the BCJ model an inverse hyperbolic sine function is used (converted to a log function in equation (3.31)). In each model the temperature acts to degrade the stress. In the BCJ model this occurs through the temperature dependence of the initial yield parameter Y. In the Johnson Cook model the thermal degradation is given directly in terms of a temperature function ϑ^*, which has a similar effect to the damage term ϕ in the BCJ model; it isotropically shrinks the yield surface.

3.3.7 Demonstration of BCJ Model Behavior

In this section the effect of hardening and recovery, thermal softening and porous damage, as predicted by the BCJ model, are examined using the flow expression described in equation (3.25). The constants required in the BCJ equations (summarized in Table 3.1) are given in Table 3.2 (unless otherwise stated). These values are typical of a steel alloy.

BCJ Parameters used in 1D Example					
Parameter		***Value***	***Parameter***		***Value***
Initial Temperature	θ_0	$273K$	Kinematic Hardening Modulus	C_9	0
Melt Temperature	θ_m	$1700K$		C_{10}	0
Thermal Softening Exponent	t	1	Kinematic Dynamic Recovery Modulus	C_{11}	0
Reference Strain Rate	f	$1s^{-1}$		C_{12}	0
Magnitude of Rate Effect	V	$16MPa$	Kinematic Static Recovery Modulus	C_{13}	0
Initial Yield Stress	C_1	$950MPa$		C_{14}	0
Hall-Petch Effect	C_2	0	Void Nucleation	$\mathcal{N}$	0
Isotropic Hardening Modulus	C_3	$-20MPaK^{-1}$	Void Growth	$\mathcal{G}$	0
	C_4	$22500MPa$	Void Coalescence	$\mathcal{C}$	0
Isotropic Dynamic Recovery Modulus	C_5	$1.3\times10^{-13}Pa$	Specific Heat	c_{pt}	500
	C_6	$500K$	Density	ρ	$2700kgm^{-3}$
Isotropic Static Recovery Modulus	C_7	0	Heat Fraction	h_c	0.9
	C_8	0			

Table 3.2 BCJ constants used in 1d examples: consistent with a 4340 steel alloy

Isotropic static recovery R_s and all kinematic hardening h and recovery effects (r_d, r_s) are neglected here for simplicity. This is achieved by setting the constants $C_7 - C_{14}$ to zero. The grain size hardening effect is also ignored by setting C_2 to zero.

Hardening/Recovery H , R_d

Initially the evolution of porosity ϕ and temperature ϑ are ignored i.e. zero porosity and isothermal conditions are assumed. Only the dynamic recovery term in equation (3.12) is active giving an expression for the isotropic hardening stress:

$$\dot{\kappa} = \left(H\left(\vartheta\right) - R_d\left(\vartheta\right)\kappa^2 \right) \left\| \mathbf{D}_p \right\| \tag{3.32}$$

It is interesting to note that under isothermal conditions the isotropic hardening/recovery stress κ reaches a saturation level κ_{sat} when the rat of change of κ is zero i.e. $\dot{\kappa} = 0$ in equation (3.32):

$$\kappa_{sat} = \sqrt{\frac{H\left(\vartheta\right)}{R_d\left(\vartheta\right)}} \tag{3.33}$$

This saturation stress manifests itself as a plateau in the predicted stress-strain response. Staying within the framework of a uniaxial compression problem, the isotropic hardening stress, equation (3.12), is simplified as:

$$\dot{\kappa} = \sqrt{\frac{2}{3}} \left(H\left(\vartheta\right) - R_d\left(\vartheta\right)\kappa^2 \right) \dot{\varepsilon} \tag{3.34}$$

where the rate of plastic deformation $\left\| \mathbf{D}_p \right\|$ has been rewritten in terms of the total strain rate $\dot{\varepsilon}$. Should dynamic recovery also be neglected by setting $R_d\left(\vartheta\right) = 0$ in equation (3.34), the isotropic hardening equation (3.32) becomes:

$$\dot{\kappa} = \sqrt{\frac{2}{3}} H\left(\vartheta\right) \dot{\varepsilon} \tag{3.35}$$

which is a simple linear hardening response as shown in (Figure 3.9). However when dynamic recovery $R_d\left(\vartheta\right)$ is considered the stress reaches a saturation level as described in equation (3.33)

and illustrated in (Figure 3.9) at a temperature of $273K$. At elevated temperatures $(450K, 600K)$ the temperature dependent hardening modulus $H(\vartheta)$ decreases and the recovery modulus $R_d(\vartheta)$ increases with temperature according to equations (3.13). Both result in a lower saturation stress κ_{sat}, equation (3.33), as shown in (Figure 3.9). Note that only the isotropic hardening stress κ is plotted in (Figure 3.9); hence the thermal softening effect on the initial yield stress $Y(\vartheta)$ is not observable in this plot.

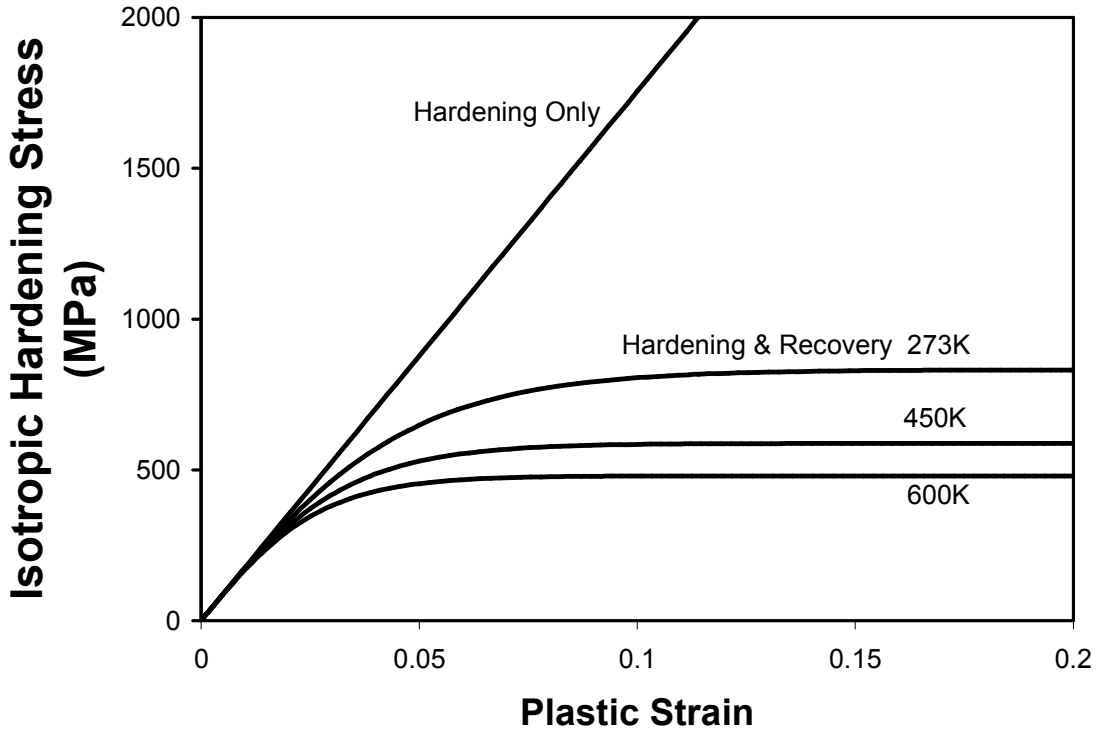

Figure 3.9. The BCJ model used here reduces to a linear hardening model when recovery is neglected. Otherwise a saturation stress occurs, equation (3.33).

Thermal Softening ϑ

The effect of adiabatic temperature rise, equation (3.21), on the flow stress, equation (3.25), is now considered; again porosity ϕ is neglected in equation (3.25). The evolution of the temperature function ϑ^*, described in equation (3.11), is shown in (Figure 3.10). The corresponding adiabatic flow stress is also shown and compared to the isothermal flow stress curve. The rising temperature acts to decrease the flow stress by:

- reducing the rate independent initial stress $Y(\vartheta)$, equation (3.11)
- reducing the isotropic hardening stress κ, equation (3.32) via
    - the hardening modulus $H(\vartheta)$, equation (3.13)
    - the recovery modulus $R_d(\vartheta)$, equation (3.13)

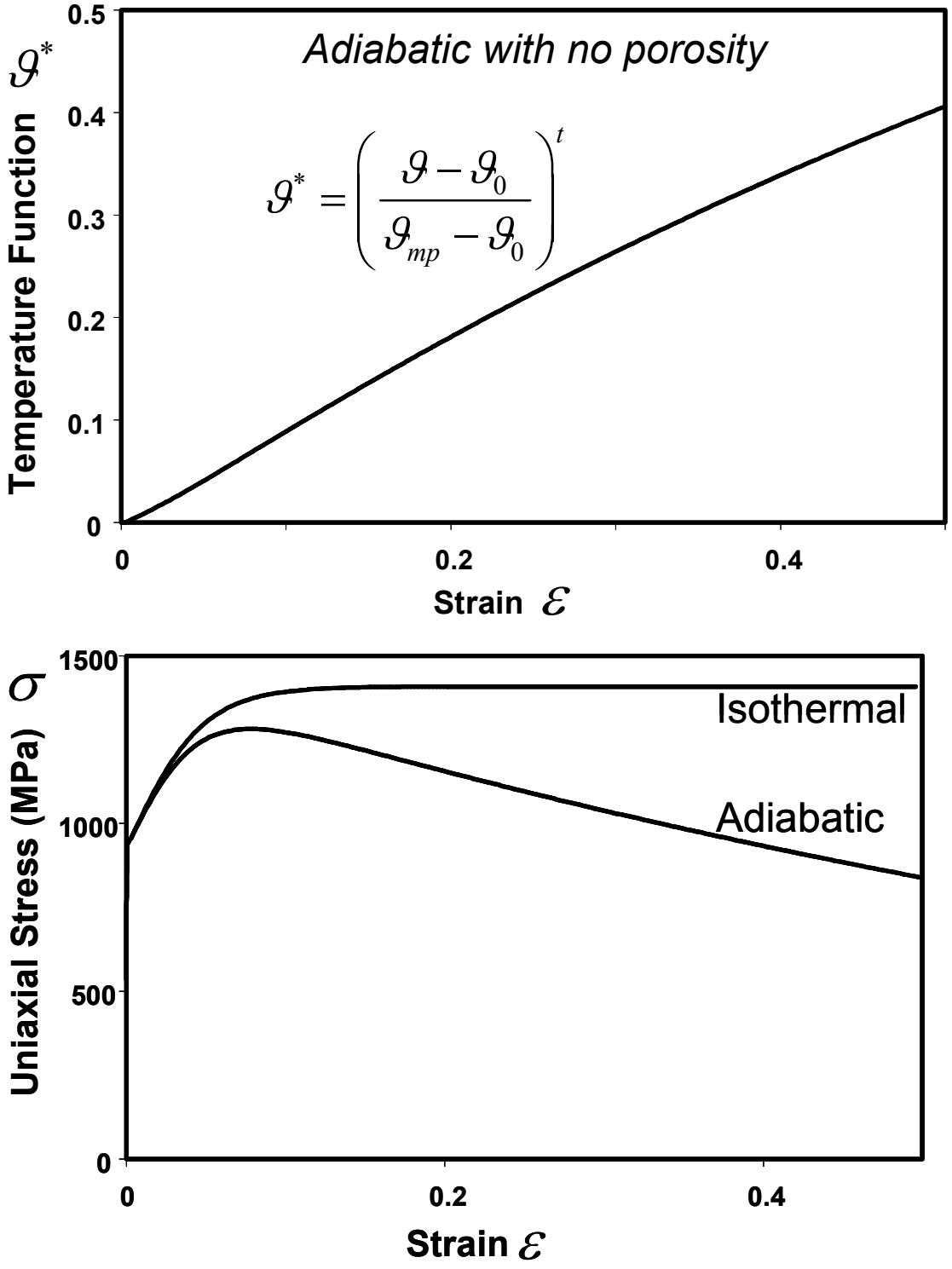

Figure 3.10. The temperature rise which occurs under adiabatic conditions is shown along with the resulting thermal softening effect.

Isothermal Porosity Damage

Porosity damage ϕ is now considered, first under isothermal conditions and then under adiabatic loading conditions. Increasing porosity has the effect of isotropically shrinking the yield surface as described by in equation (3.25). Here a very simple linear relationship between porosity ϕ and strain is used as illustrated defined in (Figure 3.11):

$$\begin{aligned} \dot{\phi} &= 0 \quad \varepsilon \le 0.2 \\ \dot{\phi} &= \dot{\varepsilon} \quad \varepsilon > 0.2 \end{aligned} \tag{3.36}$$

This simple expression is used here for illustration purposes only (the nucleation, growth and coalescence expression given by equations (3.15), (3.16) and (3.18) are much more physical but require several parameters). Porosity is zero until a strain of 20% and then grows linearly to a value of 0.3 at a plastic strain of approximately 50%.

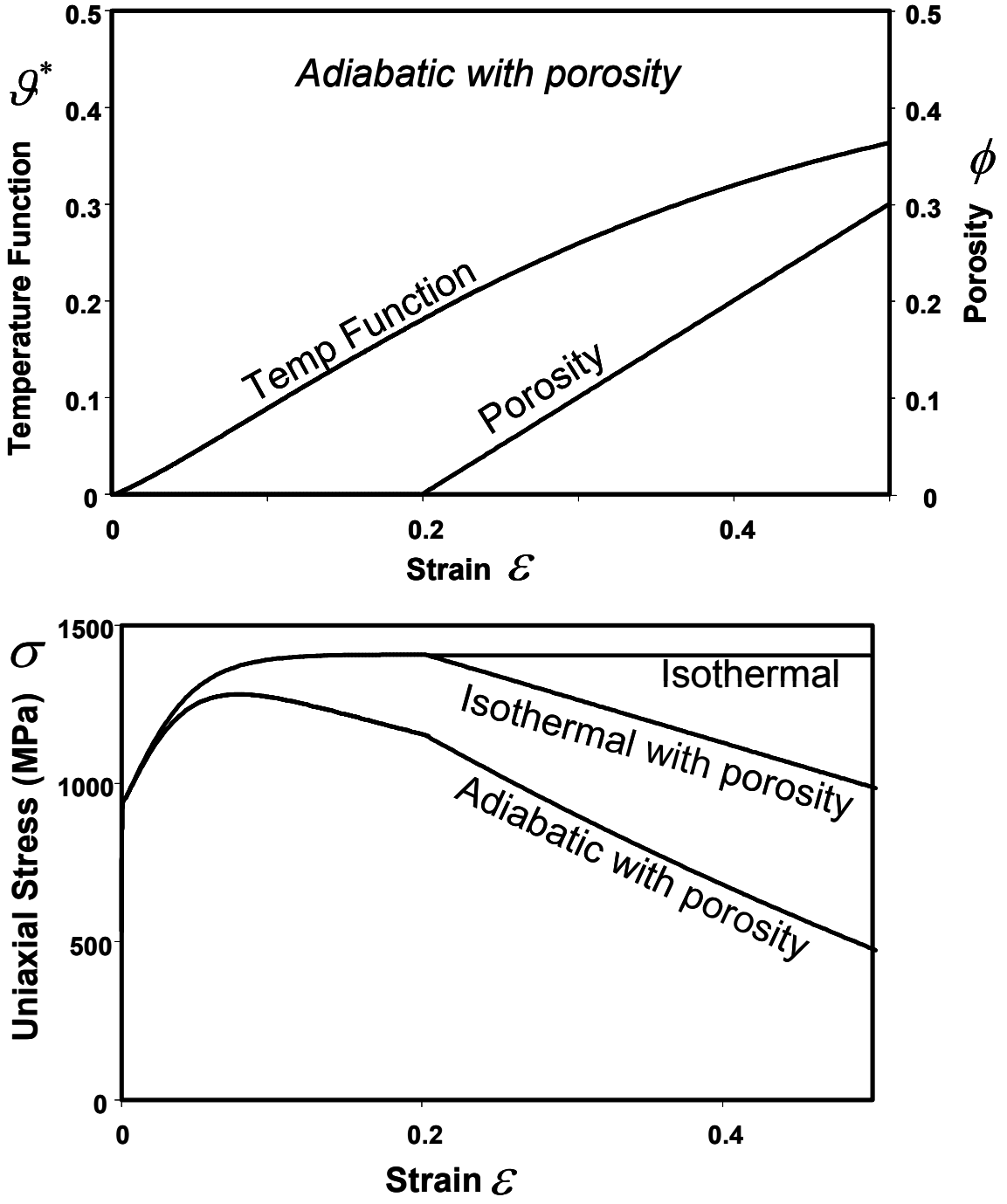

Figure 3.11. The effect of porosity is shown under isothermal conditions. The combined thermal and porosity effects are then shown; the instability point is a function of both porosity and temperature.

The porosity softening effect is first considered under isothermal conditions. It is shown in (Figure 3.11) that the stress immediately begins to degrade once the porosity begins to grow. The combined softening effect due to evolving porosity ϕ and adiabatic thermal softening ϑ^* is also shown. Both softening effects act to overcome the work hardening. Again the influence of damage can be observed after 20% strain is reached.

In conclusion, the BCJ model can capture hardening, recovery, thermal softening and porous damage effects. Each extra set of physics requires an extra set of material constants. A summary of the constitutive relationship is given below:

Summary

Cause: Increasing Strain Rate

Effects: (a) Increasing rate dependent initial yield stress $\Upsilon(\dot{\varepsilon})$, equation (3.26); dynamic recovery terms becomes more important than static recovery terms, equation (3.12).

Cause: Increasing Temperature

Effects: (a) Decreasing initial yield stress $Y(\vartheta)$, equation (3.11); decreasing hardening moduli $\left[H(\vartheta), h(\vartheta)\right]$ and increasing dynamic $\left[R_d(\vartheta), r_d(\vartheta)\right]$ and static $\left[R_s(\vartheta), r_s(\vartheta)\right]$ recovery moduli, equation (3.13).

Cause: Increasing Porosity

Effect: Decreasing flow stress, equation (3.25).

3.4 Constitutive Models – Crystal Plasticity

The crystal plasticity formulation (Asaro 1983a) has been used successfully in the past to represent the details of crystallographic deformation in metallic single crystals and polycrystals e.g. see (Bruzzi et al. 2001; McHugh et al. 1993; McHugh and Mohrmann 1997). The kinematical theory for the mechanics of crystals is based on the work of (Hill 1966; Hill and Rice 1972; Rice 1971). What follows is a summary of crystal plasticity theory based on the approach of (Asaro 1983b). Although both poly- and single crystal models exist, the length scales of interest here can be modeled using single crystal plasticity only. Plastic deformation is assumed to occur via crystallographic dislocation based slip; diffusion, twinning and grain boundary sliding deformation mechanisms are not considered. The key assumption is that the resolved shear stress on each slip plane drives slip on that plane. Details of the constitutive model implementation (integration) can be found in (Huang 1991).

3.4.1 Kinematics of Crystal Plasticity

The crystal lattice structure undergoes elastic deformation and rigid rotation as well as crystalline slip i.e. dislocation motion accommodates material flow through the crystal lattice. The total deformation gradient can be written as:

$$\mathbf{F} = \mathbf{F}^{*} \bullet \mathbf{F}^{p} \tag{3.37}$$

where $\mathbf{F}^{p}$ is that part of the deformation gradient associated with plastic shear and $\mathbf{F}^{*}$ describes the elastic stretching and rotation of the lattice. The kinematics of elastic-plastic deformation of crystalline solids is illustrated in (Figure 3.12) in terms of the reference, intermediate and current deformed configurations. It is assumed that the elastic properties are independent of plastic slip,

hence the stress can be determined form the elastic/rotation part $\mathbf{F}^*$. The rate of change of $\mathbf{F}^p$ at a continuum point is related to the slip rate on the α slip systems $\dot{\gamma}^\alpha$ by:

$$\dot{\mathbf{F}}^p \bullet \left(\mathbf{F}^p\right)^{-1} = \sum_\alpha \dot{\gamma}^\alpha \mathbf{s}^\alpha \mathbf{m}^\alpha \tag{3.38}$$

where $\mathbf{s}^\alpha$ and $\mathbf{m}^\alpha$ are the slip direction and normal to the slip plane in the reference configuration. The sum is over all of the activated slip systems.

In the current deformed configuration (Figure 3.12) the slip direction is given by (Asaro 1983a)

$$\mathbf{s}^{*\alpha} = \mathbf{F}^* \bullet \mathbf{s}^\alpha \tag{3.39}$$

and the normal to the slip plane is given by

$$\mathbf{m}^{*\alpha} = \mathbf{m}^\alpha \bullet \left(\mathbf{F}^*\right)^{-1} \tag{3.40}$$

The velocity gradient in the current configuration is

$$\mathbf{L} = \dot{\mathbf{F}} \bullet \mathbf{F}^{-1} = \mathbf{D} + \mathbf{W} \tag{3.41}$$

where the rate of deformation and spin tensor are given by $\mathbf{D}$ and $\mathbf{W}$ respectively. Each can be further decomposed into the elastic/rotation and plastic parts:

$$\mathbf{D} = \mathbf{D}^* + \mathbf{D}^p \qquad \mathbf{W} = \mathbf{W}^* + \mathbf{W}^p \tag{3.42}$$

such that

$$\mathbf{D}^* + \mathbf{W}^* = \dot{\mathbf{F}}^* \bullet \left(\mathbf{F}^*\right)^{-1} \qquad \mathbf{D}^p + \mathbf{W}^p = \sum_\alpha \dot{\gamma}^\alpha \mathbf{s}^\alpha \mathbf{m}^\alpha \tag{3.43}$$

Crystalline slip is assumed to obey Schmid's law (Asaro 1983a; Asaro 1983b) which means the slip rate $\dot{\gamma}^\alpha$ can be written in terms of the Schmidt stress $\boldsymbol{\tau}^\alpha$ on that particular slip system. The Schmid stress can be interpreted as the resolved shear stress when elastic lattice deformation is negligible. In the presence of finite elastic lattice deformations, there are several generalizations

of the Schmid stress (Asaro and Rice 1977). Here the definition of the Schmid stress used by (Rice 1971) is used, given in terms of the Cauchy stress $\boldsymbol{\sigma}$ as:

$$\tau^{\alpha} = \mathbf{m}^{*\alpha} \bullet \frac{\rho_0}{\rho} \boldsymbol{\sigma} \bullet \mathbf{s}^{*\alpha} \tag{3.44}$$

where ρ_0 and ρ_0 are the mass density in the reference and current configurations. The corresponding rate of change of Schmid stress has been given by (Hill and Rice 1972) as:

$$\dot{\tau}^{\alpha} = \mathbf{m}^{*\alpha} \bullet \left[\overset{\nabla}{\boldsymbol{\sigma}}^{*} + \boldsymbol{\sigma}\left(\mathbf{I} : \mathbf{D}^{*}\right) - \mathbf{D}^{*} \bullet \boldsymbol{\sigma} + \boldsymbol{\sigma} \bullet \mathbf{D}^{*} \right] \bullet \mathbf{s}^{*\alpha} \tag{3.45}$$

where the Jaumann rate $\overset{\nabla}{\boldsymbol{\sigma}}^{*}$ is the corotational stress rate on axis that rotate with the crystal lattice.

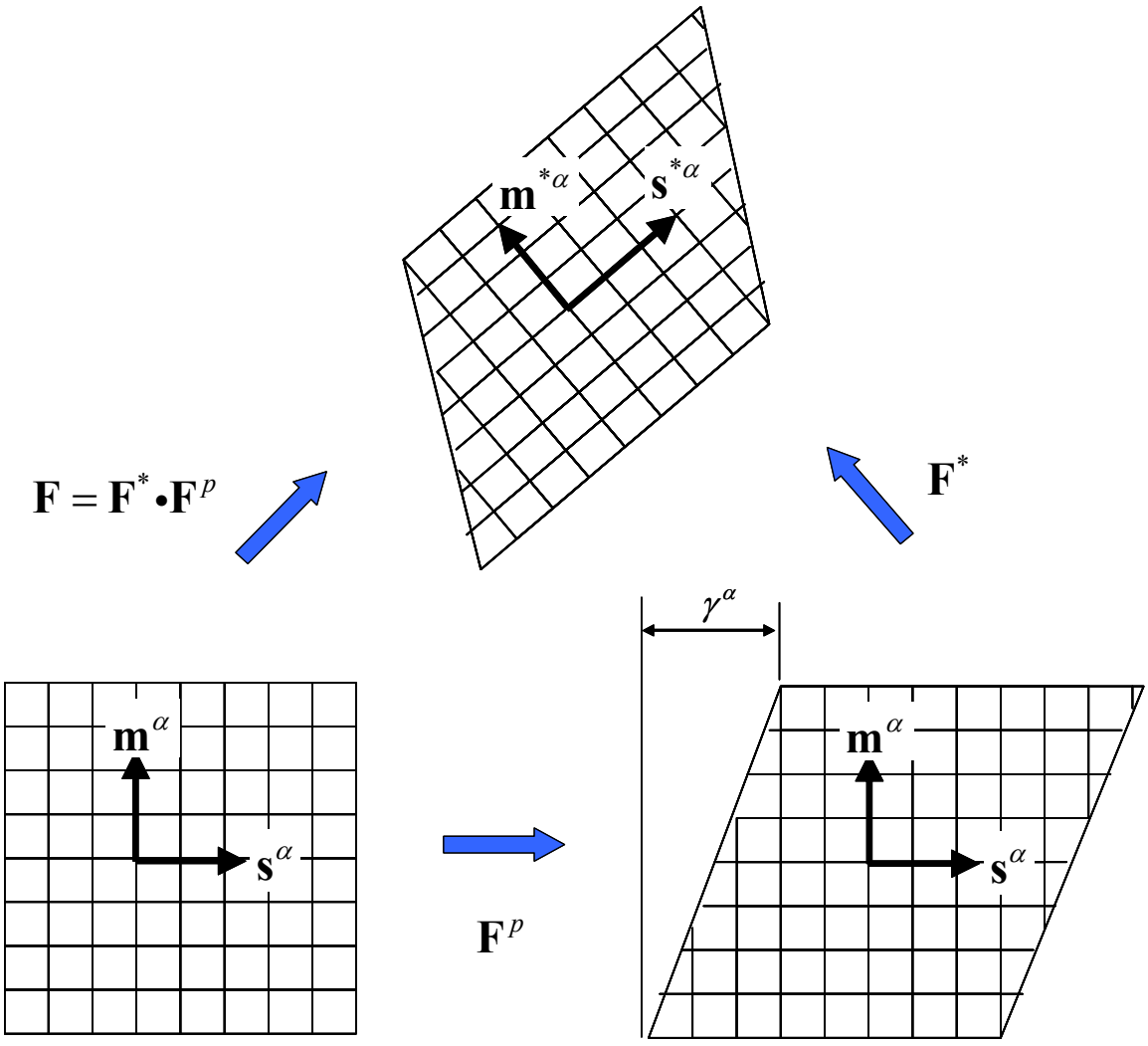

Figure 3.12. A multiplicative decomposition of the deformation gradient; the deformation gradient is separated into the plastic part $\mathbf{F}^p$ and the part which describes elastic stretching and rigid body rotation $\mathbf{F}^*$.

3.4.2 Rate of Slip

The slip rate on the αth slip plane is commonly given in terms of the phenomenological Schmid's Law:

$$\dot{\gamma}^{\alpha} = \dot{a}\,\mathrm{sgn}\left(\tau^{\alpha}\right)\left\{\left|\frac{\tau^{\alpha}}{g^{\alpha}}\right|\right\}^{m} \tag{3.46}$$

where m is the rate sensitivity parameter and $\dot{a}$ is the reference strain rate. This rate equation for the plastic strain is analogous to equation (3.9) used in the BCJ Internal State Variable model; the key difference is that now a set of α equations are required to define the strain rate on each slip system. The current strength of each slip system is given by the hardening variable g^{α}.

3.4.3 Rate, Temperature and Grain Size Dependent Hardening

Here each slip system is assumed to have the same initial strength g_0. A self hardening power law function for the slip planes is used such that the strength of slip plane α is given by:

$$g^{\alpha} = g_0\left(1+\frac{\gamma^{\alpha}}{\gamma_0}\right)^{n} \tag{3.47}$$

where g_0 is the initial strength, γ^{α} is the slip on the α slip plane, γ_0 is the reference accumulated plastic strain and n is the hardening exponent. This is analogous to the hardening/recovery stresses defined in the BCJ model, equation (3.12). Other more complicated (latent hardening) functions may be used where the hardening effect on a slip plane is related to the accumulated strain on other planes.

This slip plane hardening function describes the increases in stress required to move a dislocation along the slip plane due to dislocation entanglement and pile up at obstacles such as stacking fault intersections (Figure 3.5). Other hardening effects, such as grain boundary hardening may be accounted for by incorporating a Hall-Petch type term:

$$g^{\alpha} = g_0 \left(1 + \frac{\gamma^{\alpha}}{\gamma_0} \right)^n + k_d d^{-1/2} \tag{3.48}$$

where k_d is a constant derived from experiment (Roebuck et al. 1984) and d is the grain size. Smaller grain sizes increase the strength of the slip planes. A temperature dependence of slip system hardening can also be included:

$$g^{\alpha} = \left[g_0 \left(1 + \frac{\gamma^{\alpha}}{\gamma_0} \right)^n + k_d d^{-1/2} \right] \left(1 - \vartheta^* \right)$$

where (3.49)

$$\vartheta^* = \left(\frac{\vartheta - \vartheta_0}{\vartheta_m - \vartheta_0} \right)^t$$

ϑ is the temperature in Kelvin, ϑ_m is the melt temperature, ϑ_0 is the reference temperature, t is the thermal softening exponent. Increasing temperature reduces the yield strength of the slip planes.

3.4.4 J2 Flow versus Crystal Plasticity

It is interesting to compare the crystal plasticity model to a conventional isotropic metal plasticity approach; the J2 flow theory of metal plasticity (Belytschko et al. 2000) is used here for comparison. A cobalt alloy is chosen as the material. Cobalt has an FCC lattice structure with twelve sets of slip systems, with the closed packed slip plane being 111 and slip direction type

<110>. The values for each material parameter in the crystal plasticity model, equations (3.46) and (3.49) are given in Table 3.3.

Crystal Plasticity parameters used to compare with J2 Flow			
Parameter	*Value*	*Equation*	*Description*
E	$211GPa$	-	Elastic Modulus
ν	0.31		Poisson's Ratio
m	10	(3.46)	Rate Sensitivity Parameter
$\dot{a}$	$0.001s^{-1}$	(3.46)	Reference Strain Rate
g_0	$74MPa$	(3.49)	Initial Strength of Slip Planes
γ_0	0.3125	(3.49)	Reference Accumulated Strain
n	0.2995	(3.49)	Hardening Exponent
ϑ_m	$1768K$	(3.49)	Temperature effect on slip
ϑ_m	$273K$	(3.49)	Reference Temperature
t	1	(3.49)	Thermal Softening Exponent
k_d	$2.145Nmm^{-3/2}$	(3.49)	Hall-Petch effect on slip

Table 3.3 Crystal Plasticity parameters from experiment for a cobalt alloy (Quinn et al. 1997)

A J2 flow theory with power law hardening is calibrated to the average behavior of single crystal. In (Figure 3.13) a 2D plane strain simulation is performed in which the alloy matrix is represented by (a) the J2 theory of plasticity and (b) single crystal plasticity theory. The accumulated plastic strain is plotted on the undeformed and deformed configurations in each

case. The initial 2D void area (and 3D cylinder volume) fraction is 1%. Biaxial tensile strain loading conditions are applied. When J2 theory is used, the surrounding material deforms isotropically and the void expands hydrostatically. The sides of the voids flatten as it begins to interact with neighboring voids (periodic boundary conditions have been applied). In the case of crystal plasticity, the matrix displays favored slip (plastic deformation) directions resulting in a hexagonal void shape as predicted by (Sigl and Exner 1987). These slip directions used in the crystal plasticity model are shown in the top pane in (Figure 3.14) in relation to the crystallographic structure. The crystallographic orientation introduced through the crystal plasticity formulation can be observed clearly in the void growth simulation when the stress field is plotted on the undeformed configuration in the bottom pane of (Figure 3.14).

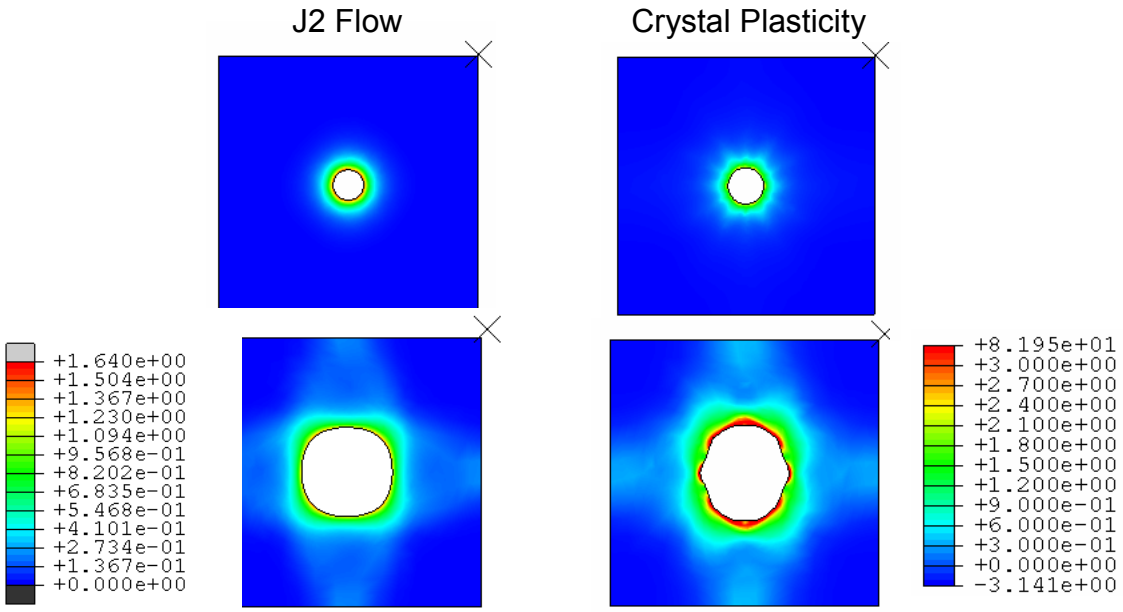

Figure 3.13. Plastic strain contours around a growing void obtained using (a) J2 flow theory and (b) crystal plasticity to represent the alloy matrix. The void shape is related to the crystallographic texture when crystal plasticity theory is used.

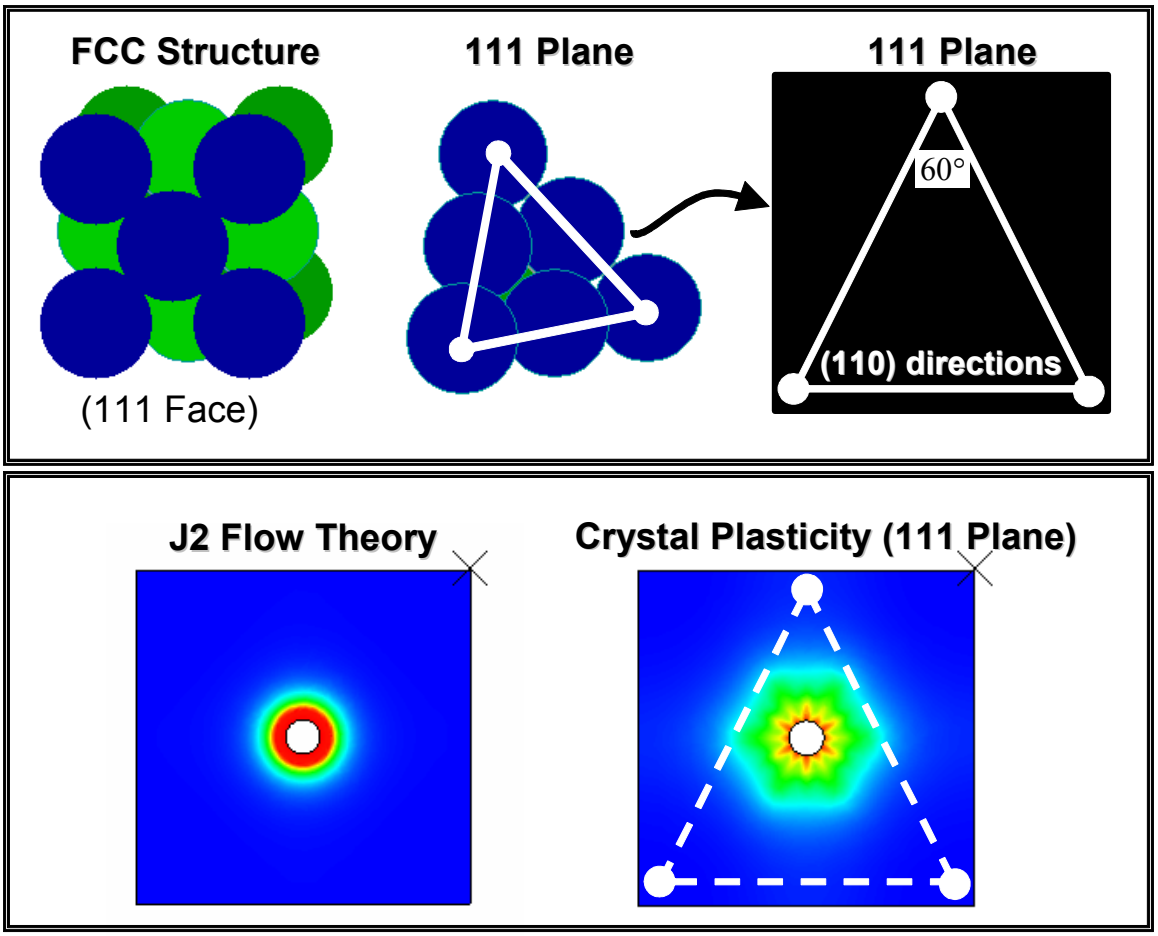

Figure 3.14. The crystal orientation used in the crystal plasticity model is shown in the top pane. The stress field obtained through the crystal plasticity formulation is clearly related to the crystallographic structure in the bottom pane

A cell containing several voids is now studied to investigate how each model handles the interaction between voids in a locally heterogeneous system. The crystal plasticity model predicts a stronger interaction between voids as the plastic flow occurs more readily accommodating increased void growth. In (Figure 3.15) the void lying in the upper right corner does not interact with the others when the J2 flow theory is used. When crystal plasticity is used

the interaction is clear; the void interacts with the others via the active slip systems which lie at 60 degrees.

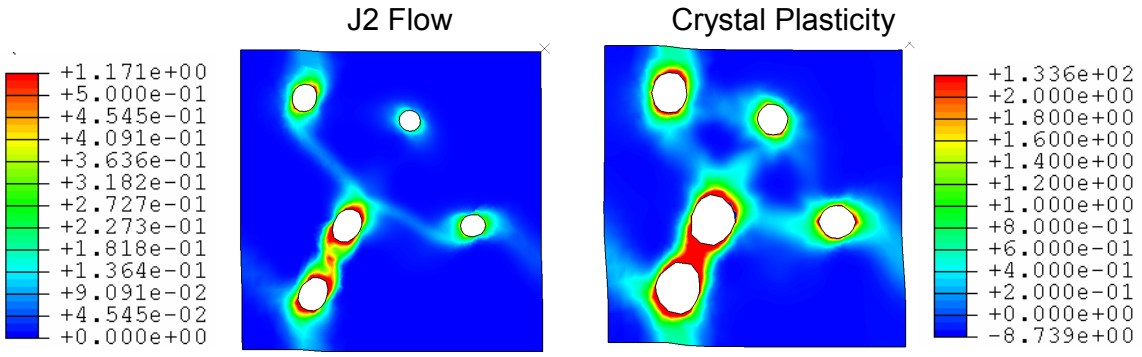

Figure 3.15. Plastic strain contours in a multi-void simulation. Greater interaction is predicted between voids aligned in preferred directions when using the crystal plasticity formulation

4 Hierarchical Model of Cemented Carbide Composites

In this chapter a hierarchical approach (Hao et al. 2004; Hao et al. 2003) is employed to develop a homogenized macroscale constitutive model for a WC-Co composite. The goal is to use this homogenized constitutive relation within a fracture simulation in order to gauge the effect of the microstructural parameters (cobalt volume fraction f and grain size d) on crack behavior. The key micromechanics of WC-Co deformation have been described in Chapter 2. The general forms of the constitutive relationships used in this chapter have been described in Chapter 3. An overview of the hierarchical approach used here is given in (Figure 4.1).

The behavior of the brittle carbide grains and ductile cobalt binder are calibrated to separate homogenized constitutive relationships using input from empirical data and microscale computational cell modeling. A homogenized constitutive relationship for the WC-Co composite is then calibrated to the results of macroscale computational cell models in which the carbide and cobalt microstructural features are directly modeled.

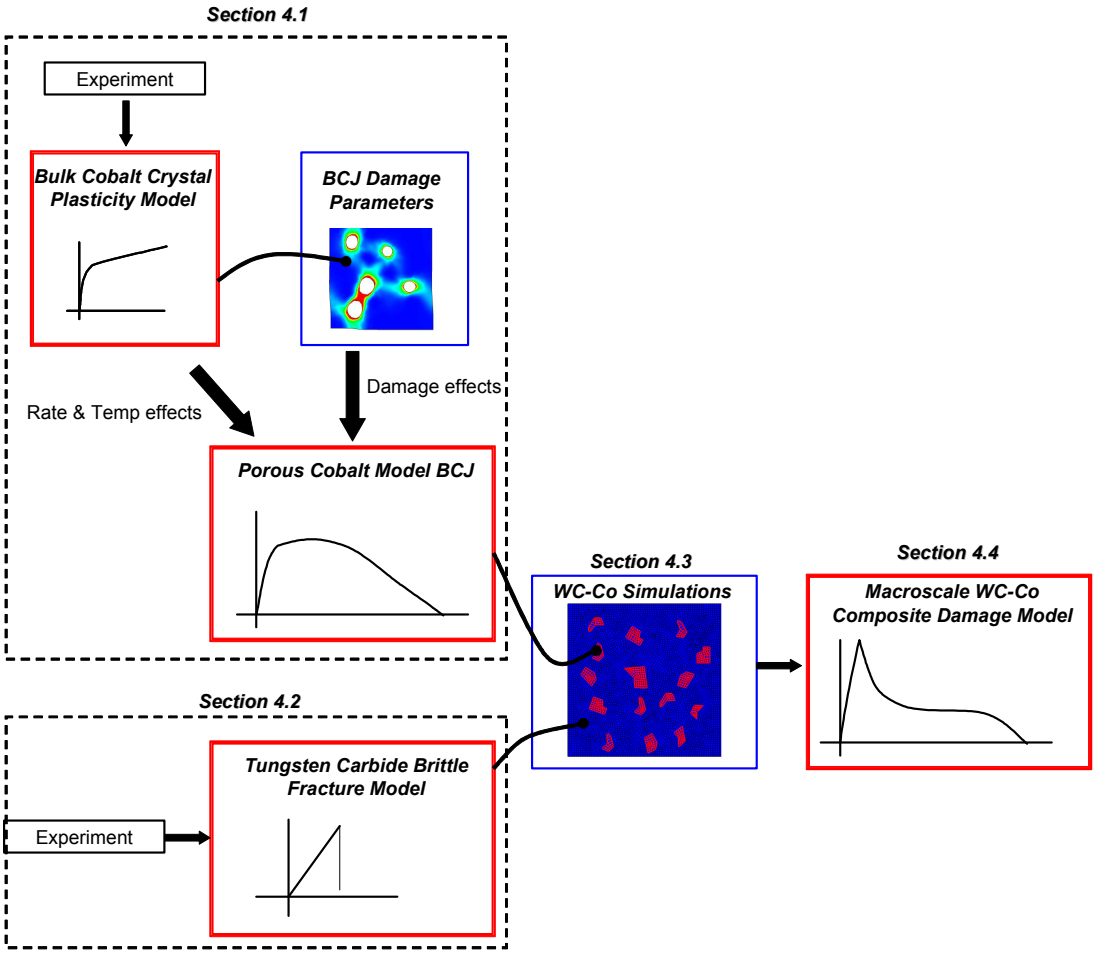

Figure 4.1. A hierarchical approach to forming a constitutive model for a WC-Co composite.

The hierarchical approach can be divided into three distinct stages:

- (Section 4.1): A porous cobalt plasticity model (BCJ) is constructed. The BCJ porosity damage parameters are determined using computational simulations of void growth in a crystal plasticity cobalt matrix.
- (Section 4.2): A brittle fracture model is calibrated to experimental data for tungsten carbide.

- (Section 4.3): A macroscale computational cell model of the WC-Co composite is constructed using the constitutive relations developed in Sections 4.1 and 4.2. The effect of varying each of the important microstructural parameters is investigated.
- (Section 4.4): A composite damage constitutive model is proposed, based on modified BCJ model, and calibrated to the results of the parametric study performed in Section (4.3).
- (Section 4.5): The composite damage model is applied within a numerical fracture toughness simulator.

The final WC-Co composite model developed in Section 4.4 gives the macroscale constitutive response directly in terms of the key underlying microscale parameters and macroscale boundary conditions;

- volume fraction of cobalt f
- cobalt grain size d
- temperature ϑ
- triaxiality T
- microvoid porosity ϕ
- brittle damage D
- deformation rate $\|\mathbf{D}\|$

4.1 Porous Cobalt Binder Model

The role of the cobalt binder in cemented carbides is well established empirically and is discussed in Section 2.1.1. In this section, a BCJ constitutive model (see Chapter 3 for details on the BCJ constitutive model) is calibrated to the rate $\|\mathbf{D}\|$, temperature ϑ, cobalt grain size d and microvoid porosity ϕ dependent plastic flow within the cobalt binder. Practically speaking this is achieved by finding the material parameters relating to:

(a) Microvoid porosity evolution, Sections 4.1.1-4.1.4

- Nucleation parameter $\mathcal{N}$, equation (3.15), is developed in Section 4.1.1
- Growth parameter $\mathcal{G}$, equation (3.16) is developed in Sections 4.1.2 and 4.1.3
- Coalescence parameter $\mathcal{C}$, equation (3.18) is developed in Section 4.1.4

(b) Plastic flow in the cobalt binder, Section 4.1.5

- Magnitude of rate effect V, equation (3.9)
- Reference strain rate f, equation (3.9)
- Rate independent Yield Stress $Y(\vartheta)$, equation (3.11)
- Isotropic hardening modulus $H(\vartheta)$, equation (3.13)
- Isotropic dynamic recovery modulus $R_d(\vartheta)$, equation (3.13)

The porous damage and plastic flow equations are combined in a single BCJ damage model which is validated against computational cell model results in Section 4.1.6. Finally in Section 4.1.7, the inverse strength-ductility relationship built into the model, is commented on.

4.1.1 Void Nucleation Parameter $\mathcal{N}$

The *physics* of void nucleation in cobalt has been described in Chapter 2, Section 2.1.4 and a set of continuum equations for nucleation, growth and coalescence of voids are described in Section 3.3.4. An expression for the rate of change of number of nucleated voids per unit volume was given in equation (3.15), and is repeated here for convenience:

$$\dot{\eta} = \mathcal{N} \left\| \mathbf{D}_p \right\| \tag{4.1}$$

Macroscopically speaking, vacancy based microvoid nucleation in cobalt is a stress and strain controlled process. With reference to Section 2.1.4, higher stress indicates a large density of stacking fault intersections, which are responsible for vacancy creation. Larger plastic strains indicate a large dislocation density, which facilitates vacancy mobility and hence microvoid nucleation via vacancy clustering. Here, microvoid nucleation is assumed to be normally distributed about a mean value of plastic strain $\varepsilon_{\mathcal{N}}$ (Chu and Needleman 1980); however we incorporate a simple stress dependency; the mean nucleation strain $\varepsilon_{\mathcal{N}}$ is a function of the initial yield stress Υ. This is represented in a continuum sense by:

$$\mathcal{N} = \frac{\mathcal{N}^*}{s_{\mathcal{N}} \left(2\pi\right)^{0.5}} \exp\left\{ -\frac{1}{2} \left(\frac{\varepsilon^p - \varepsilon_{\mathcal{N}}\left(\Upsilon\right)}{s_{\mathcal{N}}} \right)^2 \right\} \tag{4.2}$$

where $\mathcal{N}^*$ is the maximum number of nucleated voids per unit area in 2D assumed to be $2\times10^{10} m^{-2}$ here (Shi and Barnby 1984), s_n is the standard deviation of nucleation about a mean value of strain $\varepsilon_{\mathcal{N}}$. Here a standard deviation of $s_n = 0.05$ is used.

A relationship between the mean strain at nucleation $\varepsilon_{\mathcal{N}}$ and the initial yield stress Υ must be defined. In general, higher stresses indicate more vacancies, hence the mean distance between vacancies is reduced and less plasticity is required for void clustering to occur. In other words higher stress requires lower strain for nucleation to occur. The relationship between the average strain at nucleation $\varepsilon_{\mathcal{N}}$ and the initial yield stress Y, equation (3.11), is approximated here as a simple inverse equation:

$$\varepsilon_{\mathcal{N}} = \frac{D_1}{Y} \tag{4.3}$$

(Sokolov et al. 1969) performed uniaxial mechanical tests on a cobalt alloy and recorded the initial yield stress as $Y = 1GPa$. The ultimate tensile strength occurred at a uniaxial strain of $\varepsilon_{UTS} = 0.2$. Assuming the ultimate tensile strength coincides with the mean strain at nucleation (i.e. $\varepsilon_{UTS} = \varepsilon_{\mathcal{N}}$) it is possible to calibrate equation (4.3) to this data point, giving a value of $D_1 = 2 \times 10^8 Pa$. The resulting relationship is plotted in (Figure 4.2). It is noted that this is a fairly rough approximation; for example the triaxiality and temperature effect on nucleation is not considered. It may be possible to determine a more accurate relationship through empirical data or via molecular level simulations of vacancy formation and clustering.

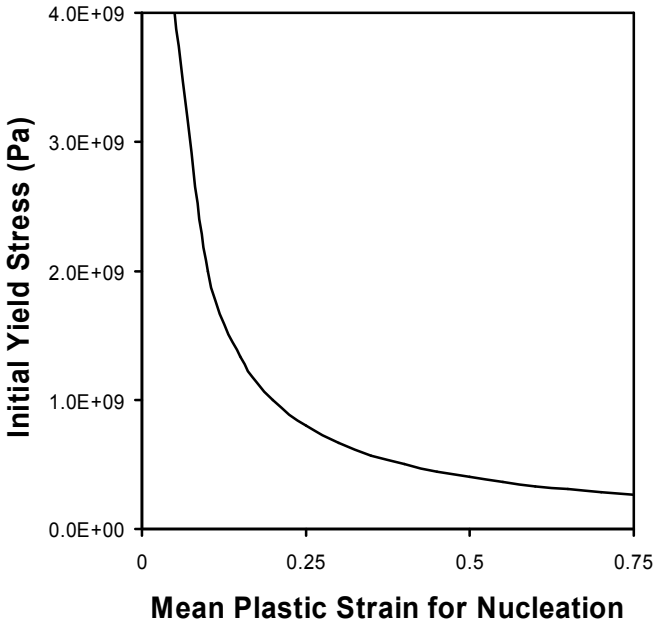

Figure 4.2. An inverse relationship between initial yield stress Υ and mean strain for void nucleation $\varepsilon_{\mathcal{N}}$.

4.1.2 Void Growth Parameter $\mathcal{G}$

An expression for void growth is given by equation (3.16), and is repeated here for convenience. The void growth equation is generally given in terms of the plastic deformation rate $\|\mathbf{D}_p\|$:

$$\dot{v} = \mathcal{G}\|\mathbf{D}_p\| \tag{4.4}$$

The physical parameters which control void growth are contained in the expression for $\mathcal{G}$:

$$\mathcal{G} = \mathcal{G}(\vartheta, T, d) \tag{4.5}$$

where ϑ is the temperature, T is the triaxiality, d is the cobalt grain size. An expression for the void growth parameter $\mathcal{G}$ is now developed from computational cell models in which a growing void is modeled directly. The effect of temperature ϑ, triaxiality T and cobalt grain size d can be gauged by varying each in a parametric study, Section 4.1.3.

Void Growth Computational Cell Model

The microvoid growth simulation set-up is briefly described here; the 2D mesh and slip plane directions are illustrated in (Figure 4.3). The key aspects of the void growth simulation are summarized as:

- Two-dimensional plane strain finite element (ABAQUS 2004) simulations
- A single pre-nucleated 2D void (3D cylinder) of radius 20nm (see Section 2.1.4) is modeled
- The initial 2D void area (3D cylinder volume) fraction is 0.8%
- Fully periodic displacement boundary conditions (Appendix A1) are applied to induce true Mises strains of approximately 30-40% and stress triaxiality is kept constant throughout the simulation (Appendix A2).
- A crystal plasticity model (Asaro 1983b) is used to model the bulk cobalt matrix surrounding the void. Crystal plasticity offers a more accurate model for the alloy matrix at the nanometer scale than isotropic plasticity models such as J2 flow. More details on the crystal plasticity formulation are given in Chapter 3, Section 3.4.
- A Taylor factor of 3.03 is used to convert the tensile stress-strain experimental data (Roebuck et al. 1984) for cobalt to a power law self hardening function for each slip plane, equation (3.47). The Taylor factor is the ratio between the macroscopic flow stress and the critical resolved shear stress on a slip plane as shown in (Figure 4.4). As there are several discrete slip systems in alloys, an arithmetic mean of the individual Taylor factors is used (Courtney 2000).

- The grain size hardening effect on the cobalt plastic slip behavior is incorporated in equation (3.47) and calibrated to the experimental observations of (Poech et al. 1991).
- The temperature dependence of slip plane hardening in equation (3.47) is calibrated to the experimental observations of (Sokolov et al. 1969).
- The rate parameters for cobalt, equation (3.44) are taken from (Sigl and Exner 1987)

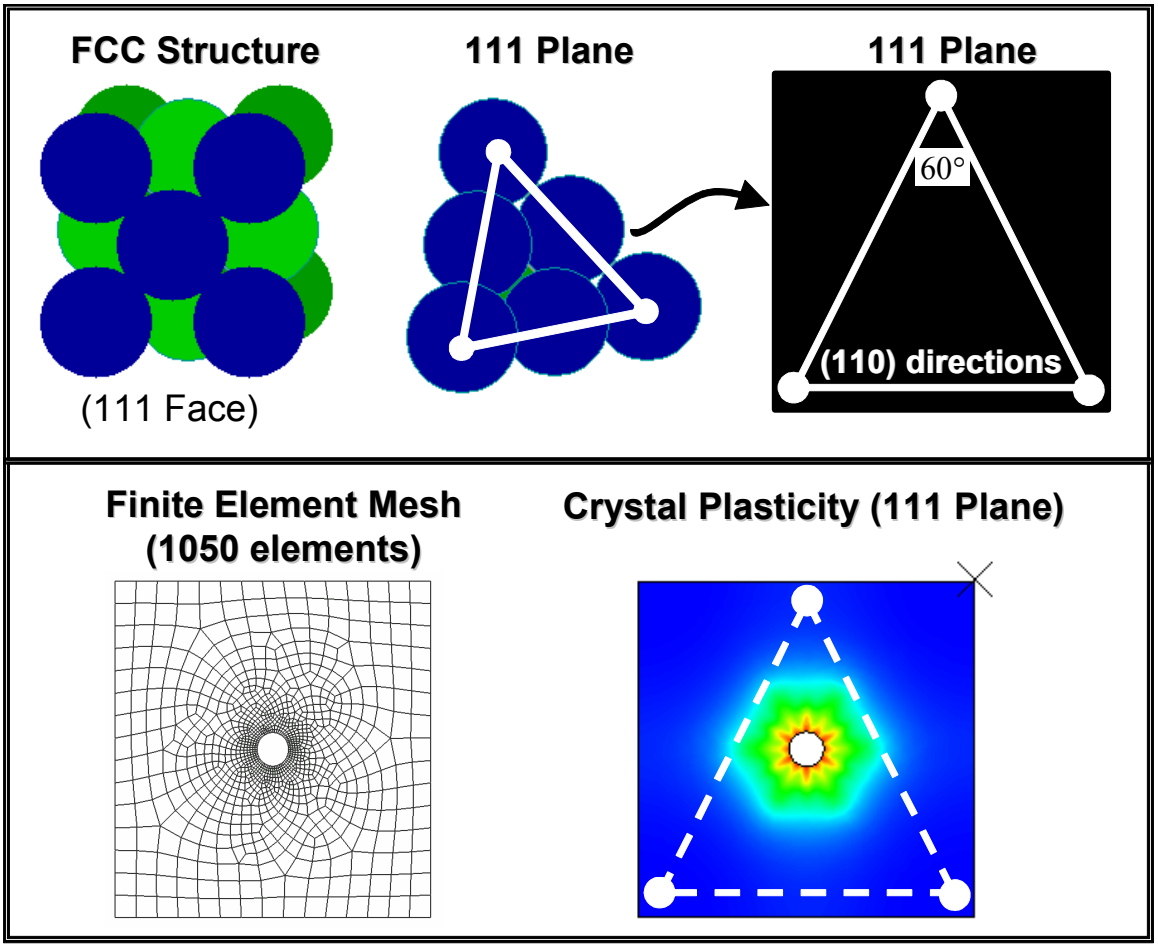

Figure 4.3. The crystallographic orientation used in the 2D void growth simulations. The finite element mesh is also shown.

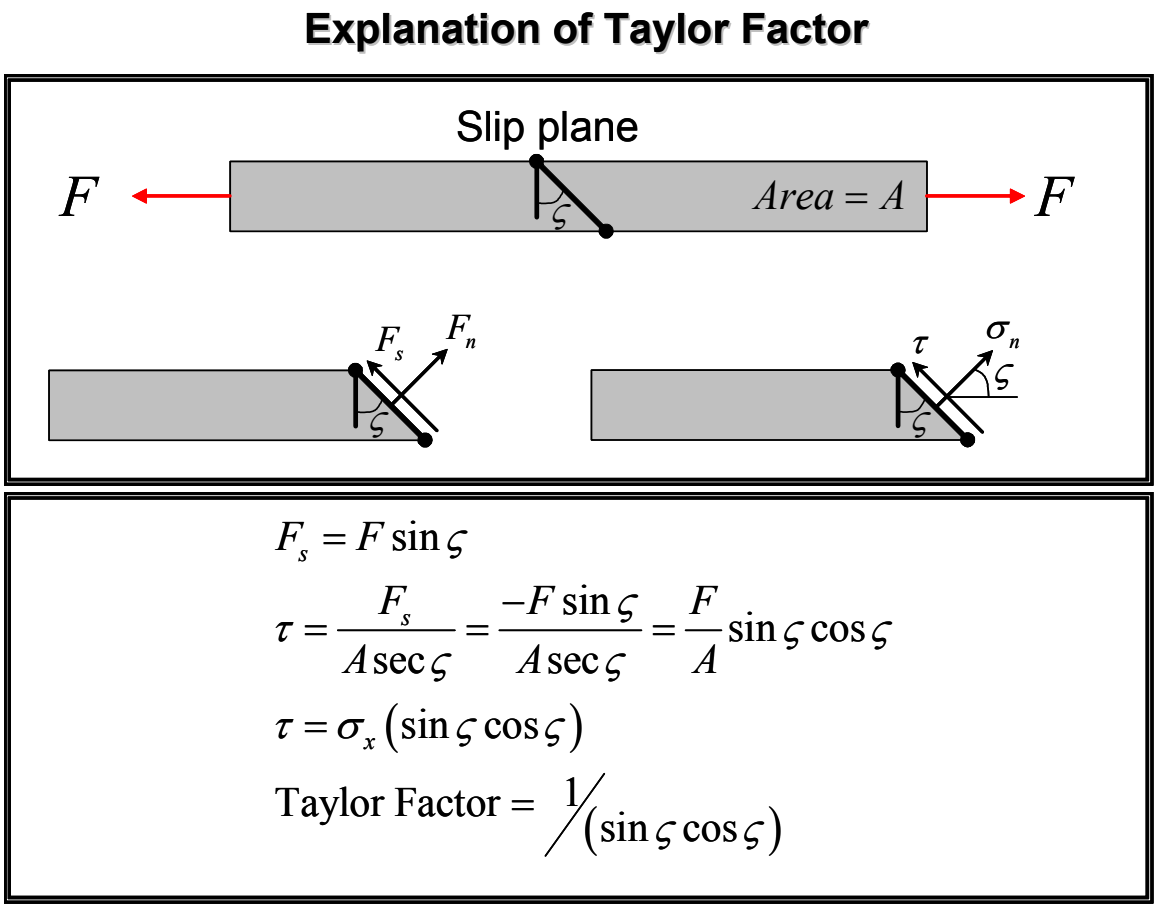

Figure 4.4. A brief explanation of the Taylor factor. It relates the uniaxial stress to the resolved shear stress on a slip plane.

Values for each material constant used in the crystal plasticity representation of cobalt, equations (3.44) and (3.47) are given in Table 4.1.

Crystal Plasticity Parameters for Cobalt used Void Growth Simulations			
Constant	***Value***	***Equation***	***Description***
E	$211 GPa$	-	Elastic Modulus
ν	0.31		Poisson's Ratio
m	10	(3.44)	Rate Sensitivity Parameter
$\dot{a}$	$0.001 s^{-1}$	(3.44)	Reference Strain Rate
g_0	$74 MPa$	(3.47)	Initial Strength of Slip Planes
γ_0	0.3125	(3.47)	Reference Accumulated Strain
n	0.2995	(3.47)	Hardening Exponent
ϑ_m	$1768 K$	(3.47)	Temperature effect on slip
ϑ_m	$273 K$	(3.47)	Reference Temperature
t	1	(3.47)	Thermal Softening Exponent
k_d	$2.145 Nmm^{-3/2}$	(3.47)	Hall-Petch effect on slip

Table 4.1 Parameters used for a crystal plasticity model of cobalt

4.1.3 Void Growth Parametric Study

The effect of triaxiality T, cobalt grain size d and temperature ϑ on void growth are now examined by varying each parameter in the void growth computational cell model. Unless otherwise stated the triaxiality $T = 0.5$, grain size $d = 5\mu m$ and temperature $\vartheta = 298K$. An expression for the void growth parameter $\mathcal{G} = \mathcal{G}(\vartheta, T, d)$, equation (4.5), is then proposed and calibrated to the data from the parametric study.

Triaxiality T

The 2D computational cell model, containing a single void, is loaded under constant triaxiality quasi-static fully periodic loading conditions. Stress triaxiality is defined as:

$$T = \frac{\sqrt{2} I_1}{3\sqrt{J_2}} \tag{4.6}$$

where I_1 is the first stress invariant and J_2 is the second stress invariant. As shown in (Figure 4.5), an average strain is applied in the y direction and the triaxiality is held constant using a feedback loop and an applied lateral pressure (See Appendix A2 for details). This is repeated for several triaxialities; each time the resulting 2D void volume (area) fraction is plotted with respect to the plastic strain in (Figure 4.6). As expected, higher triaxiality results in increased void growth as a function of Mises strain. The void growth rate becomes non-linear at higher plastic strains, particularly at triaxialities greater than 0.5. The void configuration at a Mises strain of 0.3 is shown for each triaxiality in (Figure 4.7).

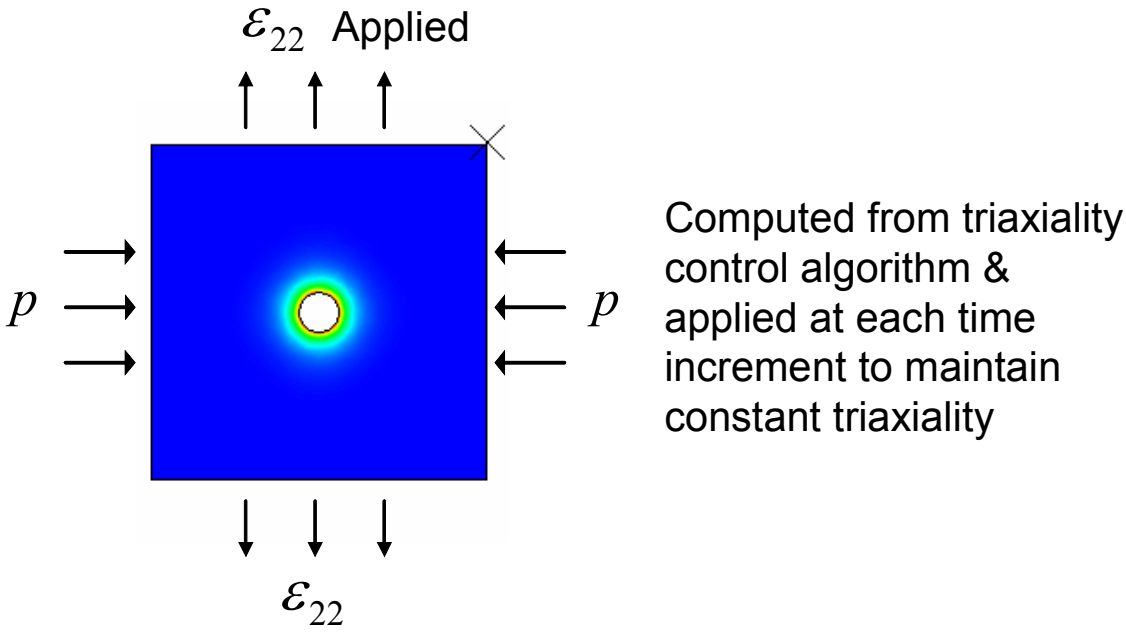

Figure 4.5. Stress triaxiality is fixed by applying an evolving lateral pressure

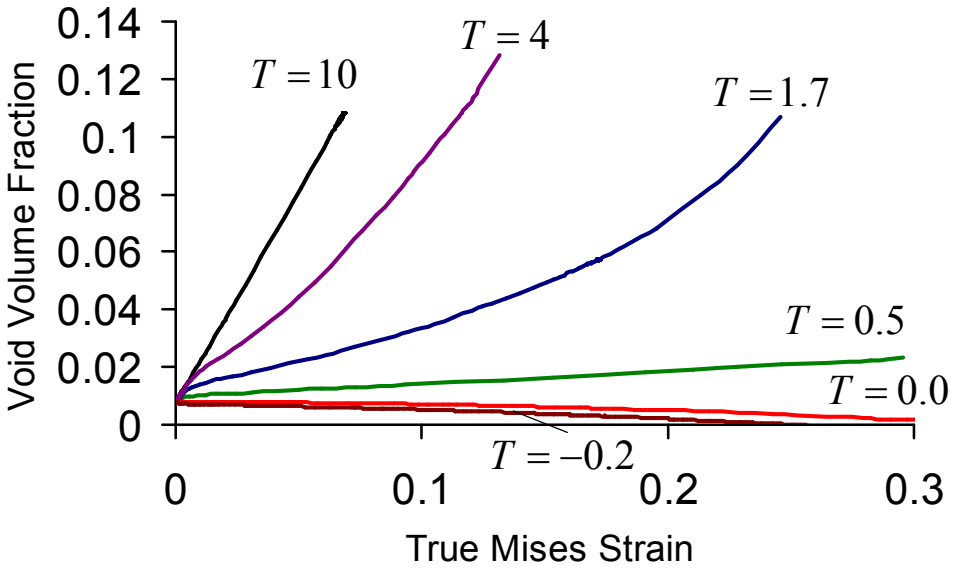

Figure 4.6. Void growth increases with increasing triaxiality. Note that in negative triaxiality $T = -0.2$ the void actually shrinks

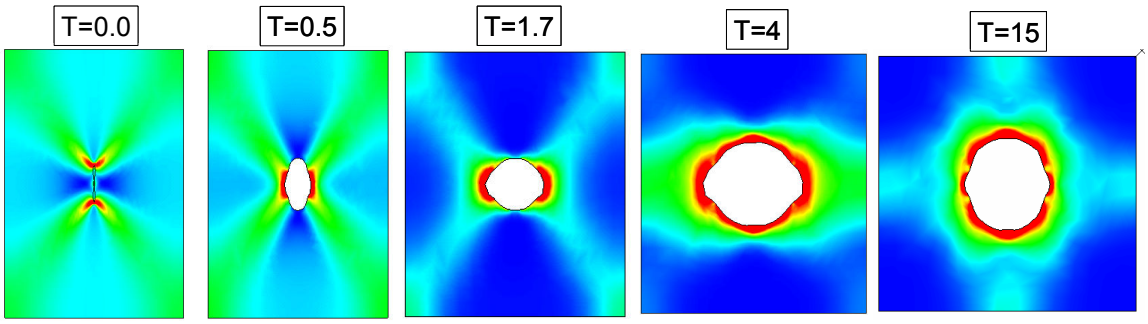

Figure 4.7. At low triaxiality voids collapse, at high triaxiality they grow at small plastic strains

Cobalt Grain Size d

The cobalt grain size d is varied in the slip strength equation (3.47). The single void cell model is again loaded under quasi-static loading conditions. The cobalt grain size d is varied from $d = 10nm$ to $d = 5000nm$. The numerical experiment is repeated at a triaxiality of $T = 2.0$. It is clear from (Figure 4.8) that decreasing the cobalt grain size d has the effect of encouraging void growth as a function of plastic strain regardless of the triaxiality. Hence although a smaller cobalt grain size strengthens the cobalt matrix, it also encourages void growth (at constant triaxiality and temperature).

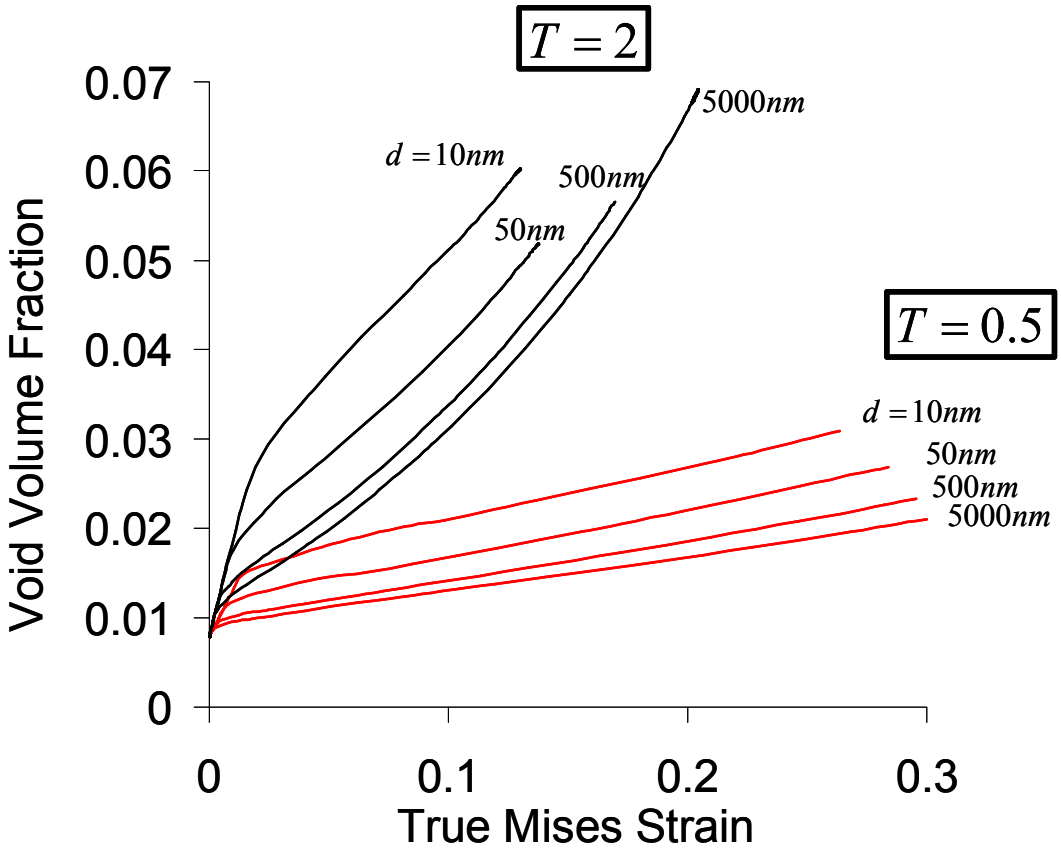

Figure 4.8. The void growth rate is predicted to increase as grain size decreases

Temperature ϑ

In the crystal plasticity model the slip system strength is temperature dependent, equation (3.47). Three temperatures are used in this equation; $400K, 700K$ and $1100K$. Isothermal conditions are assumed. A small temperature dependence is observed in the resulting void growth illustrated in (Figure 4.9). It is noted that (Horstemeyer et al. 2000b) observed an increase in void growth with temperature (at constant triaxiality) using an isotropic plasticity model for the alloy matrix. In the current material, the temperature effect is quite small compared to the effect of changing the cobalt grain size d or triaxiality T.

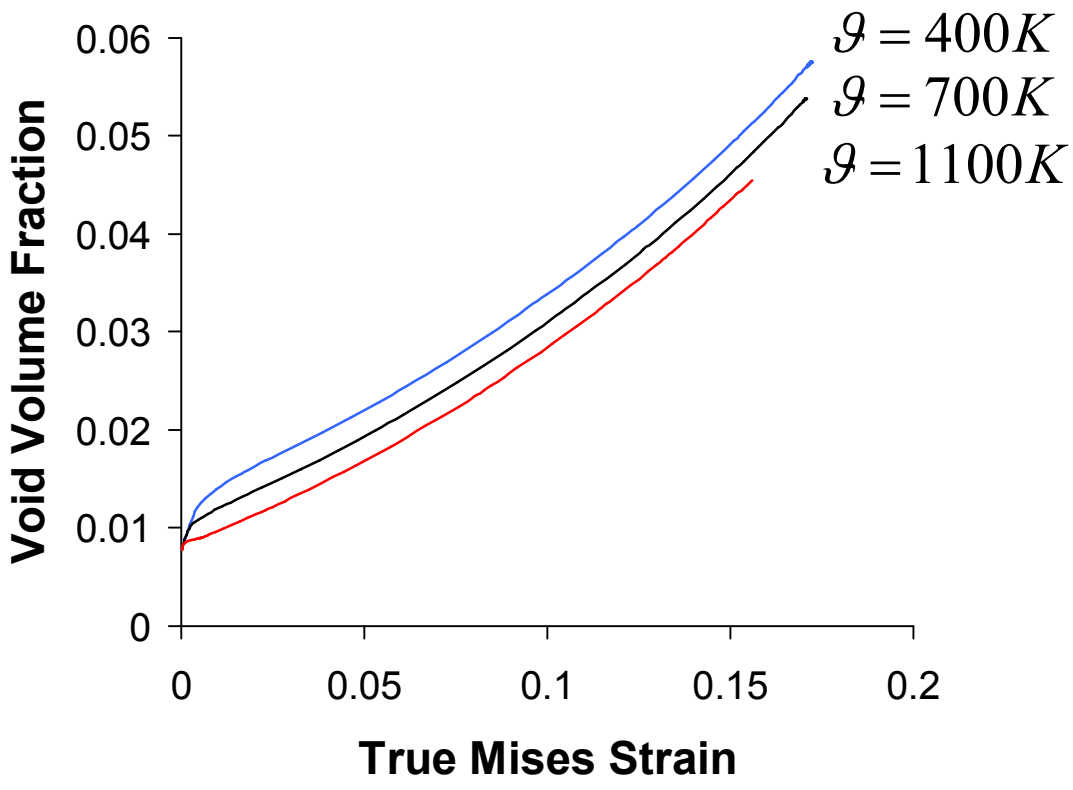

Figure 4.9. A small temperature effect is observed; decreasing void growth is predicted with temperature.

Calibrating the Void Growth Parameter $\mathcal{G}(\vartheta, T, d)$

The final expression for void growth is clearly triaxiality T and grain size d dependent from (Figure 4.7) and (Figure 4.8). As the temperature ϑ effect on void growth is small compared to the other effects it is neglected here. A simple form which captures the triaxiality and grain size dependency is given by:

$$\mathcal{G} = D_2 T + \frac{D_3}{\sqrt{d}} \tag{4.7}$$

The constants D_2 and D_3 are computed by calibrating this equation to the data in (Figure 4.8) and (Figure 4.6). A good fit is given by $D_2 = 0.16 \times 10^{-12} m^2$ and $D_3 = 1 \times 10^{-8} m^{3/2}$. The correlation is illustrated by comparing the void growth expression (4.4), with the parameter $\mathcal{G}$ given by equation (4.7), to the void growth simulations. The comparison for different triaxialities is shown in (Figure 4.10) and the comparison for different cobalt grain sizes is shown in (Figure 4.11).

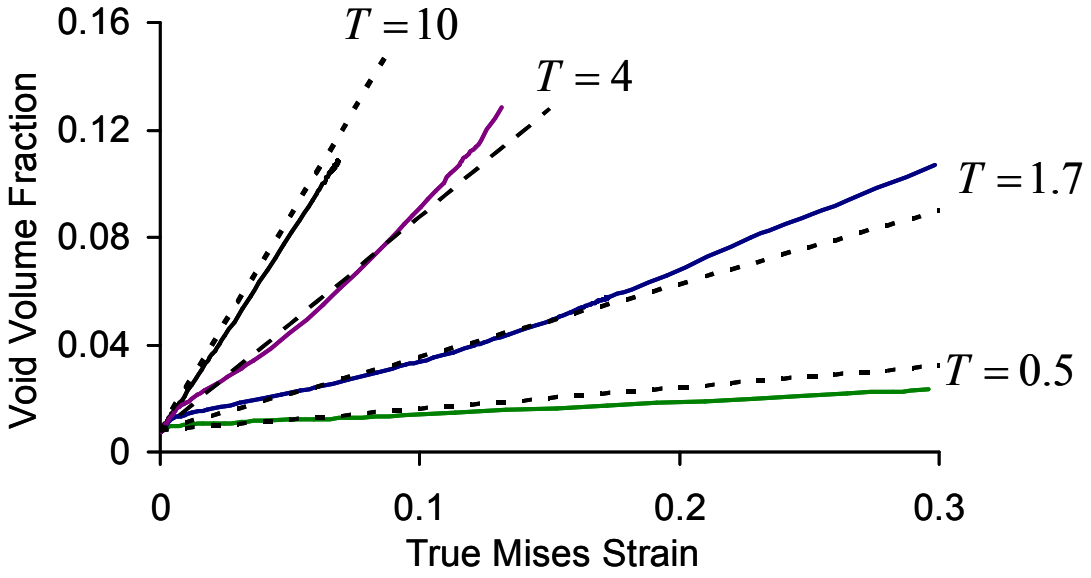

Figure 4.10. The void growth equation (4.7) (dashed lines) is compared to the void growth simulations (solid lines) under different triaxialities.

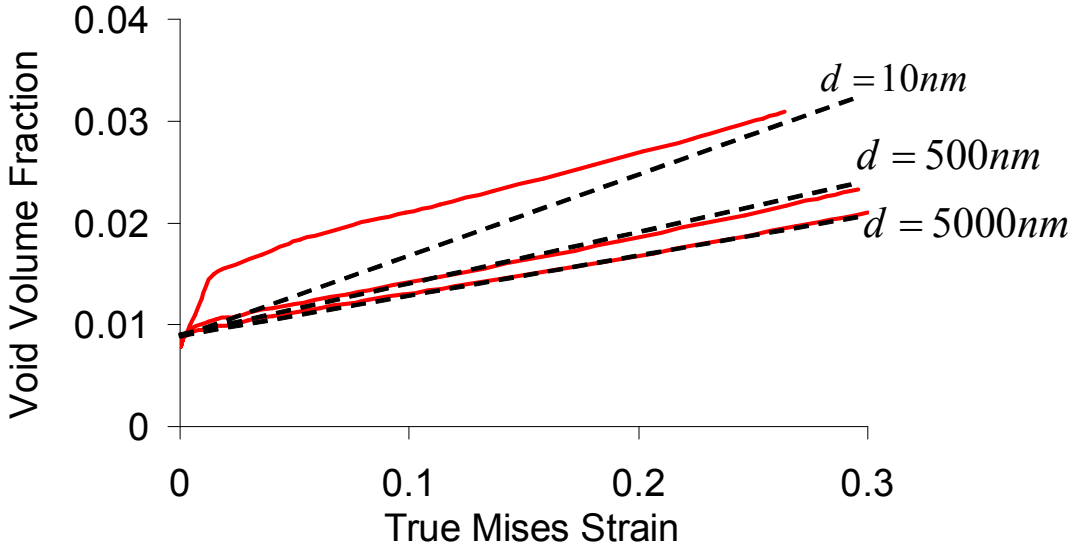

Figure 4.11. The void growth equation (4.7) (dashed lines) is compared to the void growth simulations (solid lines) with different grain sizes.

4.1.4 Void Coalescence $\mathscr{C}$

Void coalescence occurs when the stress fields induced by neighboring voids begin to interact. Void growth is accelerated by the presence of a near-by void as shown in (Figure 4.12) for two different void configurations; a single isolated void and a system of five interacting voids. In the multivoid system the average spacing between void is equal to five void diameters. In the single void system the average spacing between voids is ten diameters (voids are arranged periodically).

The initial void volume fraction in the multi-void system is five times that of the single void simulation. The void volume fraction of the cluster simulation is therefore divided by five to make a comparison between the two void growth rates in (Figure 4.12). The accelerated void growth arising from coalescence effects is usually accounted for in the porous damage equation by including a contribution to the porosity arising from coalescence ϕ_{coal} as described by equation (3.18) and repeated here for convenience:

$$\phi_{coal} = \mathscr{C}\eta v \tag{4.8}$$

Here the dimensionless coalescence parameter $\mathscr{C}$ is written in terms of the current porosity ηv:

$$\mathscr{C} = D_4 + D_5 \eta v \tag{4.9}$$

No coalescence criterion is used to indicate the onset of coalescence; coalescence is predicted as long as voids exist i.e. $\eta v > 0$ in equation (4.8). This is in contrast to the approach of (Tvergaard and Needleman 1981) and in the adiabatic shear band modeling performed in this thesis (Chapter 8) in which coalescence initiates at a critical void volume fraction. Values of $D_4 = 1$ and $D_5 = 1$ are used here; these values give a good correlation between the porous BCJ model and cell models as shown in the comparisons made in Section 4.1.6.

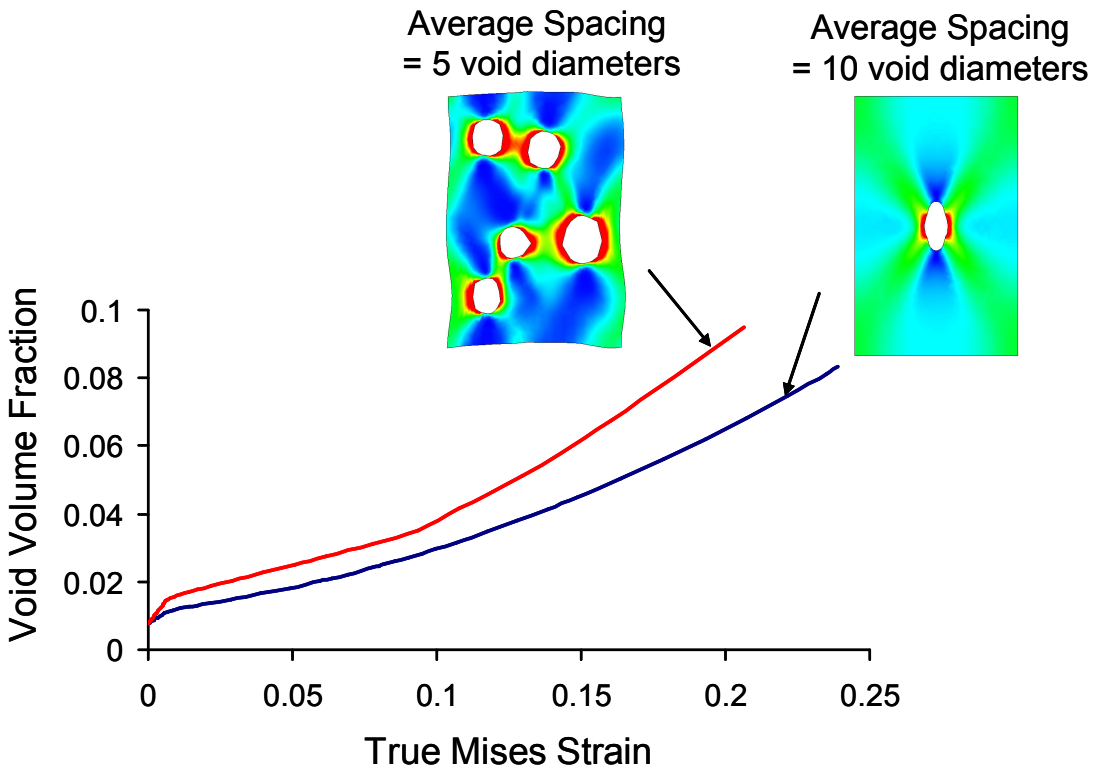

Figure 4.12. Void growth is accelerated by the presence of nearby voids.

This completes the evolution equations for void nucleation, growth and coalescence. The nucleation, growth and coalescence equations along with the material constants are summarized in Table 4.2.

Damage Equations for the Cobalt BCJ Model				
Mechanism	***Parameter***	***Eqn***	***Constant***	***Value***
Nucleation	$\mathcal{N} = \frac{\mathcal{N}^*}{s_{\mathcal{N}}(2\pi)^{0.5}} \exp\left\{-\frac{1}{2}\left(\frac{\varepsilon^p - \varepsilon_{\mathcal{N}}(\Upsilon)}{s_{\mathcal{N}}}\right)^2\right\}$	(4.2)	$\mathcal{N}^*$	$2\times10^{10}\,m^{-2}$
			s_N	0.05
	$\varepsilon_N = \frac{D_1}{Y}$	(4.3)	D_1	$2\times10^{8}\,Pa^{-1}$
Growth	$\mathcal{G} = D_2 T + \frac{D_3}{\sqrt{d}}$	(4.7)	D_2	$0.16\times10^{-12}\,m$
			D_3	$1\times10^{-8}\,m^{3/2}$
Coalescence	$\mathcal{C} = D_4 + D_5 \eta v$	(4.9)	D_4	1
			D_5	1

Table 4.2 A summary of the microvoid damage equations and parameters for cobalt. Equation numbers are shown.

4.1.5 Rate, Temperature and Grain Size Effects on Plastic Flow

The porosity parameters for void nucleation, growth and coalescence have been determined in Sections 4.1.1-4.1.4. To complete the porous cobalt BCJ model, plastic flow parameters given in Table 4.3 must be determined. These parameters can be determined to the known rate, temperature and grain size dependent plastic flow behavior. This usually involves calibrating to experiment. Here the BCJ model (neglecting porosity) is calibrated to the known crystal plasticity model described in Section 4.1.2. The resulting BCJ constants are in Table 4.3. For a description of how to determine the BCJ constants see Appendix A3.

BCJ Parameters calibrated from Crystal Plasticity Model			
Parameter		***Value***	***Equation***
Reference Strain Rate	f	$0.001 s^{-1}$	(3.9)
Magnitude of Rate Effect	V	$69 MPa$	
Initial Temperature	θ_0	$298 K$	(3.11)
Melt Temperature	θ_m	$1768 K$	
Thermal Softening Exponent	t	1	
Initial Yield Stress	C_1	$750 MPa$	
Hall-Petch Effect	C_2	$3.35\times10^{5}\, Pam^{1/2}$	
Isotropic Hardening Modulus	C_3	$-69 MPaK^{-1}$	(3.12) & (3.13)
	C_4	$31 GPa$	
Isotropic Dynamic Recovery Modulus	C_5	$1.674\times10^{-6}\, Pa^{-1}$	
	C_6	0	
Isotropic Static Recovery Modulus	C_7	$0.02 Pa^{-1}s^{-1}$	
	C_8	$-1877 K$	
Kinematic Hardening Modulus	C_9	0	
	C_{10}	0	
Kinematic Dynamic Recovery Modulus	C_{11}	0	
	C_{12}	0	
Kinematic Static Recovery Modulus	C_{13}	0	
	C_{14}	0	
Elastic Modulus	E	$211 GPa$	-
Poisson's Ratio	ν	0.31	

Table 4.3 Constants which describe the BCJ plasticity model for the cobalt binder. Equation numbers are shown

Note that kinematic hardening and recovery are not considered (constants $C_9 - C_{14}$ are zero) i.e. only isotropic hardening/recovery is modeled (constants C_3 - C_8 are non-zero).

The damage evolution equations in Table 4.2 are now used within the BCJ model described in Table 4.3 to form a complete strain rate, temperature, triaxiality, grain size and porous damage dependent constitutive model for the cobalt binder, equation (3.9)-(3.12). The key relationships in the cobalt binder constitutive model can be summarized as follows:

- Initial yield stress is related to the temperature, strain rate and cobalt grain size
- Subsequent dislocation hardening and recovery is related to the temperature
- Void nucleation is related to the initial yield stress and plastic strain
- Void growth rate is related to the triaxiality, plastic strain and cobalt grain size

4.1.6 Porous Cobalt BCJ Plasticity Model: Validation

The BCJ porous cobalt plasticity model developed in Section 4.1.1-4.1.5 (summarized in Table 4.2 and Table 4.3) is now compared to the average response of a voided cobalt computational cell (the matrix in the cell is modeled using crystal plasticity). The purpose of this exercise is to ensure the BCJ model is replicating the correct response i.e. the response of a porous cobalt alloy. Microvoid nucleation is not considered in either the cobalt cell (in which a population of pre-existing voids is modeled) or the BCJ model. An initial porosity of 1% is used in the BCJ model; this is consistent with the initial porosity in the voided cobalt cell model.

Different loading triaxialities T, cobalt grain sizes d, average loading rates $\|\mathbf{D}\|$ and temperatures ϑ are examined. In each case the calibrated BCJ model shows good correlation with the directly modeled microstructure simulation. (Figure 4.13) shows the triaxiality comparison and the resulting plastic strain contours at a Mises strain of 0.3. (Figure 4.14) shows the temperature comparison. (Figure 4.15) shows the rate comparison. (Figure 4.16) shows the cobalt grain size comparison.

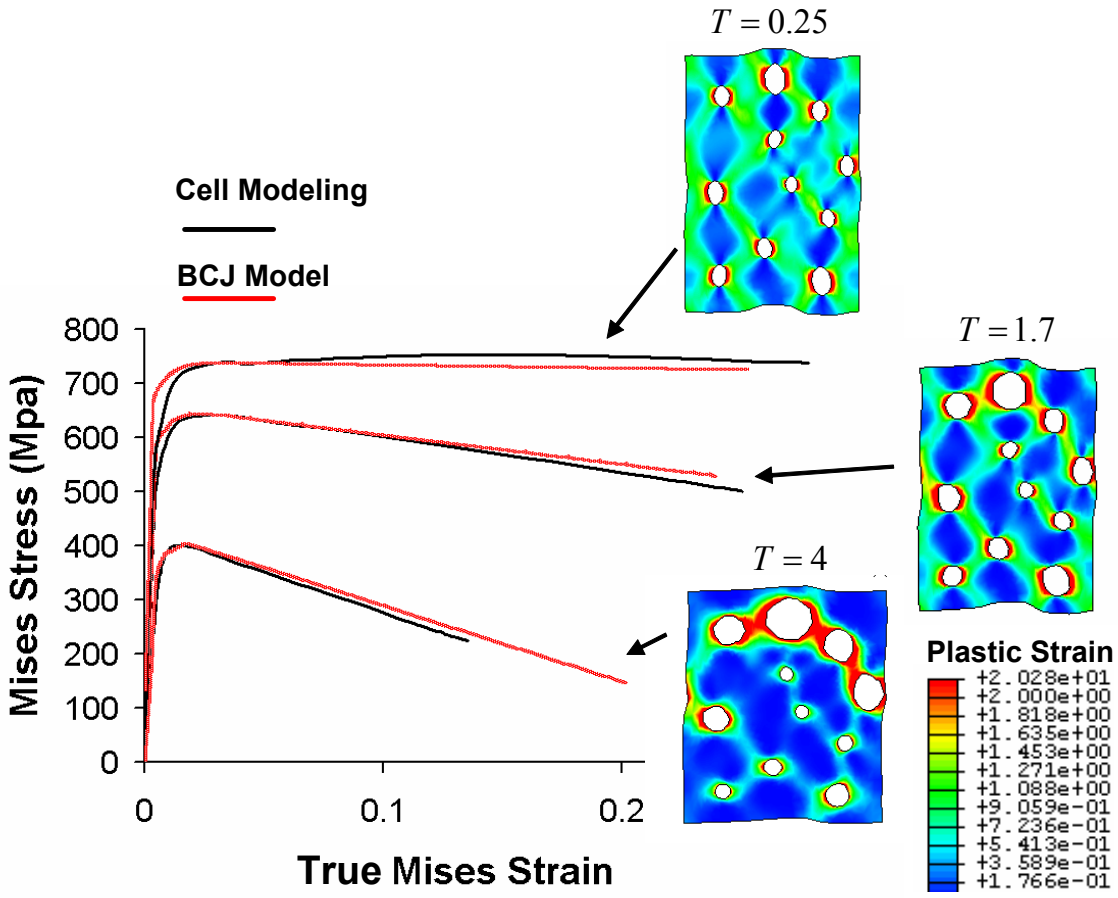

Figure 4.13. A comparison of the final BCJ model and multivoid simulations under different triaxialities

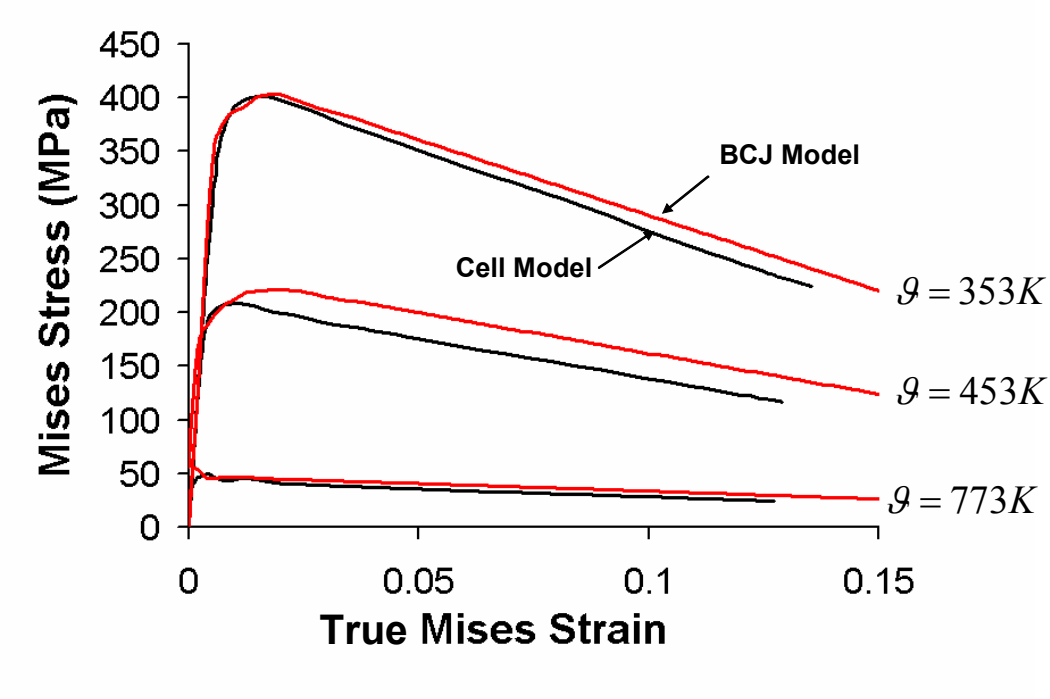

Figure 4.14. A comparison of the final BCJ model and multivoid simulations under different temperatures

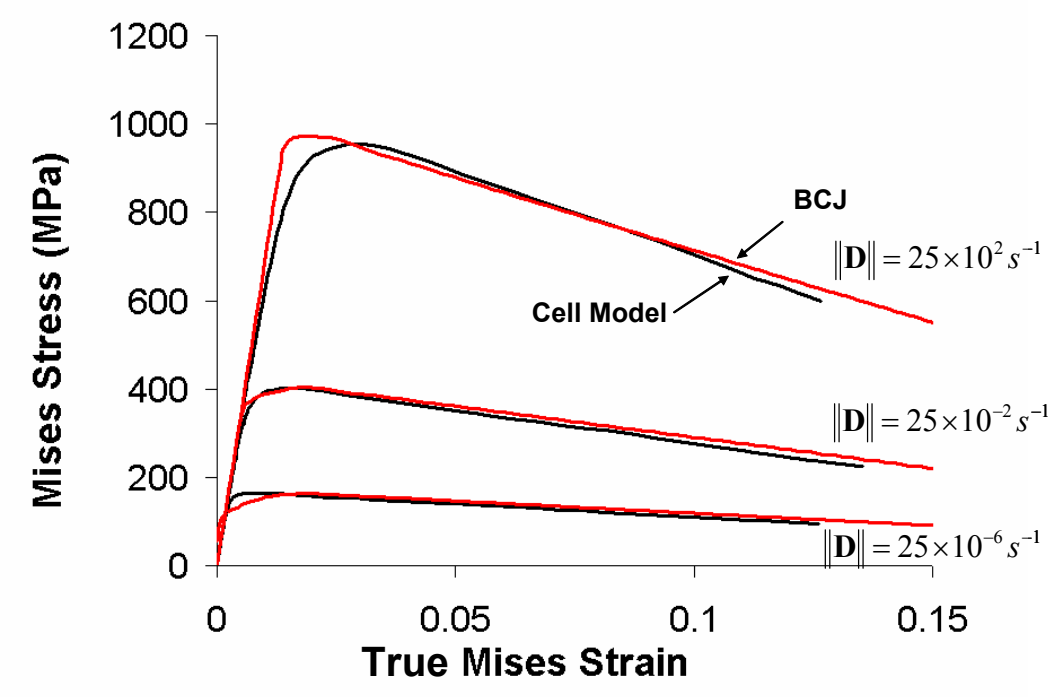

Figure 4.15. A comparison of the final BCJ model and multivoid simulations under different loading rates

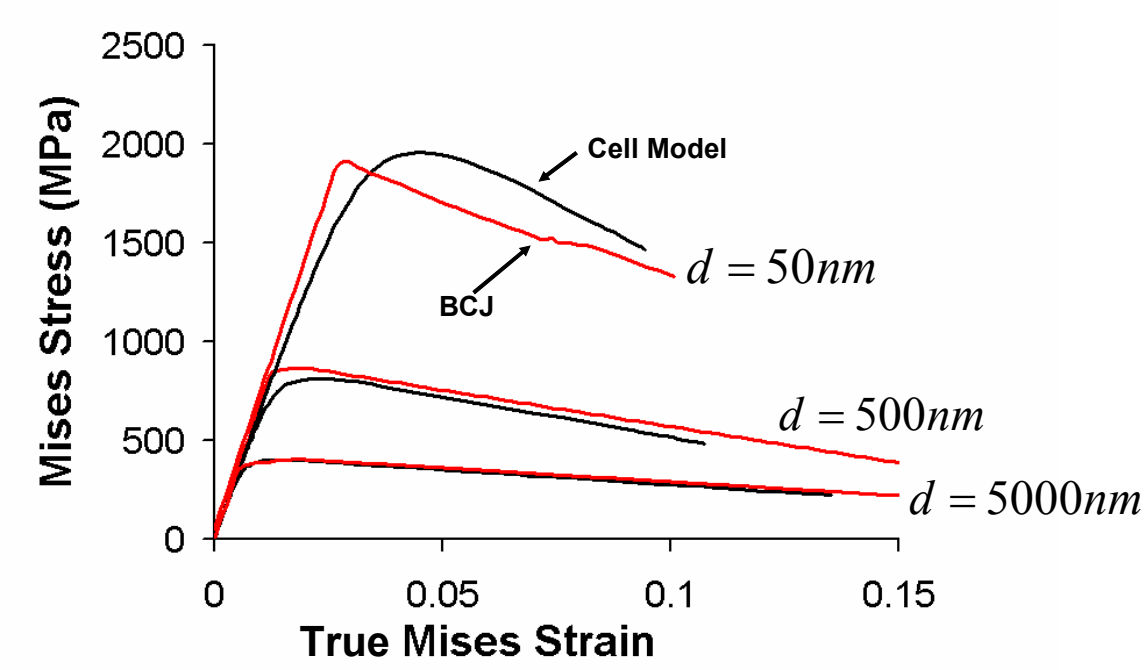

Figure 4.16. A comparison of the final BCJ model and multivoid simulations under different grain sizes

4.1.7 Inverse Strength-Ductility Relationship - Cobalt

In (Figure 4.17) the stress-plastic strain curves obtained from the BCJ model are illustrated using three different grain sizes (temperature $\vartheta = 353K$, triaxiality $T = 0.6$ and quasi-static loading). Smaller cobalt grain sizes increase the initial yield stress Y as expected from equation (3.11). A side effect of the higher stress level is that the mean strain for microvoid nucleation ε_N occurs sooner due to inverse relationship between ε_N and initial yield stress, equation (4.3). Hence an inverse strength-ductility relationship is built into the model of the cobalt binder.

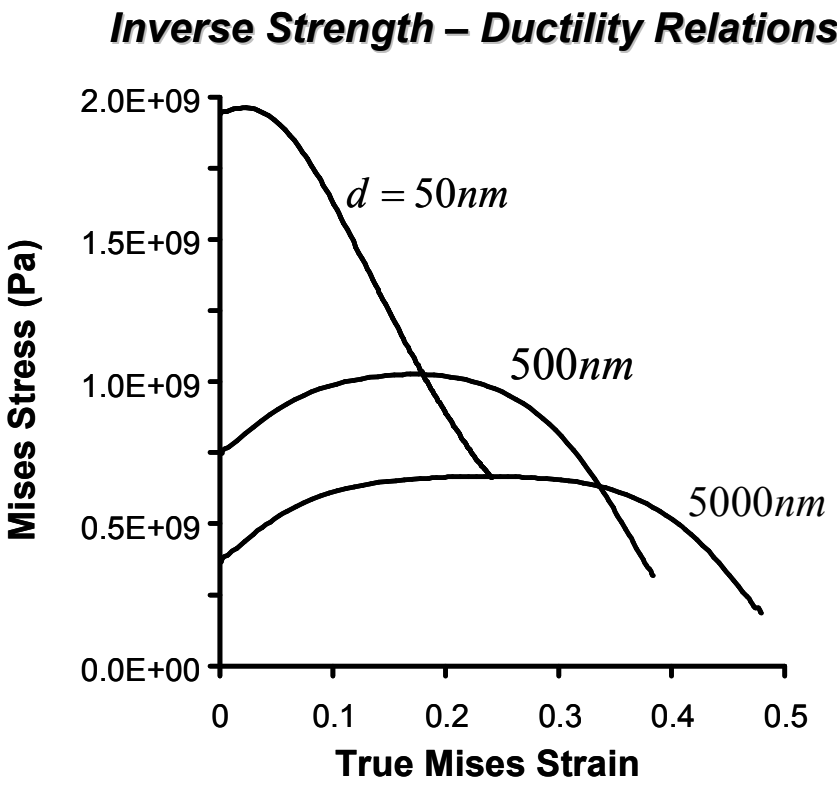

Figure 4.17. The BCJ model developed for cobalt includes an inverse strength-ductility relationship via equation (4.3).

4.2 Tungsten Carbide Material Model

In this sub-section, a simple brittle fracture model is calibrated to the experimentally observed behavior of tungsten carbide in terms of the tensile strength σ_f and critical energy release rate G. The role of the carbide grains in a WC-Co composite is well established empirically and is discussed in Section 2.1.1. Tungsten carbide exhibits a classical brittle failure mechanism over a wide range of temperatures.

A smeared crack continuum approach implemented in (ABAQUS 2004) is used here to represent brittle fracture of the carbide. Individual "macro" cracks are not modeled: rather, the presence of

cracks enters into the model through the effect cracks have on the stress and material stiffness. A material point behaves elastically and 'fractures' when a Rankine criteria is satisfied i.e. when $\max(\sigma_1, \sigma_2) > \sigma_f$ where σ_f is the tensile strength. This criterion states that a crack forms when the maximum principal tensile stress exceeds the tensile strength of the brittle material. The crack surface is taken to be normal to the direction of the maximum tensile principal stress. Note that in compression a simple linear elastic response is assumed here.

The model has memory of this crack direction, and subsequent cracks at the point under consideration can only form in directions orthogonal to the first crack (ABAQUS 2004). Hence in 2D plane strain the effects of three orthogonal 'cracks' can be modeled at a material point, corresponding to the three direct stress components.

The stresses are *not* set to zero when fracture occurs. The post fracture stress at a carbide material point is controlled by the critical energy release rate G; this material constant is equal to the area under the curve of applied stress and displacement across the crack faces (Figure 4.18). In order to compute a 'crack normal displacement' at a material point, the strain at the material point must be multiplied by some length measure. In numerical models this characteristic length is equal to the size of the finite element mesh size. The element size here is interpreted as the square root of the area of the 2D finite element in which the material point is situated. The use of the energy release rate and a characteristic length to control the post fracture behavior is considered to allay concerns about mesh sensitivity (Hilleborg et al. 1976). A schematic of the stress normal to the crack face (direct stress σ_n) is plotted as a function of the

displacement across the crack faces (crack normal displacement u_n) in (Figure 4.18). Experimental values (memsnet.org 2006b) for the tensile strength σ_f and energy release rate G are used here and are summarized in Table 4.4.

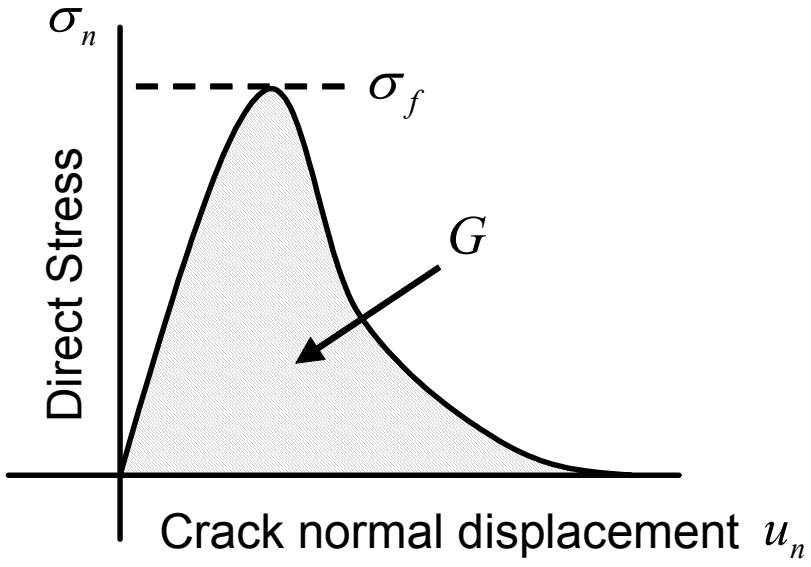

Figure 4.18. The post fracture stress level depends on the energy release rate G.

Tungsten Carbide Elastic-Brittle Fracture Damage Model			
Constant	**Value**	**Constant**	**Value**
E **(Young's Modulus)**	$700GPa$	υ **(Poisson's Ratio)**	0.25
σ_y **(Tensile Strength)**	$1.5GPa$	G **(Energy Release Rate)**	$2\times10^{9}\,Jm^{-2}$

Table 4.4 Material constants for carbide elastic – brittle fracture constitutive relationship

4.3 WC-Co Composite Constitutive Model

In this Section the BCJ constitutive model developed for the porous cobalt in Section 4.1, and the brittle fracture model developed for the tungsten carbide in Section 4.2, are employed to model the micromechanics of a WC-Co composite; the discrete grains and binder are modeled directly. A parametric study is performed to quantify the effect of each microstructural parameter investigated so far. The results of the parametric study are then used to calibrate a homogenized composite model which is proposed in Section 4.4.

As a reminder, the porous cobalt BCJ model (Section 4.1) describes plastic flow in terms of

- rate $\|\mathbf{D}\|$
- temperature ϑ
- cobalt grain size d
- porosity evolution ϕ
- triaxiality T

and is summarized in Tables 4.2 and 4.3.

The tungsten carbide model (Section 4.2) describes brittle fracture in terms of

- tensile strength σ_f
- critical energy release rate G

and is summarized in Table 4.4.

The final composite response is a function of the micromechanics within the cobalt binder and carbide grains. For simplicity, the interface between the materials is assumed to be perfectly

bonded and so the final composite response is not a function of the interfacial behavior. As the individual cobalt and carbide phases are being modeled in this Section, the relative fraction of each material also influences the overall composite response. This parameter is described through the volume fraction of cobalt, f. A summary of the final composite design parameters is given in Table 4.5.

Key Design Parameters for the Final WC-Co Composite	
Design Parameter	***Description***
d	Cobalt Grain Size
f	Cobalt Volume Fraction
T	Triaxiality
ϑ	Temperature
$\|\mathbf{D}\|$	Rate of Deformation
σ_f	Carbide Tensile Strength

Table 4.5 Key design parameters for the final WC-Co constitutive relation

In Section 4.3.1 the results of a typical WC-Co simulation are illustrated to demonstrate the form of the average constitutive response; stress degradation exhibits brittle and ductile failure stages. A microstructural parametric study is then performed in Section 4.3.2 – the key microstructural parameters are varied and the constitutive response is observed; a summary is given toward the end of this Section 4.3.2.

4.3.1 General Form of the Composite Constitutive Response

A 2D plane strain cell model of the composite system is constructed and discretized using 10500 finite elements a shown in (Figure 4.19). The cobalt volume fraction is 15%. Fully periodic quasi-static displacement boundary conditions are applied under isothermal conditions, $\vartheta = 353K$. The cobalt grain size $d = 500nm$. Triaxiality is held constant at $T = 0.5$ using the method explained in Appendix A2. Hence an average strain is applied in the 'y' direction and a lateral pressure is applied in the 'x' direction to maintain a constant triaxiality. The average Mises stress and strain are computed using the averaging equations (3.4) and (3.5) and are plotted in (Figure 4.19) along with the resulting total Mises strain and plastic Mises strain contours. Note that plastic strain only occurs in the cobalt – the carbide is elastic.

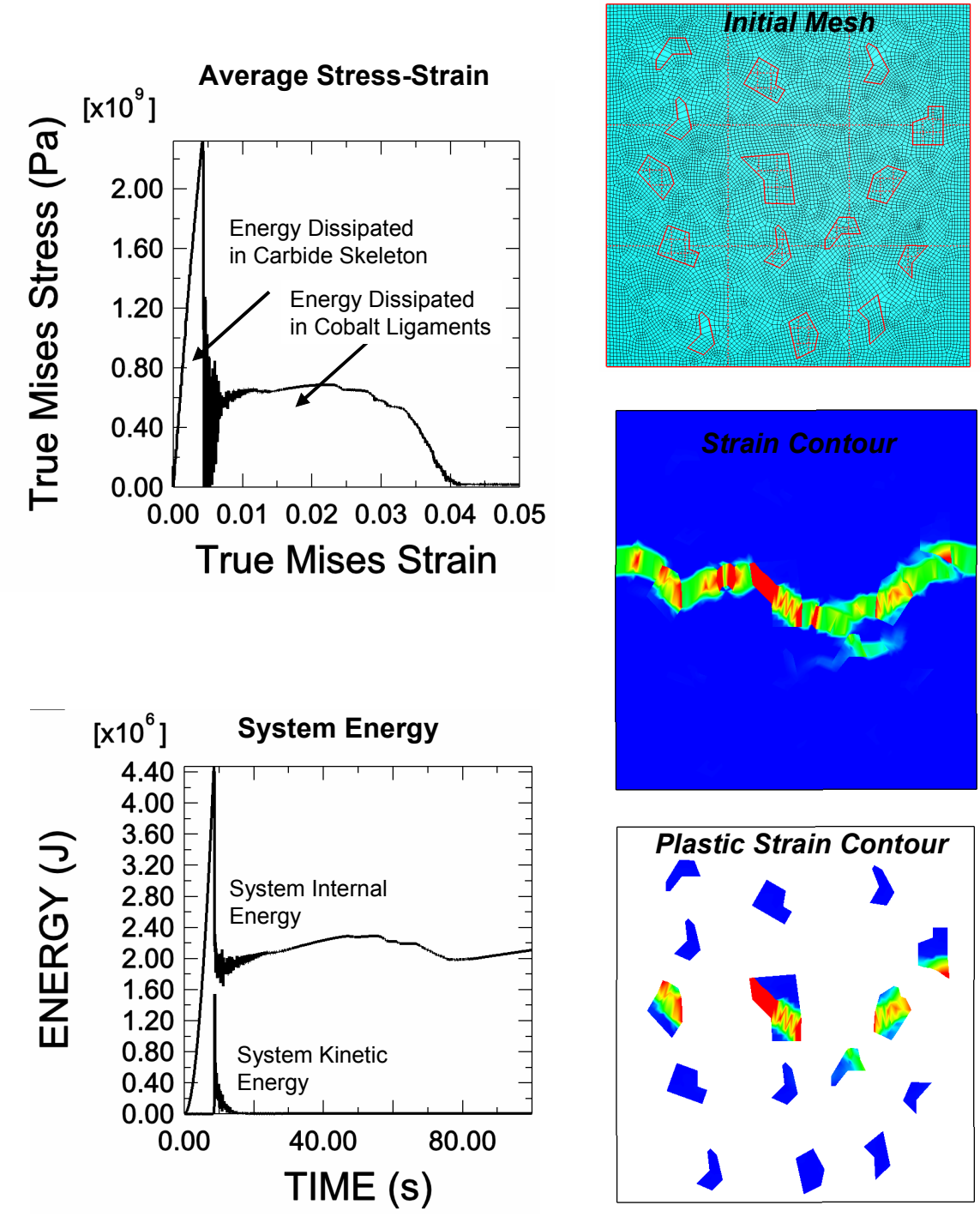

Figure 4.19. The composite model mesh is shown. The Mises strain and plastic strain contours are shown to illustrate the combined brittle-ductile fracture path. The average composite stress and strain are plotted to show the brittle stress collapse followed by plastic flow.

The average WC-Co constitutive response shown in (Figure 4.19) is shown schematically in (Figure 4.20). The composite initially deforms elastically; the composite elastic modulus is computed as 600GPa which is close to the experimentally observed Young's modulus of 595GPa (Connolly and McHugh 1999) for a WC-Co composite with a similar composition. At a true strain of approximately 0.5% the carbide rapidly fractures and the stress collapses. The peak stress just before fracture is called the fracture stress Y_0 here. The only resistance to deformation is then provided by the cobalt which bridges the brittle crack at several points i.e. a multiligament zone (MLZ) forms. The stress within the deforming cobalt ligaments saturates, giving an overall composite stress saturation called the post fracture strength S here. As the ductile cobalt deforms further, microvoid nucleation occurs at the composites mean nucleation strain $\bar{\varepsilon}_N$. These voids grow and weaken the cobalt, eventually leading to composite rupture at a nominal strain of approximately 3.5%.

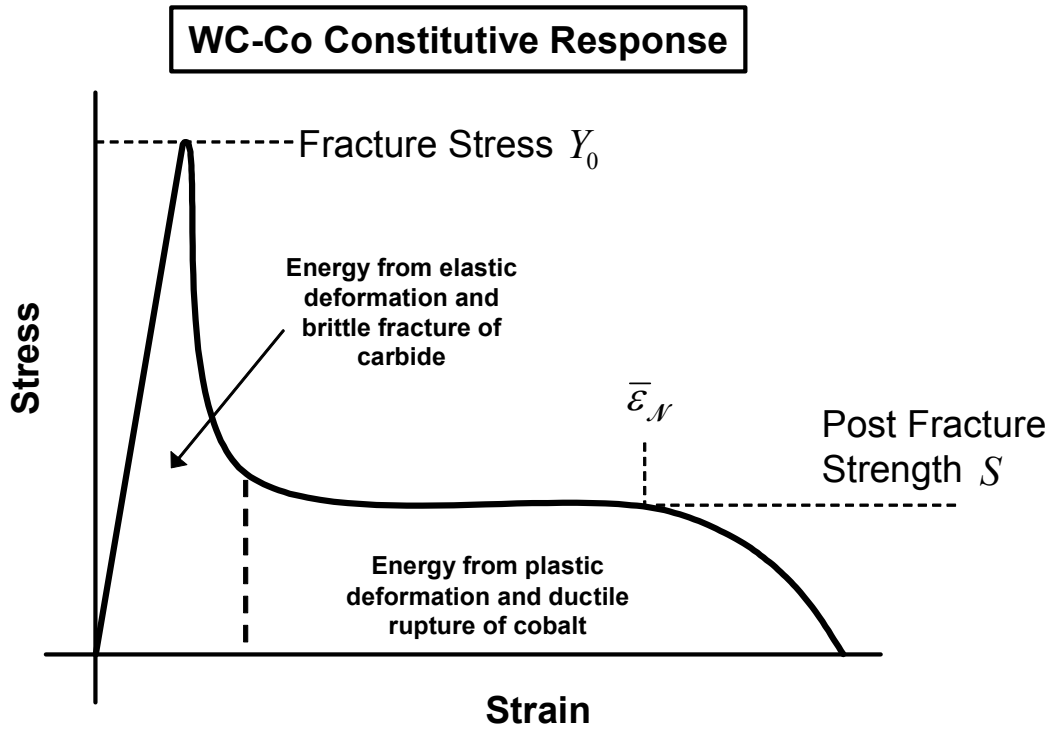

Figure 4.20. A schematic of the important features of the WC-Co composite response predicted in the computational model of (Figure 4.19). The unique feature of this work is that the tail end of this curve is modeled in a homogenized constitutive relation (Section 4.4).

The largest contribution to strain energy density or area under the stress-strain curve arises during the post-carbide fracture stage of deformation during which the cobalt provides the remaining resistance to deformation. A unique feature off this work is that the post-fracture plastic flow stage of deformation is incorporated in the final hierarchical constitutive relation in Section 4.4. This stage contributes greatly to the mechanical response in the crack tip region where multi-ligament zones arise, blunting the brittle crack. Conventional constitutive relations for ductile reinforced composites often neglect this stage of deformation.

Although quasi-static loading is applied, rapid carbide failure temporarily introduces a significant amount of kinetic energy into the system (a dynamic explicit finite element code is used). However this kinetic energy soon dissipates and the quasi-static condition is again satisfied i.e. the system internal energy is much greater than the kinetic energy as shown in (Figure 4.19).

4.3.2 Microstructural Parametric Study

Before attempting to develop a form for the composite constitutive response, it is pertinent to investigate the effect of varying each of the key microstructural parameters:

- rate $\|\mathbf{D}\|$
- temperature ϑ
- cobalt grain size d
- triaxiality T
- cobalt volume fraction f

In an effort to include a statistical variation in the microstructure, three microstructural arrangements are used for each parameter investigated and the average constitutive response of the three is considered to be sufficient. The three microstructural arrangements are shown in (Figure 4.21). The irregular shaped zones are pools of cobalt engulfed in carbide grains. Unless otherwise stated the (average) cobalt grain size is $d = 500\text{nm}$, cobalt volume fraction $f = 0.15$, temperature $\vartheta = 353K$, stress triaxiality $T = 0.5$ and loading is performed quasi-statically.

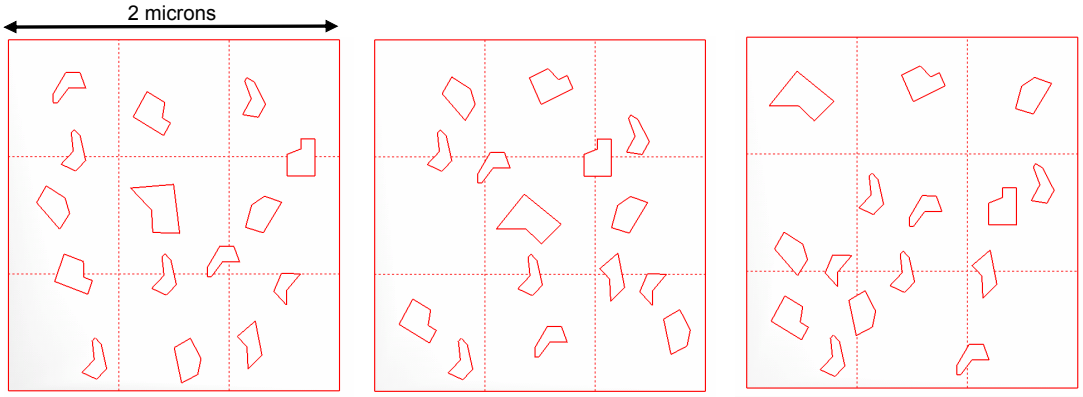

Figure 4.21. The geometry of the cell models used to perform a parametric study of the importance of each design variable

Cobalt Grain size d

The cobalt grain size d is varied in the expression which describes the initial yield stress Y in the cobalt, equation (3.11), Table 4.3. Three cobalt grain sizes are chosen: 50nm, 500nm, 5000nm. The resulting average composite Mises stress-strain curves are plotted in (Figure 4.22).

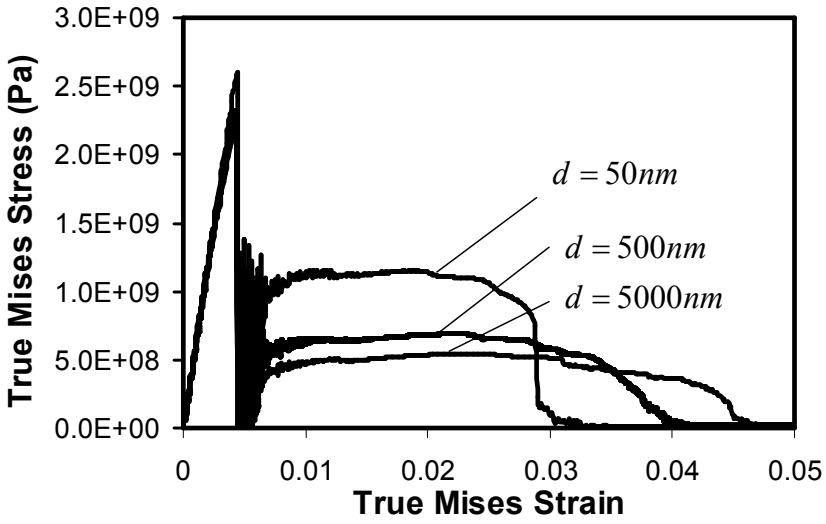

Figure 4.22. Decreasing the cobalt grain size d increases the post fracture strength S but decreases ductility

Microstructure Cause: Smaller cobalt grain sizes d are stronger according to the Hall-Petch relationship built into the cobalt's initial yield stress, equation (3.11).

Macroscale Effect: As the composite's post-fracture response is controlled by the resistance to plasticity in the cobalt binder, higher post fracture strength S is predicted with decreasing grain size d. However the higher stress levels reduce the mean nucleation strain ε_N in the cobalt, equation (4.3) resulting in lower composite ductility (strain at complete failure).

Cobalt Volume Fraction f

The cobalt volume fraction is varied directly in the cell models by expanding them about their centroids. Three cobalt volume fractions are examined; 5%, 15% and 25%. The resulting macroscale stress-strain curves are plotted in (Figure 4.23).

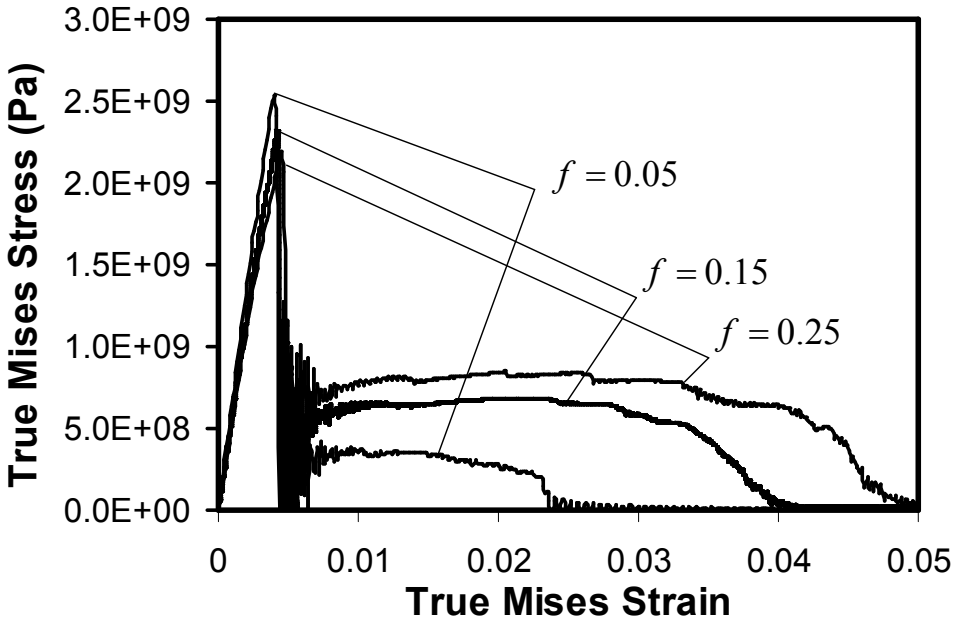

Figure 4.23. Increasing the cobalt volume fraction f increases the post fracture strength S and ductility.

Microstructure Cause: Increasing cobalt volume fraction f is accommodated by reducing the amount of carbide.

Macroscale Effect: Less carbide results in a lower fracture stress, Y_0 . However the increasing amount of cobalt increases the post-fracture strength S and increases composite ductility.

Overall the area under the stress-strain curve increases substantially indicating that increasing the cobalt fraction f is a good toughening mechanism; more energy is dissipated propagating a crack through the cobalt regions, than through the carbide.

Temperature ϑ

The cell models are now loaded at four different temperatures, 353K 453K, 553K and 653K. Isothermal conditions are assumed during each simulation. The composite stress-strain response for each case is plotted in (Figure 4.24).

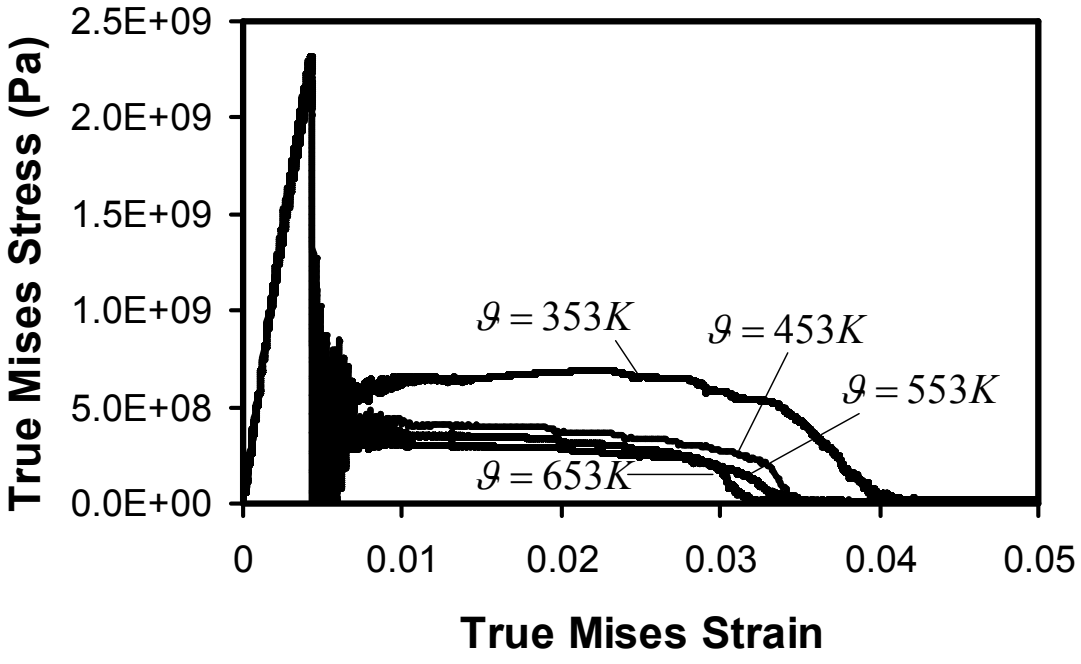

Figure 4.24. Increasing the temperature ϑ decreases the post fracture strength S.

Microstructure Cause: Increasing the temperature acts to degrade the initial yield stress Y, equation (3.11) and hardening modulus H, equation (3.13) within the cobalt zones.

Macroscale Effect: This results in lower post fracture strength S. Composite ductility also degrades because the strain localizes much more in the cobalt, encouraging microvoid nucleation.

Loading Rate $\|\mathbf{D}\|$

The effect of strain rate on the average composite behavior is determined by varying the velocity of the boundary conditions applied to the computational cells. The macroscale loading rate is varied from $\|\mathbf{D}\| = 5\times10^{-4}s^{-1}$ which is essentially quasi-static, to $\|\mathbf{D}\| = 5s^{-1}$. The stress-strain curves for each case are shown in (Figure 4.25).

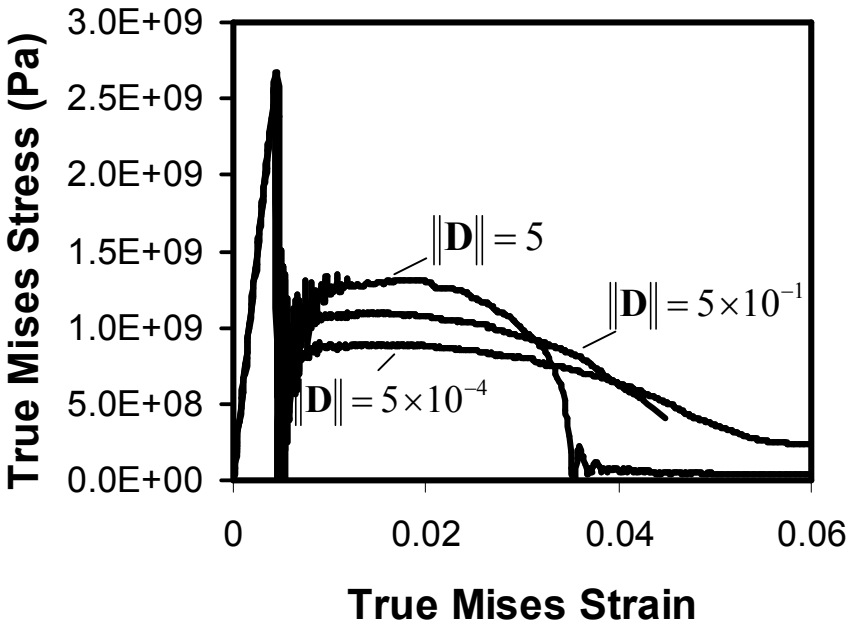

Figure 4.25. Increasing the loading rate $\|\mathbf{D}\|$ increases the post fracture strength S

Microstructure Cause: Rate hardening increases the strength of the plastically deforming cobalt binder.

Macroscale Effect: Increasing post fracture strength S. Again, higher stress levels in the cobalt leads to earlier microvoid nucleation and a reduced composite ductility as shown in (Figure 4.25).

Triaxiality T

The effect of triaxiality T on the average composite behavior is determined by varying the applied triaxiality on the computational cells boundary. Four triaxiality levels are applied; 0.5, 0.6, 0.8 and 1.2. The resulting stress-strain curves are shown in (Figure 4.26).

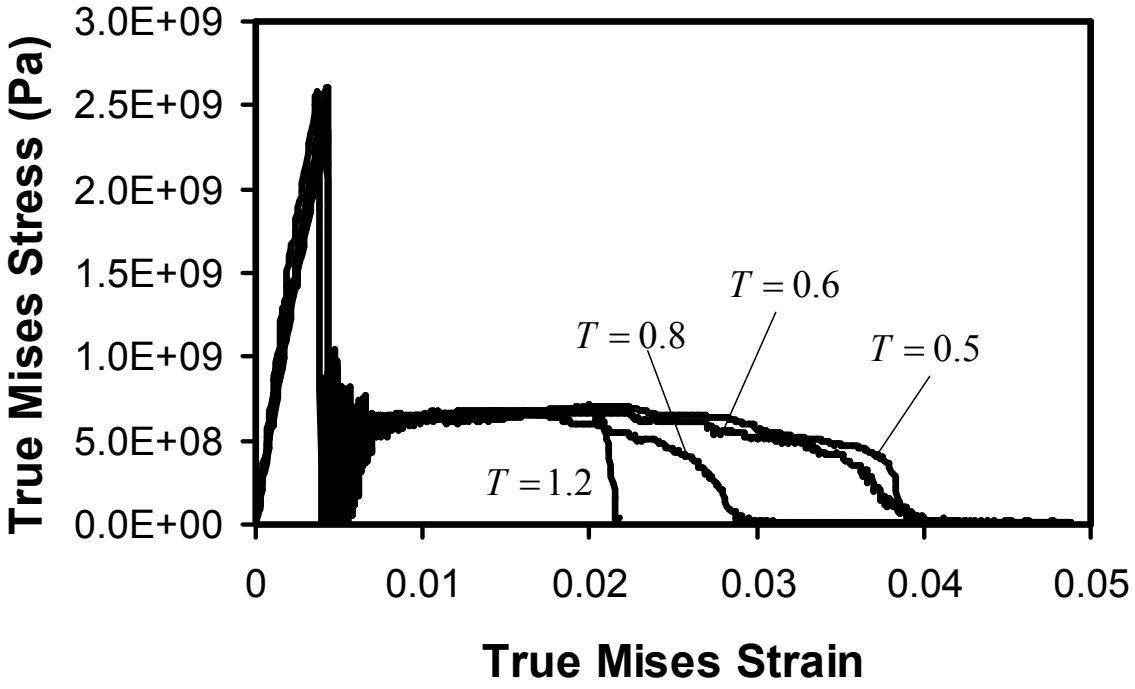

Figure 4.26. Increasing triaxiality T reduces the ductility

Microstructure Cause: Higher triaxiality at the level of the prescribed boundary conditions naturally leads to higher triaxiality within the cobalt regions.

Macroscale Effect: This generates much greater void growth in the cobalt, equation (4.7), leading to lower overall ductility.

Summary of Parametric Study

The computational parametric study has yielded the key micromechanical relationships in the composite. In terms of materials design the key observations are summarized in a schematic form of the stress-strain curve (Figure 4.27) and in Table 4.6.

Increasing Parameter	**Composite Fracture Stress** Y_0	**Composite Post Fracture Strength** S	**Composite Ductility**
Cobalt Volume Fraction f	Down	Up	Up
Cobalt Grain Size d	-	Down	Up
Temperature ϑ	-	Up	Up
Rate $\|\mathbf{D}\|$	-	Up	Down

Table 4.6 Design relationships in a WC-Co, predicted through computational cell modeling

- Fracture stress can be increased by reducing the cobalt fraction f .
- Post fracture strength can be increased by decreasing the temperature ϑ, increasing the loading rate $\|\mathbf{D}\|$, increasing the grain size d, increasing the cobalt fraction f.
- Ductility can be increased by increasing the loading rate $\|\mathbf{D}\|$, increasing the grain size d or decreasing the temperature.

Each of these microstructure-property relationships is now built into a macroscale constitutive relationship for the WC-Co composite in Section 4.4.

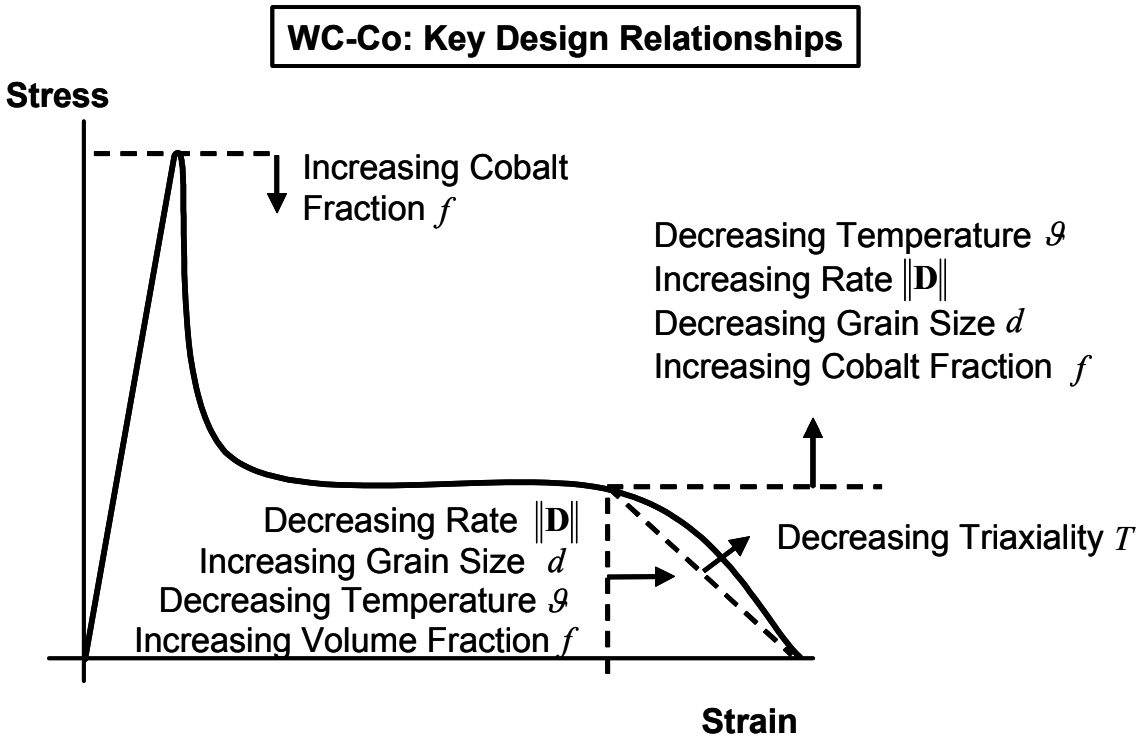

Figure 4.27. Design relationships in a WC-Co, predicted through computational cell modeling

4.4 Calibrating a Macroscale BCJ Composite Constitutive Model

The parametric study performed in Section 4.3.2 is now used as a starting point to develop a modified BCJ constitutive relationship for the WC-Co composite. The BCJ model (Section 3.3) is extended in Section 4.4.1 to incorporate the effects of brittle and ductile damage. Expressions for the degradation of the flow stress are developed in Section 4.4.2 in terms of individual brittle and ductile damage contributions. Evolution equations for the brittle and ductile damage measures are given in Section 4.4.3 and 4.4.4 respectively. The final composite model is reviewed in Section 4.4.5.

4.4.1 Yield Surface with Combined Brittle and Ductile Damage

Expressions for the plastic stage of deformation of the WC-Co composite are concentrated on here. Prior to plastic deformation, an isotropic elastic response is assumed with a Young's modulus of 595GPa and poison's ratio of 0.22 (Connolly and McHugh 1999). The damage effect in the elastic regime is given by equation (3.8).

A simple flow rule φ_{WC-Co} is proposed here which captures the important characteristics of the composite deformation:

$$\begin{aligned} &\varphi_{WC-Co} = \sigma_{eq} - Y = 0 \\ &where \\ &Y = Y_0 - Y_{WC}\left(D\right) - Y_{Co}\left(\phi\right) \\ \\ &\varphi_{WC-Co} \le 0 \quad \text{Elastic} \\ &\varphi_{WC-Co} > 0 \quad \text{Plastic} \end{aligned} \tag{4.10}$$

where σ_{eq} is the equivalent Mises stress which is equal to $\sqrt{3J_2}$ and Y is the yield stress which is given in terms of:

- The composite fracture stress Y_0
- Stress degradation due to brittle fracture in the carbide is given by Y_{WC} which evolves as a function of a brittle damage parameter, D.
- Stress degradation due to ductile rupture in the cobalt binder is given by Y_{Co}, which evolves as a function of microvoid porosity ϕ.

Evolution equations relating these stress degradation measures to their associated damage term must be developed in order complete the constitutive relation. The individual stress degradation effects are illustrated schematically in (Figure 4.28). The Mises strain at the composite scale is called $\bar{\varepsilon}$ to avoid confusion with previous small scale strain measures.

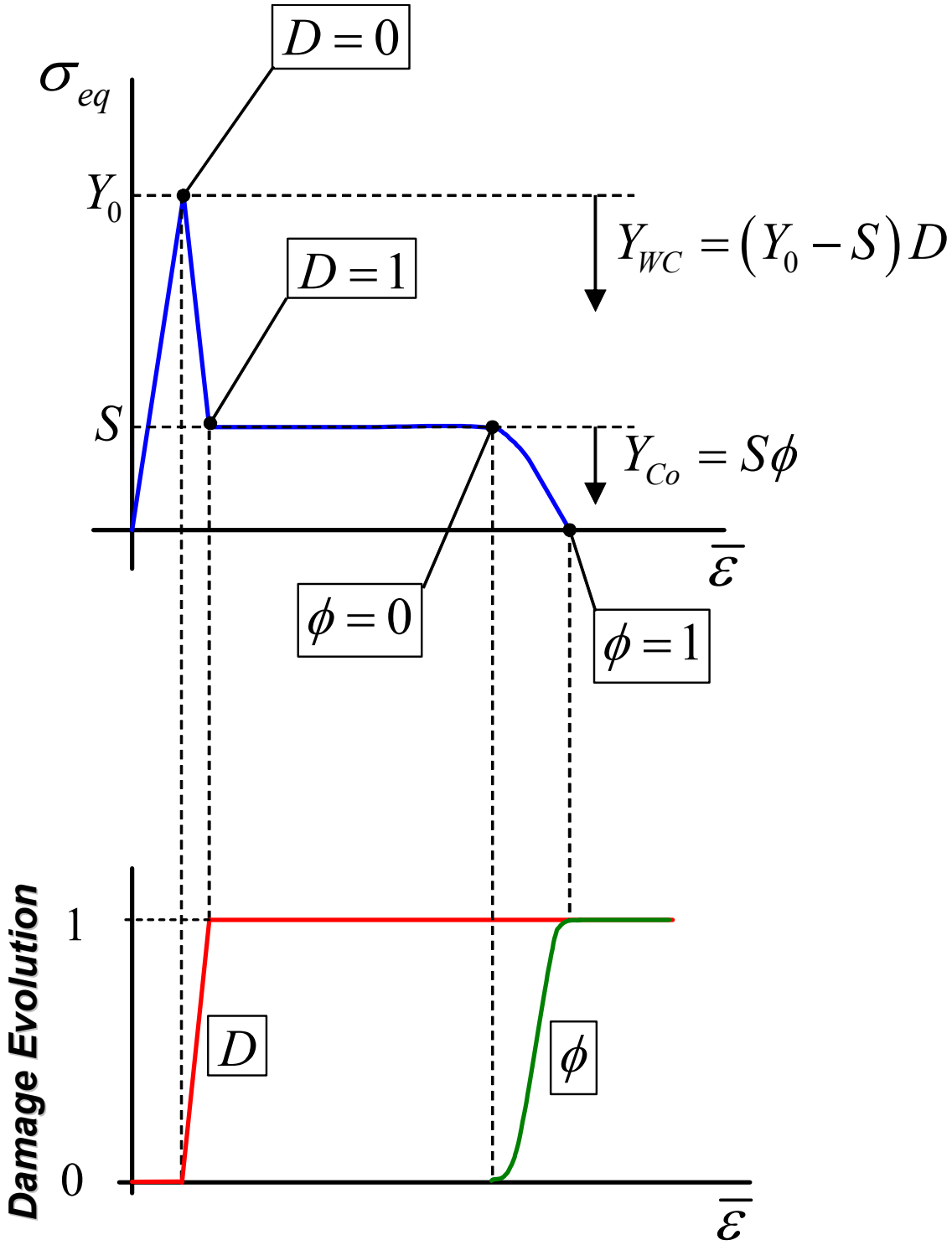

Figure 4.28. A schematic showing the effect of the brittle damage D, equation (4.20), and ductile damage ϕ, equation (3.17), on the composite flow stress, equation (4.10).

4.4.2 Composite Flow Relation and Brittle/Ductile Stress Degradation

From the numerical parametric study, (Figure 4.23), the fracture stress Y_0 shown schematically in (Figure 4.28) is related to the cobalt volume fraction f by a linear relationship:

$$Y_0 = A_1 f + A_2 \tag{4.11}$$

where $A_1 = -2GPa$ and $A_2 = 3GPa$.

The stress degradation due to damage is separated into two parts; stress degradation Y_{WC} due to brittle damage D and stress degradation Y_{Co} due to porous damage ϕ. Both can be defined via the post fracture strength S shown schematically in (Figure 4.28). The stress degradation due to carbide fracture Y_{WC} grows from zero to a value equal to $Y_0 - S$, as the carbide damage D grows from zero to one:

$$Y_{WC} = \left(Y_0 - S\right) D \tag{4.12}$$

The stress degradation due to ductile failure Y_{Co} grows from zero to S as the microvoid porosity ϕ grows from zero to one:

$$Y_{Co} = S\phi \tag{4.13}$$

From the numerical parametric study performed in the previous Section (4.3), the post fracture strength S is related to plastic flow in the cobalt binder; in particular it is controlled by:

- Cobalt volume fraction f
- Cobalt grain size g
- Temperature ϑ
- Strain Rate $\|\mathbf{D}\|$

Based on the observation made in the parametric study, a suitable form for the post fracture stress is proposed here as:

$$S = S_0 + A_8 \sinh^{-1}\left[\frac{\dot{\bar{\varepsilon}}}{A_9}\right]$$
$$S_0 = \left(A_3 f\right)\left(A_4 d^{A_5}\right)\left(A_6 + A_7 \vartheta\right) \tag{4.14}$$

where $\dot{\bar{\varepsilon}}$ is the macroscale rate of accumulated plastic strain, S_0 describes the effects of cobalt fraction f, cobalt grain size d and temperature ϑ.

The nonlinear inverse hyperbolic sine term gives the rate effect on the post yield stress. This is chosen such that composite plastic flow in the post fracture regime can be modeled using the BCJ plasticity formulation, Section 3.1. For example consider the predicted material response after the carbide has completely fractured i.e. $D = 1$. In this case the stress degradation due to carbide fracture Y_{WC}, (Figure 4.28), equation (4.12), is simply:

$$Y_{WC} = \left(Y_0 - S\right) \tag{4.15}$$

The yield surface, equation (4.10), is now:

$$\varphi_{WC-Co} = \sigma_{eq} - S + Y_{Co} = 0, \quad D = 1 \tag{4.16}$$

Substituting the stress degradation due to microvoiding Y_{Co}, given by equation (4.13), the yield surface expression can be rewritten as:

$$\varphi_{WC-Co} = \sigma_{eq} - S\left(1-\phi\right) = 0, \quad D = 1 \tag{4.17}$$

Substituting equation (4.14) into the flow rule of equation (4.17) gives:

$$\varphi_{WC-Co} = \sigma_{eq} - \left(S_0 + A_8 \sinh^{-1}\left[\frac{\dot{\bar{\varepsilon}}}{A_9}\right]\right)\left(1-\phi\right) = 0, \quad D = 1 \tag{4.18}$$

Rearranging this, an expression for the strain rate is:

$$\dot{\bar{\varepsilon}} = A_9 \sinh\left(\frac{\sigma_{eq} - S_0(1-\phi)}{A_8(1-\phi)}\right) \tag{4.19}$$

which is in the form of the BCJ rate of plastic deformation equation, (3.22).

The material constants $A_3 - A_9$ are determined by calibrating equation (4.14) to the cell model data contained in (Figure 4.22), (Figure 4.23), (Figure 4.24) and (Figure 4.25). In each case the change in the post fracture strength S is compared to the change in the parameter ($f, d, \vartheta, \dot{\bar{\varepsilon}}$) and calibrated to equation (4.14) using a least square fit. The constants $A_3 - A_9$ are given in Table 4.7. Evolution equations for the carbide damage D and cobalt porosity ϕ are developed in Section 4.4.3 and 4.4.4.

4.4.3 Isotropic Damage Evolution – Brittle Damage Arising in the Carbide

The rapid stress collapse due to the carbide fracture Y_{WC}, (Figure 4.28), is represented in equation (4.12) in terms of the brittle damage D. An expression for the evolving brittle damage D is proposed here as:

$$D = 1 - \exp\left(-A_{10}\bar{\varepsilon}^{p}\right) \tag{4.20}$$

where $\bar{\varepsilon}^{p}$ is the macroscale (composite) accumulated plastic strain. The dimensionless parameter A_{10} controls the strain interval over which this function grows from a value of zero to one i.e. how rapidly the carbide fracture occurs. Hence the value of this parameter is related to the energy release rate G of brittle tungsten carbide introduced in Section 4.2.

From the observation made in the parametric study performed in Section 4.3.2 it is clear that the brittle fracture and resulting stress degradation are rapid; a value of $A_{10} = 1\times10^{3}$ capture the rapid nature of the partial stress collapse well while maintaining computational efficiency (i.e. without resorting to an extremely small time step to capture the rapid stress collapse).

4.4.4 Isotropic Damage Evolution – Ductile Damage Arising in the Cobalt

The damage accumulation in the cobalt binder, due to nucleation and growth of microvoids, also contributes to the stress degradation in (Figure 4.28). This microvoid damage has already been examined in detail in Section 4.1. The resulting void equations (4.1), (4.4) and (4.8) are summarized in Table 4.2. These equations describe how microvoids nucleate, grow and coalesce

in the cobalt. However those equations are written in terms of the rate of plastic deformation within the binder which is renamed $\|\mathbf{D}_p\|_{Co}$ here for clarity.

In the final composite constitutive model being developed in this section, the deformation measures are macroscale (composite) quantities which describe the average composite state. In general the rate of plastic deformation within the cobalt $\|\mathbf{D}_p\|_{Co}$ is always higher than the composite scale rate of plastic deformation, called $\|\mathbf{D}_p\|_{WC-Co}$ here to distinguish between the two quantities. A scaling factor is introduced here in order to make use of the cobalt scale nucleation, growth and coalescence equations (4.1), (4.4) and (4.8), within the macroscale WC-Co constitutive model.

A relationship between the rate of plastic deformation within the cobalt and the composite scale rate of plastic deformation is proposed in terms of the cobalt volume fraction f:

$$\|\mathbf{D}_p\|_{WC-Co} = f\|\mathbf{D}_p\|_{Co} \tag{4.21}$$

In composites containing a larger cobalt fraction f, the cobalt strain $\|\mathbf{D}_p\|_{Co}$ is lower at a particular value of composite strain $\|\mathbf{D}_p\|_{WC-Co}$. As the cobalt volume fraction f approaches unity the two measures coincide; the composite would be 100% cobalt. Conversely as the fraction of cobalt goes to zero, the composite plastic strain goes to zero.

The nucleation η, growth v and coalescence ϕ_{coal} equations (4.1), (4.4) and (4.8) can now be scaled accordingly and used as macroscale microvoid porosity equations. The constitutive parameters for the macroscale modified BCJ composite model are summarized in Table 4.7.

WC-Co Composite BCJ Model Constants			
A_1	$-2GPa$	A_6	2.0
A_2	$3GPa$	A_7	$-3\times10^{-3}K^{-1}$
A_3	$4GPa$	A_8	$70MPa$
A_4	$11.63m^{0.17}$	A_9	$1\times10^{-2}s^{-1}$
A_5	-0.17	A_{10}	1×10^{3}

Table 4.7 Constants required in the composite BCJ model, equation (4.14) and equation (4.20)

4.4.5 Macroscale Constitutive Model - Overview

The final macroscale constitutive relation is outlined briefly to highlight the key relationships. (Figure 4.29) shows the effect of cobalt grain size d, cobalt volume fraction f, temperature ϑ, rate $\|\mathbf{D}\|$ and triaxiality T predicted by the modified BCJ composite model; these correlate well with the behavior observed in the computational cell models (Figure 4.22), (Figure 4.23), (Figure 4.24), (Figure 4.25) and (Figure 4.26). The control values used to compute the constitutive curves in (Figure 4.29) are $d = 500nm$, $f = 0.15$, $\vartheta = 353K$, $\|\mathbf{D}\| = 5\times10^{-6}s^{-1}$, $T = 0.75$.

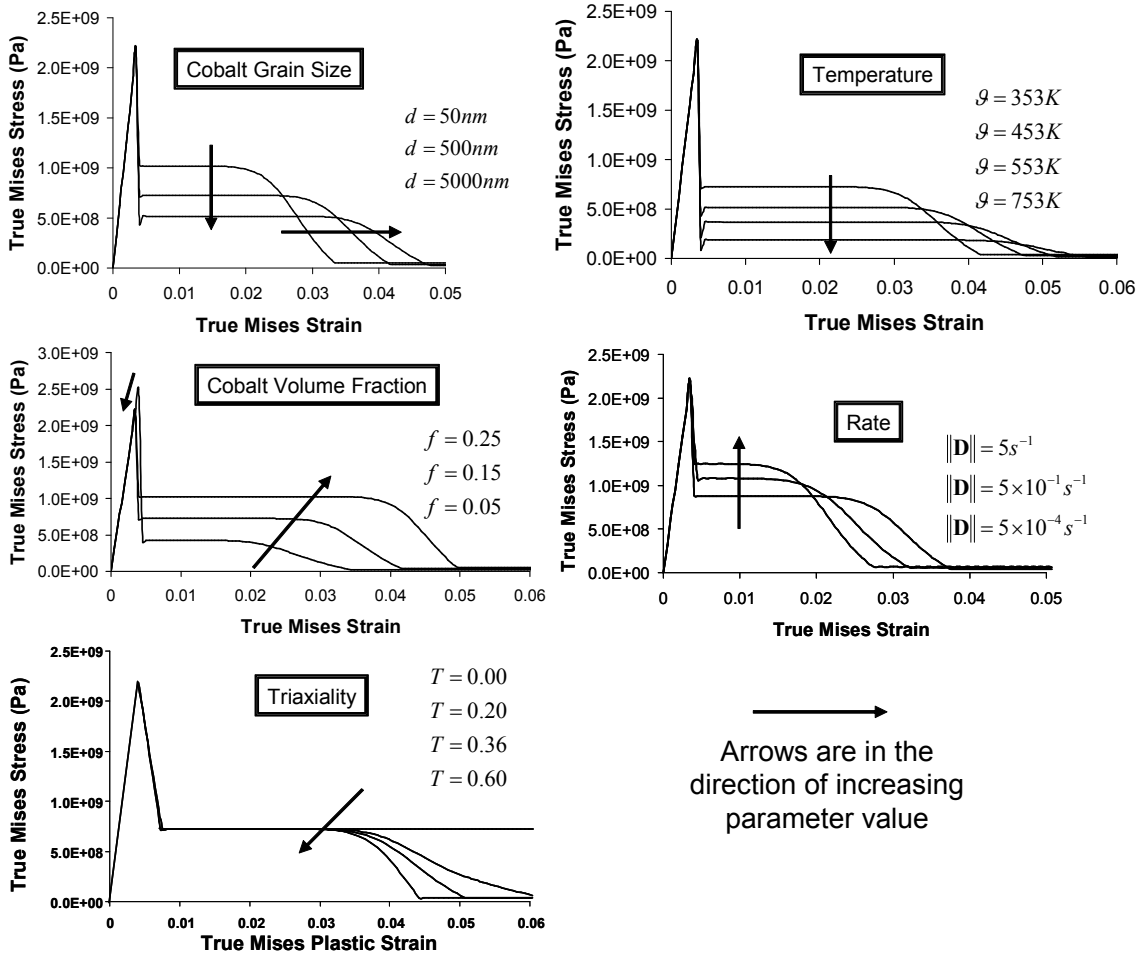

Figure 4.29. An overview of the relationships in the WC-Co composite constitutive model

The ability of the model to capture the *post carbide-fracture ductile behavior* is particularly important. Experimentally determined mechanical constitutive relations for WC-Co are generally performed using a macroscale sample on the order of centimeters. Due to the rapid nature of fracture in tension and the large size of the tensile specimen in comparison to the failure region, the important post fracture ductile behavior cannot be captured as illustrated schematically in (Figure 4.30). In such cases compression tests is usually favored. However compression testing completely fails to capture the key micromechanics responsible for failure under positive

triaxiality loading i.e. stretching and failure of the cobalt binder. This is a crucial aspect of the material response particularly in the process zone ahead of a crack tip i.e. in the area within a few microns of the crack tip where plasticity will occur, blunting the crack tip.

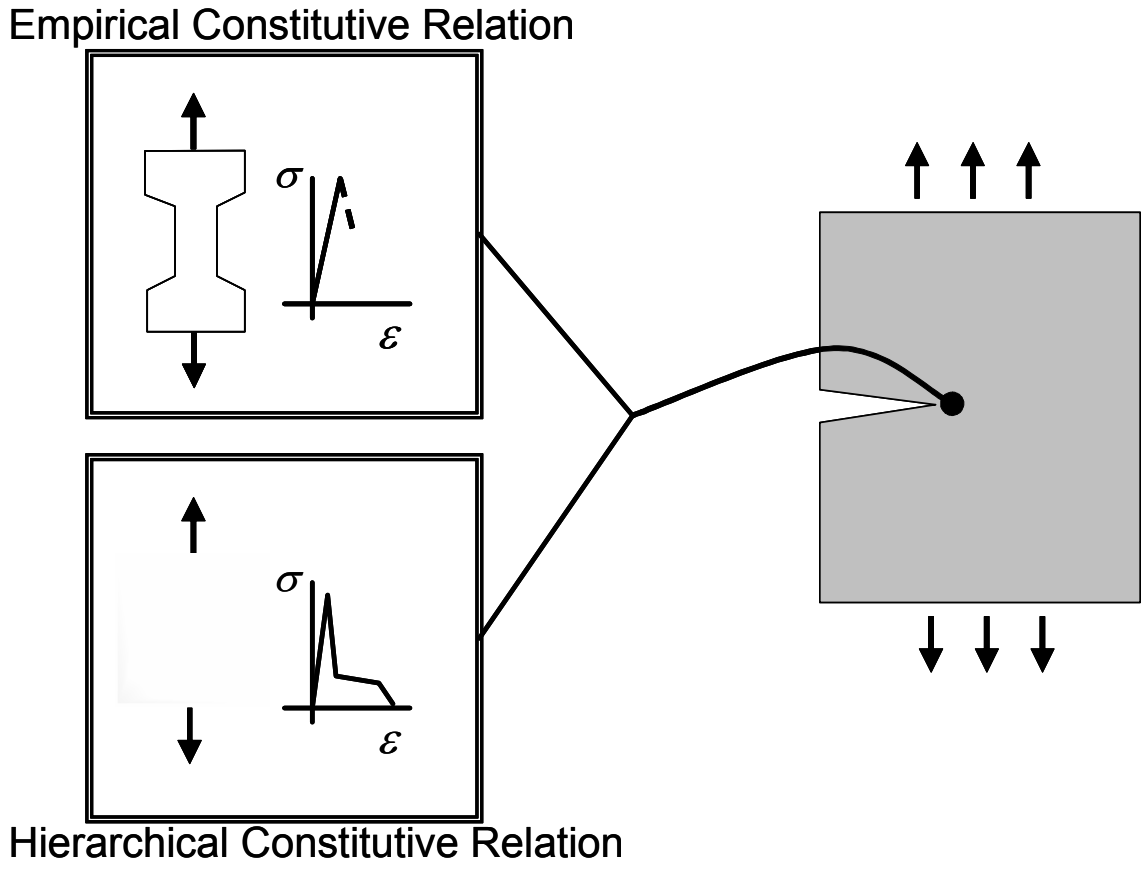

Figure 4.30. Empirical versus computational hierarchical micromechanical constitutive relationship

4.5 Toughness Prediction via a Numerical Fracture Model

The developed macroscale constitutive model is now applied within a conventional finite element model of a body with a pre-crack i.e. an elementary fracture toughness simulator. The model set-up is given in Section 4.5.1. The shortcomings of this model are described in Section 4.5.2. In Section 4.5.3 the resistance to crack growth (stress intensity factor) is computed as a function of different microstructural parameters; grain size d, cobalt volume fraction f and temperature ϑ.

4.5.1 Model Set Up

The model is loaded under Mode I conditions, with the assumptions of linear elastic fracture mechanics with small scale yielding i.e. any plasticity is confined to a very small region (compared to the sample) near the crack tip. A crack of length $a = 6\mu m$ is modeled in a long finite width ($W = 24\mu m$) specimen as illustrated in (Figure 4.31). The following condition for mode I stress intensity factor K_I applies:

$$K_I = \sigma_\infty 1.5\sqrt{\pi a} \qquad (4.22)$$

where σ_∞ is the applied remote stress and the shape effects are incorporated through the geometrical parameter given by 1.5. Stress boundary conditions are applied on the top and bottom surfaces of the model shown in (Figure 4.31). The stress is ramped linearly, which has the effect of linearly increasing the stress intensity factor K_I.

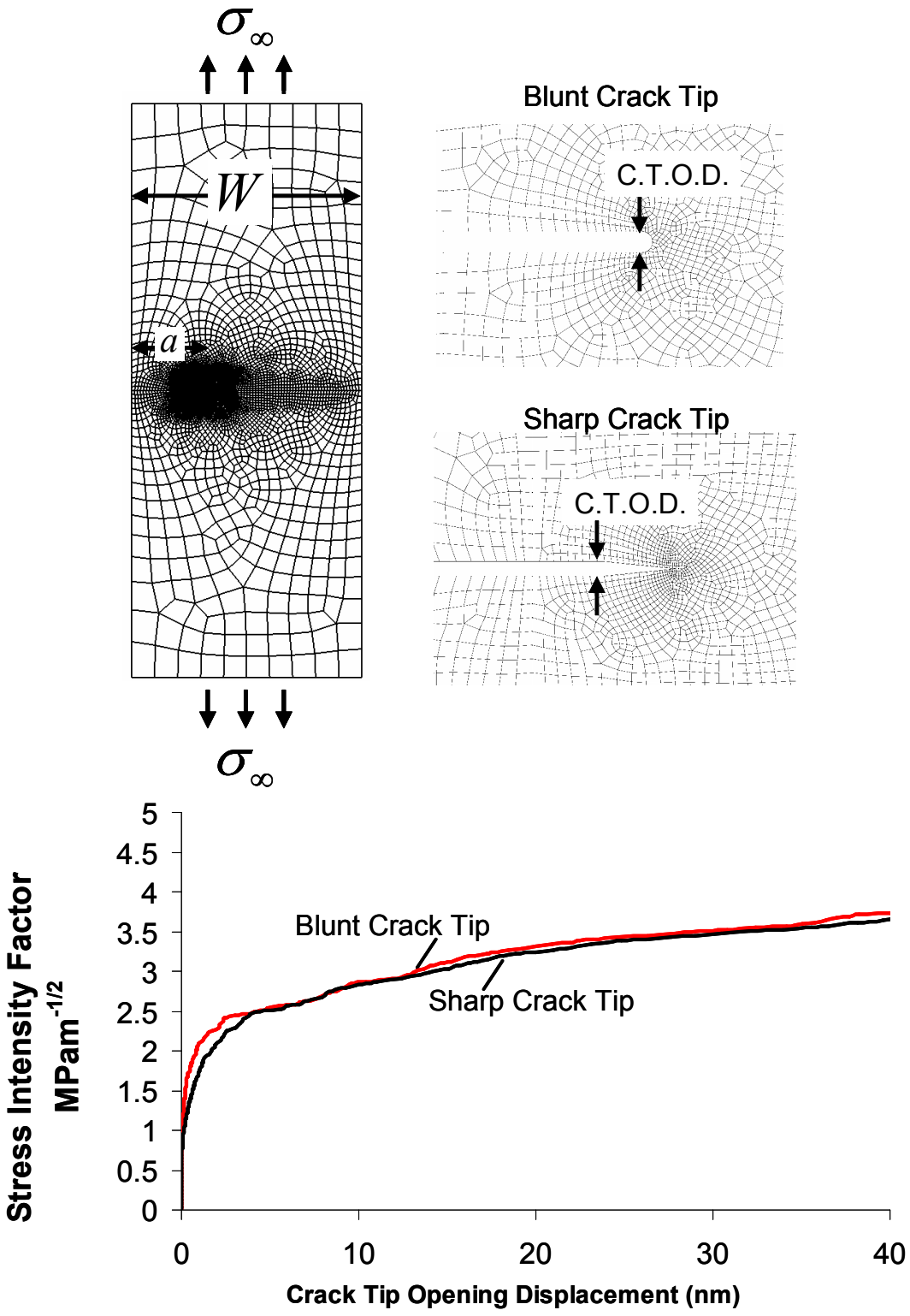

Figure 4.31. The crack geometry has little bearing on the predicted crack behavior due to strain localization.

4.5.2 Crack Tip Blunting

In materials containing a ductile phase a substantial contribution to the macroscale toughness is derived from crack tip blunting. Unfortunately this phenomenon is not captured in the current continuum model as the strain tends to localize unphysically in a single band of elements immediately ahead of the crack tip when carbide fracture occurs. This is a well known problem in continuum mechanics; material softening results in a loss of rank-one stability in the associated continuum governing partial differential equations. (Bazant and Belytschko 1987) have shown that the governing partial differential equations change type from elliptic to hyperbolic in such cases and the macroscale deformation localizes unphysically to a set of measure zero. Even in the case of an initially blunt crack tip the resulting spurious strain localization prevents any subsequent crack blunting (Figure 4.32).

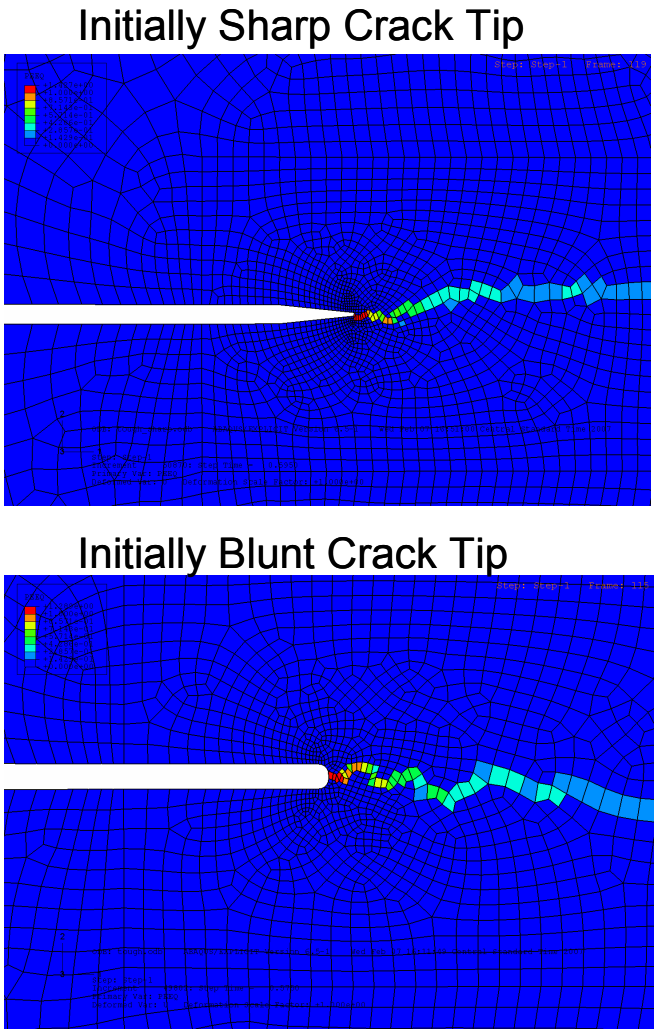

Figure 4.32. The initially blunt crack behaves similarly to the sharp crack

4.5.3 Effect of material parameters

Although numerical problems exist due to the spurious localization, the qualitative effect of varying each material parameter can be observed in the stress intensity verses crack tip opening displacement curves. In the following study toughness refers to the area under the stress-strain curves in (Figure 4.29). Contours of plastic strain are shown for each case at a stress intensity factor of $K = 4.5 MPam^{1/2}$.

Cobalt volume fraction f

Increasing cobalt volume fraction f increases the composite toughness as shown in (Figure 4.29). This results in an increasing stress intensity factor (Figure 4.33) and reduced crack growth; hardly any crack growth occurs in the case of $f = 0.25$.

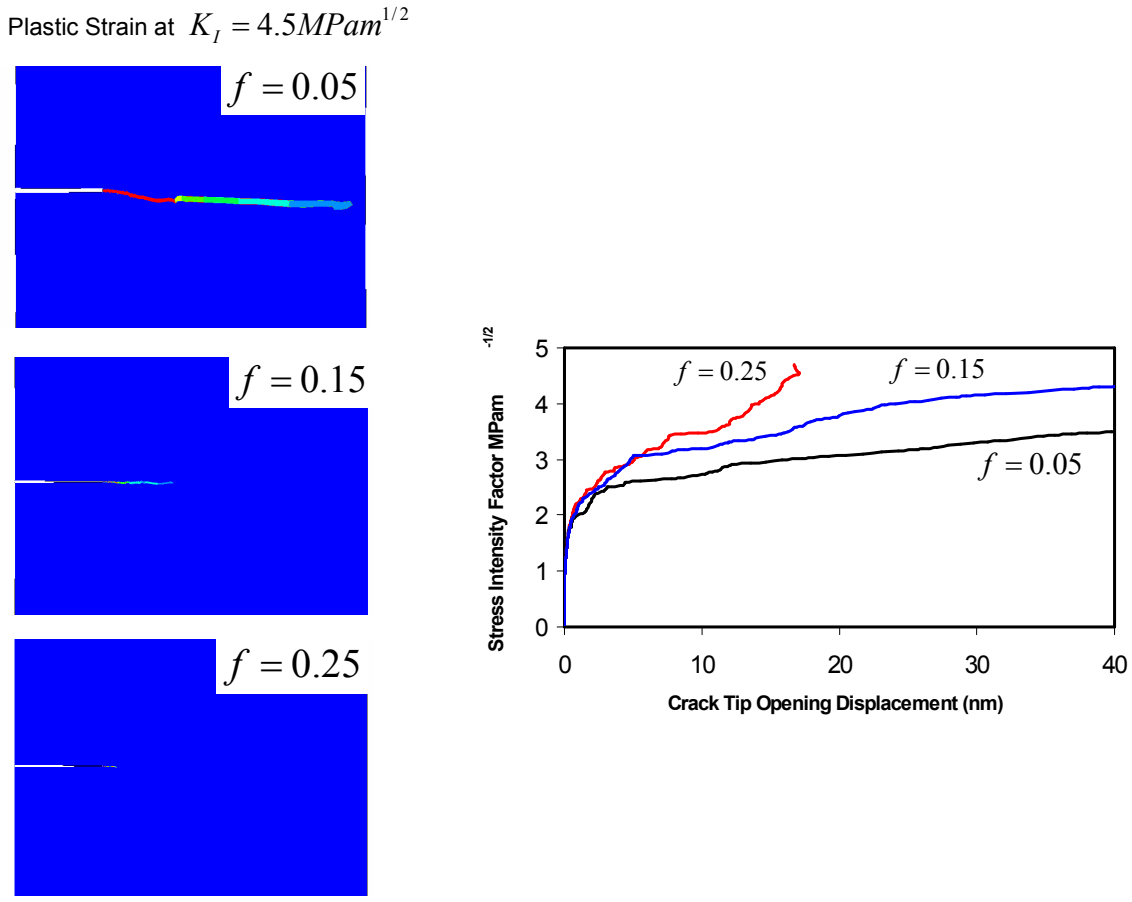

Figure 4.33. Increasing cobalt volume fraction f increases the stress intensity factor

Temperature ϑ

Increasing temperature ϑ reduces the toughness (Figure 4.29) and subsequently the stress intensity factor (Figure 4.34) and increased crack growth occurs.

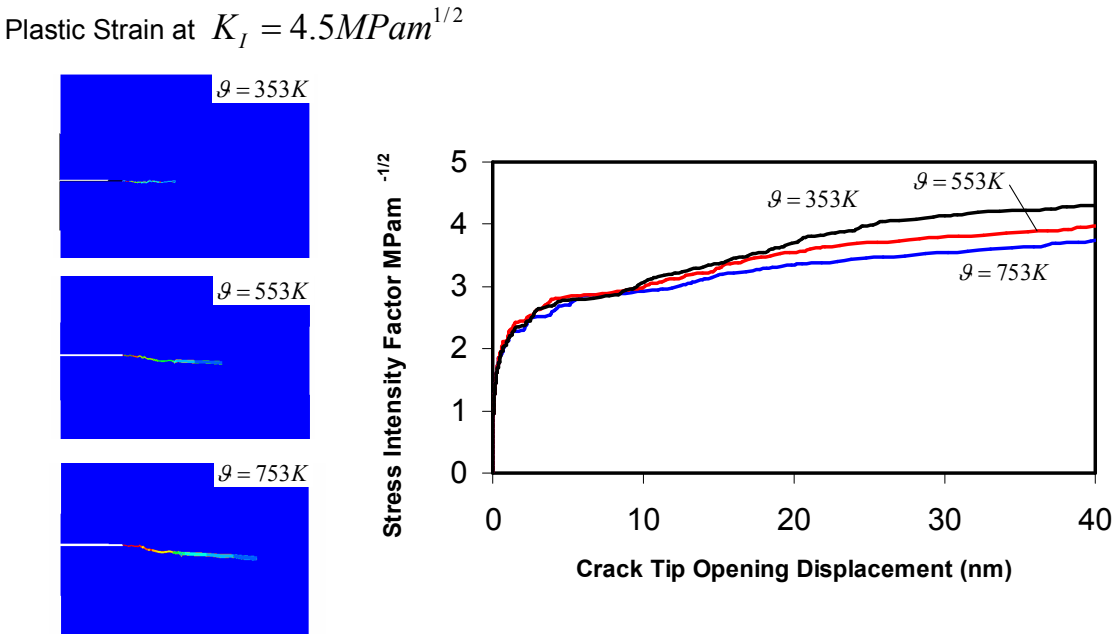

Figure 4.34. Increasing temperature results in a lower stress intensity factor.

Cobalt grain size d

Increasing grain size d does not seem to change the toughness in (Figure 4.29). The resulting stress intensity curve does not change much with grain size; a very small decrease is predicted with increasing grain size as shown in (Figure 4.35). In reality a larger grain size d is known to distribute the plastic strain over a larger area within the microstructure. This acts to blunt the crack tip and absorb more energy. In the conventional continuum model this length scale effect cannot be captured. However a multiresolution continuum model is used in Chapter 7 in which the grain size effect is captured directly and the resulting stress intensity factor increases with grain size (Figure 7.14).

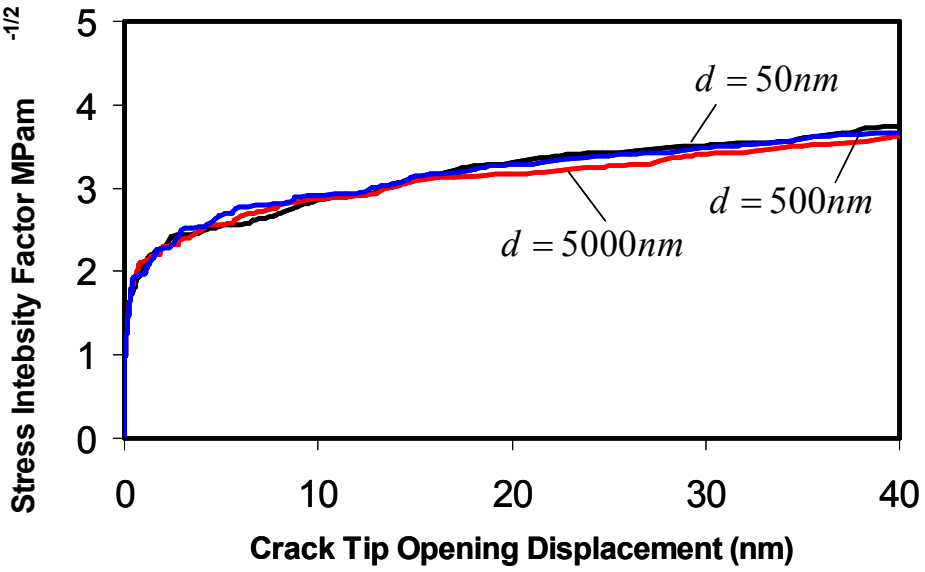

Figure 4.35. Stres intensity shows a small drop with increasing grain size.

4.5.4 Discussion of Results

The stress intensity factor computed in each case for crack propagation is significantly lower than the experimentally determined value of fracture toughness i.e.16.7MPam$^{-1/2}$ (McHugh and Connolly 2003) – the toughening effect of crack blunting is missing due to the unphysical nature of strain localization ahead of the crack tip. This problem has also been encountered by (McHugh and Connolly 2003) who computed unphysically low fracture toughness values from their simple computational cell models of WC-Co. The authors recognized that the unphysically small fracture toughness values were mainly due to a lack of any physical length scale in their model. Deformation localized in a mesh dependent manner, preventing the cobalt phase from contributing significantly to crack resistance. The authors recognized that the strain could be 'forced' to localize over a predetermined length scale by using elements of that size. Hence they suggested using elements which are the same size as the cobalt grains. However it has been shown in Section 2.1, (figure 2.5), that inhomogeneous deformation in WC-Co composites occurs at smaller scales within the cobalt grains when microstructural instability events occur.

In this thesis the problem of unphysical strain localization (and subsequent unphysical toughness predictions) is combated via a multiresolution continuum theory (MRCT). This theory aims to capture all of the characteristic length scales of inhomogeneous deformation while remaining in the context of continuum mechanics. The multiresolution continuum theory is developed in Chapter 5 from the standpoint of a second gradient formulation. The extra microstress constitutive relations which are introduced to capture inhomogeneous deformation at each scale are described further in Chapter 6. The multiresolution formulation is then applied to the WC-Co

composite in Chapter 7. More physical toughness predictions, in terms of the key microstructural parameters, are then obtained using a multiresolution analysis.

5 Multiresolution Continuum Theory (MRCT)

The underlying theme of this thesis is to predict macroscale mechanical properties as a function of the microstructure via numerical modeling. In Chapter 4 a homogenized continuum approach is used to perform numerical fracture toughness predictions for a cemented carbide; however predicted fracture toughness values were substantially lower than those observed experimentally. The fundamental problem with such an approach is that the scales of the underlying deformation mechanisms are lost during the homogenization process; the resulting continuum model is incapable of replicating the inhomogeneous deformation which is crucial in terms of toughness predictions.

This is a well known problem, particularly when modeling materials which soften due to cracks, shear bands and other micromechanical phenomena causing material degradation. (Bazant and Belytschko 1987) have shown that in such cases the continuum governing partial differential equations change type from elliptic to hyperbolic and the deformation localizes unphysically to a set of measure zero. In terms of the numerical fracture toughness simulations in Chapter 4, all of the strain localizes within a single band of finite elements and the predicted model response is highly mesh dependent. Conventional continuum approaches also fail to predict a scale effect in strain *hardening* materials. For example (Zbib and Aifantis 2003) discussed how deformation in work hardening alloys is size dependent over length scales ranging from a few nanometers to 100μm. The basic observation is that deformation at smaller scales results in more geometrically necessary dislocations (GNDs) and hence a stronger material response i.e. *smaller is stronger*.

The focus of this Chapter is to develop an efficient theory which can replicate the scale associated with each deformation mechanism within the context of a continuum model. This enables a more physical prediction of macroscale properties based on the inhomogeneous deformation at each scale. A preview of the proposed (MRCT) theory is given in Section 5.1.

The remainder of Chapter 5 is structured as follows:

A simple 1D example is used in Section 5.2 to illustrate how a conventional continuum approach cannot replicate the scale of inhomogeneous deformation. The ability of a higher order continuum theory to regularize the inhomogeneous deformation over a physical length scale is shown. The disadvantages of this approach are used as a motivation for developing a multiresolution higher order continuum theory (MRCT) in Section 5.3. Section 5.4 illustrates the usefulness of the microstresses for materials which undergo inhomogeneous deformation at multiple scales, and the microstructure transition points which determine when inhomogeneous deformation transitions from one scale to another. Section 5.5 describes a technique which reduces the number of degrees of freedom used in the proposed MRCT analysis.

5.1 Proposed Multiresolution Theory - Preview

The proposed theory follows from the work of (McVeigh et al. 2006a; Vernerey 2006; Vernerey et al. 2007a; b). This theory can replicate the evolving scale and magnitude of inhomogeneous deformation directly in terms of a parameterized description of the evolving microstructure. Remaining within the context of continuum mechanics, the conventional governing equations are supplemented with extra microstresses and higher order microstresses; these extra stress

measures capture microstructural length scale information which is usually lost in a conventional continuum approach. Each continuum microstress is interpreted as the resistance to inhomogeneous deformation at a particular scale. Each microstress is accompanied by a higher order stress which can be shown to be the first moment of the microstress.

The extra microstress measures are simply extra continuum degrees of freedom; this is an efficient alternative to direct numerical simulation of the microstructure, bypassing the need to model complicated microstructural geometries in large scale simulations while still including the length scales associated with the microstructural features. In terms of the numerical implementation, a single finite element mesh can still be used to solve the resulting multiresolution governing equations.

Extra microscale constitutive relations for the microstresses are used at each scale of inhomogeneous deformation and are unique to this theory. As with the macroscale constitutive relations, the microscale relations are pre-derived separately using computational cell models of the underlying microstructure.

The multiresolution approach is essentially an intelligent variable length scale gradient enhanced model which acts to regularize strain over a length scale which evolves with the microstructure. This is particularly useful in materials where the scale f inhomogeneous deformation changes rapidly when microstructural transition events occur. For example in alloys when microvoid nucleation occurs deformation quickly localizes to the scale of the nucleated microvoids.

5.2 Higher Order Continuum Theory

A simple 1D example is introduced in Section 5.2.1 to illustrate how a conventional continuum approach fails to replicate the scale of inhomogeneous deformation in a strain softening alloy. A higher order continuum theory is introduced in Section 5.2.2. This theory is applied to the 1D problem in Section 5.2.3 and successfully regularizes the deformation over a physically consistent length scale. The disadvantages of this higher order gradient enhanced approach are discussed in Section 5.2.4.

5.2.1 Unphysical Inhomogeneous Strain Localization

Consider a simple 1D problem in which a linear elastic-plastic rod is stretched. The material is considered to undergo linear strain *softening* immediately upon yielding as shown in (Figure 5.1). The elastic modulus is $E = 80GPa$, initial yield stress is $\sigma_0 = 160MPa$ and the linear softening modulus is $150MPa$; the resulting softening response is shown in (Figure 5.1). J2 flow theory is used to represent the plastic behavior.

A conventional finite element analysis is employed to solve for the displacement; the conventional governing equations of a continuum are given in equation (1.5). The rod is discretized and quasi-static displacement boundary conditions are applied. The central element is given an initial perturbation of 1% reduction in yield stress. As shown in (Figure 5.1) the strain localizes in a single element (which was initially perturbed), regardless of the mesh discretisation used. The macroscale performance is illustrated in terms of the rod's force-extension behavior, shown in (Figure 5.1). The reaction force F varies with the element size used due to the spurious

nature of strain localization; the predicted performance and properties are mesh dependent. Of course in reality the only length scale which should affect the macroscale performance is given by the microstructure. For example in alloys post instability inhomogeneous deformation occurs at a scale related to the spacing of nucleated voids.

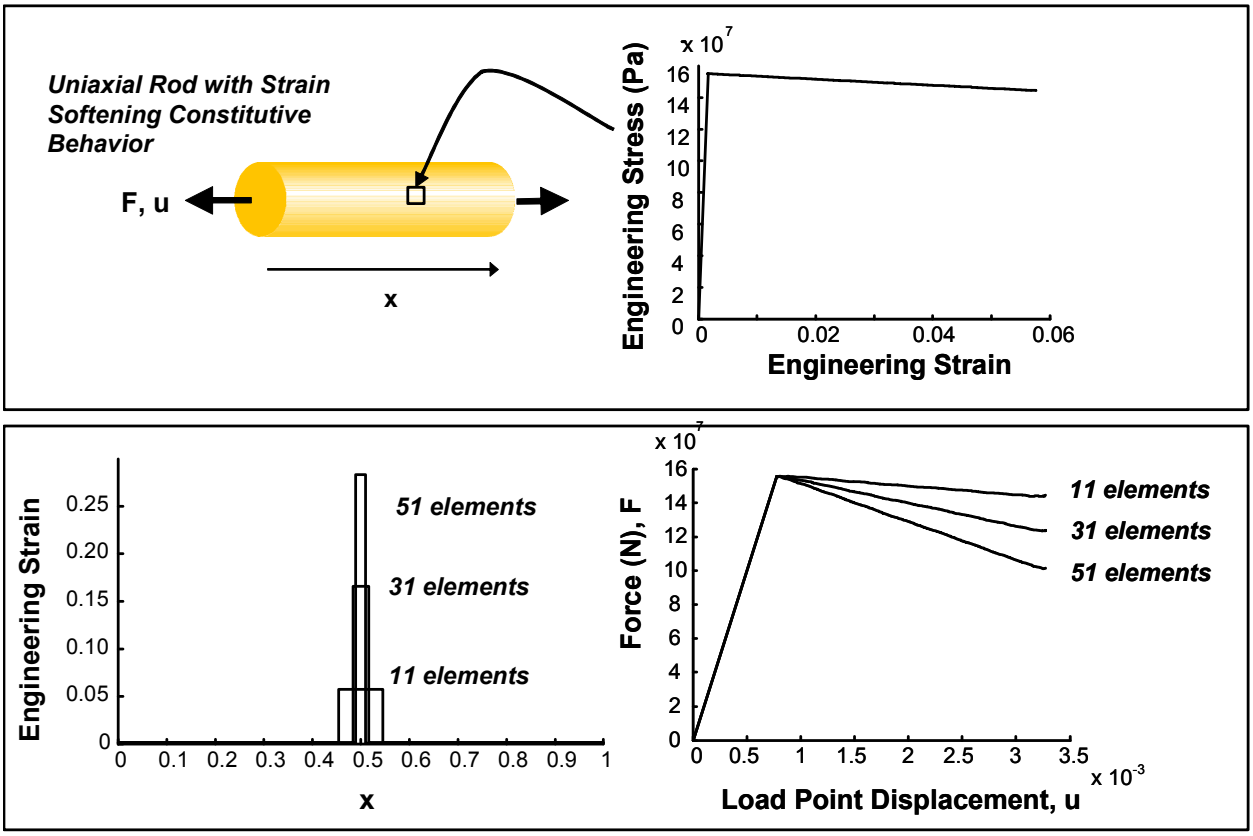

Figure 5.1. 1D problem illustrating mesh dependency in strain softening materials

5.2.2 Strain Gradient Theory- Extending the Hill-Mandel Lemma

Gradient enhanced continuum theories regularize (smooth) inhomogeneous deformation over a physically consistent length scale. The basic assumption used in gradient enhanced models is that the Hill-Mandel Lemma (Hill 1963; 1966; Hill and Rice 1972) can be extended to include higher

order terms. The Hill-Mandel Lemma essentially approximates the virtual power density δp of a continuum material point as a volume average of the virtual power density δp_m in a representative volume element (RVE) V_0 of the microstructure:

$$\begin{aligned}\delta p &= \frac{1}{V_0}\int_{V_0} \delta p_m dV_0 \\ &= \frac{1}{V_0}\int_{V_0} \boldsymbol{\sigma}_m : \delta \mathbf{L}_m dV_0\end{aligned} \tag{5.1}$$

In this expression the internal power density δp_m has first been rewritten in terms of the power conjugate stress $\boldsymbol{\sigma}_m$ and velocity gradient fields $\mathbf{L}_m$ computed within the RVE. Assuming $\mathbf{L}_m$ is fairly constant within the RVE (homogeneous deformation assumption), the virtual internal power can be approximated in terms of the continuum Cauchy stress $\boldsymbol{\sigma}$ and velocity gradient $\mathbf{L}$.

$$\delta p = \boldsymbol{\sigma} : \delta \mathbf{L} \tag{5.2}$$

where

$$\boldsymbol{\sigma} = \frac{1}{V_0}\int_{V_0} \boldsymbol{\sigma}_m dV_0 \tag{5.3}$$

and

$$\mathbf{L} = \frac{1}{V_0}\int_{V_0} \mathbf{L}_m dV \tag{5.4}$$

Gradient enhanced models extend this approximation to higher order; equation (5.2) becomes:

$$\delta p = \boldsymbol{\sigma} : \delta \mathbf{L} + \overline{\boldsymbol{\beta}} \vdots \delta \mathbf{G} \tag{5.5}$$

where $\mathbf{G}$ is a third order tensor representing the second gradient of velocity i.e. it is the power conjugate of the higher order couple stress $\overline{\boldsymbol{\beta}}$.

The external virtual power is given by:

$$\delta P_{ext} = \int_{\Omega} \mathbf{b} \bullet \delta \mathbf{v} d\Omega + \int_{\Gamma} \left(\mathbf{t} \bullet \delta \mathbf{v} + \mathbf{r} \bullet D\delta \mathbf{v} \right) d\Gamma \tag{5.6}$$

where $\mathbf{b}$ and $\mathbf{t}$ are the body force and surface traction in the conventional continuum sense, $\mathbf{r}$ is a double stress traction vector which balances the higher order tractions at the surface Γ, D is the normal gradient on the surface given by $D = \mathbf{N} \bullet \nabla$ where $\mathbf{N}$ is the unit normal to the surface Γ. The resulting equilibrium equations and boundary conditions are:

$$\boxed{\begin{aligned} &\nabla \bullet \left(\boldsymbol{\sigma} - \left(\nabla \bullet \bar{\boldsymbol{\beta}} \right)^T \right) + \mathbf{b} = 0 \quad \text{in } \Omega \\ &\left.\begin{aligned} &\mathbf{t} = \mathbf{N} \bullet \left(\boldsymbol{\sigma} - \left(\nabla \bullet \bar{\boldsymbol{\beta}} \right)^T \right) + \left(\nabla^S \bullet \mathbf{N} \right) \mathbf{N} \bullet \left(\mathbf{N} \bullet \bar{\boldsymbol{\beta}} \right)^T - \nabla^S \bullet \left(\mathbf{N} \bullet \bar{\boldsymbol{\beta}} \right)^T \\ &\mathbf{r} = \mathbf{N} \bullet \bar{\boldsymbol{\beta}} \bullet \mathbf{N} \end{aligned} \right\} \text{ on } \Gamma \end{aligned}} \tag{5.7}$$

where ∇^S is the surface gradient defined by $\nabla^S = \left(\mathbf{I} - \mathbf{NN} \right) \bullet \nabla$ and the full gradient is indicated by ∇. The equilibrium equation includes the higher order stress $\bar{\boldsymbol{\beta}}$ which gives a continuum point a stabilizing 'non-local' character.

5.2.3 Strain Gradient Constitutive Equations

With reference to the governing equations, equation (5.7), two constitutive relationships are required: $\dot{\boldsymbol{\sigma}}(\mathbf{L})$ and $\dot{\bar{\boldsymbol{\beta}}}(\mathbf{G})$ to solve the boundary value problem. Only one component of the stress tensor $\boldsymbol{\sigma}$ is required in the 1D analysis, called σ here. The same linear elastic-plastic constitutive response illustrated in (Figure 5.1) is used to define the conventional stress-strain relationship. Only one component of the second gradient of velocity $\mathbf{G}$ and higher order couple

stress $\overline{\boldsymbol{\beta}}$ are considered in the 1D problem. These are called $\overline{\beta}$ and G here and are assumed to be related via the materials elastic modulus E as:

$$\dot{\overline{\beta}} = El^2 G \tag{5.8}$$

where l is the physical length parameter required to make the expression dimensionally consistent. The 1D strain softening problem is now solved using equation (5.7). The resulting strain profile is illustrated in (Figure 5.2) for several element sizes. The inhomogeneous strain profile and load point force are now independent of the mesh discretisation used. The scale of the inhomogeneous deformation is controlled by the length parameter l, equation (5.8). This type of approach has been developed by several authors e.g. (Aifantis 1992) to model strain softening materials. A similar approach has been used by (Gao et al. 1999) to model strain gradient hardening in alloys.

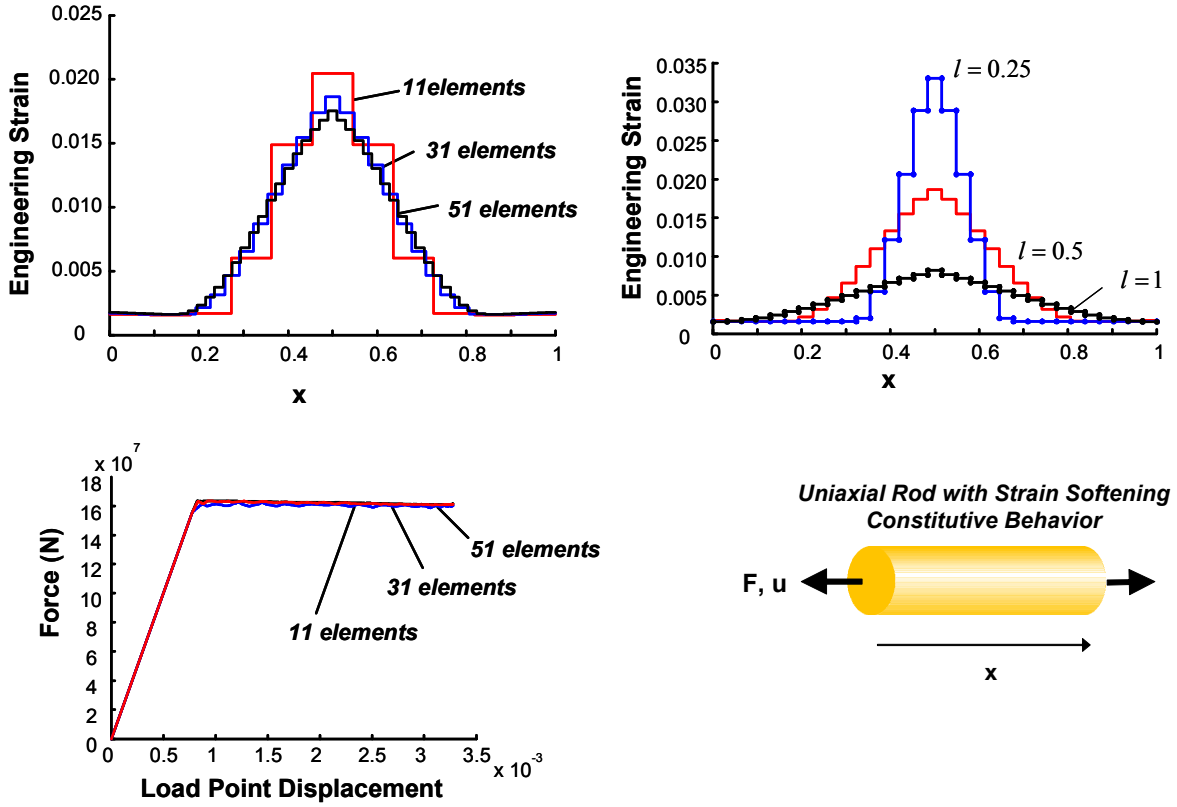

Figure 5.2. 1D problem illustrating the regularizing length scale introduced using a gradient method

5.2.4 Strain Gradient Theory - Disadvantages

A physical interpretation of the higher order stress $\bar{\boldsymbol{\beta}}$, and its relationship to the conventional stress measure $\boldsymbol{\sigma}$, has not been well established. The higher order stress $\bar{\boldsymbol{\beta}}$ has been computed by (Kouznetsova et al. 2002) as the average moment of the stress over an RVE. This embeds a length scale in the model related to the size of the RVE. Often the inhomogeneous deformation occurs at much smaller scales i.e. the embedded length scale should relate to the smaller scales. The moments associated inhomogeneous deformation at these smaller scales are lost when averaging at the much larger RVE scale. Furthermore several distinct scale of inhomogeneous

deformation may occur in a material at disparate length scales; the current gradient enhanced approach, equations (5.7), embeds a single length scale in the continuum model i.e. only a single scale of inhomogeneous deformation can be considered.

Determination of the higher order constitutive relationship has proven difficult, particularly from physical experiments. (Kouznetsova et al. 2002) attempted to determine the relationship numerically 'on the fly'; the higher order constitutive relationship was computed from computational RVEs at each material (integration) point. A further difficulty is that the second gradient of the displacement (strain gradient) must be computed in the gradient continuum. In a finite element implementation this requires at least C^1 interpolation functions to capture a linear variation in strain within an element.

The concept of using gradient terms to capture a length scale effect in the continuum model is now employed to develop a multiresolution continuum theory in Section 5.3. This theory overcomes the disadvantages of the gradient enhanced theory outlined in Section 5.2.

5.3 A General Higher Order Multiresolution Continuum Theory

In this Section the Hill equation (1.1) is extended in such a way that the resulting continuum governing equations can replicate the inhomogeneous deformation observed at multiple length scales within the RVE. For example in (Figure 5.3), a simplified RVE is shown in which strong inhomogeneous deformation arises between debonded particles, at a scale V_1 which is clearly smaller than the RVE V_0. In (Figure 5.4) inhomogeneous strain occurs at two distinct scales V_1

and V_2 due to the presence of two scales of debonding particles. We begin however, by assuming inhomogeneous deformation occurs at a single distinct scale V_1 similar to (Figure 5.3). The theory is then extended to handle an arbitrary number of scales of inhomogeneous deformation.

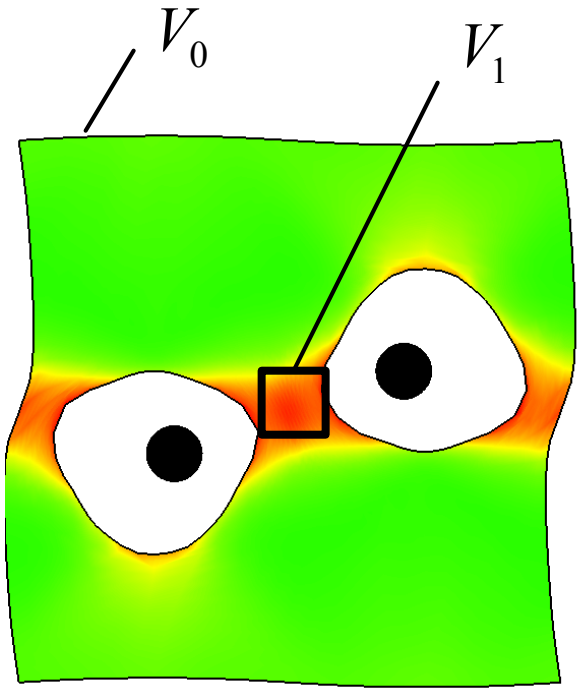

Figure 5.3. Inhomogeneous deformation between two voids

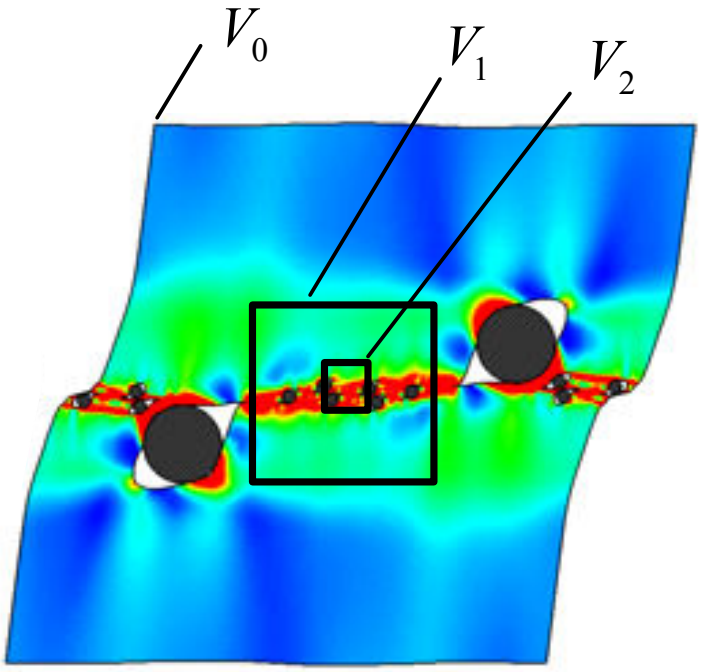

Figure 5.4. Two scales of inhomogeneous deformation between voids at two scales

5.3.1 Inhomogeneous Internal Power Density

The continuum virtual internal power density can be decomposed into contributions arising from homogeneous and *inhomogeneous* deformation:

$$\delta p = \delta p^{\text{hom}} + \delta p^{\text{inh}} \tag{5.9}$$

The homogeneous contribution to the virtual internal power density, δp^{hom}, has been defined in equations (5.1) and (5.2) as the average virtual power density at the RVE scale V_0:

$$\delta p^{\text{hom}} = \frac{1}{V_0}\int_{V_0} \delta p_m dV_0 = \frac{1}{V_0}\int_{V_0} \boldsymbol{\sigma}_m : \delta \mathbf{L}_m dV_0 = \boldsymbol{\sigma} : \delta \mathbf{L} \tag{5.10}$$

The inhomogeneous contribution to the virtual internal power δp^{inh} is defined as the difference between

- the *average* virtual power density at the scale of the inhomogeneous deformation V_1 and
- the *average* virtual power density at the RVE scale V_0

$$\delta p^{\text{inh}} = \frac{1}{V_1}\int_{V_1} \delta p_m dV_1 - \frac{1}{V_0}\int_{V_0} \delta p_m dV_0 \tag{5.11}$$

Rewriting the first integrand in terms of the power conjugate local stress $\boldsymbol{\sigma}_m$ and velocity gradient $\mathbf{L}_m$ fields within the RVE and the second integral using the Hill-Mandel relation in equation (5.10):

$$\begin{aligned} \delta p^{\text{inh}} &= \frac{1}{V_1}\int_{V_1} \left(\boldsymbol{\sigma}_m : \delta\mathbf{L}_m\right) dV_1 - \boldsymbol{\sigma} : \delta\mathbf{L} \\ &= \frac{1}{V_1}\int_{V_1} \left(\boldsymbol{\sigma}_m : \delta\mathbf{L}_m - \boldsymbol{\sigma} : \delta\mathbf{L}\right) dV_1 \end{aligned} \tag{5.12}$$

With reference to equation (5.12), the relative power $\boldsymbol{\sigma}_m : \mathbf{L}_m - \boldsymbol{\sigma} : \mathbf{L}$ contour is plotted on an RVE V_0 containing two debonded particles in (Figure 5.5), labeled 'Inhomogeneous Power'. The tensor norm of the inhomogeneous velocity gradient field $\left\|\mathbf{L}_m - \mathbf{L}\right\|$ is also plotted for reference, labeled "Inhomogeneous Velocity Gradient". As expected the inhomogeneous power field is greatest where the inhomogeneous deformation is greatest - between the neighboring voids in this case where strain localization occurs.

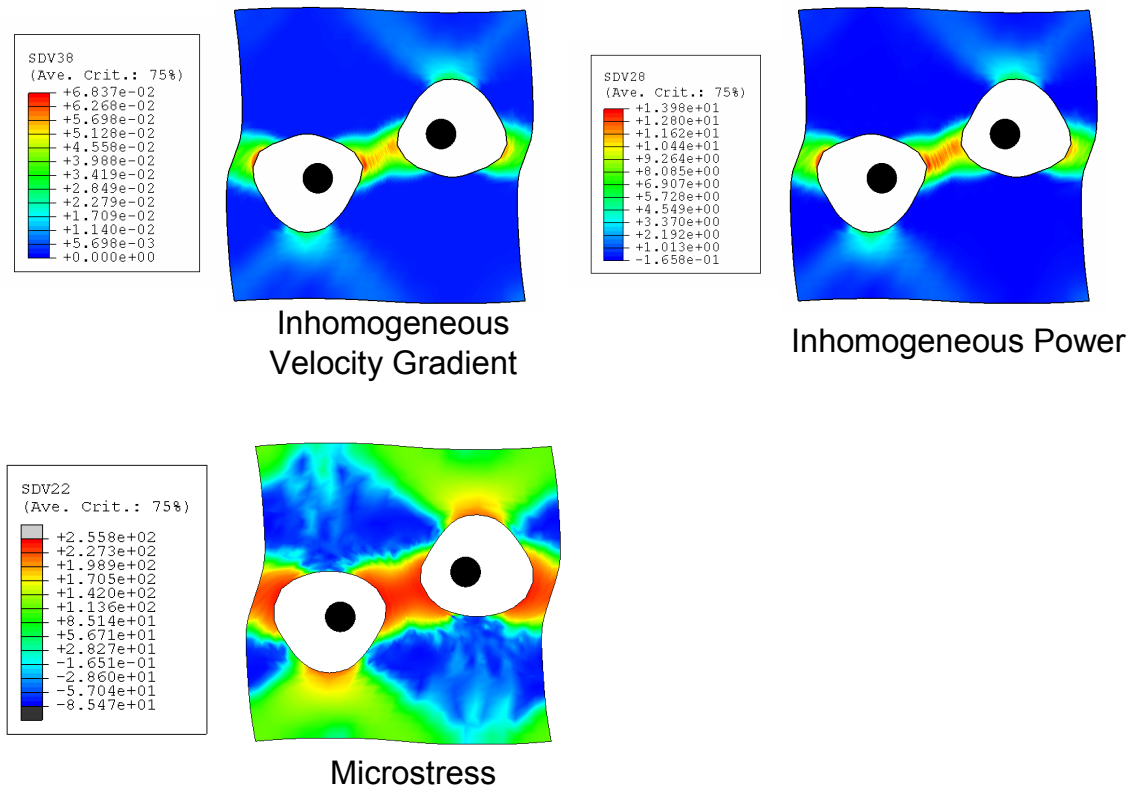

Figure 5.5. Local measures of the Inhomogeneous velocity gradient $\|\mathbf{L}_m - \mathbf{L}\|$, inhomogeneous power $\boldsymbol{\sigma}_m : \mathbf{L}_m - \boldsymbol{\sigma} : \mathbf{L}$ and inhomogeneous microstress $\boldsymbol{\beta}_m$ are plotted as contours.

Given the power decomposition equation (5.12), it is possible to diverge in one of either two directions:

- Formulate a coupled continuum-discrete microstructure (DNS) simulation in which the homogeneous power contribution, equation (5.10) is computed via a conventional continuum and the inhomogeneous contribution, equation (5.12) is computed via a superimpose simulation of the detailed microstructure. This involves two separate, coupled simulations i.e. a coarse and fine scale.

- Formulate a multiresolution continuum formulation in which the homogeneous, equation (5.10), and inhomogeneous, equation (5.12), contributions are coupled and both are computed within the same (higher order) homogenized continuum simulation. In this case the inhomogeneous contribution is represented via extra continuum fields; detailed microstructure simulations are not performed.

Although both approaches have merit, the latter is more suitable for modeling larger domains as no discrete microstructural features need to be modeled, boundary conditions between scales are redundant and dynamic problems involving wave effects can be handled efficiently because no interscale boundaries exist. This approach is described in Sections 5.3.2-5.3.5.

The continuum-DNS approach is described in (Liu and McVeigh 2007) in a hierarchical and concurrent framework. The continuum-DNS approach is also extended by (Liu and McVeigh 2007) to the atomic scale by writing the atomic scale virtual power in terms of force and displacement measures via a virtual atom cluster homogenization technique.

5.3.2 Inhomogeneous Power Equivalence Relationship

The inhomogeneous contribution to the internal power, equation (5.12), is now developed into a continuum expression in order to formulate a set of multiresolution continuum governing equations. As shown in (Figure 5.5), there is a strong relationship between the local inhomogeneous power density $\boldsymbol{\sigma}_m : \mathbf{L}_m - \boldsymbol{\sigma} : \mathbf{L}$ and local inhomogeneous velocity gradient $\mathbf{L}_m - \mathbf{L}$. This motivates us to rewrite equation (5.12):

$$\begin{aligned}\delta p^{\text{inh}} &= \frac{1}{V_1}\int_{V_1}\left(\boldsymbol{\sigma}_m : \delta\mathbf{L}_m - \boldsymbol{\sigma} : \delta\mathbf{L}\right) dV_1 \\ &= \frac{1}{V_1}\int_{V_1}\boldsymbol{\beta}_m : \left(\delta\mathbf{L}_m - \delta\mathbf{L}\right) dV_1\end{aligned} \tag{5.13}$$

where a variational power equivalence relationship has been used:

$$\boldsymbol{\beta}_m : \left(\delta\mathbf{L}_m - \delta\mathbf{L}\right) = \boldsymbol{\sigma}_m : \delta\mathbf{L}_m - \boldsymbol{\sigma} : \delta\mathbf{L} \tag{5.14}$$

This expression introduces and defines a local microstress $\boldsymbol{\beta}_m$ which is a power conjugate of the local inhomogeneous velocity gradient $\mathbf{L}_m - \mathbf{L}$ within the microstructure. This microstress forms the basis of the proposed multiresolution approach as is plotted in (Figure 5.5) based on the definition given in equation (5.14). Just as the stress $\boldsymbol{\sigma}_m$ gives a measure of the resistance to deformation within the microstructure, $\boldsymbol{\beta}_m$ is a measure of the resistance to inhomogeneous deformation within the microstructure.

5.3.3 Continuum Microstress from Microscale Homogenization

The inhomogeneous averaging volume V_1 used in equation (5.13) defines the scale of the inhomogeneous deformation. At this scale it is reasonable to assume that the local strain varies linearly. A linear approximation of the local velocity gradient $\mathbf{L}_m$ within the volume V_1 is given by defining two continuum quantities:

$$\begin{aligned}\mathbf{L}^1 &= \frac{1}{V_1}\int_{V_1}\mathbf{L}_m dV \\ \mathbf{G}^1 &= \frac{1}{V_1}\int_{V_1}\mathbf{L}_m \bar{\nabla} dV\end{aligned} \tag{5.15}$$

where $\mathbf{L}^1$ is the volume average of the local velocity gradient and $\mathbf{G}^1$ is the volume average of the local gradient of the velocity gradient in V_1. Furthermore $\mathbf{y}$ is the local position with respect to the center of V_1. A linear approximation of the local velocity gradient can be made:

$$\mathbf{L}_m = \mathbf{L}^1 + \mathbf{G}^1 \bullet \mathbf{y} \tag{5.16}$$

Substituting for the local velocity gradient $\mathbf{L}_m$ in equation (5.13), the inhomogeneous virtual internal power density of a continuum point can now be written as

$$\begin{aligned} \delta p^{\text{inh}} &= \left(\frac{1}{V_1} \int_{V_1} \boldsymbol{\beta}_m dV_1 \right) : \left(\delta \mathbf{L}^1 - \delta \mathbf{L} \right) + \left(\frac{1}{V_1} \int_{V_1} \boldsymbol{\beta}_m \otimes \mathbf{y} dV_1 \right) \vdots \delta \mathbf{G}^1 \\ &= \boldsymbol{\beta}^1 : \left(\delta \mathbf{L}^1 - \delta \mathbf{L} \right) + \overline{\boldsymbol{\beta}}^1 \vdots \delta \mathbf{G}^1 \end{aligned} \tag{5.17}$$

where the continuum microstress $\boldsymbol{\beta}^1$ and the microstress couple $\overline{\boldsymbol{\beta}}^1$ are:

$$\begin{aligned} \boldsymbol{\beta}^1 &= \frac{1}{V_1} \int_{V_1} \boldsymbol{\beta}_m dV_1 \\ \overline{\boldsymbol{\beta}}^1 &= \frac{1}{V_1} \int_{V_1} \boldsymbol{\beta}_m \otimes \mathbf{y} dV_1 \end{aligned} \tag{5.18}$$

This expression contains volume averages of the microstress $\boldsymbol{\beta}_m$ and its first moment $\boldsymbol{\beta}_m \otimes \mathbf{y}$ at the scale of the inhomogeneous deformation. These volume averages are interpreted as *continuum* microstresses, resolved to the scale V_1.

The continuum microstress $\boldsymbol{\beta}^1$ and the microstress couple $\overline{\boldsymbol{\beta}}^1$ together represent the average resistance to inhomogeneous deformation at scale V_1. For example in (Figure 5.5) the continuum microstress $\boldsymbol{\beta}^1$ would be a volume average of the local microstress $\boldsymbol{\beta}_m$ at the scale of the inhomogeneous deformation, V_1 i.e. between the voids.

The total virtual power density expression is given by summing the homogeneous and inhomogeneous contribution to the virtual internal power density, equation (5.9):

$$\begin{aligned}\delta p &= \delta p^{\text{hom}} + \delta p^{\text{inh}} \\ &= \boldsymbol{\sigma} : \delta \mathbf{L} + \boldsymbol{\beta}^{1} : \left(\delta \mathbf{L}^{1} - \delta \mathbf{L} \right) + \overline{\boldsymbol{\beta}}^{1} \vdots \delta \mathbf{G}^{1}\end{aligned} \tag{5.19}$$

5.3.4 Extension to Multiple Scales of Inhomogeneous Deformation

In many materials, inhomogeneous deformation may occur at successively smaller and distinct scales (Figure 5.4) as the microstructure evolves. The virtual internal power density can be written in terms of the homogeneous contribution and the inhomogeneous contributions arising from each scale:

$$\begin{aligned}\delta p &= \delta p^{\text{hom}} + \sum_{n=1}^{N} \delta p_{n}^{\text{inh}} \\ &= \boldsymbol{\sigma} : \delta \mathbf{L} + \sum_{n=1}^{N} \frac{1}{V_{n}} \int_{V_{n}} \left(\boldsymbol{\sigma}_{m} : \delta \mathbf{L}_{m} - \boldsymbol{\sigma} : \delta \mathbf{L} \right) dV_{n}\end{aligned} \tag{5.20}$$

where n nested averaging volumes have been defined; each represents a scale at which inhomogeneous deformation occurs. As discussed in Section 5.3.1, this expression can be used as a framework for performing multiple nested coupled concurrent simulations (Liu and McVeigh 2007) involving both continuum and discrete microstructure scales. However, as before we proceed in the multiresolution continuum framework. Following the same approach as before, the resulting internal power expression is:

$$\delta p^{\text{int}} = \boldsymbol{\sigma} : \delta \mathbf{L} + \sum_{n=1}^{N} \left(\boldsymbol{\beta}^{n} : \left(\delta \mathbf{L}^{n} - \delta \mathbf{L} \right) + \overline{\boldsymbol{\beta}}^{n} \vdots \delta \mathbf{G}^{n} \right) \tag{5.21}$$

where the continuum microstress at scale n is given by:

$$\boldsymbol{\beta}^n = \frac{1}{V_n}\int_{V_n} \boldsymbol{\beta}_m dV_n$$
$$\bar{\boldsymbol{\beta}}^n = \frac{1}{V_n}\int_{V_n} \boldsymbol{\beta}_m \otimes \mathbf{y} dV_n \qquad (5.22)$$

Again, each of the continuum measures $\boldsymbol{\sigma}, \boldsymbol{\beta}^n, \bar{\boldsymbol{\beta}}^n, \mathbf{L}, \mathbf{L}^n$ and $\mathbf{G}^n$ are written either directly or indirectly in terms of volume averages of the local fields $\boldsymbol{\sigma}_m$ and $\mathbf{L}_m$. The continuum microstress $\boldsymbol{\beta}^n$ is now simply the average resistance to inhomogeneous deformation at scale V_n.

Embedded Length Scales

The key to this theory is that several length scales, given by the characteristic sizes of the averaging volumes V_n, are embedded directly via the microstress couple $\bar{\boldsymbol{\beta}}^n$ averaging operation in equation (5.18). Although other higher order theories introduce stress couples, the difference here is that a microstress couple $\bar{\boldsymbol{\beta}}^n$ is averaged directly at each scale of inhomogeneous deformation. This naturally introduces length scales l^n which are equal to the width of the square averaging volumes V_n.

This becomes clearer in Chapter 6 where the microstress couples $\bar{\boldsymbol{\beta}}^n$ behave in an elasto-plastic manner. In the resulting microstress elastic constitutive relation, equation (6.10), a length scale parameter l^n arises naturally when the averaging operation, equation (5.22), is performed at scale V_n. In the plastic regime the same length scale is implicitly embedded in the microstress $\bar{\boldsymbol{\beta}}^n$ flow relation, equation (6.15).

The key multiresolution relationships are summarized in table 5.1

Continuum Tensor...	**…is a Volume Average of Microstructure Field…**	**…at Scale**
$\boldsymbol{\sigma}$	$\boldsymbol{\sigma}_m$	V_0
$\boldsymbol{\beta}^n$	$\boldsymbol{\beta}_m$	V_n
$\overline{\boldsymbol{\beta}}^n$	$\boldsymbol{\beta}_m \otimes \mathbf{y}$	V_n
$\mathbf{L}$	$\mathbf{L}_m$	V_0
$\mathbf{L}^n$	$\mathbf{L}_m$	V_n
$\mathbf{G}^n$	$\mathbf{L}_m \bar{\nabla}$	V_n
Power Equivalence	$\boldsymbol{\beta}_m : \left(\mathbf{L}_m - \mathbf{L}\right) = \boldsymbol{\sigma}_m : \mathbf{L}_m - \boldsymbol{\sigma} : \mathbf{L}$	
Virtual Internal Power Density	$\delta p = \boldsymbol{\sigma} : \delta\mathbf{L} + \sum_{n=1}^{N} \boldsymbol{\beta}^n : \left(\delta\mathbf{L}^n - \delta\mathbf{L}\right) + \overline{\boldsymbol{\beta}}^n \vdots \delta\mathbf{G}^n$	

Table 5.1 Continuum Measures and their origin within the microstructure

5.3.5 Multiresolution Governing Equations

The principal of virtual power is used along with the divergence theorem to derive the multiresolution continuum governing equations.

Internal Power

The total virtual power density is the sum of the homogeneous and inhomogeneous parts, integrated over the entire body:

$$\delta P_{int} = \int_{\Omega} \left\{ \boldsymbol{\sigma} : \delta \mathbf{L} + \sum_{n=1}^{N} \left(\boldsymbol{\beta}^n : (\delta \mathbf{L}^n - \delta \mathbf{L}) + \overline{\boldsymbol{\beta}}^n \vdots \delta \mathbf{G}^n \right) \right\} d\Omega \tag{5.23}$$

Each of the continuum measures $\boldsymbol{\sigma}, \boldsymbol{\beta}^1, \overline{\boldsymbol{\beta}}^1, \mathbf{L}, \mathbf{L}^1, \mathbf{G}^1$ are written either directly or indirectly in terms of volume averages (over V_1 or V_0) of the known local fields $\boldsymbol{\sigma}_m, \mathbf{L}_m$ within the RVE.

External Power and Kinetic power

The external virtual power is obtained by extending the conventional external power expression:

$$\begin{aligned}
\delta P_{ext} &= \int_{\Omega} \left(\mathbf{b} \bullet \delta \mathbf{v} + \sum_{n=1}^{N} \mathbf{B}^n : \delta \mathbf{L}^n \right) d\Omega + \int_{\Gamma} \left(\mathbf{t} \bullet \delta \mathbf{v} + \sum_{n=1}^{N} \mathbf{R}^n : \delta \mathbf{L}^n \right) d\Gamma \\
\delta P_{kin} &= \int_{\Omega} \rho \dot{\mathbf{v}} \bullet \delta \mathbf{v} + \sum_{n=1}^{N} \left(\boldsymbol{\gamma}^n \bullet \mathbf{I}^n \right) : \delta \mathbf{L}^n d\Omega \\
\boldsymbol{\gamma}^n &= \dot{\mathbf{L}}^n + \mathbf{L}^n \bullet \mathbf{L}^n \\
\mathbf{I}^n &= \frac{1}{V_n} \int_{V_n} \rho^n \mathbf{y} \otimes \mathbf{y} d\Omega
\end{aligned} \tag{5.24}$$

The virtual external power is written in terms of the double traction forces $\mathbf{R}^n$ and the body couple stresses $\mathbf{B}^n$ which balance the microstresses on the surface Γ and within the body Ω respectively. In a conventional continuum, applying a body force **b** or surface traction **t** will

drive a velocity gradient $\mathbf{L}$ within the body; similarly the body couple stress $\mathbf{B}^n$ and double traction force $\mathbf{R}^n$ drive the inhomogeneous velocity gradient $\mathbf{L}^n - \mathbf{L}$.

The virtual kinetic power is based on an extension of the expression developed by (Mindlin 1964) to multiple scales (Vernerey 2006; Vernerey et al. 2007a; b). This introduces micro-accelerations $\boldsymbol{\gamma}^n$ at each scale and relative densities ρ^n which are the difference in average density between neighboring scales. The vector $\mathbf{y}$ gives the coordinate with respect to the center of the averaging volume V_n.

Governing Equations

By applying divergence theorem and making use of the arbitrariness of the variations $\delta\mathbf{v}$ and $\delta\mathbf{L}^n$, the resulting equilibrium equations and boundary conditions are:

$$\begin{aligned}
&\left(\boldsymbol{\sigma} - \sum_{n=1}^{N} \boldsymbol{\beta}^n\right) \bullet \nabla + \mathbf{b} = \rho \dot{\mathbf{v}} \quad \text{in} \quad \Omega \\
&\nabla \bullet \bar{\boldsymbol{\beta}}^n - \boldsymbol{\beta}^n + \mathbf{B}^n = \boldsymbol{\gamma} \bullet \mathbf{I}^n \quad \text{in} \quad \Omega \\
&\mathbf{t} - \mathbf{N} \bullet \left(\boldsymbol{\sigma} - \sum_{n=1}^{N} \boldsymbol{\beta}^n\right) = \mathbf{0} \quad \text{on} \quad \Gamma_t \\
&\mathbf{R}^n = \mathbf{r}^n \mathbf{N} = \mathbf{N} \bullet \bar{\boldsymbol{\beta}}^n : (\mathbf{N}\mathbf{N}) \quad \text{on} \quad \Gamma_{R^n}
\end{aligned} \tag{5.25}$$

which are identical to those proposed by (Vernerey 2006; Vernerey et al. 2007a; b). A key advance here is that the technique for deriving these governing equations from the standpoint of RVE modeling gives rise to a natural and systematic framework for deriving microstress and microstress couple constitutive relationships.

In order to solve the governing equations, with applied boundary conditions, several constitutive relationships must be defined to relate the continuum stress and deformation measures. These constitutive relationships, and how to derive them, are described in Chapter 6.

5.3.6 Application to 1D Strain Softening Problem

The multiresolution approach, equation (5.25), is used to model the 1D strain softening introduced in Section 5.2.1. The governing equations (5.25) are used with $N=1$. Only a single component of the microstress, $\boldsymbol{\beta}^1$ and microstress couple $\overline{\boldsymbol{\beta}}^1$ are required in the 1D analysis performed here. These are written as β^1 and $\overline{\beta}^1$. For simplicity, each is considered to obey a linear elastic relationship:

$$\begin{aligned} \dot{\beta}^1 &= E(L^1 - L) \\ \dot{\overline{\beta}}^1 &= E\left(l\right)^2 G^1 \end{aligned} \tag{5.26}$$

where E is the elastic modulus, l is the length scale associated with the inhomogeneous averaging volume V_1, $L^1 - L$ is the inhomogeneous velocity gradient and G^1 is the second micro-velocity gradient. The length scale parameter l is given a value of 0.5. Velocity boundary conditions are applied as before. The engineering strain measures ε^1 and ε corresponding to the velocity gradients L^1 and L are plotted in (Figure 5.6) along with the strain gradient corresponding to G^1. The result is almost identical to that obtained using standard strain gradient theory, (Figure 5.2).

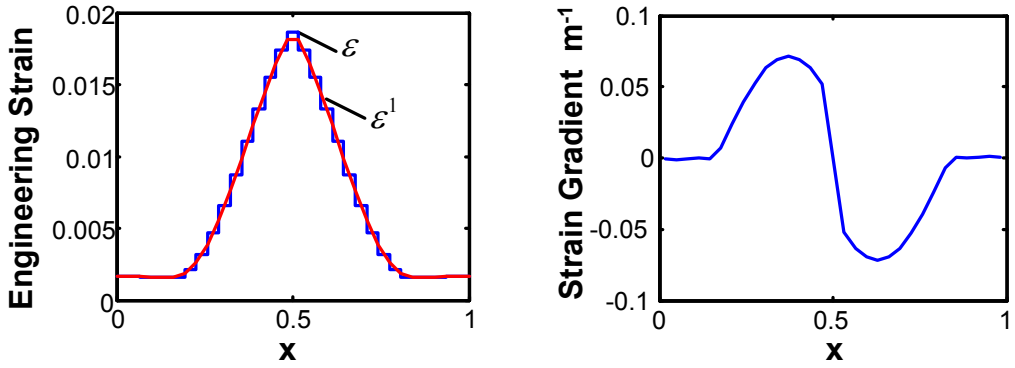

Figure 5.6. A length scale is introduced through the multiresolution theory

A comparison between the multiresolution theory developed here and an existing 'Lagrange Multiplier' approach used by (Herrmann 1983; Kouznetsova et al. 2002; Xia and Hutchinson 1996) is given in the Appendix A6. In that approach a Lagrange multiplier behaved in a similar manner to the microstress $\boldsymbol{\beta}^n$ introduced in the current formulation. However the Lagrange multiplier was not interpreted as having any physical meaning. Here the behavior of the microstress is explored in Section 5.4

5.4 Exploring the Multiresolution Microstresses

In this section the microstress $\boldsymbol{\beta}^n$ and microstress couple $\overline{\boldsymbol{\beta}}^n$ are explored; in particular the influence they have on the macroscale constitutive response. In Section 5.3 the microstress $\boldsymbol{\beta}^n$ is introduced and defined as the average resistance to inhomogeneous deformation at scale n, equations (5.14) and (5.22). Here the effect of microstress failure is examined. This reduction in resistance to inhomogeneous deformation has an obvious consequence - the deformation becomes increasingly inhomogeneous i.e. it localizes at a smaller scale. A systematic approach to

determining microscale constitutive relationships which describe the microstress $\boldsymbol{\beta}^n$ and microstress couple $\overline{\boldsymbol{\beta}}^n$ is given in Chapter 6.

5.4.1 Illustrative Example: Shear Problem

A two dimensional plane strain quasi-static shear problem is used to illustrate the microstress behavior. The alloy plate is loaded under shear boundary conditions. The stress-strain constitutive relation illustrated in (Figure 5.7) is used to model the flow stress in a J2 Mises type plasticity model and used to represent the alloy plate's constitutive response. The alloy work hardens before reaching a shear instability point at approximately 4% after which strain softening occurs.

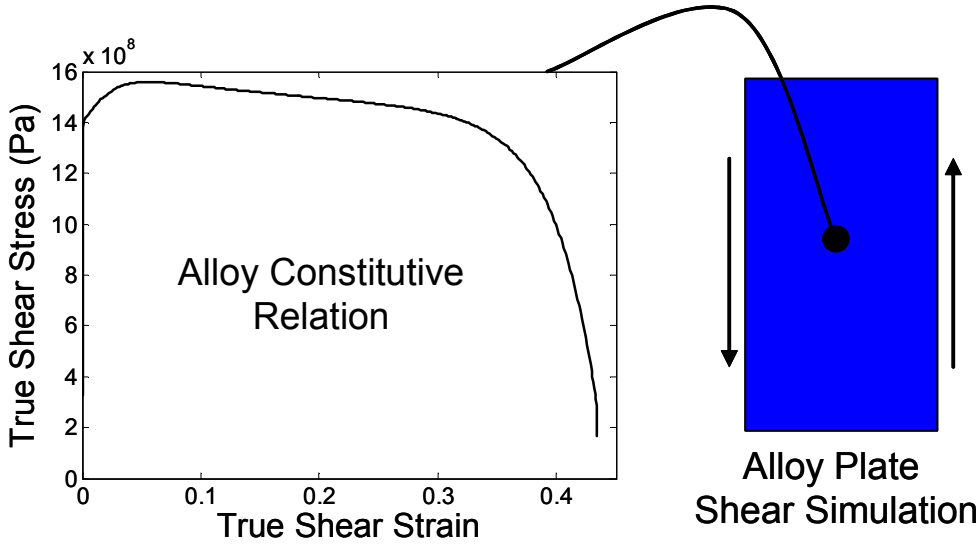

Figure 5.7. A simple shear strain softening constitutive relation is used to model a 2D plane strain plate

5.4.2 Conventional Continuum versus Multiresolution

The shear problem outlined in (Figure 5.7) is first solved using a conventional continuum approach, equations (1.5). (Figure 5.8) shows that the strain tends to localize unphysically in a single element, regardless of the element size used.

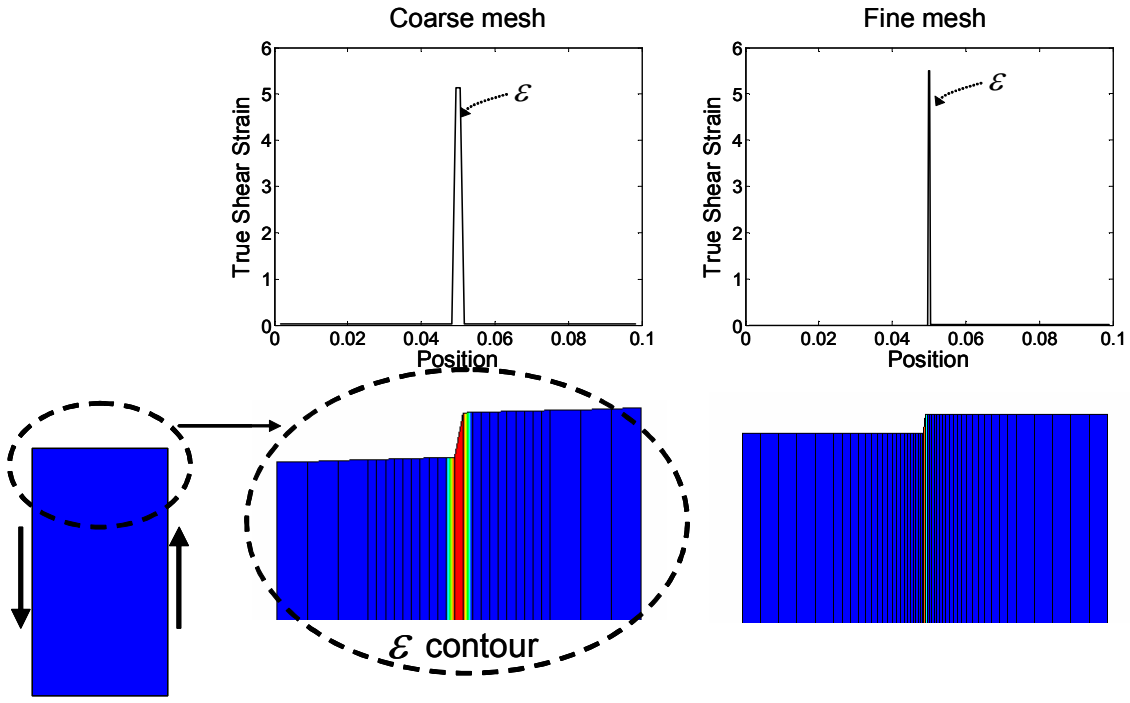

Figure 5.8. Unphysical mesh dependent strain localization occurs

The multiresolution continuum approach is now used, equation (5.25), with the same shear boundary conditions. It is assumed that inhomogeneous strain occurs at *three* successively smaller scales given by l^1, l^2 and l^3 (e.g. the steel alloy described in Chapter 2). The criteria for determining when inhomogeneous deformation transitions from scale l^1 to l^2 to l^3 is given in terms of the shear strain:

- During the elastic and plastic work hardening regime deformation is homogeneous and none of the microstresses are active
- When the shear strain at a material point reaches 0.04 the material begins to soften as shown in the constitutive relation in (Figure 5.7). Inhomogeneous deformation at scale l^1 commences. Microstress $\boldsymbol{\beta}^1$ and microstress couple $\overline{\boldsymbol{\beta}}^1$ are active
- When the shear strain reaches **0.175** at a material point, the inhomogeneous deformation transitions to scale l^2. Microstress $\boldsymbol{\beta}^1$ and microstress couple $\overline{\boldsymbol{\beta}}^1$ fail. Microstress $\boldsymbol{\beta}^2$ and microstress couple $\overline{\boldsymbol{\beta}}^2$ are active.
- When the shear strain reaches **0.35** at a material point, the inhomogeneous deformation transitions to scale l^3. Microstress $\boldsymbol{\beta}^2$ and microstress couple $\overline{\boldsymbol{\beta}}^2$ fail. Microstress $\boldsymbol{\beta}^3$ and microstress couple $\overline{\boldsymbol{\beta}}^3$ are active.
- When the shear strain reaches **0.5** at a material point, the material breaks. The microstress $\boldsymbol{\beta}^3$ and microstress couple $\overline{\boldsymbol{\beta}}^3$ fail.

A simple approach to the microstress constitutive relationships is used; each is considered to behave in a linear elastic manner when active as shown in (Figure 5.9). When inhomogeneous deformation is due to transition to scale $n+1$, the microstress $\boldsymbol{\beta}^n$ and microstress couple $\overline{\boldsymbol{\beta}}^n$ fail immediately (they are set to zero) as shown in (Figure 5.9).

In (Figure 5.9) the shear strain contour is shown and the shear strain profile across the sample is plotted. The strain is regularized at scale l^1 while $\boldsymbol{\beta}^1$ is active, l^2 while $\boldsymbol{\beta}^2$ is active and l^3 while

$\boldsymbol{\beta}^3$ is active. The values of the scale transition strains used here (**0.175, 0.35, 0.5**) have not been rigorously determined from experiment or simulation. However the change in characteristic length scale of the inhomogeneous deformation does correspond to meaningful microstructural instability events in engineering materials. These microstructural instability events or transitions are discussed briefly in Section 5.4.3.

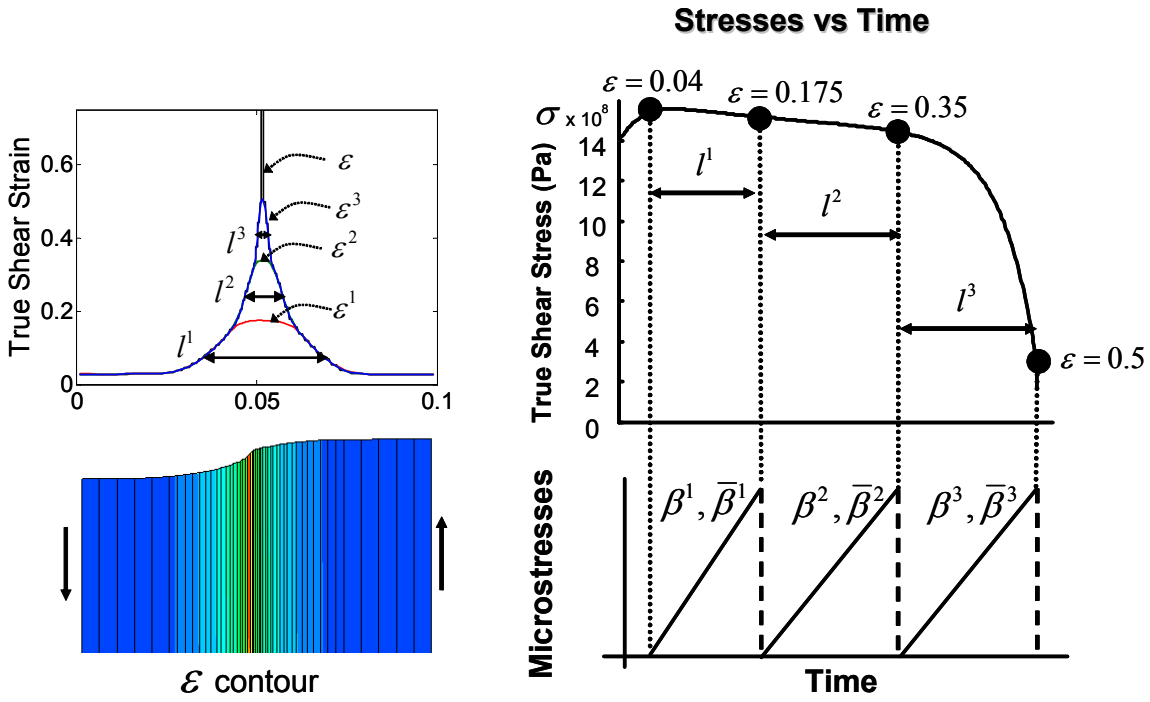

Figure 5.9. N **length scales can be introduced by using** N **microstresses** $\boldsymbol{\beta}^n$ **and** N **microstress couples** $\bar{\boldsymbol{\beta}}^n$**.**

5.4.3 Microstructure Instability Events

In Sections 5.4.2 the microstresses are assumed to fail at particular predefined shear strains during the course of the simulation. When microstresses $\boldsymbol{\beta}^n$ and $\bar{\boldsymbol{\beta}}^n$ are active they regularize the

deformation at scale n. If these microstresses fail, the inhomogeneous deformation is regularized at scale $n+1$ by the microstresses $\boldsymbol{\beta}^{n+1}$ and $\overline{\boldsymbol{\beta}}^{n+1}$ and so on.

Microstress failure is indicative of a microstructural instability event; these events are responsible for the transition of inhomogeneous deformation from one scale to the next. In multiscale material systems such as high strength steels and cemented carbides (Chapter 2) these instability events are well defined and can be determined using computational direct numerical simulations of the microstructure, as will be shown in detail in Chapter 7. The microstructure instability events in WC-Co are described in Section 2.1.6 and for a steel alloy in Section 2.2.2. Fortunately these events can often be predicted by homogenized constitutive relationships. For example a simple porous metal plasticity constitutive model tracks evolving void nucleation and coalescence – both can be used to determine when microstructural instability events occur. In terms of the multiresolution theory this is useful because the failure of the microstresses (which coincide with various microstructure instabilities) can be linked to the macroscale constitutive response. Hence the evolving microstructure is predicted by the macroscale constitutive model, which in turn provides information about when the microstresses should fail i.e. when the inhomogeneous deformation should transition to another scale.

5.5 Reduction to a Variable Length Scale Elastic Micrograd ient Model

The multiscale theory outlined in Sections 5.3 and 5.4 is useful for incorporating microscopic length scale effects in the macroscale solution. However, with each additional scale of analysis beyond the conventional macroscale, a further four degrees of freedom $\left(L^n_{11}, L^n_{22}, L^n_{33}, L^n_{12}\right)$ are

introduced at each node in a two dimensional finite element analysis, and six $\left(L_{11}^n, L_{22}^n, L_{33}^n, L_{12}^n, L_{13}^n, L_{23}^n\right)$ in a three dimensional analysis.

As described previously each microstress (and its associated microstress couple) represents the resistance to inhomogeneous deformation at a particular scale. In most materials the inhomogeneous deformation transitions to successively smaller scales when microstructural instabilities occur (as described in Section 5.4.3). The transition from scale n to scale $n+1$ generally occurs quite rapidly in as a function of the microstructural evolution.

In terms of the multiresolution continuum theory, this means that the inhomogeneous microstresses are successively dominant. Hence as microstress $\boldsymbol{\beta}^n$ fails, the next microstress $\boldsymbol{\beta}^{n+1}$ begins to dominate and so on until each microstress has failed. It is therefore possible to replace each of the microstresses $\boldsymbol{\beta}^n$ with a single *multiscale* microstress $\boldsymbol{\beta}^{ms}$ which takes the place of the N microstresses in equation (5.25). The resulting governing equations are given by:

$$\begin{aligned}
\nabla\bullet\left(\boldsymbol{\sigma}-\boldsymbol{\beta}^{ms}\right)+\mathbf{b}&=\rho\dot{\mathbf{v}} \quad \text{in} \quad \Omega\\
\nabla\bullet\bar{\boldsymbol{\beta}}^{ms}-\boldsymbol{\beta}^{ms}+\mathbf{B}&=\boldsymbol{\gamma}\bullet\mathbf{I}^n \quad \text{in} \quad \Omega\\
\mathbf{t}&=\mathbf{N}\bullet\left(\boldsymbol{\sigma}-\boldsymbol{\beta}^{ms}\right) \quad \text{on} \quad \Gamma_t\\
\mathbf{R}=\mathbf{r}\mathbf{N}&=\mathbf{N}\bullet\bar{\boldsymbol{\beta}}^{ms}:\left(\mathbf{N}\mathbf{N}\right) \quad \text{on} \quad \Gamma_R
\end{aligned} \tag{5.27}$$

This *multiscale* microstress $\boldsymbol{\beta}^{ms}$ and its associated *multiscale* higher order microstress $\bar{\boldsymbol{\beta}}^{ms}$ ensure that the inhomogeneous deformation occurs at the appropriate scale. In terms of microstress constitutive relationships, the Jaumann rate of the multiscale microstress $\overset{\nabla}{\boldsymbol{\beta}}^{ms}$ and higher order microstress $\overset{\nabla}{\bar{\boldsymbol{\beta}}}^{ms}$ are given in terms of elastic relationships:

$$\begin{aligned}\overset{\nabla}{\boldsymbol{\beta}}^{ms} &= \mathbb{C}^{ms} \bullet \left(\mathbf{L}^{ms} - \mathbf{L}\right)^{e} \\ \overset{\nabla}{\overline{\boldsymbol{\beta}}}^{ms} &= \overline{\mathbb{C}}^{ms} \bullet \left(\mathbf{L}^{ms} \overleftarrow{\nabla}\right)^{e}\end{aligned} \tag{5.28}$$

where $\mathbb{C}^{ms}$ and $\overline{\mathbb{C}}^{ms}$ are the multiscale microscale elastic matrices (we assume these are isotropic here). Note that $\overline{\mathbb{C}}^{ms}$ contains an embedded length scale which determines the scale at which the microstresses act.

The multiscale microscale elastic matrices $\mathbb{C}^{ms}$ and $\overline{\mathbb{C}}^{ms}$ can be determined via a representative volume element (RVE) of the microstructure. Assume the local inhomogeneous velocity gradient $\left(\mathbf{L}_m - \mathbf{L}\right)$, equation (5.14), is related to the rate of change of the local microstress $\boldsymbol{\beta}_m$ within the RVE by:

$$\dot{\boldsymbol{\beta}}_m = \mathbf{C}_m : \left(\mathbf{L}_m - \mathbf{L}\right) \tag{5.29}$$

where $\mathbf{C}_m$ is the local elastic tensor. Using the averaging equations (5.18) the elastic constants $\mathbb{C}^{ms}$ and $\overline{\mathbb{C}}^{ms}$ are given by:

$$\mathbb{C}^{ms} = \frac{1}{V_{ms}} \int_{V_{ms}} \mathbf{C}_m dV \tag{5.30}$$

and

$$\mathbb{C}^{ms} = \frac{1}{V_{ms}} \int_{V_{ms}} \mathbf{C}_m \otimes \mathbf{y} \otimes \mathbf{y} dV \tag{5.31}$$

where V_{ms} is the volume which encompasses the currently *dominant* inhomogeneous deformation. Assuming $\mathbf{C}_m$ is constant within the evolving 2D area V_{ms}, the elastic constants become:

$$\mathbb{C}^{ms} = \mathbf{C}_m$$
$$\bar{\mathbb{C}}^{ms} = \frac{\left(l^{ms}\right)^2}{12}\,\mathbf{C}_m \otimes \mathbf{I} \tag{5.32}$$

where $\mathbf{I}$ is the identity tensor and l^{ms} is the length of one side of area domain V_{ms}. The key to this approach is that the averaging volume V_{ms} (and hence the length scale l^{ms}) is now a dynamic parameter i.e. it evolves with the scale of the inhomogeneous deformation.

In the multiresolution formulation, equation (5.25), the length parameter l^{ms} can be used to control the scale at which regularization occurs in a manner which is consistent with the evolving microstructure. This is achieved by switching the length scale l^{ms} to the appropriate scale when a microscale instability event occurs. A simple 2D quasi-static shear example is again used to illustrate the concept; the same example was used in Section 5.4.2. The microstresses $\boldsymbol{\beta}^1, \boldsymbol{\beta}^2, \boldsymbol{\beta}^3$ and higher order microstresses $\bar{\boldsymbol{\beta}}^1, \bar{\boldsymbol{\beta}}^2, \bar{\boldsymbol{\beta}}^3$ are replaced by a single multiscale microstress $\boldsymbol{\beta}^{ms}$ and higher order microstress $\bar{\boldsymbol{\beta}}^{ms}$. For simplicity the microscale instability points are assumed to occur at shear strains of $\varepsilon = 0.175, 0.3, 0.5$. That is the inhomogeneous deformation transitions to a smaller scale when each of these strain levels is reached.

The length scale parameter l^{ms} embedded in the higher order constitutive relationship $\dot{\bar{\boldsymbol{\beta}}}^{ms}\left(\nabla \mathbf{L}^{ms}\right)$ varies with time as shown in (Figure 5.10):

$$\begin{aligned} l^{ms} &= 0.05 \quad \text{when} \quad \varepsilon^p < 0.175 \\ l^{ms} &= 0.01 \quad \text{when} \quad 0.35 > \varepsilon^p \geq 0.175 \\ l^{ms} &= 0.002 \quad \text{when} \quad \varepsilon^p > 0.5 \end{aligned} \tag{5.33}$$

The length scales in equation (5.33) have been chosen for illustration. In a real heterogeneous material these length scales are chosen to correspond to the characteristic length scales of inhomogeneous deformation.

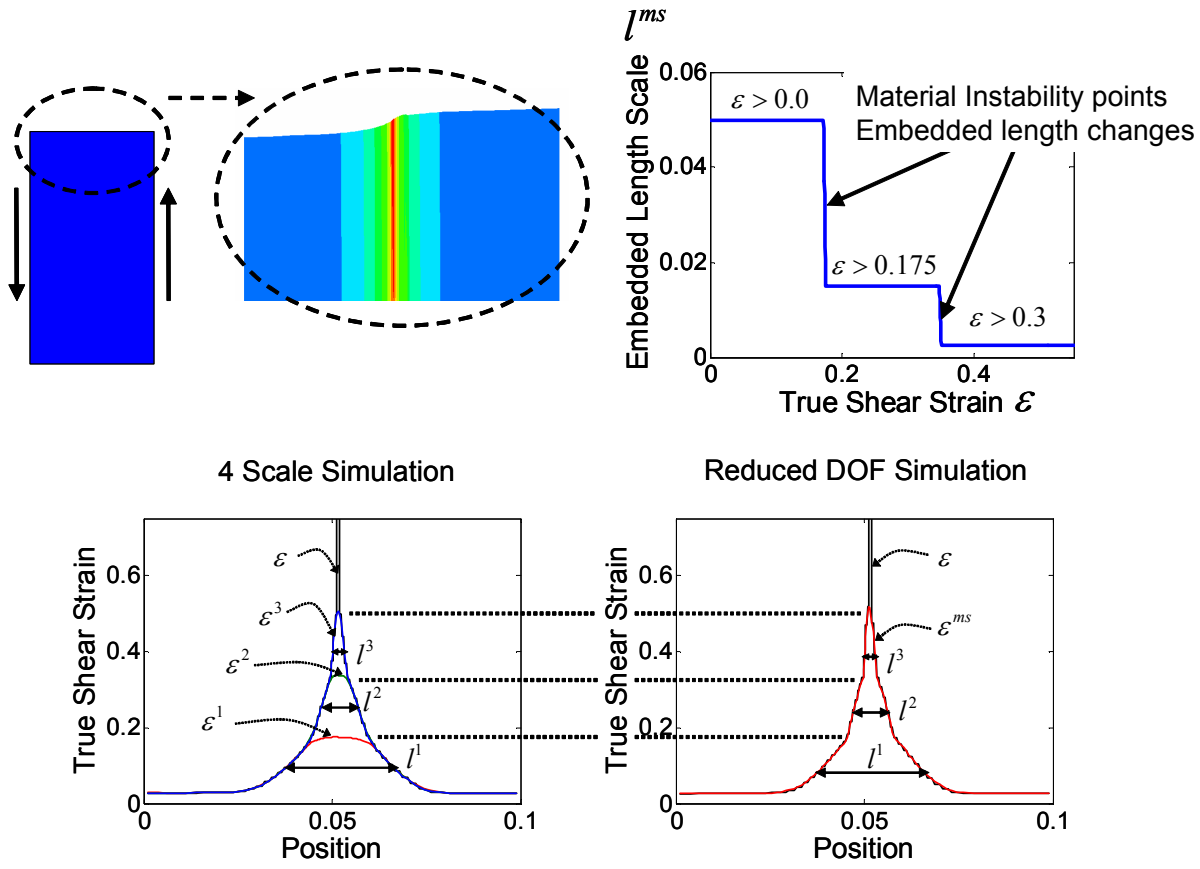

Figure 5.10. The N microstresses $\boldsymbol{\beta}^n$ and N microstress couples $\overline{\boldsymbol{\beta}}^n$ can be replaced by a single multiscale microstress $\boldsymbol{\beta}^{ms}$ and a single microstress couple $\overline{\boldsymbol{\beta}}^{ms}$ with a variable length scale.

The resulting shear strain profile is plotted in (Figure 5.10) for the case where three individual microstress couples $\overline{\boldsymbol{\beta}}^1\left(l^1\right), \overline{\boldsymbol{\beta}}^2\left(l^2\right), \overline{\boldsymbol{\beta}}^3\left(l^3\right)$ were used and for the reduced case where only a single microstress couple $\boldsymbol{\beta}^{ms}\left(l^{ms}\right)$ is considered. In the case where three microstresses are used,

the appropriate microstress is set to zero when an instability event occurs according to equation (5.33) as shown in (Figure 5.9). In the reduced model the instability points correspond to a rapid decrease in the characteristic length scale l^{ms} as shown in (Figure 5.10). This immediately impacts the microstress couple $\boldsymbol{\beta}^{ms}\left(l^{ms}\right)$ through the constitutive equation (5.8).

As shown in (Figure 5.10) the plastic strain profile across the sample, and the timing of scale switching is practically identical for both simulations. The reduced simulation achieves a reduction in computation time of over 60% in this simple example; the total number of degrees of freedom at each node is six, compared to fourteen for the full four scale 2D analysis. Furthermore there is now a single elastic microscale stress update, compared with having three elasto-plastic microscale stress updates in the full four scale approach.

6 Microscale Constitutive Relationships

The macroscale constitutive relationships used in this thesis have been described in detail in Chapter 3. The goal of this Chapter is to develop elasto-plastic constitutive relationships for the continuum microstresses $\dot{\boldsymbol{\beta}}^n\left(\mathbf{L}^n-\mathbf{L}\right)$ and $\dot{\bar{\boldsymbol{\beta}}}^n\left(\mathbf{G}^n\right)$, introduced through the multiresolution continuum theory (MRCT), Chapter 5, equations (5.22).

A form for the microstress constitutive relationships based on conventional associative plasticity constitutive models is proposed in Section 6.1. A procedure is outlined in Section 6.2 to calibrate such a constitutive model to the average microstress at the scale of the inhomogeneous deformation in a representative volume element (RVE) cell model. Scalar effective measures of the microstresses are used. The approach is illustrated for a voided alloy and a steel alloy in Section 6.3 (see Section 2.2 for a description of the micromechanics of a steel alloy).

6.1 Constitutive Relations and Flow Rule

In terms of constitutive modeling the microstresses $\boldsymbol{\beta}^n$ and $\bar{\boldsymbol{\beta}}^n$ are treated as any other stress i.e. it is assumed they can be characterized by an elastic and plastic stage of deformation. The elastic part of the microstress constitutive relationships is described in Section 6.1.1 and the plastic stage, which occurs after a microstress yields, is described in Section 6.1.2.

6.1.1 Microstress Elastic Constitutive Relationship

A Jaumann rate of microstresses has been developed by (Vernerey et al. 2007b) as:

$$\begin{aligned}\left[\overset{\nabla}{\boldsymbol{\beta}}^{n}\right]_{ij} &= \left[\dot{\boldsymbol{\beta}}^{n}\right]_{ij} - \left[\mathbf{W}\right]_{ik}\left[\boldsymbol{\beta}^{n}\right]_{kj} - \left[\boldsymbol{\beta}^{n}\right]_{ik}\left[\mathbf{W}\right]_{jk} \\ \left[\overset{\nabla}{\overline{\boldsymbol{\beta}}}^{n}\right]_{ijk} &= \left[\dot{\overline{\boldsymbol{\beta}}}^{n}\right]_{ijk} - \left[\overline{\boldsymbol{\beta}}^{n}\right]_{pjk}\left[\mathbf{W}\right]_{ip} - \left[\overline{\boldsymbol{\beta}}^{n}\right]_{ipk}\left[\mathbf{W}\right]_{jp} - \left[\overline{\boldsymbol{\beta}}^{n}\right]_{ijp}\left[\mathbf{W}\right]_{kp}\end{aligned} \tag{6.1}$$

where indicial notation is used to better represent the third order tensor operations and $\mathbf{W}$ is the rotation tensor. An elastic-plastic decomposition is given by:

$$\begin{aligned}\left(\mathbf{L}^{n} - \mathbf{L}\right) &= \left(\mathbf{L}^{n} - \mathbf{L}\right)^{e} + \left(\mathbf{L}^{n} - \mathbf{L}\right)^{p} \\ \left(\mathbf{L}^{n}\overset{\leftarrow}{\nabla}\right) &= \left(\mathbf{L}^{n}\overset{\leftarrow}{\nabla}\right)^{e} + \left(\mathbf{L}^{n}\overset{\leftarrow}{\nabla}\right)^{p}\end{aligned} \tag{6.2}$$

The elastic constitutive relations at each scale are given by:

$$\begin{aligned}\overset{\nabla}{\boldsymbol{\beta}}^{n} &= \mathbb{C}^{n} \bullet \left(\mathbf{L}^{n} - \mathbf{L}\right)^{e} \\ \overset{\nabla}{\overline{\boldsymbol{\beta}}}^{n} &= \overline{\mathbb{C}}^{n} \bullet \left(\mathbf{L}^{n}\overset{\leftarrow}{\nabla}\right)^{e}\end{aligned} \tag{6.3}$$

where $\mathbb{C}^{n}$ and $\overline{\mathbb{C}}^{n}$ are the elastic matrices (we assume these are isotropic here) at the *nth* scale. Note that $\overline{\mathbb{C}}^{n}$ contains an embedded length scale and the elastic update at each scale is assumed to be independent of the others i.e. no scale coupling exists in the elastic regime.

6.1.2 Flow Rule

The plastic part of the microscale constitutive relations are based on a set of flow rules; one for each microstress and higher order microstress:

$$\left(\mathbf{L}^n - \mathbf{L}\right)^p = \dot{\lambda}^n \frac{\partial \varphi^n}{\partial \boldsymbol{\beta}^n}$$
$$\left(\mathbf{L}^n \overleftarrow{\nabla}\right)^p = \dot{\overline{\lambda}}^n \frac{\partial \overline{\varphi}^n}{\partial \overline{\boldsymbol{\beta}}^n} \tag{6.4}$$

Although microstress and deformation measures are being used, this expression is completely analogous to conventional associative plasticity models found in (Belytschko et al. 2000) for example. The same consistency conditions apply i.e. the microstresses must stay on their yield surfaces:

$$\varphi^n = 0, \quad \dot{\varphi}^n = 0$$
$$\overline{\varphi}^n = 0, \quad \dot{\overline{\varphi}}^n = 0 \tag{6.5}$$

The form of the microscale plastic potentials φ^n and $\overline{\varphi}^n$ is generally problem specific. In the problems of interest in this thesis, the microscale behavior is generally dominated by deviatoric plastic flow. Hence simple Mises type yield surfaces are used to describe the post yield behavior of the microstresses:

$$\varphi^n = \left(\frac{\beta^n}{\beta_y^n}\right)^2 - 1 = 0$$
$$\overline{\varphi}^n = \left(\frac{\overline{\beta}^n}{\overline{\beta}_y^n}\right)^2 - 1 = 0 \tag{6.6}$$

where β^n and $\overline{\beta}^n$ are equivalent scalar measures of the microstress $\boldsymbol{\beta}^n$ and microstress couple $\overline{\boldsymbol{\beta}}^n$ respectively. The functions β_y^n and $\overline{\beta}_y^n$ are isotropic hardening functions which describe the contraction or expansion of the microstress yield surfaces.

6.2 Calibrating Microscale Constitutive Relations to RVE Simulations

A method for determining the microscale elastic constants is discussed in Section 6.2.1. A general approach is then outlined for determining the microstress hardening functions β_y^n and $\bar{\beta}_y^n$, equation (6.6), from computational RVE model simulations in Section 6.2.2.

6.2.1 Elastic Constants

It is assumed that the local inhomogeneous velocity gradient $\left(\mathbf{L}_m - \mathbf{L}\right)$ is related to the local microstress $\boldsymbol{\beta}_m$ within the RVE by:

$$\dot{\boldsymbol{\beta}}_m = \mathbf{C}_m : \left(\mathbf{L}_m - \mathbf{L}\right)^e \tag{6.7}$$

where $\mathbf{C}_m$ is a local inhomogeneous elastic tensor in the microstructure. Substituting this into the microstress averaging equations (5.18) the elastic constants $\mathbb{C}^n$ and $\bar{\mathbb{C}}^n$ are given by:

$$\mathbb{C}^n = \frac{1}{V_n}\int_{V_n} \mathbf{C}_m dV \tag{6.8}$$

and

$$\mathbb{C}^n = \frac{1}{V_n}\int_{V_n} \mathbf{C}_m \otimes \mathbf{y} \otimes \mathbf{y} dV \tag{6.9}$$

Note that the averaging operation for $\bar{\mathbb{C}}^n$ incorporates a length scale related to the size of the averaging volume V_n. For reference, assuming the local inhomogeneous elastic tensor $\mathbf{C}_m$ is constant within the 2D area V_n, the elastic constants become:

$$\mathbb{C}^n = \mathbf{C}_m$$
$$\overline{\mathbb{C}}^n = \frac{\left(l^n\right)^2}{12}\,\mathbf{C}_m \otimes \mathbf{I} \tag{6.10}$$

where $\mathbf{I}$ is the identity tensor and l^n is the length of one side of the averaging volume V_n. This explicitly shows that a length scale parameter l^n is embedded in the model through the elastic part of the microstress constitutive relationship.

6.2.2 Plastic Constants

The goal here is to illustrate a method for finding the microstress hardening functions β_y^n and $\overline{\beta}_y^n$. These microstress hardening functions describe how the equivalent microstresses β^n and $\overline{\beta}^n$ evolve, equation (6.6). Motivated by the power equivalence equation (5.14) a local *plastic* work rate equivalence relationship is defined as:

$$\boldsymbol{\beta}_m : \left(\mathbf{D}_m^p - \mathbf{D}^p\right) = \boldsymbol{\sigma}_m : \mathbf{D}_m^p - \boldsymbol{\sigma} : \mathbf{D}^p \tag{6.11}$$

where $\mathbf{D}_m^p$ is the local plastic rate of deformation within the microstructure (RVE) and $\mathbf{D}^p$ is the average plastic rate of deformation at the RVE (macro) scale. The concept of equivalence of plastic work rate (Belytschko et al. 2000) is now used to rewrite the inhomogeneous plastic work expression in terms of scalar equivalent measures. The left hand side of this expression is first rewritten in terms of an equivalent local microstress β_m and local strain rate $\dot{\Sigma}_m^p$:

$$\boldsymbol{\beta}_m : \left(\mathbf{D}_m^p - \mathbf{D}^p\right) = \beta_m \dot{\Sigma}_m^p \tag{6.12}$$

where

$$\beta_m = \sqrt{\frac{3}{2}\boldsymbol{\beta}_m^{dev} : \boldsymbol{\beta}_m^{dev}}$$
$$\dot{\Sigma}_m^p = \sqrt{\frac{2}{3}\left(\mathbf{D}_m^p - \mathbf{D}^p\right) : \left(\mathbf{D}_m^p - \mathbf{D}^p\right)} \tag{6.13}$$

and $\boldsymbol{\beta}_m^{dev}$ is the deviatoric part of the local microstress $\boldsymbol{\beta}_m^{dev}$. Equation (6.11) can now be rewritten using the equivalent scalar description given by equation (6.12):

$$\beta_m = \frac{\boldsymbol{\sigma}_m : \mathbf{D}_m^p - \boldsymbol{\sigma} : \mathbf{D}^p}{\dot{\Sigma}_m^p} \tag{6.14}$$

This is a computable expression for the local equivalent microstress field β_m within the microstructure. The equivalent microstresses at scale n are simply volume averages of the local equivalent microstress field β_m over V_n:

$$\beta^n = \frac{1}{V_n}\int_{V_n} \beta_m \, dV$$
$$\bar{\beta}^n = \left\| \left(\frac{1}{V_n}\int_{V_n} \beta_m \mathbf{y} dV \right) \right\| \tag{6.15}$$

where $\| \ \|$ is the magnitude of a vector and the local coordinate relative to the center of the averaging volume V_n is given by $\mathbf{y}$. The equivalent inhomogeneous strain Σ^n and strain gradient $\bar{\Sigma}^n$ are similarly given by:

$$\Sigma^n = \frac{1}{V_n}\int_{V_n} \Sigma_m^p \, dV$$
$$\bar{\Sigma}^n = \frac{1}{V_n}\int_{V_n} \sqrt{\left(\nabla_{y_1}\Sigma_m^p\right)^2 + \left(\nabla_{y_2}\Sigma_m^p\right)^2} dV \tag{6.16}$$

where ∇_{y_1} and ∇_{y_2} are the gradients in the y_1 and y_2 directions respectively.

A length scale parameter l^n does not explicitly appear in equation (6.15), as it does in the elastic relation, equation (6.10). However the microstress couple $\bar{\beta}^n$ is still a function of scale as the moment arm $\mathbf{y}$ appears in equation (6.15); this ensures that a scale effect is present even during the plastic stage of the microstress constitutive response.

The microstress hardening functions, $\beta_y^n\left(\Sigma^n\right)$ and $\bar{\beta}_y^n\left(\bar{\Sigma}^n\right)$, used in the microstress yield surfaces, equations (6.6), are calibrated to the microstress relationships $\beta^n\left(\Sigma^n\right)$ and $\bar{\beta}^n\left(\bar{\Sigma}^n\right)$, equations (6.15) and (6.16). The steps outlined in equations (6.14)-(6.16) are illustrated schematically in (Figure 6.1).

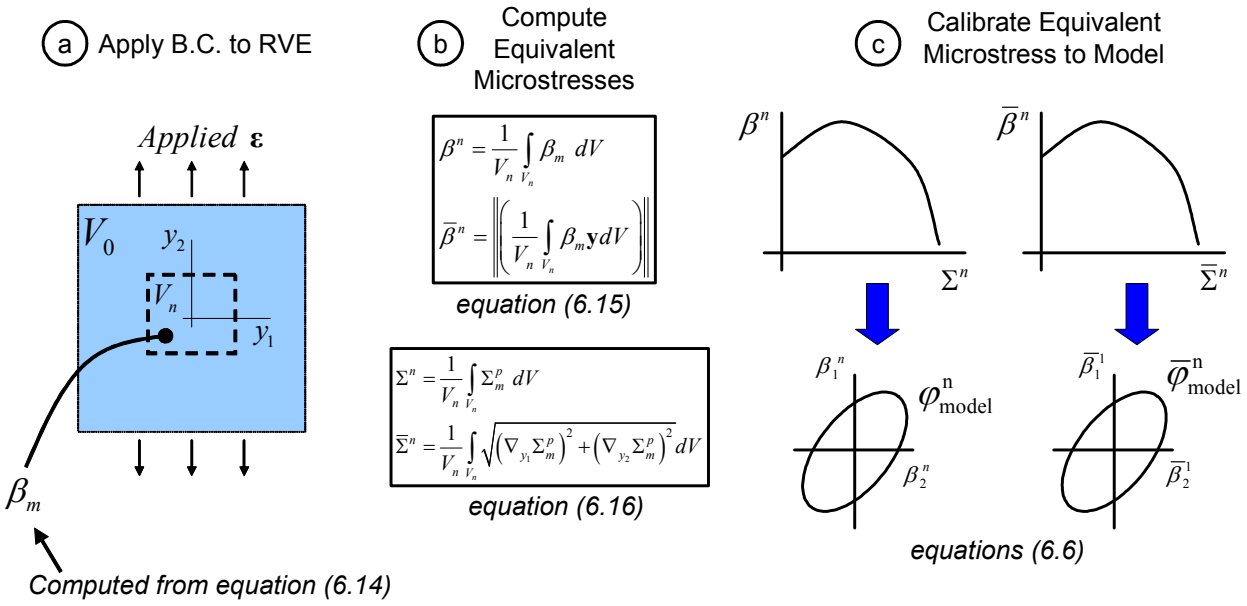

Figure 6.1. Method to calibrate microstress constitutive models to computational RVE models

The location of the averaging volume V_n within the RVE is determined by the location of the inhomogeneous deformation occurring at scale n. This is usually obvious from strain contours particularly in materials where severe localization occurs between microstructural features e.g. strain localization between neighboring voids. The size of the averaging volume is chosen such that the strain varies approximately linearly within the averaging volume; this is consistent with the approximation made about the local deformation in equation (5.15). The averaging volume V_n is then superimposed onto the RVE as shown in (Figure 6.1) and the averaging operation described by equations (6.15) and (6.16) can be performed.

The macroscale and microscale constitutive model development is summarized in tables 6.1 and 6.2.

Averaging Operation	**Scalar Measure**	**Constitutive Model**
$\boldsymbol{\sigma} = \frac{1}{V_0}\int_{V_0} \boldsymbol{\sigma}_m dV$	$\sigma = \sqrt{\frac{3}{2}\boldsymbol{\sigma}^{dev} : \boldsymbol{\sigma}^{dev}}$	φ_{model}
$\mathbf{D}^p = \frac{1}{V_0}\int_{V_0} \mathbf{D}_m^p dV$	$\varepsilon^p = \int_t \left(\sqrt{\frac{2}{3}\mathbf{D}^p : \mathbf{D}^p} \right) dt$	

Table 6.1 Macroscale averaging equations (3.4) and (3.5) used to determine average stress and strain within an RVE microstructure for the purposes of developing a constitutive model

Scalar Measure	Averaging Operation	Constitutive Model
$\beta_m = \dfrac{\boldsymbol{\sigma}_m : \mathbf{D}_m^p - \boldsymbol{\sigma} : \mathbf{D}^p}{\dot{\Sigma}_m^p}$	$\beta^n = \dfrac{1}{V_n}\int_{V_n} \beta_m \, dV$	$\varphi^{\mathrm{n}}_{\mathrm{model}}$
$\dot{\Sigma}_m^p = \sqrt{\dfrac{2}{3}\left(\mathbf{D}_m^p - \mathbf{D}^p\right) : \left(\mathbf{D}_m^p - \mathbf{D}^p\right)}$	$\Sigma^n = \dfrac{1}{V_n}\int_{V_n} \Sigma_m^p \, dV$	
$\beta_m = \dfrac{\boldsymbol{\sigma}_m : \mathbf{D}_m^p - \boldsymbol{\sigma} : \mathbf{D}^p}{\dot{\Sigma}_m^p}$	$\overline{\beta}^n = \left\| \left(\dfrac{1}{V_n}\int_{V_n} \beta_m \mathbf{y} dV \right) \right\|$	$\overline{\varphi}^{\mathrm{n}}_{\mathrm{model}}$
$\dot{\Sigma}_m^p = \sqrt{\dfrac{2}{3}\left(\mathbf{D}_m^p - \mathbf{D}^p\right) : \left(\mathbf{D}_m^p - \mathbf{D}^p\right)}$	$\overline{\Sigma}^n = \dfrac{1}{V_n}\int_{V_n} \sqrt{\left(\nabla_{y_1} \Sigma_m^p\right)^2 + \left(\nabla_{y_2} \Sigma_m^p\right)^2} dV$	

Table 6.2 Local and average inhomogeneous stress and strain measures used to develop a microscale constitutive model.

6.3 Physical Material Systems

Two material systems are now chosen to illustrate how macro and microscale constitutive relationships can be extracted through computational cell modeling; a porous alloy and an alloy with two populations of embedded particles.

6.3.1 Voided Alloy: A Conventional Homogenization Approach

Consider an elasto-plastic body containing a periodic arrangement of pre-existing voids. The representative volume element (RVE) consists of a single void in an elasto-plastic matrix as shown in (Figure 6.2). Displacement boundary conditions are applied to the left and right sides of the RVE to strain it in the direction shown in (Figure 6.2) by 15%. Lateral contraction is constrained to zero, resulting in quite substantial triaxiality and void growth. As the void grows, plastic deformation within the matrix localizes at the scale of the void (contour of true plastic strain in the loading direction is shown). The true plastic strain in the loading direction is plotted across a section of the RVE to highlight this naturally arising physical length scale, l, which is on the order of the void size. The average constitutive response $\sigma\left(\varepsilon^p\right)$ is plotted using the RVE averaging operation defined in equations (3.4) and (3.5).

This average constitutive response, shown in (Figure 6.2), is used to define the flow stress $\sigma_y\left(\varepsilon^p\right)$ in a J2 flow plasticity model, as a series of data points. The softening J2 plasticity model is now used within a finite element analysis to model the behavior of a homogenized continuum, shown on the right in (Figure 6.2). The same boundary conditions are applied. The

conventional governing equations (1.5) are solved using a finite element approach. The governing equations and constitutive relations are summarized as:

$$\begin{aligned} &\nabla \bullet \boldsymbol{\sigma} = 0 \quad \text{in} \quad \Omega \\ &\mathbf{u} = \bar{\mathbf{u}} \quad \text{on} \quad \Gamma_u \end{aligned} \tag{6.17}$$

and

$$\begin{aligned} &\boldsymbol{\sigma}^{\nabla} = \mathbf{C} \bullet \mathbf{D}^e \\ &\varphi_{J2=} \left(\frac{\sigma}{\sigma_y \left(\varepsilon^p \right)} \right)^2 - 1 = 0 \end{aligned} \tag{6.18}$$

where $\mathbf{C}$ is an elastic isotropic tensor with Young's Modulus $E = 200GPa$ and Poisson's ration $\nu = 0.31$. The J2 flow rule is written in terms of the Mises stress σ and the hardening relation $\sigma_y \left(\varepsilon^p \right)$ given by the curve in (Figure 6.2). As shown, the inhomogeneous deformation (contour of true plastic strain in the loading direction is shown) localizes in a mesh dependent manner once the material begins to soften. The inhomogeneous deformation which occurs in the actual microstructure is not replicated.

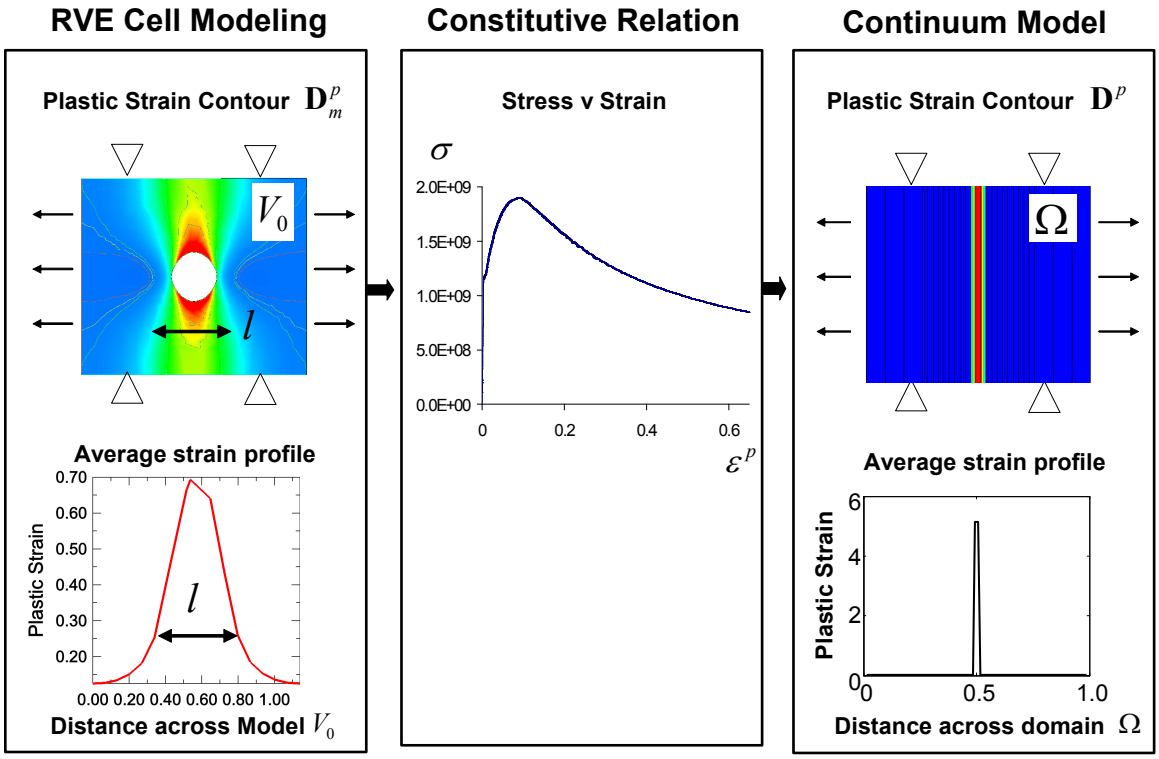

Figure 6.2. Effective plastic strain is plotted in the RVE and in the homogenized continuum model. A simple voided alloy has a natural characteristic length scale of inhomogeneous deformation i.e. the void size.

6.3.2 Voided Alloy: A Multiresolution Homogenization Approach

The multiresolution approach described in Chapter 5 is now used to model the porous material. The local microstress field β_m is plotted in the voided RVE in the left side of (Figure 6.3) using equation (6.14). The equivalent local inhomogeneous strain Σ_m^p is plotted using equation (6.13).

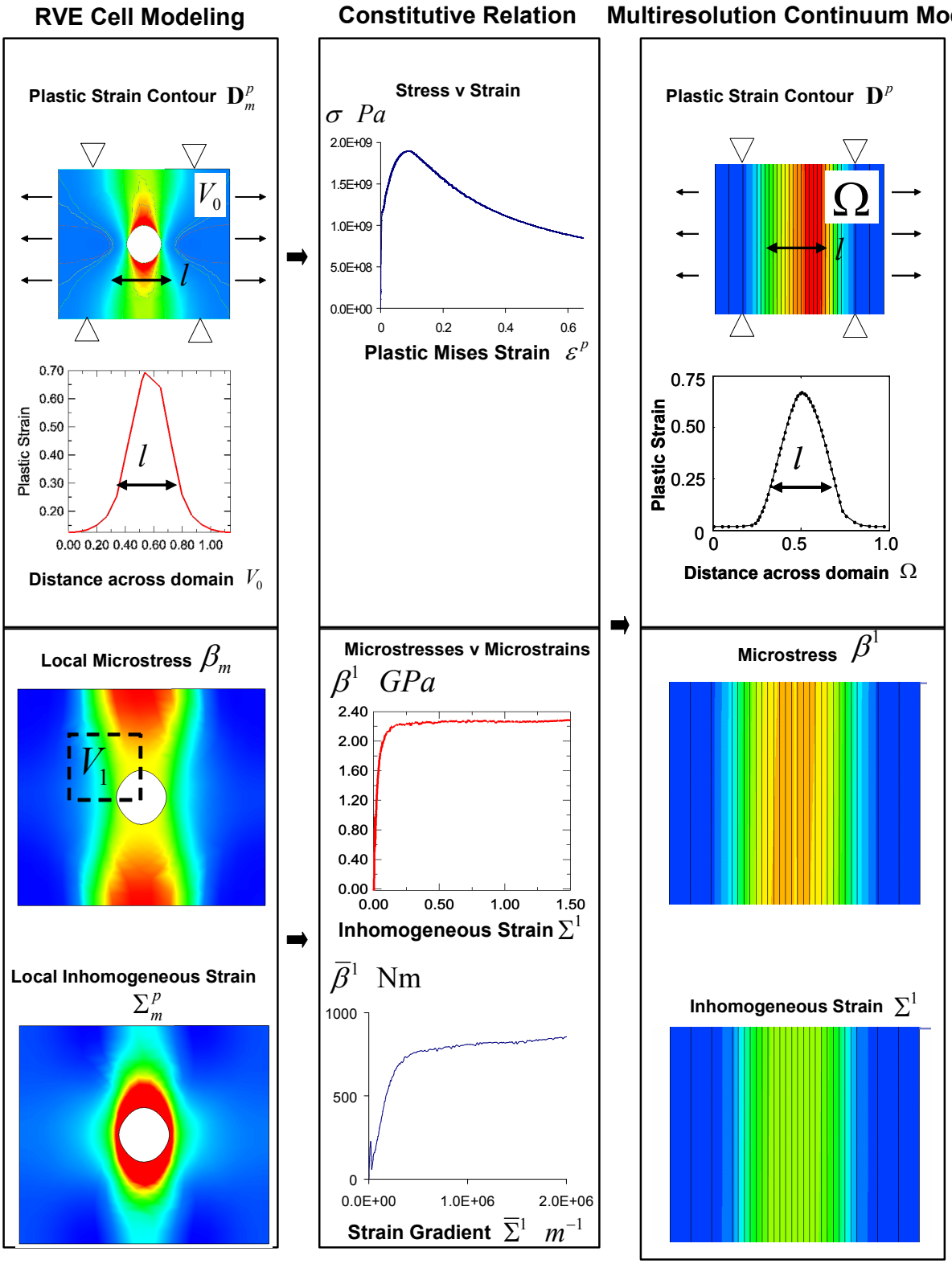

Figure 6.3. The multiresolution approach is used to embed the void length scale in the continuum model. Distances are in microns.

The averaging equations (6.15) and (6.16) are then employed to compute the microstress constitutive relationships $\beta^1\left(\Sigma^1\right)$ and $\overline{\beta}^1\left(\overline{\Sigma}^1\right)$ at the scale of the inhomogeneous deformation V_1, indicated in (Figure 6.3). As the inhomogeneous deformation increases, the alloy matrix hardens and the resistance to inhomogeneous deformation increases. This manifests as a hardening effect in the microstress response $\beta^1\left(\Sigma^1\right)$ and $\overline{\beta}^1\left(\overline{\Sigma}^1\right)$. These microstress relationships are plotted in (Figure 6.3).

The multiresolution governing equations (5.25) involve a single microstress i.e. $N=1$ i.e.:

$$\begin{aligned}&\left(\boldsymbol{\sigma}-\boldsymbol{\beta}^1\right)\bullet\nabla=0 \quad \text{in} \quad \Omega\\&\nabla\bullet\overline{\boldsymbol{\beta}}^1-\boldsymbol{\beta}^1=0 \quad \text{in} \quad \Omega\end{aligned} \tag{6.19}$$

The macroscale constitutive relation is the same as in equation (6.18):

$$\begin{aligned}&\boldsymbol{\sigma}^{\nabla}=\mathbf{C}\bullet\mathbf{D}^e\\&\varphi_{J2=}\left(\frac{\sigma}{\sigma_y\left(\varepsilon^p\right)}\right)^2-1=0\end{aligned} \tag{6.20}$$

The elastic microstress relation is given by equation (6.3):

$$\begin{aligned}&\overset{\nabla}{\boldsymbol{\beta}}^1=\mathbb{C}^1\bullet\left(\mathbf{L}^1-\mathbf{L}\right)^e\\&\overset{\nabla}{\overline{\boldsymbol{\beta}}}^1=\overline{\mathbb{C}}^1\bullet\left(\mathbf{L}^1\overline{\nabla}\right)^e\end{aligned} \tag{6.21}$$

where $\mathbb{C}^1$ and $\overline{\mathbb{C}}^1$ are given by equation (6.10):

$$\begin{aligned}&\mathbb{C}^1=\mathbf{C}_m\\&\overline{\mathbb{C}}^1=\frac{\left(l^1\right)^2}{12}\,\mathbf{C}_m\otimes\mathbf{I}\end{aligned} \tag{6.22}$$

with a length parameter $l^1 = 200nm$ (the void size) and $\mathbf{C}_m = \mathbf{C}$. The plastic microstress constitutive relationship is given by equation (6.6):

$$\varphi^1 = \left(\frac{\beta^1}{\beta_y^1\left(\Sigma^1\right)} \right)^2 - 1 = 0$$
$$\bar{\varphi}^1 = \left(\frac{\bar{\beta}^1}{\bar{\beta}_y^1\left(\bar{\Sigma}^1\right)} \right)^2 - 1 = 0 \qquad (6.23)$$

where $\beta_y^1\left(\Sigma^1\right)$ and $\bar{\beta}_y^1\left(\bar{\Sigma}^1\right)$ are given by the curves in (Figure 6.3).

The same displacement boundary conditions are applied as before i.e. constrained in the lateral direction and stretched by 15% in the loading direction. The multiresolution solution is shown on the right in (Figure 6.3). The characteristic length scale and magnitude of inhomogeneous deformation are both predicted but with much fewer degrees of freedom then in the RVE, where the void has been modeled directly. The length scales of the microstress β^1 and inhomogeneous strain Σ^1 (bottom right contour plots (Figure 6.3)) are comparable to the local microstress β_m and local inhomogeneous strain Σ_m^p within the microstructure (RVE) (bottom left contour plots (Figure 6.3)).

6.3.3 Alloy with Two Populations of Embedded Particles

A more complex problem is now illustrated in which inhomogeneous deformation occurs at two distinct scales. The material consists of an alloy matrix with embedded primary inclusions of 1 micron diameter and secondary precipitate particles with diameter 200 nanometers. The micromechanics of this system are described in more detail in Section 2.2.

A simple model is constructed which captures the key physics within the RVE. Two primary inclusions are modeled along with several secondary precipitates in the region between the inclusions. The precipitates are modeled only where they are known to debond, between the weakly bonded inclusions, creating a clear pre-defined failure path while still capturing the failure mechanism. Periodic displacement boundary conditions are applied (Appendix A1) to induce an average shear strain of 50%. The average stress and strain are computed via equations (3.4) and (3.5). The average Mises stress- plastic Mises strain curve is plotted in (Figure 6.4).

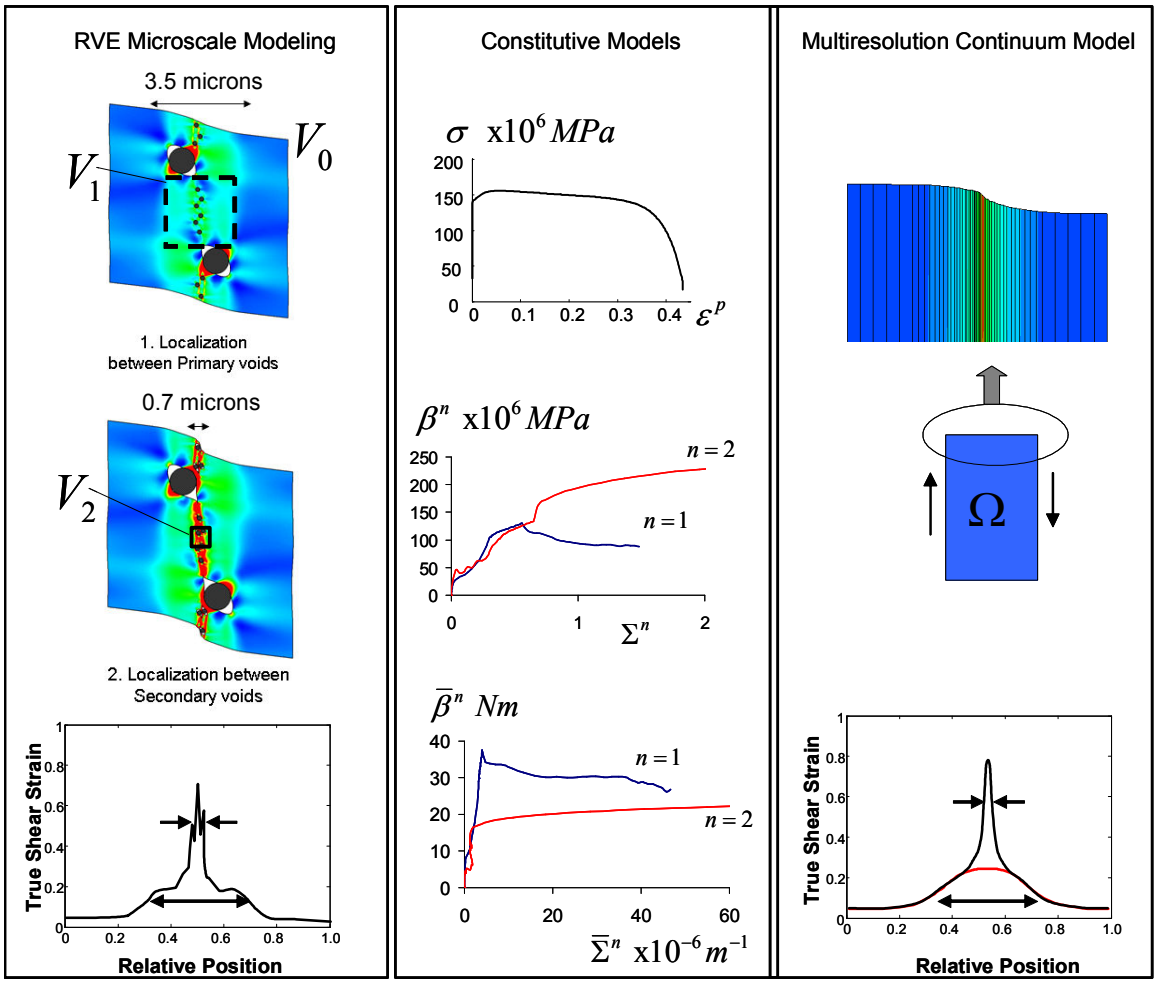

Figure 6.4. The multiresolution model is used to embed two characteristic length scales of inhomogeneous deformation related to the embedded particles.

The two characteristic length scales of inhomogeneous deformation can be observed by plotting the plastic shear strain across the RVE as shown in the bottom left corner of (Figure 6.4). The averaging equations (6.15) and (6.16) are again used to compute the microstress constitutive relationships $\beta^1\left(\Sigma^1\right)$ and $\bar{\beta}^1\left(\bar{\Sigma}^1\right)$ at the first scale of inhomogeneous deformation V_1 and the relationships $\beta^2\left(\Sigma^2\right)$ and $\bar{\beta}^2\left(\bar{\Sigma}^2\right)$ at the second scale of inhomogeneous deformation V_2. These

averaging volumes are shown in (Figure 6.4). The link between these microstress curves and the evolving microstructure is summarized as follows:

- The large primary inclusions debond at an applied strain of $\varepsilon^p = 0.05$ (*First Microstructure Instability Event*) and the deformation localizes at scale V_1. The microstress β^1 increases as the alloy matrix within V_1 work hardens.
- The secondary precipitates debond at an applied strain of $\varepsilon^p = 0.35$ (*Second Microstructure Instability Event*) and the microstress β^1 begins to degrade.
- Deformation localizes between the secondary precipitates at scale V_2. The microstress β^2 grows as the alloy matrix within V_2 work hardens.

The system is now modeled using a multiresolution approach; two microstresses are used in the governing equations (5.25):

$$\begin{aligned} \left(\boldsymbol{\sigma} - \boldsymbol{\beta}^1 - \boldsymbol{\beta}^2\right) \bullet \nabla = 0 \quad & \text{in} \quad \Omega \\ \nabla \bullet \overline{\boldsymbol{\beta}}^1 - \boldsymbol{\beta}^1 = \quad & \text{in} \quad \Omega \\ \nabla \bullet \overline{\boldsymbol{\beta}}^2 - \boldsymbol{\beta}^2 = \quad & \text{in} \quad \Omega \end{aligned} \tag{6.24}$$

The macroscale constitutive relation is the same as in equation (6.18):

$$\begin{aligned} \boldsymbol{\sigma}^{\nabla} &= \mathbf{C} \bullet \mathbf{D}^e \\ \varphi_{J2=} \left(\frac{\sigma}{\sigma_y\left(\varepsilon^p\right)} \right)^2 - 1 &= 0 \end{aligned} \tag{6.25}$$

where $\mathbf{C}$ is an elastic isotropic tensor with Young's Modulus $E = 200GPa$ and Poisson's ration $\nu = 0.31$. The hardening function $\sigma_y\left(\varepsilon^p\right)$ is given by the macroscale stress-strain curve in (Figure 6.4).

The elastic microstress relations are given by equation (6.3):

$$\begin{aligned}
\overset{\nabla}{\boldsymbol{\beta}}^1 &= \mathbb{C}^1 \bullet \left(\mathbf{L}^1 - \mathbf{L} \right)^e \\
\overset{\nabla}{\overline{\boldsymbol{\beta}}}^1 &= \overline{\mathbb{C}}^1 \bullet \left(\mathbf{L}^1 \overset{\leftarrow}{\nabla} \right)^e \\
\overset{\nabla}{\boldsymbol{\beta}}^2 &= \mathbb{C}^2 \bullet \left(\mathbf{L}^2 - \mathbf{L} \right)^e \\
\overset{\nabla}{\overline{\boldsymbol{\beta}}}^2 &= \overline{\mathbb{C}}^2 \bullet \left(\mathbf{L}^2 \overset{\leftarrow}{\nabla} \right)^e
\end{aligned} \tag{6.26}$$

where $\mathbb{C}^1, \mathbb{C}^2$ and $\overline{\mathbb{C}}^1, \overline{\mathbb{C}}^2$ are given by equation (6.10):

$$\begin{aligned}
\mathbb{C}^1, \mathbb{C}^2 &= \mathbf{C}_m \\
\overline{\mathbb{C}}^1 &= \frac{\left(l^1 \right)^2}{12} \mathbf{C}_m \otimes \mathbf{I} \\
\overline{\mathbb{C}}^2 &= \frac{\left(l^2 \right)^2}{12} \mathbf{C}_m \otimes \mathbf{I}
\end{aligned} \tag{6.27}$$

with length parameters $l^1 = 1 \mu m$ (the primary inclusion size), $l^1 = 200 nm$ (the secondary precipitate size) and $\mathbf{C}_m = \mathbf{C}$. The plastic microstress constitutive relationships are given by equation (6.6):

$$\begin{aligned}
\varphi^n &= \left(\frac{\beta^n}{\beta_y^n \left(\Sigma^n \right)} \right)^2 - 1 = 0 \qquad n = 1, 2 \\
\overline{\varphi}^n &= \left(\frac{\overline{\beta}^n}{\overline{\beta}_y^n \left(\overline{\Sigma}^n \right)} \right)^2 - 1 = 0 \qquad n = 1, 2
\end{aligned} \tag{6.28}$$

The microstress hardening functions $\beta_y^1 \left(\Sigma^1 \right), \beta_y^2 \left(\Sigma^2 \right)$ and $\overline{\beta}_y^1 \left(\overline{\Sigma}^1 \right), \overline{\beta}_y^2 \left(\overline{\Sigma}^2 \right)$ are calibrated to the microstress curves in (Figure 6.3).

The resulting multiresolution solution is shown on the right in (Figure 6.4). The two characteristic length scales of inhomogeneous deformation observed in the alloy RVE are replicated but with much fewer degrees of freedom. The first set of microstresses $\beta^1\left(\Sigma^1\right)$ and $\overline{\beta}^1\left(\overline{\Sigma}^1\right)$ regularize the solution at the scale of the primary inclusions. At a nominal strain of ~35% the secondary precipitates debond the these microstresses degrade. The second set of microstresses $\beta^2\left(\Sigma^2\right)$ and $\overline{\beta}^2\left(\overline{\Sigma}^2\right)$ then take over, regularizing the solution at the scale of the secondary precipitates.

7 Multiresolution WC-Co Composite Model

A hierarchical constitutive model for a WC-Co composite has been developed in Chapter 4. This constitutive model was used in a conventional continuum based numerical fracture toughness simulation in Section 4.5. In the current chapter fracture toughness predictions are again performed for a WC-Co composite. However the fracture simulations performed here use a multiresolution continuum (MRCT) analysis developed in Chapter 5. The same WC-Co composite constitutive relationship developed in Chapter 4 is employed at the macroscale. The extra microstress constitutive relationships required in the multiresolution analysis are developed here based on the approach outlined previously in Chapter 6.

An idealized RVE of the WC-Co microstructure is proposed in Section 7.1 and discussed in Section 7.2. The proposed RVE is then used to compute the microstress constitutive relationships in Section 7.3. Finally the multiresolution approach developed in Chapter 5 is used as the basis for numerical fracture toughness simulations (of WC-Co) in Section 7.4. A parametric study is performed to gauge the effect of the microstructural parameters on the fracture toughness. The multiresolution fracture toughness simulation results are compared to the conventional continuum results.

7.1 Idealized RVE Model for WC-Co

An idealized 2D plane strain model of the WC-Co microstructure is now presented for the purposes of determining the microscale constitutive relations, based on the approach outlined in Chapter 6. This model, shown in (Figure 7.1), captures the micromechanics which control the

strength and fracture toughness of a WC-Co composite, while remaining simple enough for efficient computation of the microstresses.

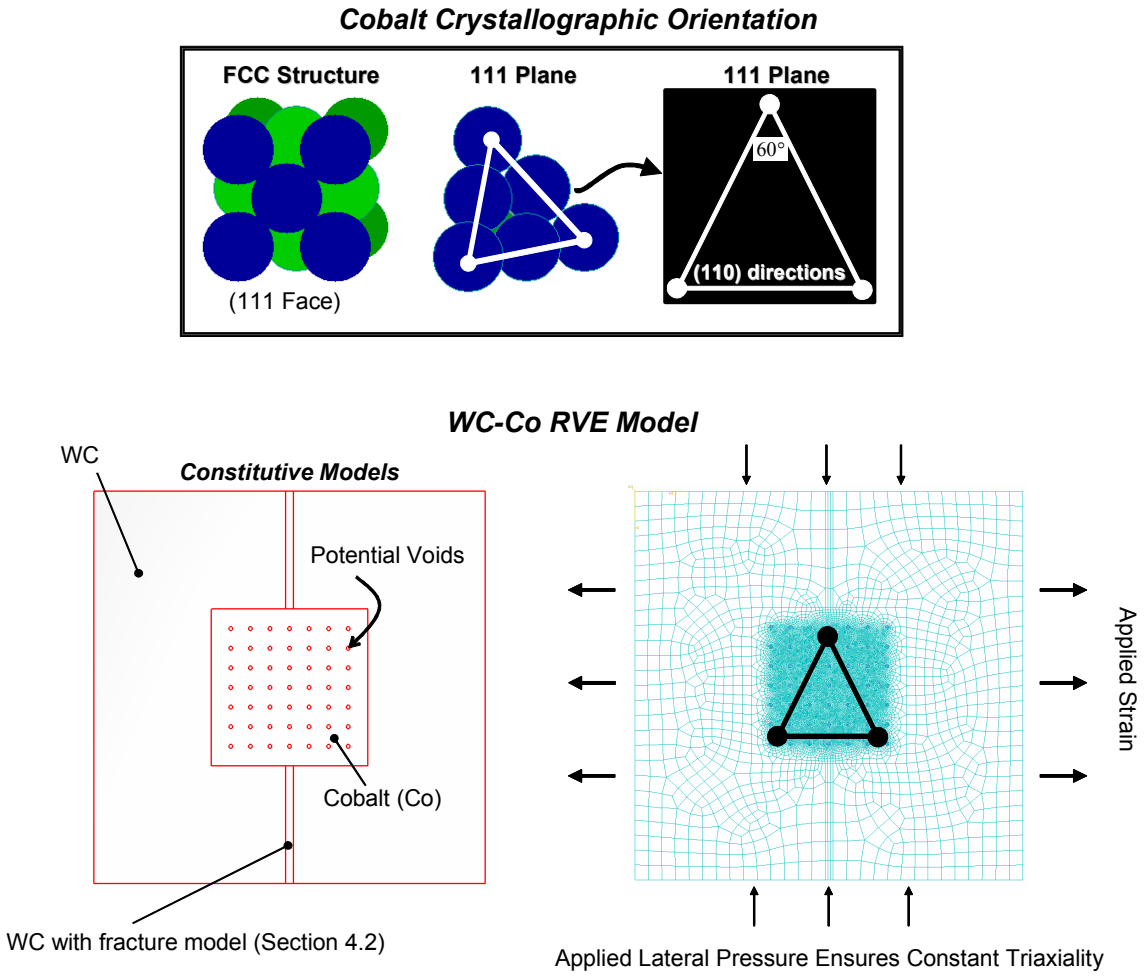

Figure 7.1. The simplified RVE for WC-Co. Crystal plasticity is used to represent the cobalt. A population of potential voids is modeled. The carbide fractures along a predefined path.

A similar model has been used previously to model ductile reinforced brittle composites by (McHugh and Connolly 2003; Spiegler and Fischmeister 1992). In the proposed RVE model the cobalt binder is modeled as a square alloy pool of side 800nm enclosed by two tungsten carbide grains; the length of one side of the RVE is 2 microns. The cobalt binder is modeled using a

single crystal plasticity formulation which has been described previously in Chapter 3 and also used in Chapter 4, Section 4.1 to perform void growth numerical experiments.

Carbide Grains

The carbide grains are modeled using the tungsten carbide constitutive model developed in Section 4.2; this is a simple linear elastic model with fracture. However carbide fracture is modeled only in the grain boundary elements as shown in (Figure 7.1). This predefines the brittle fracture path through the carbide region. A total of 19816 finite elements are used to mesh the RVE; most of these elements are concentrated in the cobalt region where the interesting inhomogeneous deformation occurs.

Microvoid Nucleation

Nucleation of microvoids in the cobalt pool (Figure 7.1) plays an important role in composite failure, as described in Section 2.1.4; microvoid nucleation is modeled in a simplified manner in the RVE. Within the cobalt, a pre-defined set of circular element groups (Figure 7.1) are given the following property: when any element in a particular group reaches the mean strain for void nucleation $\varepsilon_{\mathcal{N}}$, equation (4.3), stress is set to zero in all of the elements in that group, instantly creating a stress free void. This allows void nucleation to be modeled without explicitly creating a new void surface and by-passes complex remeshing. These element groups are called 'potential voids' here and are labeled as such in (Figure 7.1). Each is 20nm in diameter which is the size of a nucleated void used in Section 4.1.

Microstructure Parameters and Boundary Conditions

In the following analysis, the RVE is loaded quasi-statically using periodic displacement boundary conditions applied perpendicular to the grain boundary described above. The cobalt grain size is $d = 800nm$ and an isothermal temperature of $\vartheta = 353K$ is used. Constant triaxiality of $T = \frac{1}{3}$, is maintained by applying an evolving lateral pressure; this is explained further in Appendix A2. The volume (2D area) fraction of cobalt is $f = 0.15$. The orientation of the crystal lattice used in the crystal plasticity model is also shown in (Figure 7.1).

7.2 Description of RVE Micromechanics

The micromechanics of deformation within the proposed RVE is described here. The simplified RVE should capture the key micromechanics in the more complex WC-Co microstructure model used in Section 2.1. The plastic Mises strain in the RVE is illustrated in (Figure 7.2) at an applied nominal Mises strain of 5%. The stages in deformation which occurred to reach this strain level are described in terms of the microstructural instability events (a)-(d) as follows (see Section 5.4.3 for a discussion on 'microstructural instability events'):

- The composite initially deforms homogeneously as the carbide and cobalt phases deform elastically.
- Brittle fracture occurs in the carbide grains (a) and the cobalt pool behaves as a crack bridging ligament; the ligament stretches and work hardening occurs across the entire ligament l^1.

- The stress within the ligament saturates (b) as work hardening reduces. The deformation subsequently localizes ahead of the brittle crack tip l^2. This is consistent with the idea that work hardening acts to reduce strain gradients.
- The 'potential voids' within the most localized deformation region reach the nucleation criteria, equation (4.3) and become voids (c); deformation localizes between neighboring voids at scale l^3.
- As the voids grow they begin to rapidly coalesce (d), the cobalt alloy between the voids necks and final ductile occurs.

The Mises plastic strain is plotted along a section through the cobalt binder on the bottom right in (Figure 7.2) to illustrate the different length scales described above. This strain profile can be compared to the more complicated WC-Co model shown in (Figure 2.5). Both capture the characteristic length scales of inhomogeneous deformation, although the current model is much simpler. The average macroscale constitutive response is computed using the RVE averaging equations (3.4) and (3.5); the constitutive response and corresponding microstructural instability events are plotted in (Figure 7.3).

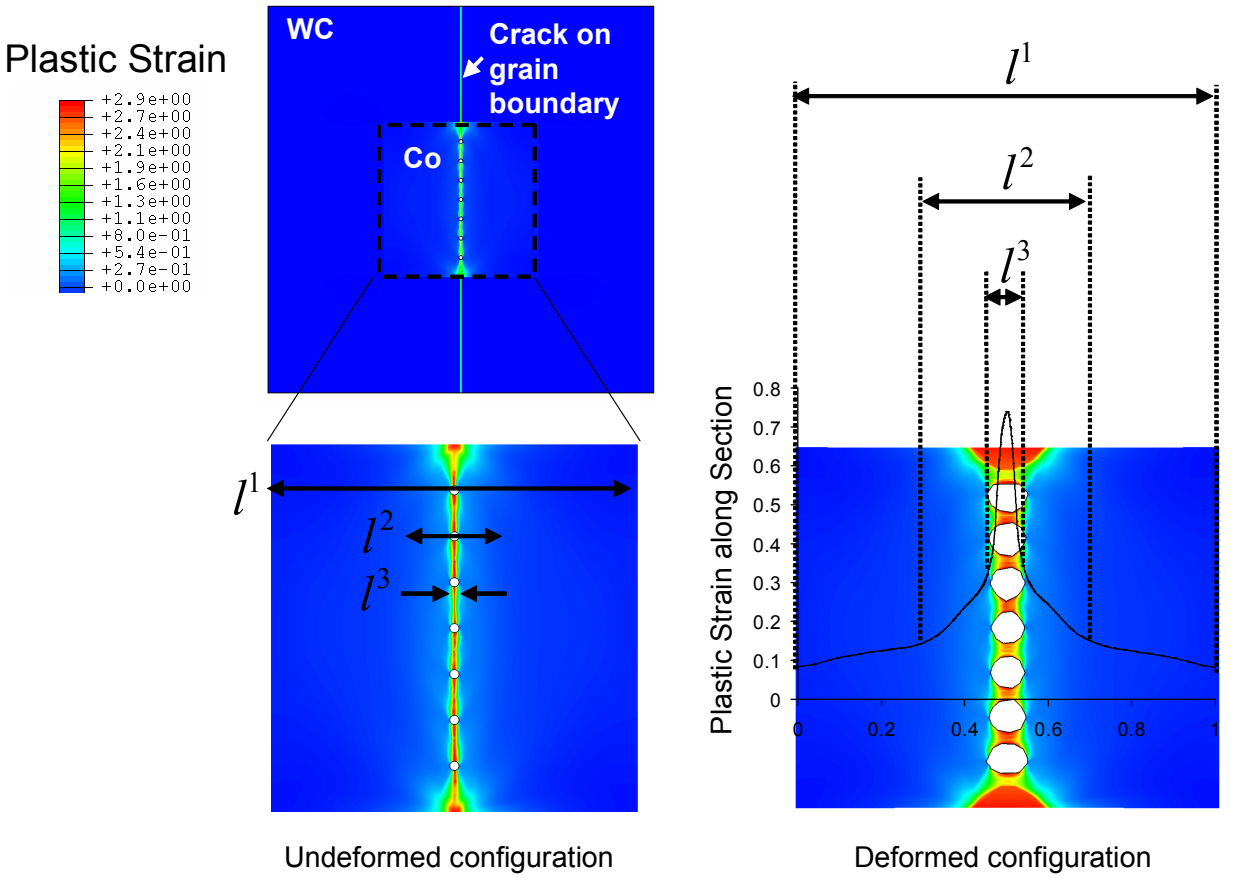

Figure 7.2. The characteristic length scales of inhomogeneous deformation in the cobalt pool, in the simplified WC-Co model. The strain profile on the bottom right can be compared to the strain profile in the more complicated model, Figure 2.5.

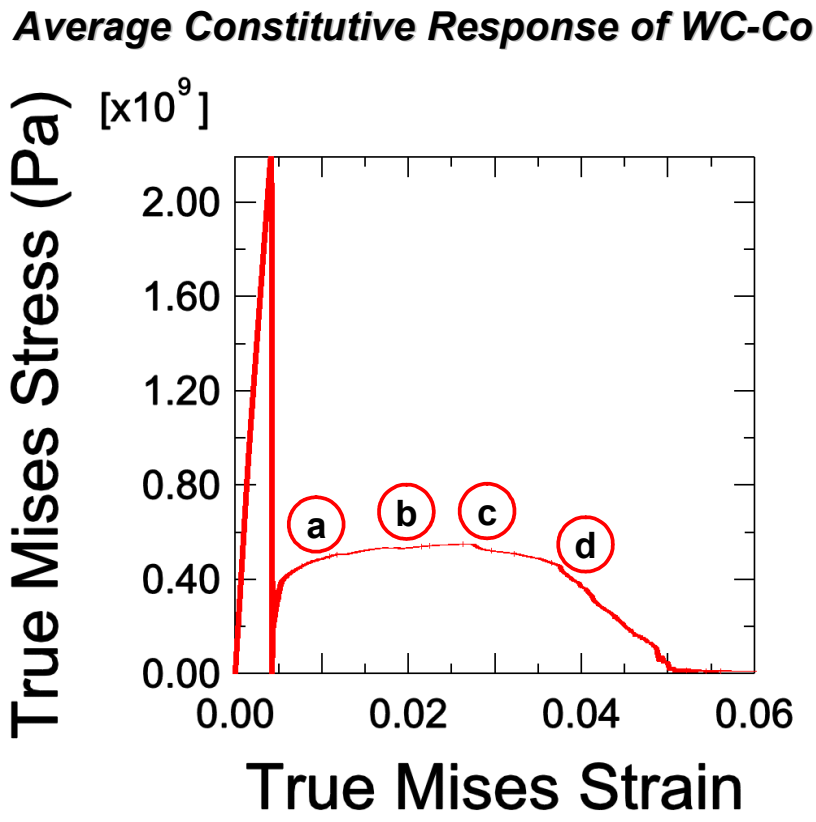

Figure 7.3. Average constitutive response of the simplified WC-Co RVE described in Section 7.1

7.3 Extracting Microstress Constitutive Relationships

The computational RVE introduced in Sections 7.1 and 7.2 is now used to compute the microstress constitutive relationships, following the approach described in Chapter 6. In particular this involves defining the

- Elastic microstress behavior i.e. the microscale elastic constants in equation (6.10). This is performed in Section 7.3.1.
- Plastic microstress behavior i.e. the microstress hardening functions at each scale β_y^n and $\bar{\beta}_y^n$ as described in equation (6.6). These functions are calibrated to the equivalent

microstresses β^n and $\overline{\beta}^n$ (computed in the RVE) in Section 7.3.2. The interaction between the microstresses β^n and $\overline{\beta}^n$ and microstructural instability events is discussed in Section 7.3.3. This interaction is built into the microstress hardening functions in Section 7.3.4.

7.3.1 Elastic Regime: Microstress Constants

The inhomogeneous elastic tensors $\mathbb{C}^n$ and $\overline{\mathbb{C}}^n$ define the elastic microstress and couple microstress responses as described in equation (6.3). These elastic tensors can be computed as volume averages of the local inhomogeneous elastic tensor $\mathbf{C}_m$ within the microstructure as described in equations (6.10). The local inhomogeneous elastic tensor $\mathbf{C}_m$ is approximated as being equal to the elastic tensor for cobalt. In an isotropic description of the local inhomogeneous elastic tensor $\mathbf{C}_m$, the Young's modulus is $211GPa$ and the Poisson's ration is 0.31.

The length scale parameters l^n are required to complete the elastic model as described in equation (6.10). These are given here according to the observations made in the RVE (Figure 7.2) i.e. they are the characteristic length scales of inhomogeneous deformation at each scale which define the averaging volumes V_n. These characteristic length scales are related to the underlying microstructural features and are summarized in Table 7.1.

Length Scale Parameter	Value	Related Microstructural Feature
l^1	0.8 microns	Cobalt Grain Size d
l^2	0.2 microns	Characteristic Brittle Crack Opening Displacement
l^3	0.05 microns	Microvoid Size

Table 7.1 Characteristic length scales of inhomogeneous deformation observed in the simplified WC-Co RVE described in Section 7.1

7.3.2 Plastic Regime: Microstress Constants

The microstress hardening functions have been introduced in equation (6.6). These functions describe the how the microstress at each scale evolves with inhomogeneous deformation. The microstresses are essentially continuum measures i.e. each microstress is computed as a volume average of a local microstress within the RVE as described in equation (6.15).

The local microstress field β_m is first computed from the known stress and strain measures using equation (6.15) as shown in (Figure 7.4). The local microstress field β_m can then be averaged at different scales V_n via equation (6.15) to extract the continuum microstresses β^n and microstress couples $\bar{\beta}^n$. These scalar microstress measures are then used to form a flow law for use in the microstress constitutive relationships, equation (6.6).

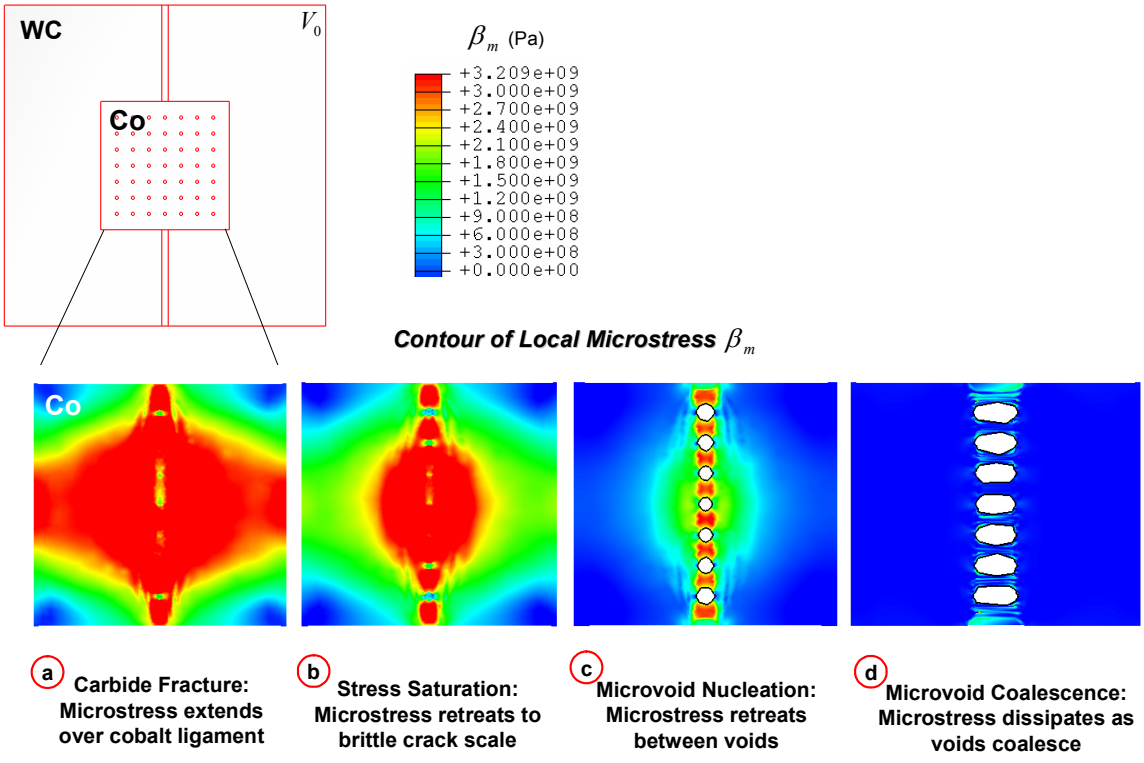

Figure 7.4. Contours of the local microstress β_m in the cobalt pool evolving with microstructure

Computing the Local Microstress Field β_m

The local microstress β_m represents the resistance to local inhomogeneous deformation within the RVE. As such it evolves with the inhomogeneous deformation in space and time:

- When carbide fracture (a) occurs (Section 4.2) the local microstress β_m extends throughout the cobalt ligament.
- As the stress within the cobalt saturates (b) the local microstress β_m retreats to the scale of the brittle crack tip.
- When microvoids nucleate (c) the local microstress β_m retreats to the scale of the microvoids.

- Finally the microvoids coalesce (d) and the local microstress dissipates as the material fails.

The microstructural instability events (a)-(d) are also labeled on the macroscale average stress-strain curve for the composite in (Figure 7.3); this illustrates that the microstress evolution and the macroscale constitutive response both depend on the evolving microstructure.

Averaging the Local Microstress Field at Each Scale

The microstresses β^n and $\overline{\beta}^n$ can now be computed by averaging the local microstress field β_m at each characteristic scale of inhomogeneous deformation n according to equation (6.15). Likewise the inhomogeneous strains Σ^n and strain gradients $\overline{\Sigma}^n$ can be computed via equation (6.16). The averaging volumes V_n are chosen such that the deformation varies linearly within it at each scale (Figure 7.5). This defines the size of the averaging volumes which in turn defines the length scales i.e. the square root of the averaging area in 2D. Only the cobalt zone in the RVE is shown in (Figure 7.5) as this is where the interesting inhomogeneous deformation occurs. The microstresses β^n and $\overline{\beta}^n$ can then be plotted against the inhomogeneous strains Σ^n and strain gradients $\overline{\Sigma}^n$ as shown in (Figure 7.6). The macroscale average constitutive response is also plotted in (Figure 7.6). The occurrence of microstructural instability events (a)-(d) is also labeled.

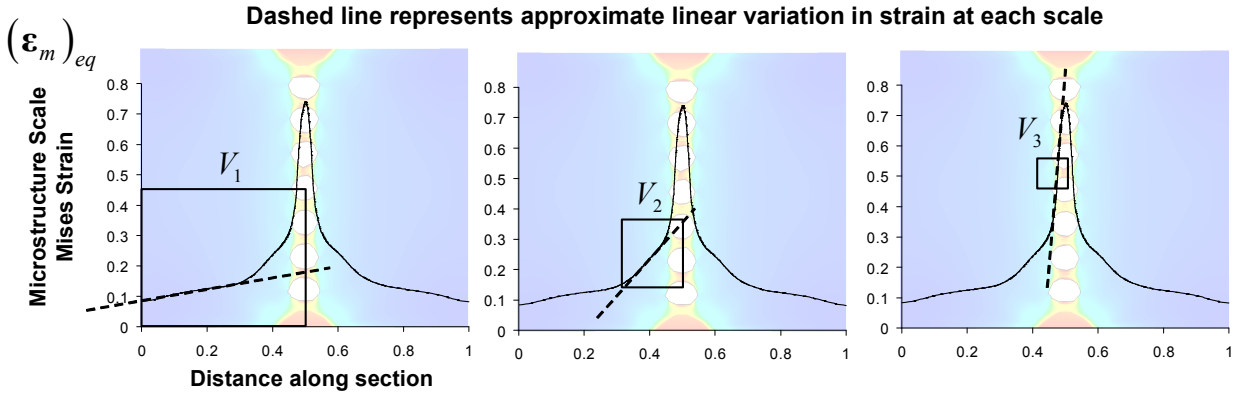

Figure 7.5. Determination of averaging volume size used at each scale. The deformation varies approximately linearly at each scale (in each averaging box).

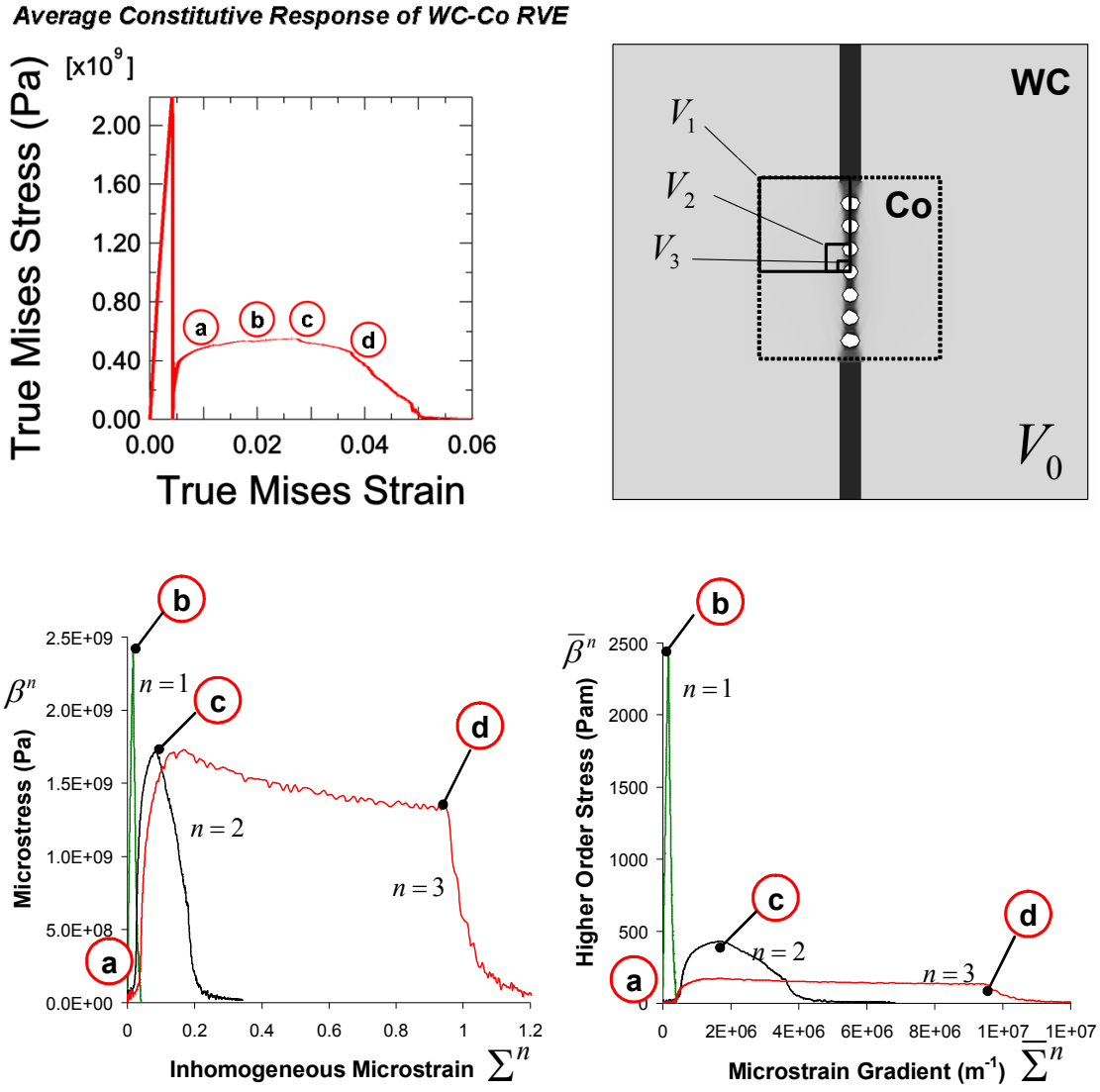

Figure 7.6. The local microstress β_m is averaged at each scale using the averaging volumes V_n. The collapse of each microstress coincides with a microstructural instability event.

7.3.3 WC-Co Microstructure Instability Points

As shown in (Figure 7.6) the various microstresses $\left(\beta^n, \bar{\beta}^n \;\; n=1,2,3\right)$ fail when specific instability events occur within the microstructure. In the WC-Co material being examined the instability events are briefly recapped as:

- (a) carbide fracture
- (b) saturation of the stress within the cobalt ahead of the brittle crack tip
- (c) microvoid nucleation
- (d) microvoid coalescence

To relationship between the microstructure instability events, the macroscale stress and the microstresses is explored further in (Figure 7.7). The macroscale stress and the microstresses are plotted as a function of time during the RVE simulation. With reference to (Figure 7.7):

- The first microstress β^1 dominates immediately after carbide fracture **(a)**. Inhomogeneous deformation occurs at scale l^1**.**
- The third curve from the top, 'Mises Stress', shows the average stress in the cobalt pool. The stress saturates in the cobalt **(b)** at around 0.4 seconds. Inhomogeneous deformation occurs at scale l^2. The microstress β^1 begins to degrade. The second microstress β^2 then dominates.
- The fourth curve from the top, 'Porosity', shows the average porosity in the cobalt pool. The voids nucleate **(c)** at approximately 0.6 seconds; the porosity increases rapidly. Inhomogeneous deformation occurs at scale l^3**.** The microstress β^2 begins to degrade. The third microstress β^3 then dominates.

- The final curve shows the average distance between voids which is an indicator of coalescence. At approximately 0.9 seconds the inter-void distance begins to decrease rapidly i.e. coalescence occurs **(d)**. The microstress β^3 begins to degrade indicating final failure.

Hence each of the microstresses begins to rapidly degrade due to some microstructural instability event. Furthermore each of these instability events has an obvious impact on the average macroscale constitutive response. In the multiresolution continuum model the microstructural evolution is described in a parameterized manner through the evolving internal state variables in the macroscale constitutive relation. In Section 7.3.4 failure of each microstress is related mathematically to the appropriate microstructural instability event, as predicted by the macroscale constitutive relation. For example the second microstress fails when void nucleation (c) is predicted by the macroscale constitutive relation via the nucleation evolution equation (4.1).

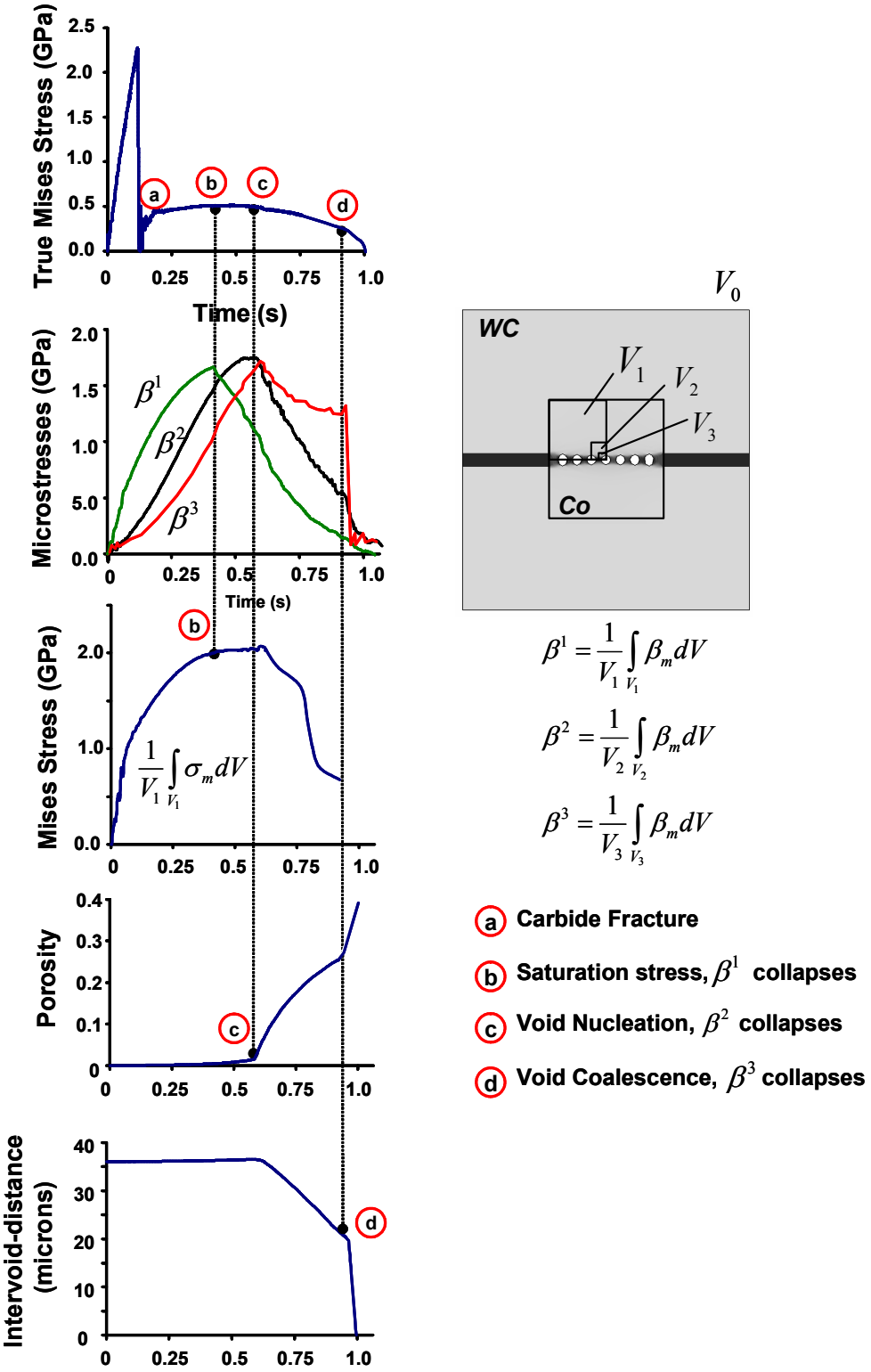

Figure 7.7. Microstress failure as a function of the evolving microstructure. The microstructural instability events (b)-(d) are compared to the microstress failure points.

7.3.4 Microstress Softening Functions

The computed microstress curves $\beta^n, \bar{\beta}^n$ in (Figure 7.6) are now calibrated to appropriate hardening/softening functions $\beta_y^n, \bar{\beta}_y^n$ for use in the microstress yield surfaces, $\varphi^n, \bar{\varphi}^n$ in equation (6.6). In a conventional linear strain hardening/softening material, two parameters are required to define a hardening law; an initial yield stress and a hardening/softening modulus. The same concept is applied here for the microstress hardening/softening functions $\beta_y^n, \bar{\beta}_y^n$ as shown in (Figure 7.8).

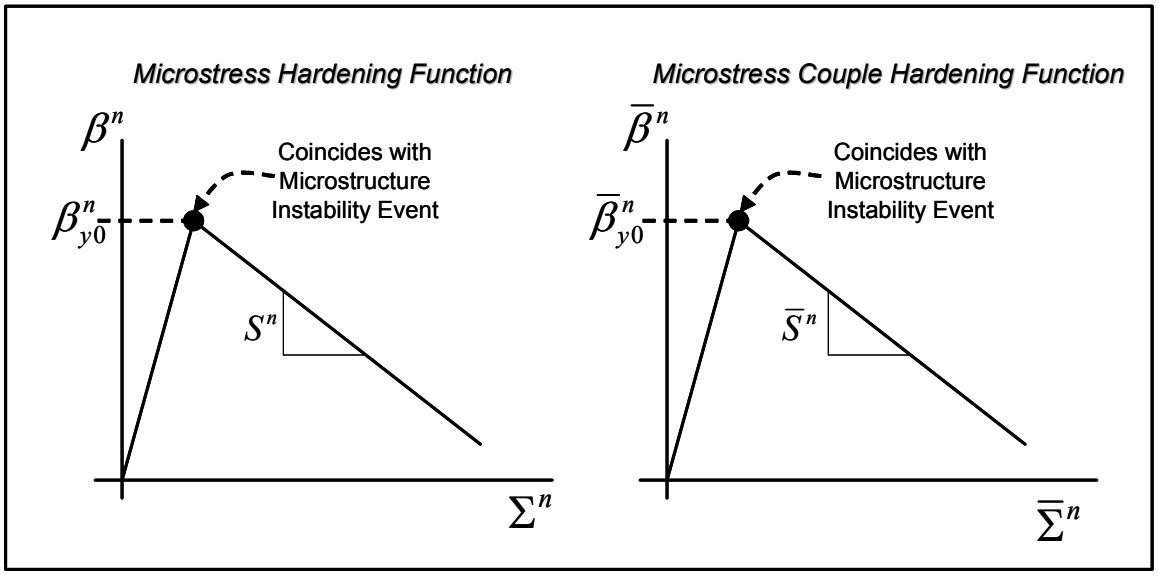

Figure 7.8. The microstress failure points are mathematically tied to the microstructure instability events

The microstress curves in (Figure 7.6) each exhibit an initial yield followed by softening. Here the initial yield of the microstresses are called β_{y0}^n and $\bar{\beta}_{y0}^n$ respectively and the softening moduli which describe the post yield softening are called S and $\bar{S}$ such that:

$$\beta_y^n = \beta_{y0}^n \left(1 + S^n \Sigma^n\right)$$
$$\bar{\beta}_y^n = \bar{\beta}_{y0}^n \left(1 + \bar{S}^n \bar{\Sigma}^n\right) \tag{7.1}$$

Initial microstresses yield $\left(\beta_{y0}^n, \bar{\beta}_{y0}^n\right)$ coincides with the microstructural instability events described in Section 7.3.3. These microstructure instability events are used here as microstress yield flags i.e. when a microstructural instability event occurs (as predicted by the macroscale constitutive relation) the microstresses at the appropriate scale $\left(\beta^n, \bar{\beta}^n\right)$ are considered to have reached microstress yield, $\beta_{y0}^n, \bar{\beta}_{y0}^n$. Hence initial microstress yield is not a pre-defined constant. Just like the macroscale initial yield stress may vary with rate or temperature, the microstress initial yield varies with microstructure.

In terms of the WC-Co composite, the microstress yields occurs as follows:

- The first set of microstresses $\beta^1, \bar{\beta}^1$ yield when the stress saturates in the cobalt. In the RVE simulation (Figure 7.3) this occurs at a *macroscale* Mises strain of approximately 2%. This macroscale stain value is called $\bar{\varepsilon}_{sat}$ here and is used as a simple indicator of stress saturation in the cobalt – it is recognized that the macroscale strain corresponding to cobalt scale stress saturation will likely be a complex function of many parameters, particularly triaxiality, temperature, rate and work hardening.
- The next set of microstresses $\beta^2, \bar{\beta}^2$ yield when microvoid nucleation occurs i.e. at the *macroscale* mean strain for void nucleation, $\varepsilon_{\mathcal{N}}$, equation (4.3).

- The final set of microstresses $\beta^3, \overline{\beta}^3$ yield when microvoid coalescence is predicted by the *macroscale* constitute model, equation (4.9). Here final coalescence is considered to begin when porosity reaches a value of 25% as shown in (Figure 7.7).

These relationships are summarized in Table 7.2.

Microstructure Instability Event	**Indicator from WC-Co Model**	**Microstress Yield** β^n_{y0}	**Microstress Couple Yield** $\overline{\beta}^n_{y0}$
Stress Saturation	$\overline{\varepsilon} = \overline{\varepsilon}_{sat} = 0.02$	$\beta^1_{y0} = \beta^1\big\|_{\overline{\varepsilon}=0.02}$	$\overline{\beta}^1_{y0} = \overline{\beta}^1\big\|_{\overline{\varepsilon}=0.02}$
Microvoid Nucleation	$\varepsilon = \varepsilon_{\mathcal{N}}$	$\beta^2_{y0} = \beta^2\big\|_{\varepsilon=\varepsilon_{\mathcal{N}}}$	$\overline{\beta}^2_{y0} = \overline{\beta}^2\big\|_{\varepsilon=\varepsilon_{\mathcal{N}}}$
Microvoid Coalescence	$\phi = 0.25$	$\beta^3_{y0} = \beta^3\big\|_{\phi=0.25}$	$\overline{\beta}^3_{y0} = \overline{\beta}^3\big\|_{\phi=0.25}$

Table 7.2 Summary of microstress failure criteria

7.4 Application to Numerical Fracture Toughness Prediction

The microscale constitutive relations developed in Sections 7.1-7.4 are now used within a multiresolution continuum based fracture toughness simulation. The problem is described in Section 7.4.1. The problems associated with a conventional continuum approach are highlighted in Section 7.4.2.

7.4.1 Fracture Simulation: Set Up

A domain reduction technique is used for efficiency as illustrated in (Figure 7.9) for a crack with tip radius of 15nm. This technique assumes that small scale yielding occurs i.e. the dimensions of the crack process zone are small compared to the characteristic dimensions of the body. Hence any plasticity is confined to the local proximity of the crack tip. Under this assumption the displacement field surrounding the crack tip shown in (Figure 7.9) can be calculated using the equations of linear elastic fracture mechanics (LEFM). The analytical expressions for the displacement field are given in terms of the radius from the crack tip R, the angle measured from the crack tip Θ, the shear modulus μ and the stress intensity factor associated with the crack tip K_I (Kanninen and Popelar 1985):

$$\begin{aligned} u_1 &= \frac{K_I}{2\mu}\sqrt{\frac{R}{2\pi}}\cos\left(\frac{\Theta}{2}\right)\left[\kappa - 1 + 2\sin^2\left(\frac{\Theta}{2}\right)\right] \\ u_2 &= \frac{K_I}{2\mu}\sqrt{\frac{R}{2\pi}}\sin\left(\frac{\Theta}{2}\right)\left[\kappa - 1 - 2\cos^2\left(\frac{\Theta}{2}\right)\right] \end{aligned} \qquad (7.2)$$

where $\kappa = 3 - 4\mu$ for plane strain. Using this equation, displacement boundary conditions can be applied on a contour around the crack to induce a known stress intensity factor.

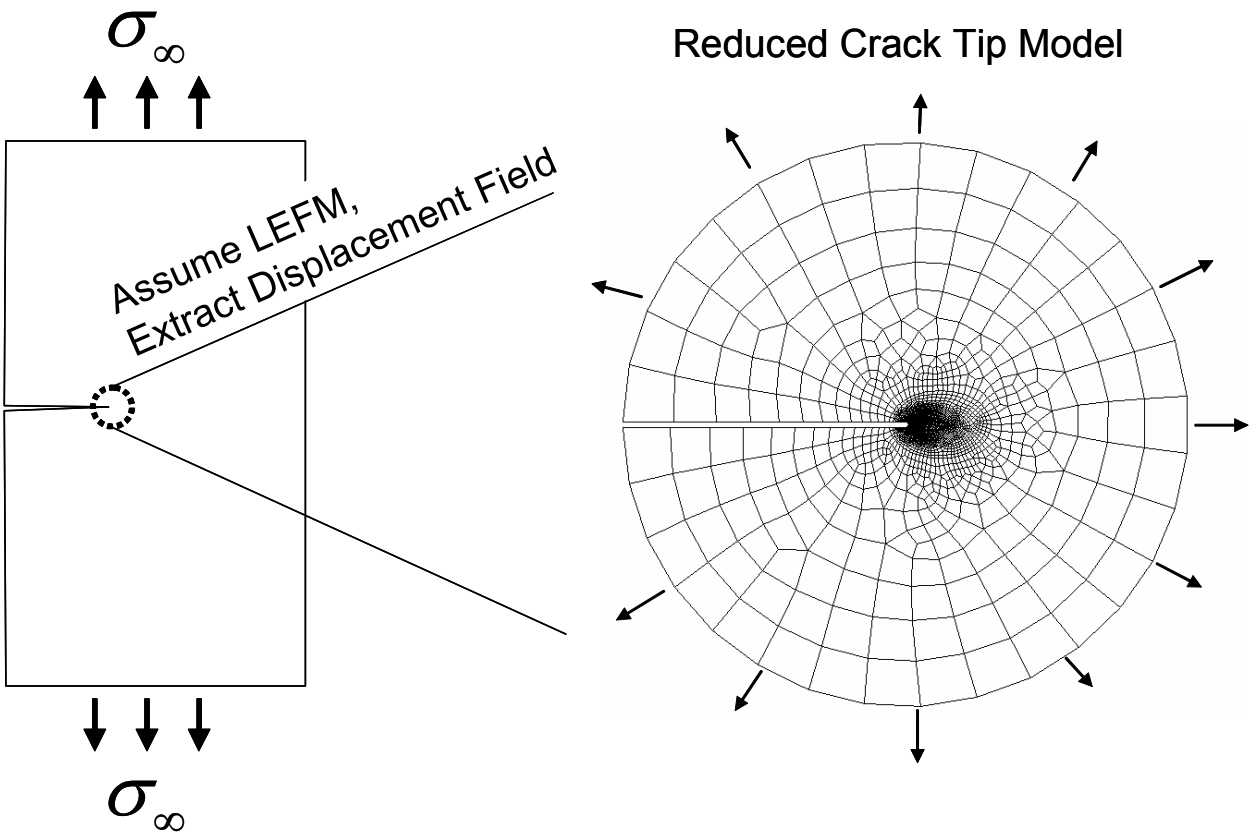

Figure 7.9. A reduced fracture model is used based on the assumption of small scale yielding

7.4.2 Conventional Continuum Analysis of Crack Growth

A conventional continuum approach is used to model crack growth using the model shown in (Figure 7.9). The microstructural parameters are: cobalt grain size $d = 500nm$, cobalt volume fraction $f = 0.15$, temperature $\vartheta = 353K$ and loading is quasi-static. The experimentally determined value of fracture toughness for this microstructure is approximately 16.7MPam$^{-1/2}$ (McHugh and Connolly 2003). (Figure 7.10) shows how the deformation localizes in an unphysical manner leading to an unphysical fracture toughness – see Section 4.5 for more details. The simplest explanation is that no physical length scales exists in the model. Hence, due to the

softening nature of the constitutive relation, the plastic deformation is distributed over the smallest length scale possible i.e. the length scale of the elements ahead of the crack tip. The toughening effect of a diffuse plastic strain field is therefore lost.

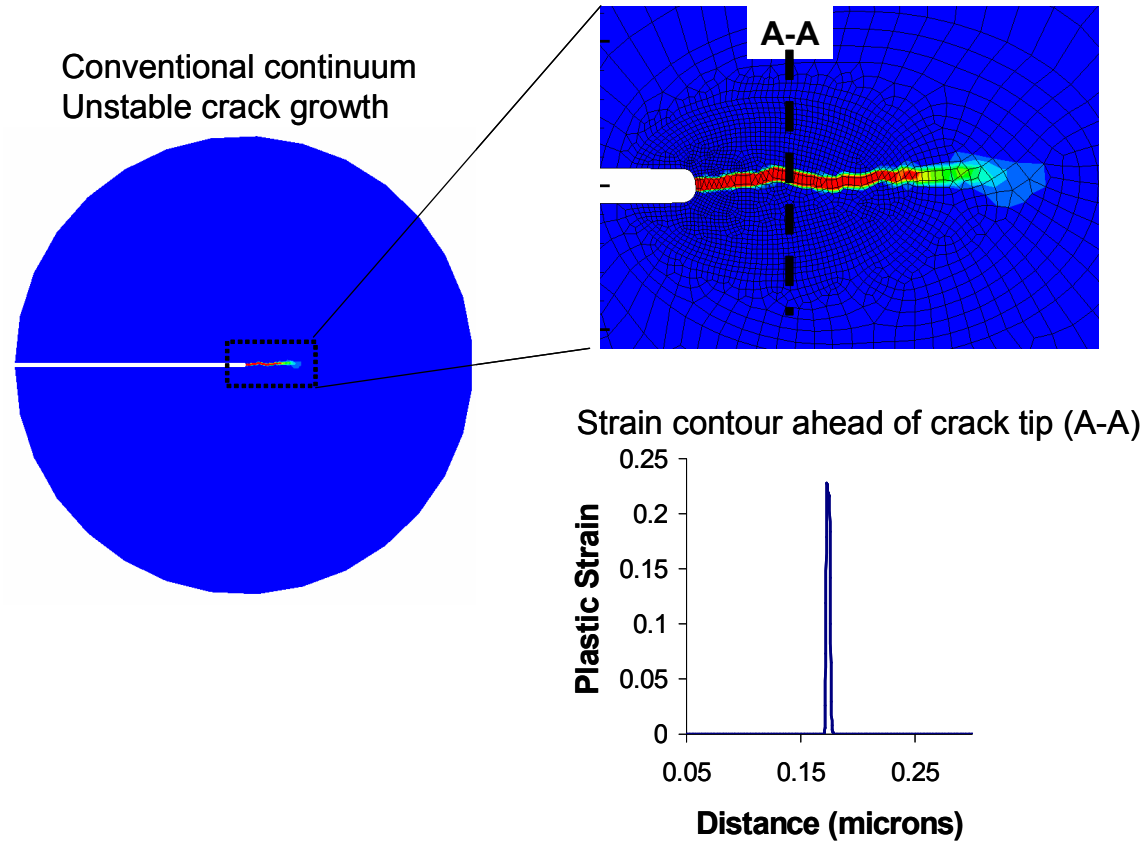

Figure 7.10. A conventional continuum approach leads to unphysical strain localization ahead of the crack tip.

7.4.3 Multiresolution Continuum Analysis of Crack Growth

The multiresolution continuum theory is now applied to the same crack growth analysis.

Governing Equations and Constitutive Relationships

A four scale analysis $(N=3)$ is performed, with governing equations given by equation (5.25) and repeated here for clarity:

$$\begin{aligned} &\boldsymbol{\sigma} - \sum_{n=1}^{N} \boldsymbol{\beta}^n = 0 \quad \text{in} \quad \Omega \quad \text{N=3} \\ &\nabla \bullet \bar{\boldsymbol{\beta}}^n - \boldsymbol{\beta}^n = 0 \quad \text{in} \quad \Omega \quad \text{n=1,2,3} \\ &\mathbf{u} = \bar{\mathbf{u}} \quad \text{on} \quad \Gamma_u \end{aligned} \tag{7.3}$$

where $\bar{\mathbf{u}}$ is the displacement boundary condition given by equation (7.2) on S. The WC-Co hierarchical constitutive relationship developed in Chapter 4 is used to define the Cauchy stress $\boldsymbol{\sigma}$; a summary of this constitutive relation is given in (Figure 4.29). The microscale constitutive relationships are elasto-plastic. The elastic equation is given by equation (6.3):

$$\begin{aligned} \overset{\nabla}{\boldsymbol{\beta}}^n &= \mathbb{C}^n \bullet \left(\mathbf{L}^n - \mathbf{L} \right)^e \qquad n = 1,2,3 \\ \overset{\nabla}{\bar{\boldsymbol{\beta}}}^n &= \bar{\mathbb{C}}^n \bullet \left(\mathbf{L}^n \overleftarrow{\nabla} \right)^e \qquad n = 1,2,3 \end{aligned} \tag{7.4}$$

and equation (6.10):

$$\begin{aligned} \mathbb{C}^n &= \mathbf{C}_m \qquad n = 1,2,3 \\ \bar{\mathbb{C}}^n &= \frac{\left(l^n \right)^2}{12} \, \mathbf{C}_m \otimes \mathbf{I} \qquad n = 1,2,3 \end{aligned} \tag{7.5}$$

where the isotropic elastic tensor $\mathbf{C}_m$ has a Young's modulus of Young's modulus is $211 GPa$ and the Poisson's ration is 0.31 (Section 7.3.1). The length scales l^n are related to the cobalt grain size, brittle crack opening size and microvoid size; these are given in Table 7.1.

The plastic part of the microstress constitutive update is performed through three sets of J2 flow models described in equation (6.6):

$$\varphi^n = \left(\frac{\beta^n}{\beta_y^n} \right)^2 - 1 = 0 \quad n = 1,2,3$$
$$\bar{\varphi}^n = \left(\frac{\bar{\beta}^n}{\bar{\beta}_y^n} \right)^2 - 1 = 0 \quad n = 1,2,3 \tag{7.6}$$

where the microstress hardening functions β_y^n and $\bar{\beta}_y^n$ are given by equation (7.1) and microstress yield $\left(\beta_{y0}^n, \bar{\beta}_{y0}^n\right)$ occurs at the microstructural instability events as described in Table 7.2.

Evolution of the Microstresses

The evolution of the microstresses is shown in (Figure 7.11). The effective (scalar) form of each microstress β^n is plotted.

- At time label (a) the microstress $\boldsymbol{\beta}^1$ is active.
- At time label (b), the first microstress $\boldsymbol{\beta}^1$ fails ahead of the crack tip (cobalt stress saturation, see Table 7.2) and the second microstress $\boldsymbol{\beta}^2$ becomes dominant.
- At time label (c), the second microstress $\boldsymbol{\beta}^2$ fails ahead of the crack tip (microvoid nucleation occurs, see Table 7.2) and the third microstress $\boldsymbol{\beta}^3$ becomes active.
- At time label (d), the third microstress fails $\boldsymbol{\beta}^3$ (due to microvoid coalescence, see Table 7.2) the material in that region is completely ruptured.

Overall a much tougher response is predicted than in the conventional continuum analysis; the plastic strain is sequentially distributed over scale l^1 (cobalt grain size), followed by l^2 (brittle crack scale) and l^3 (microvoid scale) as shown in (Figure 7.12).

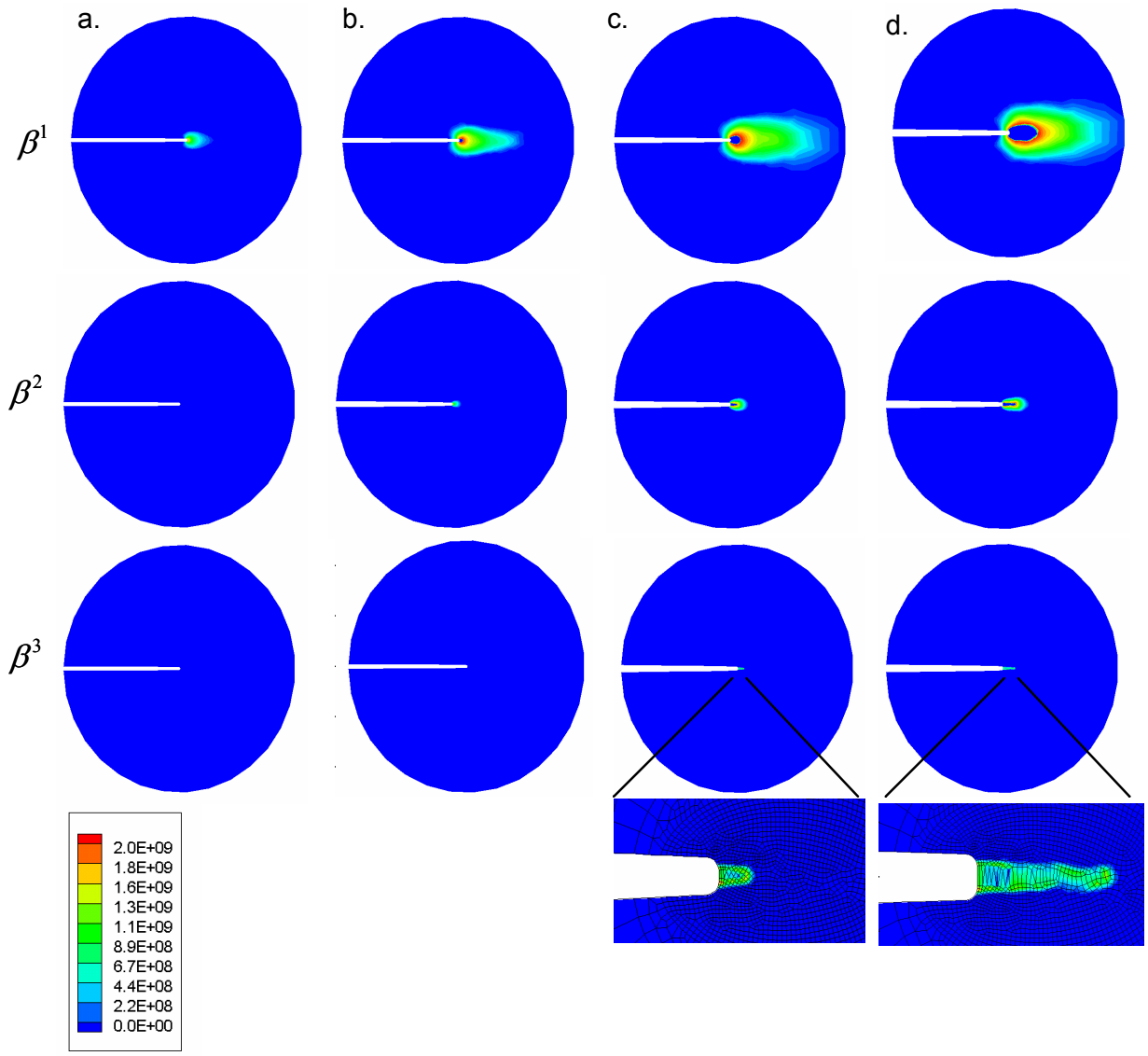

Figure 7.11. Microstress evolution in the crack tip process zone

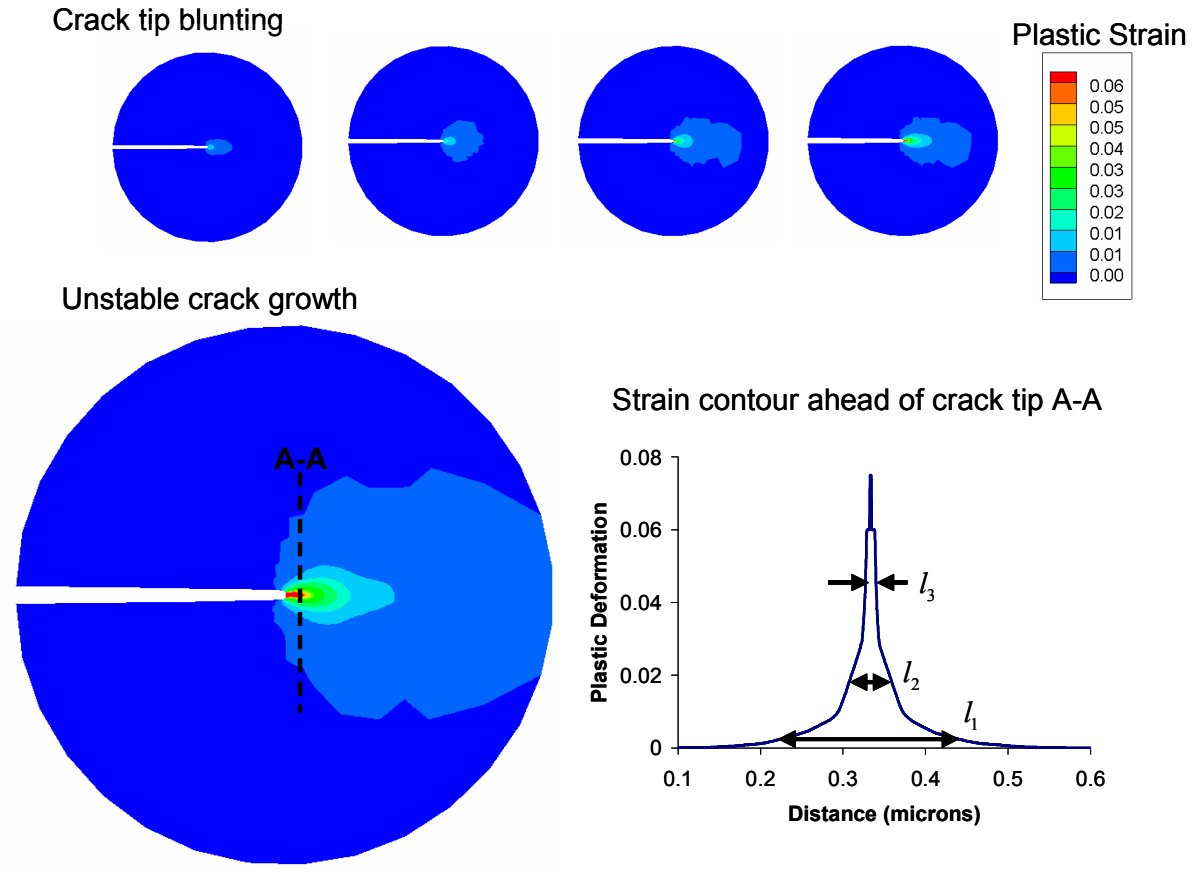

Figure 7.12. Three length scales are embedded in the multiresolution model via equation (7.5); each is related to the microstructure

A comparison between the stress intensity versus crack tip opening displacement curves for the conventional analysis and the multiresolution analysis is shown in (Figure 7.13). As expected the stress intensity factor predicted by the multiresolution analysis is higher due to the dispersed strain field.

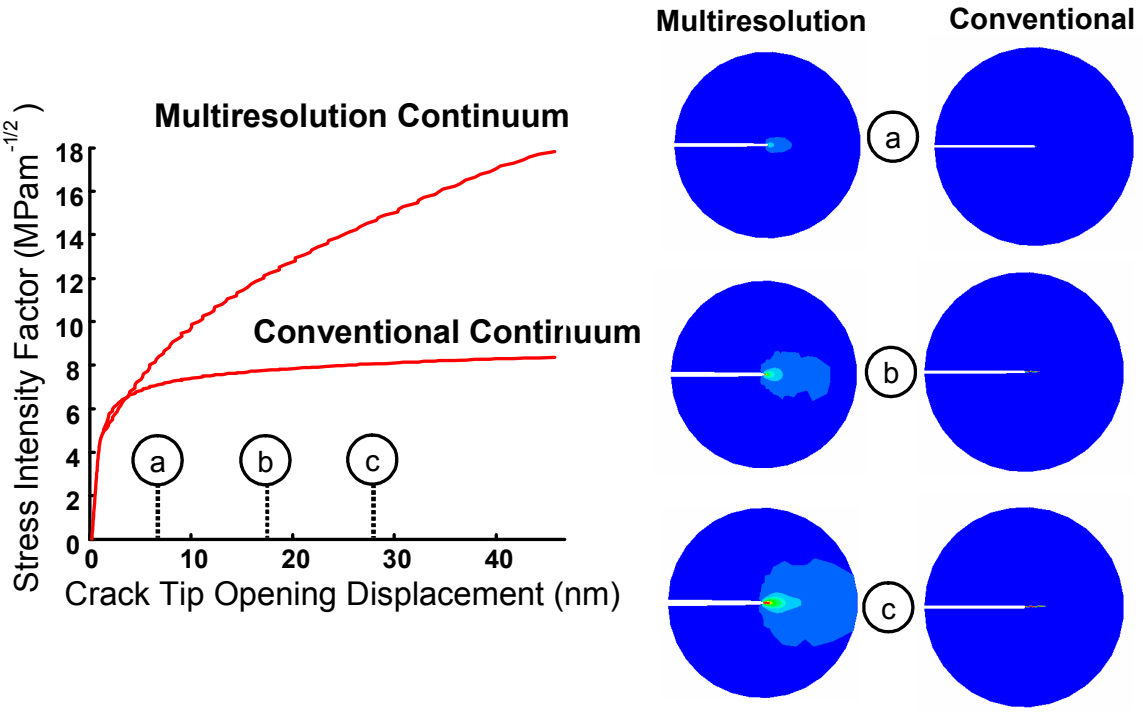

Figure 7.13. The multiresolution analysis predicts increased stress intensity as the plastic strain is dispersed over a physical area. The conventional approach suffers from unphysical localization.

7.4.4 Parametric Study

A parametric study is now performed in which the following WC-Co microstructural parameters are varied to determine their effect on crack stress intensity factor:

- cobalt grain size d
- cobalt volume fraction f
- temperature ϑ
- loading rate $\|\mathbf{D}\|$

The chosen values of each parameter are described in Table 7.3

Parameter	*Base Value*	*Value*	*Value*
d	$100nm$	$500nm$	$1000nm$
f	0.15	0.05	0.25
ϑ	$353K$	$553K$	$753K$
$\|\mathbf{D}\|$	$5\times10^{-4}s^{-1}$	$5\times10^{-1}s^{-1}$	$5s^{-1}$

Table 7.3 Parameter values used in parametric study

The results using a conventional continuum and the multiresolution continuum are compared. The stress intensity factor is plotted as a function of crack tip opening displacement for each case. The typical effect of changing each parameter on the WC-Co constitutive response is also plotted in an effort to explain why the stress intensity changes with microstructure. The area under the stress-strain curve is loosely refereed to as the 'toughness' in this Section.

Cobalt Grain Size d

Cobalt grain size is changed in equation (4.14) and when the multiresolution model is used the length scale parameter l^1 in equation (7.5) also changes with the grain size d. In (Figure 7.14) the effect of changing the cobalt grain size d is observed in the macroscale constitutive response. If a larger cobalt grain size is used, the toughness (area under the macroscale stress-strain curve) does not change much; the increase in post fracture strength is offset by the earlier void nucleation and subsequent reduction in ductility. The conventional continuum analysis predicts a slight reduction in the stress intensity factor with increasing grain size.

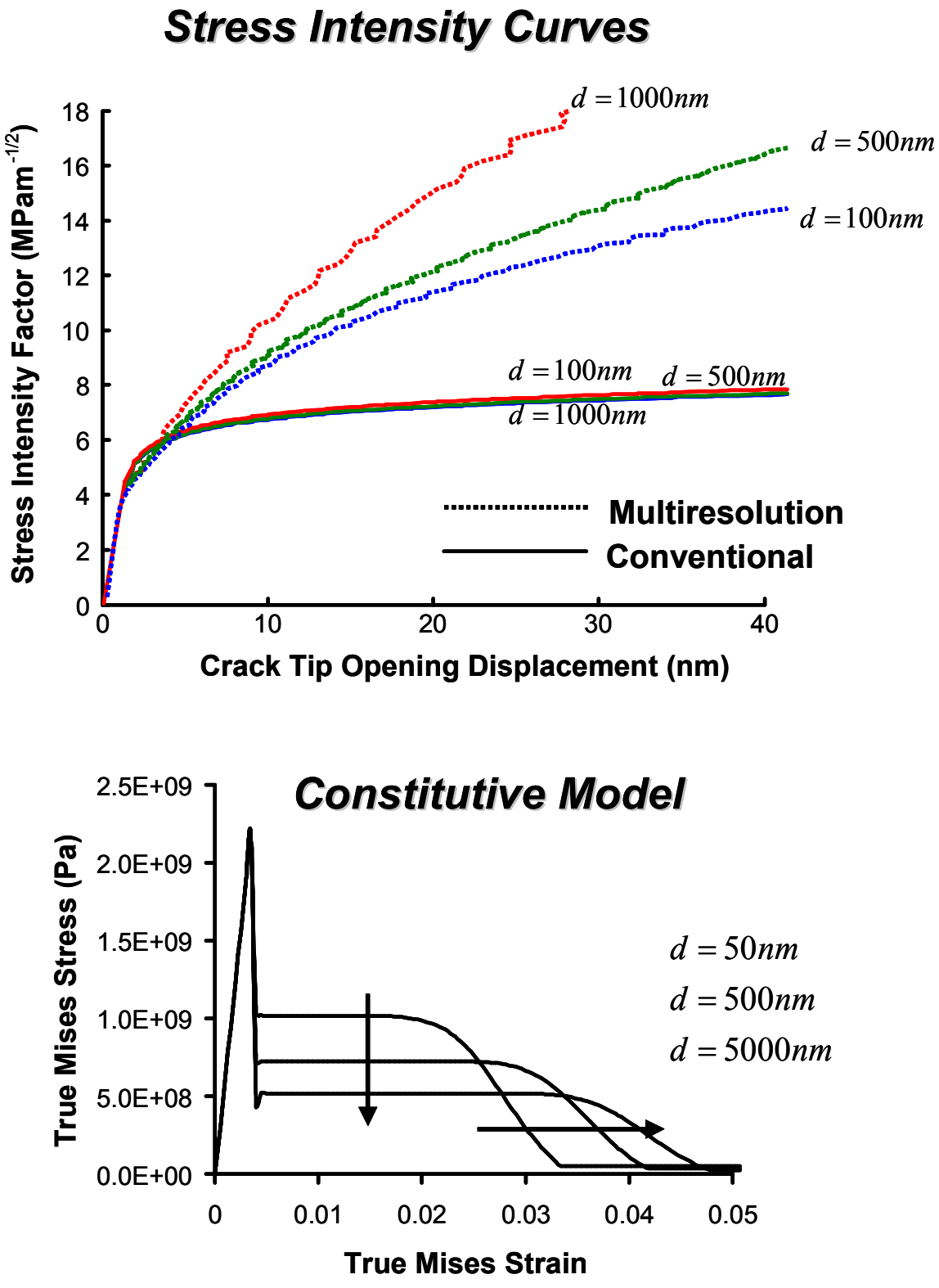

Figure 7.14. Increasing cobalt grain size increases the stress intensity

However in reality the blunting effect of increasing the cobalt grain size d is substantial; larger grains make the plastic strain extend over a larger area which blunts the crack tip. This more diffuse strain field is predicted by the multiresolution model through the embedded length scale l^1 in equation (7.5) (which is equal to the grain size d). Hence the increasing grain size d results in a higher stress intensity factor. This is a clear example of where the multiresolution theory predicts a length scale effect which is missed by the conventional continuum analysis.

Volume Fraction of Cobalt f

The volume fraction of cobalt f is changed in equation (4.14). The volume fraction of cobalt f is crucial as it determines the relative proportions of brittle and ductile material in the composite. Intuitively, an increase in the amount of tough cobalt will result in an increase in toughness as shown in the macroscale constitutive response (Figure 7.15). This increase in toughness leads to an increase in stress intensity in both the conventional continuum and multiresolution analyses as shown in (Figure 7.15). However the multiresolution approach predicts a greater toughness as the crack tip blunting effect is captured.

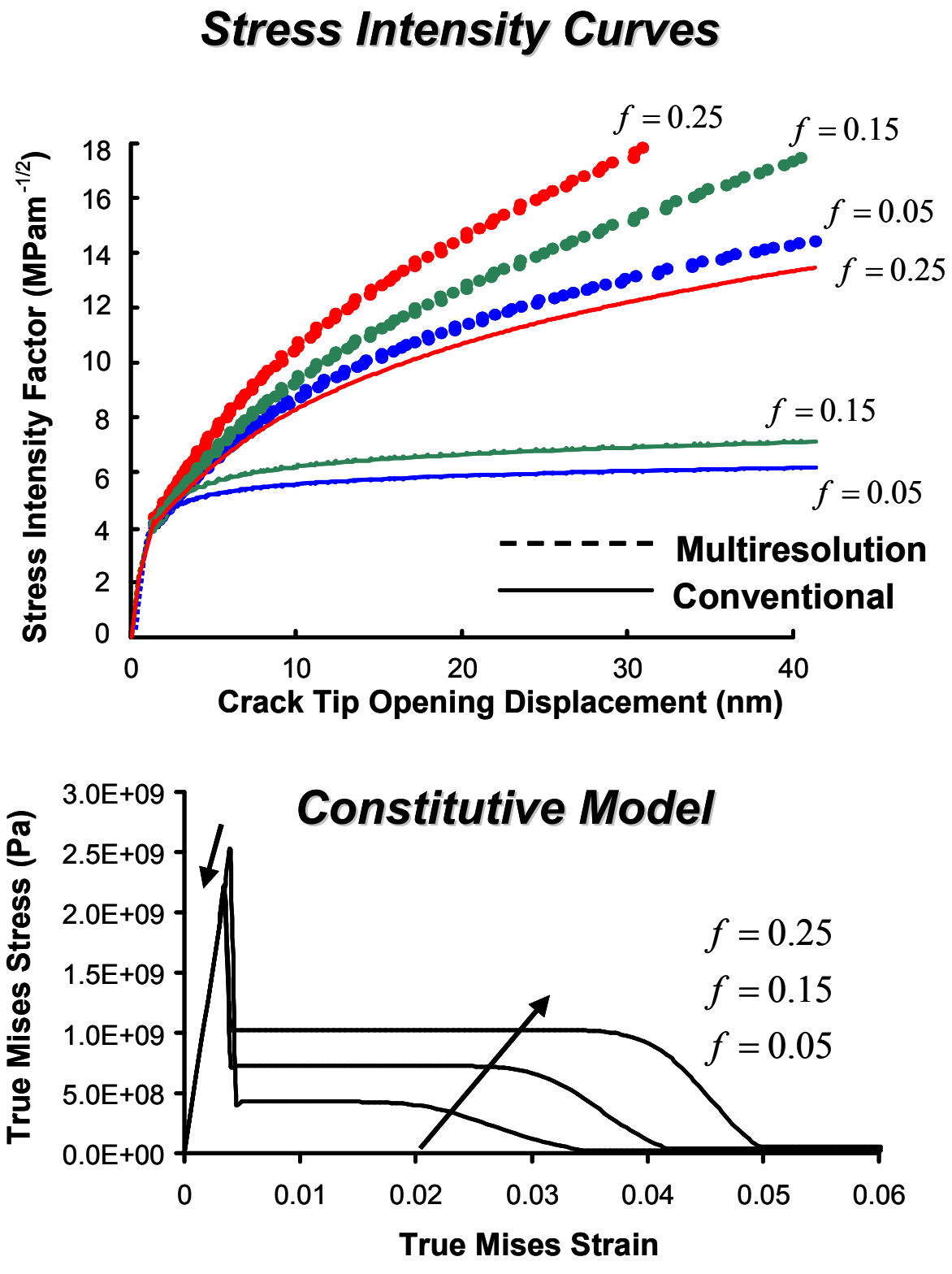

Figure 7.15. Increasing cobalt volume fraction increases the stress intensity

Temperature ϑ

Temperature ϑ is changed in equation (4.14). Temperature ϑ affects the strength of the cobalt within the WC-Co composite as described in Section 4.1.5. In general decreasing temperature strengthens the cobalt and leads to an increase in toughness as shown in the constitutive response in (Figure 7.16). This manifests itself as a higher stress intensity factor at lower temperatures in (Figure 7.16) for both the conventional continuum and multiresolution analyses. Again the multiresolution approach predicts a greater toughness as the crack tip blunting effect is captured.

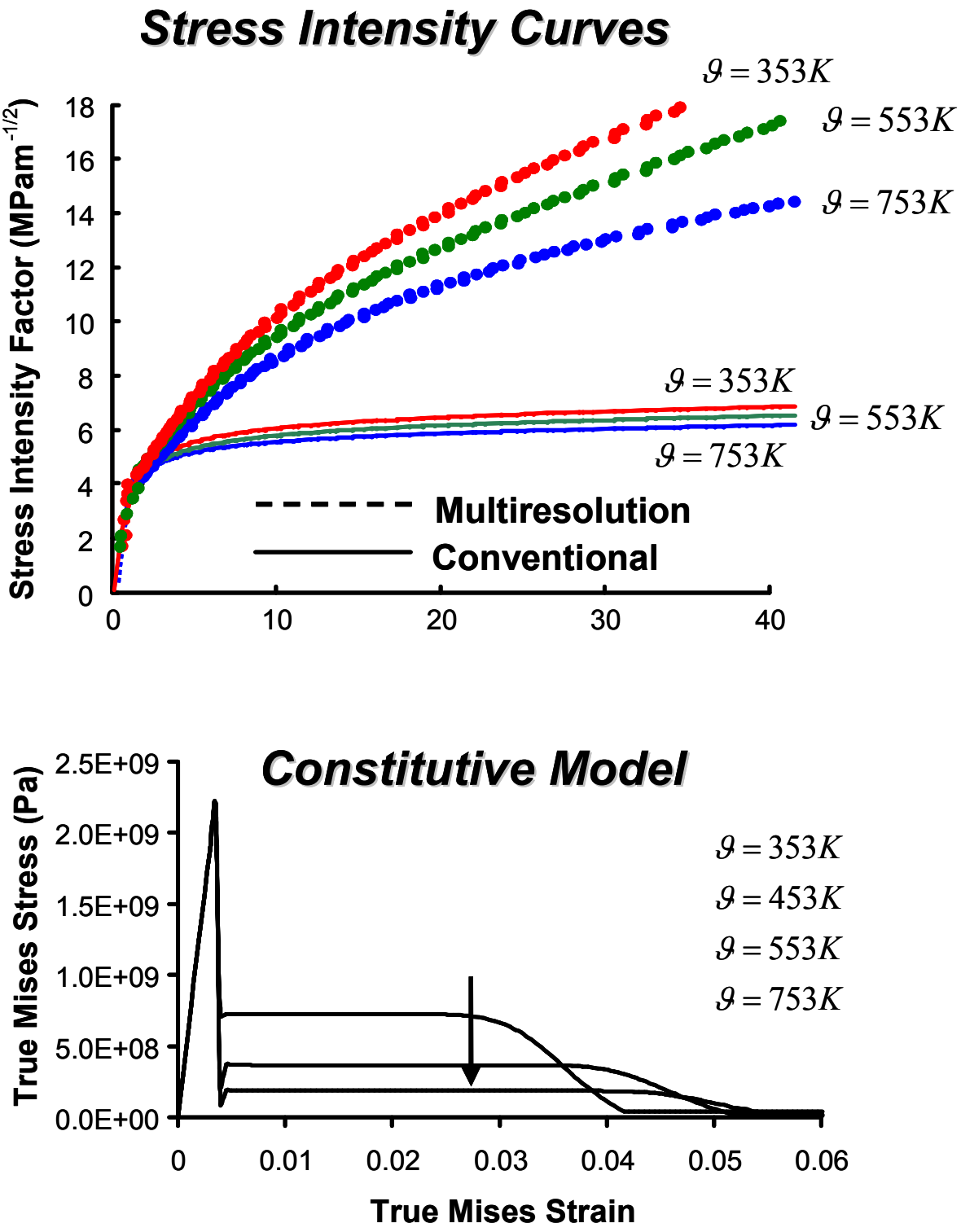

Figure 7.16. Increasing the temperature decreases stress intensity.

Rate $\|\mathbf{D}\|$

Deformation rate $\|\mathbf{D}\|$ is treated as a material parameter for the purposes of this parametric study i.e. the sample is loaded quasi-statically and the strain rate is changed artificially in equation (4.14) to gauge its effect. This has the effect of increasing the post fracture strength S of the WC-Co, equation (4.14). However void nucleation occurs sooner due to the inverse relationship between initial stress and void nucleation strain, equation (4.3), resulting in little or no increase in the toughness (area under the stress-strain curve) in (Figure 7.17). This is consistent with the resulting stress intensity curves which show little variation with rate $\|\mathbf{D}\|$ for either the conventional or multiresolution cases.

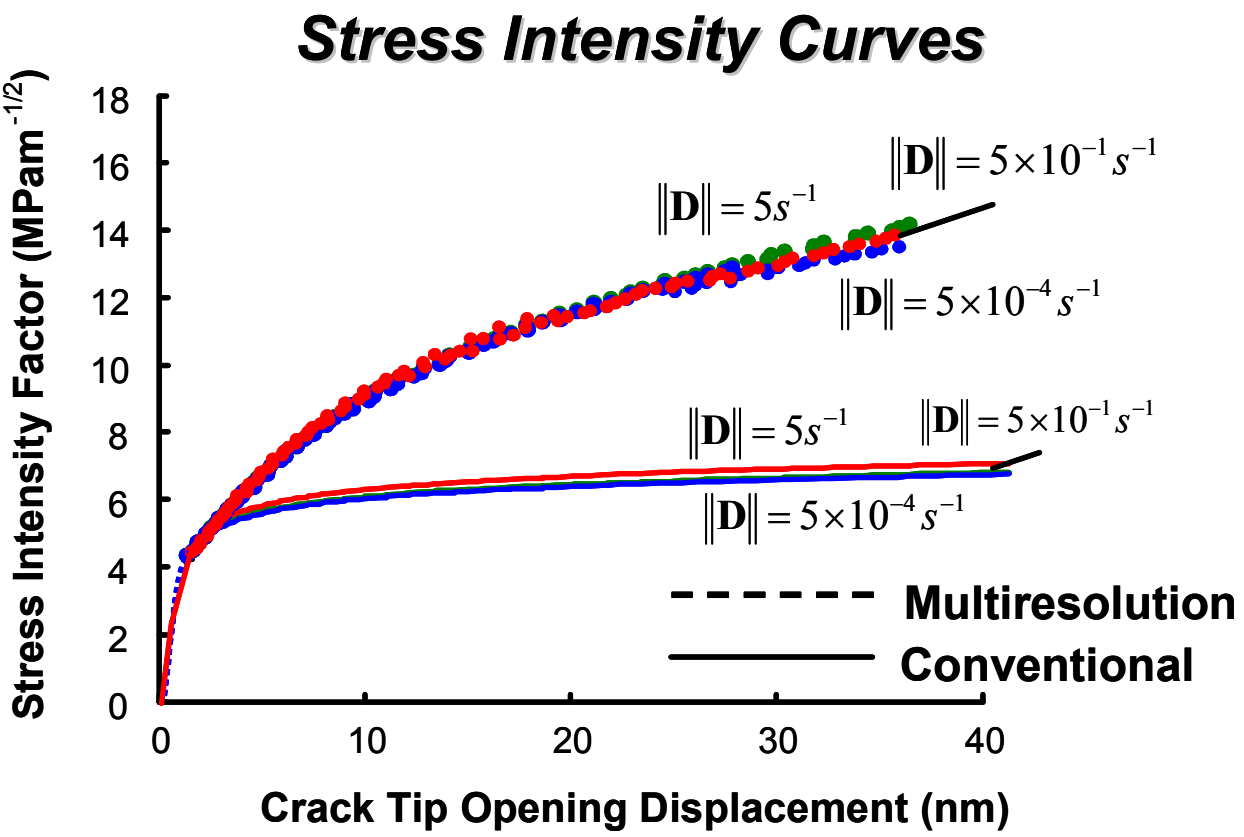

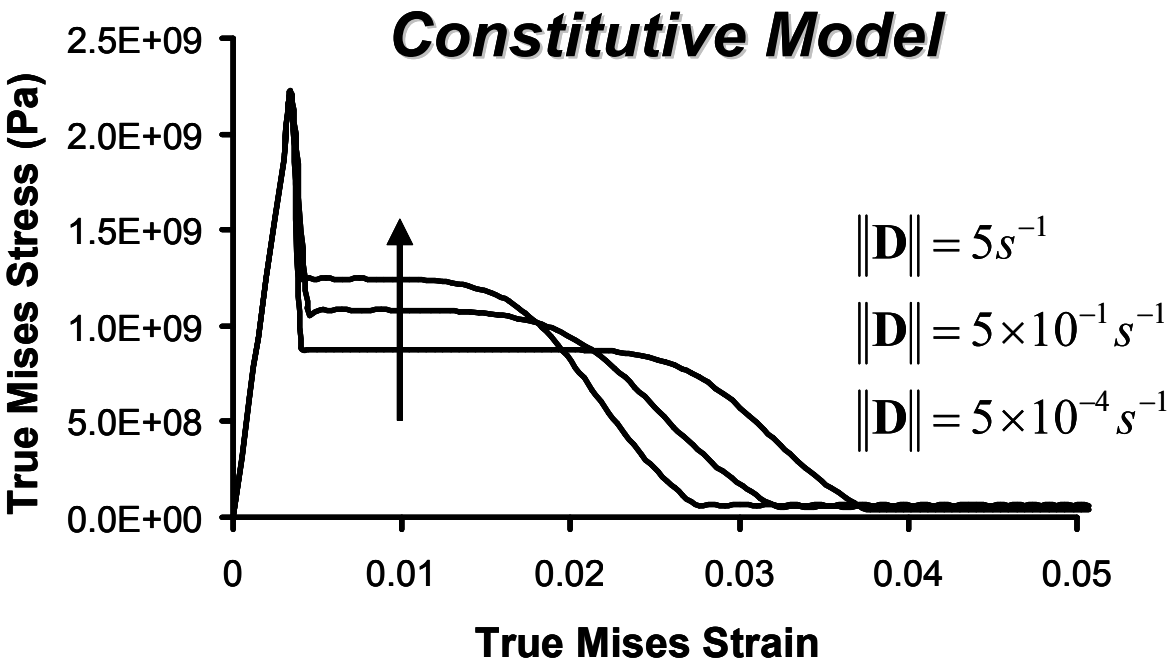

Figure 7.17. Increasing the strain rate increases stress intensity

Fracture Toughness $K_{IC} = K_{IC}\left(d, f, \vartheta, \|\mathbf{D}\|\right)$

Fracture toughness values are now determined from the stress intensity curves shown above. In (McHugh and Connolly 2003) the fracture toughness of a WC-Co composite was defined as the stress intensity factor at which the crack extends by a distance equal to the cobalt grain size d . A similar criterion is used here; the resulting fracture toughness values are plotted in (Figure 7.18) as a function of the underlying microstructure for the conventional and multiresolution cases. In each case the upper curve corresponds to the fracture toughness determined from multiresolution analysis. The lower curve corresponds to the conventional continuum analysis. In each case both models capture the design trend, however the conventional approach consistently underestimates the fracture toughness due to the lack of any physical length scale in the fracture simulation while the multiresolution approach captures the important design trends and fracture toughness values which are closer to those observed experimentally (McHugh and Connolly 2003).

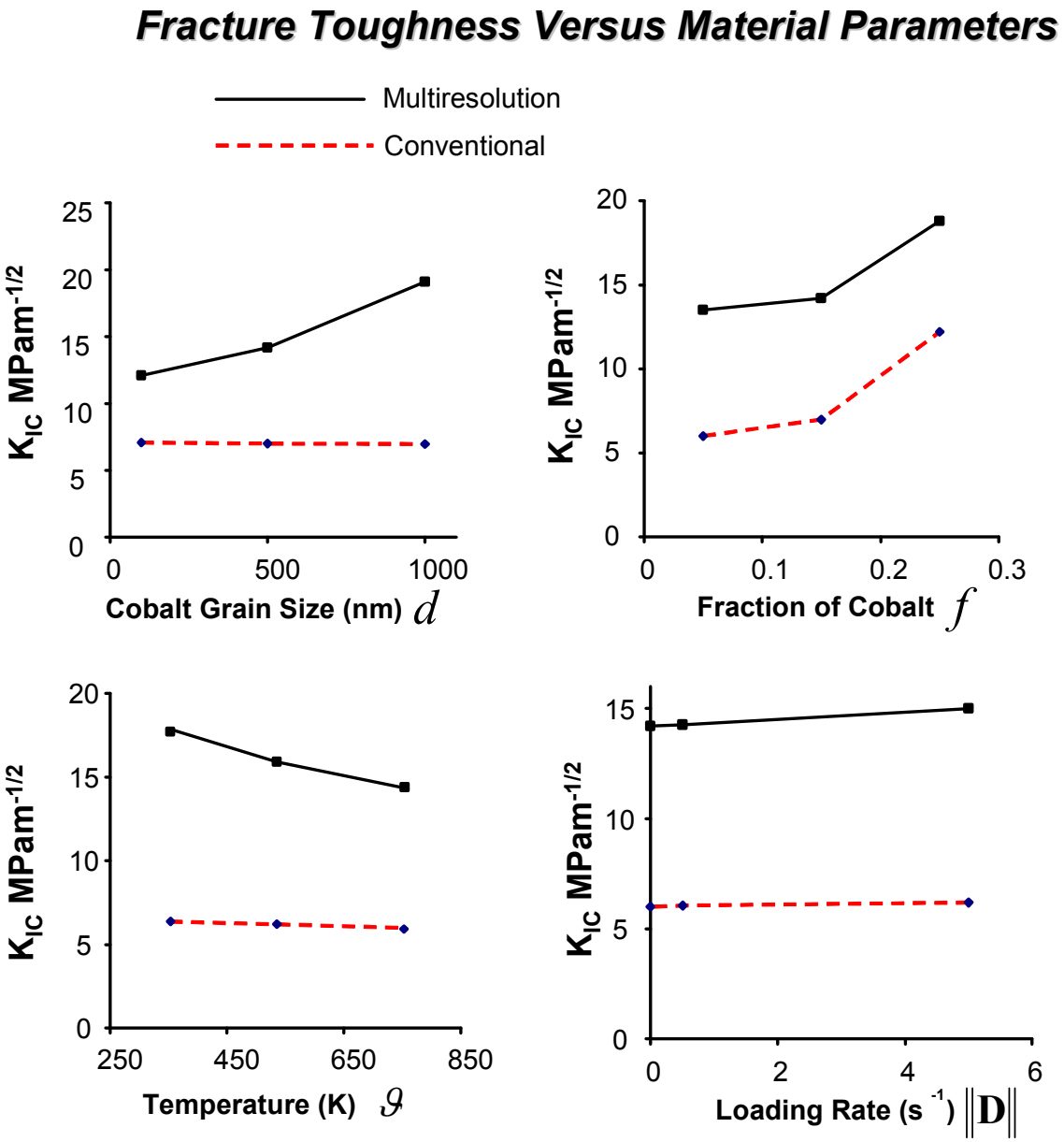

Figure 7.18. Fracture toughness scales with cobalt grain size, cobalt volume fraction and strain rate. Fracture toughness decreases with temperature

The simplest way of increasing the fracture toughness is through the addition of more cobalt during processing. However this also results in a decrease in strength as shown in (Figure 7.19). This occurs because the increasing cobalt fraction is accommodated by a decrease in the stronger carbide volume fraction.

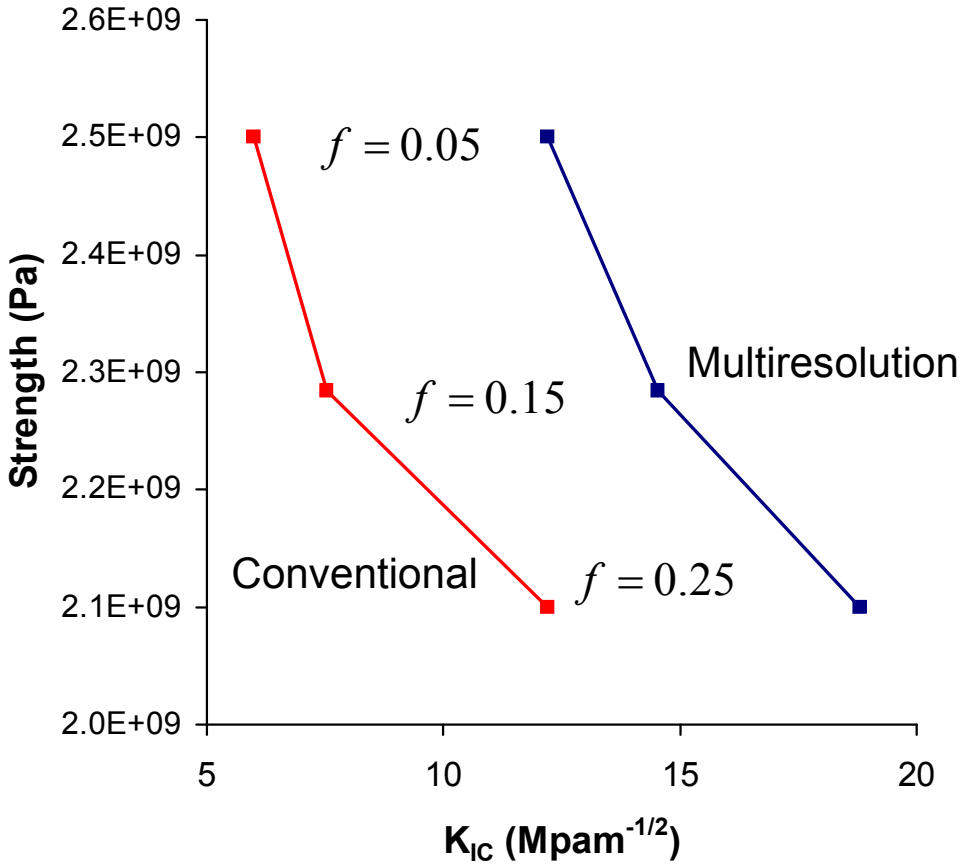

Figure 7.19. Fracture toughness shows an inverse relationship with strength when the cobalt volume fraction is varied.

7.5 Conclusion

Macroscale properties are inherently a function of the underlying micromechanics of a material. The multiresolution continuum theory used here offers a framework by which the microstructural evolution and the characteristic wavelength of deformation at each scale influences the resulting macroscale response. In the current fracture toughness simulations, toughness is predicted to increase with grain size and volume fraction of cobalt. These are both consistent with experimental observations (itia.org.uk 2006). The toughness is also predicted to increase with

loading rate –this has obvious benefits in terms of WC-Co cutting tools, however this has not been experimentally verified here. It is also interesting that a decrease in toughness is predicted with increasing temperature. In many alloys the toughness would be expected to increase with temperature due to the increased flow. However in the micromechanical model developed in Chapter 4 for WC-Co the increasing temperature weakens the ligaments severely, equation (4.14) which reduces the fracture toughness.

8 Dynamic Adiabatic Shear Bands

In Chapter 2, the micromechanics of deformation in a steel alloy are described (Section 2.2) for quasi-static loading and for dynamic loading (Section 2.3). Dynamic loading of an alloy complicates the micromechanics considerably; materials generally exhibit a stronger response when loaded at high rates. On the other hand rapid plastic flow often generates large temperature increases which result in a thermal softening effect. These effects, along with work hardening and microvoid damage, are all active during dynamic shear loading in a steel alloy.

The focus of this Chapter is to model the formation of adiabatic shear bands using a strain hardening/recovery, thermal softening, rate hardening, and damage dependent BCJ constitutive model (Chapter 3), with a variable length scale embedded through the multiresolution continuum theory (Chapter 5). The numerical model used to analyze the shear band is outlined in Section 8.1. In Section 8.2 the combined effects of microvoid damage and thermal softening are examined using a conventional continuum analysis. In Section 8.3 a length scale parameter related to the stable work hardening stage of deformation is introduced via the multiresolution formulation. In Section 8.4 a second length scale is introduced which is related to the post-instability softening stage of material deformation. Hence as the material reaches a shear instability the dominant length scale switches from the ‘hardening’ length scale to the ‘softening’ length scale. The effect of the key microstructural parameters on the shear band initiation and propagation is examined in Section 8.5. A review of microvoid nucleation, growth and coalescence in high strength steels is given in Appendix A5 where a series of 1D examples are used to describe the physics of adiabatic shear bands.

8.1 Two Dimensional Shear Bands: Set Up

The BCJ model (Bammann et al. 1990) described in Chapter 3 is used with three internal state variables:

- a scalar variable κ used to model isotropic hardening/recovery effects due to dislocation interactions (plasticity) – see equation (3.12)
- a scalar variable ϕ used to model porous damage – see equation (3.17)
- temperature ϑ used to model thermal softening and the temperature dependence of the other parameters – see equations (3.19)-(3.21). The temperature rise is due to plastic work dissipation; both adiabatic temperature rise and conductance effects are considered here.

Following the work of (Medyanik et al. 2005), the problem set up is shown in (Figure 8.1). A 2D plane strain formulation is used to model a pre-notched pate with a further pre-crack at the notch tip. The pre-crack is modeled by setting the stress to zero in three elements i.e. the pre-crack is one element wide. There are 21 elements in the lateral direction in the refined region in front of the pre-notch. Each element in this region is approximately $11\mu m$ in the 'y' direction which is small enough to model shear band widths on the order of tens of microns which are commonly reported in the literature (Wright 2002). An instantaneous velocity of 30m/s is applied to the bottom of the domain in the 'x' direction and the bottom surface is constrained in the 'y' direction. The top surface is constrained in both directions. Shear velocity boundary conditions are applied to the bottom surface.

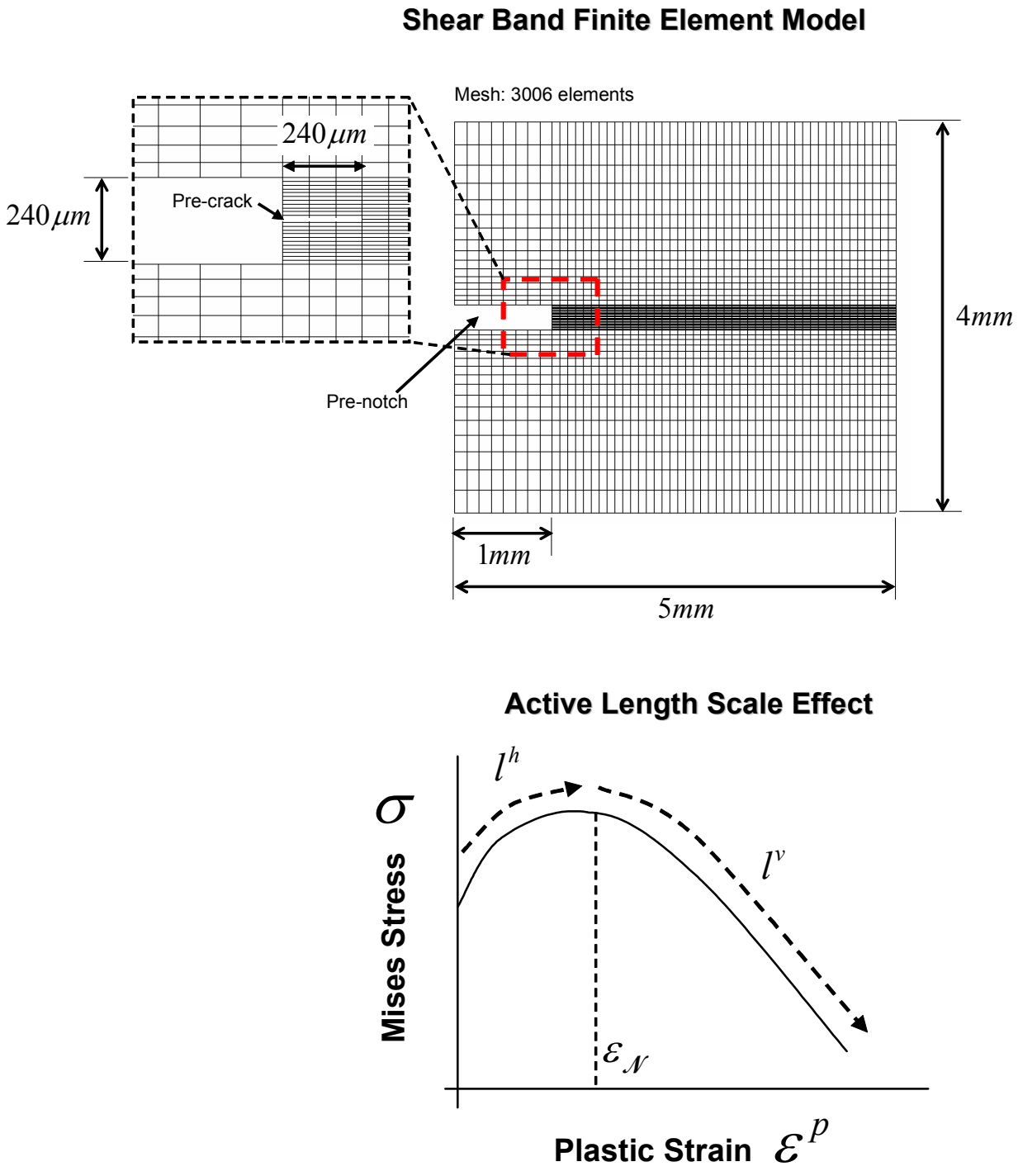

Figure 8.1. Finite element model for shear band simulations; a pre-notch and a pre-crack are modeled to initiate a shear band. The active length scales used in the multiresolution model, Section 8.4, are shown.

BCJ Parameters used in ASB Analysis					
Parameter		***Value***	***Parameter***		***Value***
Initial Temperature	θ_0	$297K$	Isotropic Static Recovery Modulus	C_7	0
Melt Temperature	θ_m	$1750K$		C_8	0
Thermal Softening Exponent	t	1.03	Kinematic Hardening Modulus	C_9	0
Reference Strain Rate	f	$1s^{-1}$		C_{10}	0
Magnitude of Rate Effect	V	$16MPa$	Kinematic Dynamic Recovery Modulus	C_{11}	0
Initial Yield Stress	C_1	$792MPa$		C_{12}	0
Hall-Petch Effect	C_2	0	Kinematic Static Recovery Modulus	C_{13}	0
Isotropic Hardening Modulus	C_3	$-20MPaK^{-1}$		C_{14}	0
	C_4	$22500MPa$	Specific Heat	c_{pt}	500
Isotropic Dynamic Recovery Modulus	C_5	$1.3\times10^{-13}Pa$	Density	ρ	$8000kgm^{-3}$
	C_6	$500K$	Heat Fraction	h_c	0.9

Table 8.1 BCJ model for a steel alloy (calibrated to the flow stress of a 4340 steel, Medyanik et al. 2005)

As stated previously the BCJ model is used to model the steel alloy. The BCJ constants are given in Table 8.1 for the flow behavior of the steel alloy being examined here; they are calibrated to an empirical rate and temperature dependent Johnson-Cook model used by (Medyanik et al. 2005). Microvoid damage is also considered here. The microvoid damage equations for a steel alloy have been developed using computational cell modeling analysis by (Vernerey 2006) and (McVeigh et al. 2006b) under quasi-static conditions; these are described in more detail in Appendix A4. Here it is assumed the same microvoid damage equations can be used under high rate loading. The damage equations for nucleation, growth and coalescence are summarized in Table 8.2. Nucleation rate $\dot{\eta}$ is considered to be normally distributed about a mean value of nucleation strain $\varepsilon_{\mathcal{N}}$ which in turn is a function of the precipitate particle interfacial strength σ^S and the second stress invariant (pressure) I_1 (Vernerey 2006). The maximum number of nucleated voids per unit area is equal the precipitate number density given by $\mathcal{N}^*$.

Void growth is described by the McClintock void growth equation (McClintock 1968) with a McClintock void growth constant, $n = 0.3$ and initial void radius equal to the precipitate radius $50nm$. Coalescence is described in terms of a coalescence criterion developed by (McVeigh et al. 2006b) in terms of the Mises plastic strain and current level of porosity.

In summary, the rate and temperature dependence of plastic flow are calibrated to empirical data while the damage equations have been developed through computational cell modeling.

Damage Phenomena	Equation	Required Constants	Value
Nucleation	$\dot{\eta} = \mathcal{N}\left\|\mathbf{D}_p\right\|$	-	-
	$\mathcal{N} = \frac{\mathcal{N}^*}{s_{\mathcal{N}}(2\pi)^{0.5}}\exp\left\{-\frac{1}{2}\left(\frac{\varepsilon^p - \varepsilon_{\mathcal{N}}}{s_{\mathcal{N}}}\right)^2\right\}$	$\mathcal{N}^*$	$2.55\times10^{12}\,m^{-2}$
		$s_{\mathcal{N}}$	0.05
	$\varepsilon_{\mathcal{N}} = \left(F_1 + F_2\sigma^S\right)\left(1 - \frac{I_1}{3\sigma^S}\right)$	F_1	–0.209
		F_2	0.228
Growth	$v = \pi r^2$	-	-
	$r = r_0\exp\left(\mathcal{G}\sqrt{3/2}\,\varepsilon^p\right)$	r_0	$50nm$
	$\mathcal{G} = \frac{\sqrt{3}}{2(1-n)}\sinh\left(\frac{\sqrt{3}}{2}(1-n)\left(\frac{2I_1}{3\sqrt{J_2}} + \frac{1}{3}\right)\right)$	n	0.3
Coalescence	$\dot{\phi}_{coal} = \mathcal{C}\left\|\mathbf{D}_p\right\|$ when $\phi + \mathrm{F}_3\varepsilon^p + \mathrm{F}_4 > 0$	F_3	0.122
		F_4	–0.124
		$\mathcal{C}$	1
Total Porosity	$\phi = \eta v + \phi_{coal}$	-	-

Table 8.2 Microvoid damage equations and parameters, from (McVeigh et al. 2006b; Vernerey 2006)

8.2 ASB: Thermal versus Void Assisted Instability

In this Section the effect of microvoid nucleation is discussed in terms of its influence on shear banding. When thermal effects are considered an adiabatic approach is used i.e. thermal conductance is neglected (in this Section only). Three cases are examined for comparison:

- Case (i) - No thermal or microvoid effects
- Case (ii) - Only thermal effects are considered (microvoiding is neglected)
- Case (iii) - Both thermal softening and microvoid nucleation are considered

As shown in (Figure 8.2) in each case the plastic strain localizes inhomogeneously at the pre-crack tip.

Case (i): When both thermal and microvoid effects are neglected the material work hardens to high strains; the resulting plastic strain is quite diffuse in front of the pre-crack. Although plastic deformation is distributed throughout the specimen, the geometrical stress concentration effect of the sharp crack tip acts to concentrate the deformation. A shear band does not form.

Case (ii): The specimen initially deforms quite homogenously as the material work hardens. However the temperature rise from plastic work dissipation leads to thermal softening in the material directly at the crack tip and a shear band propagates.

Case (iii): The specimen initially deforms quite homogenously as in Case (i) and Case (ii). However the highly localized strain at the crack tip induces microvoid nucleation, growth and coalescence. The growing porosity and increasing temperature combine to produce sever strain softening immediately ahead of the crack tip – the resulting shear band progresses rapidly.

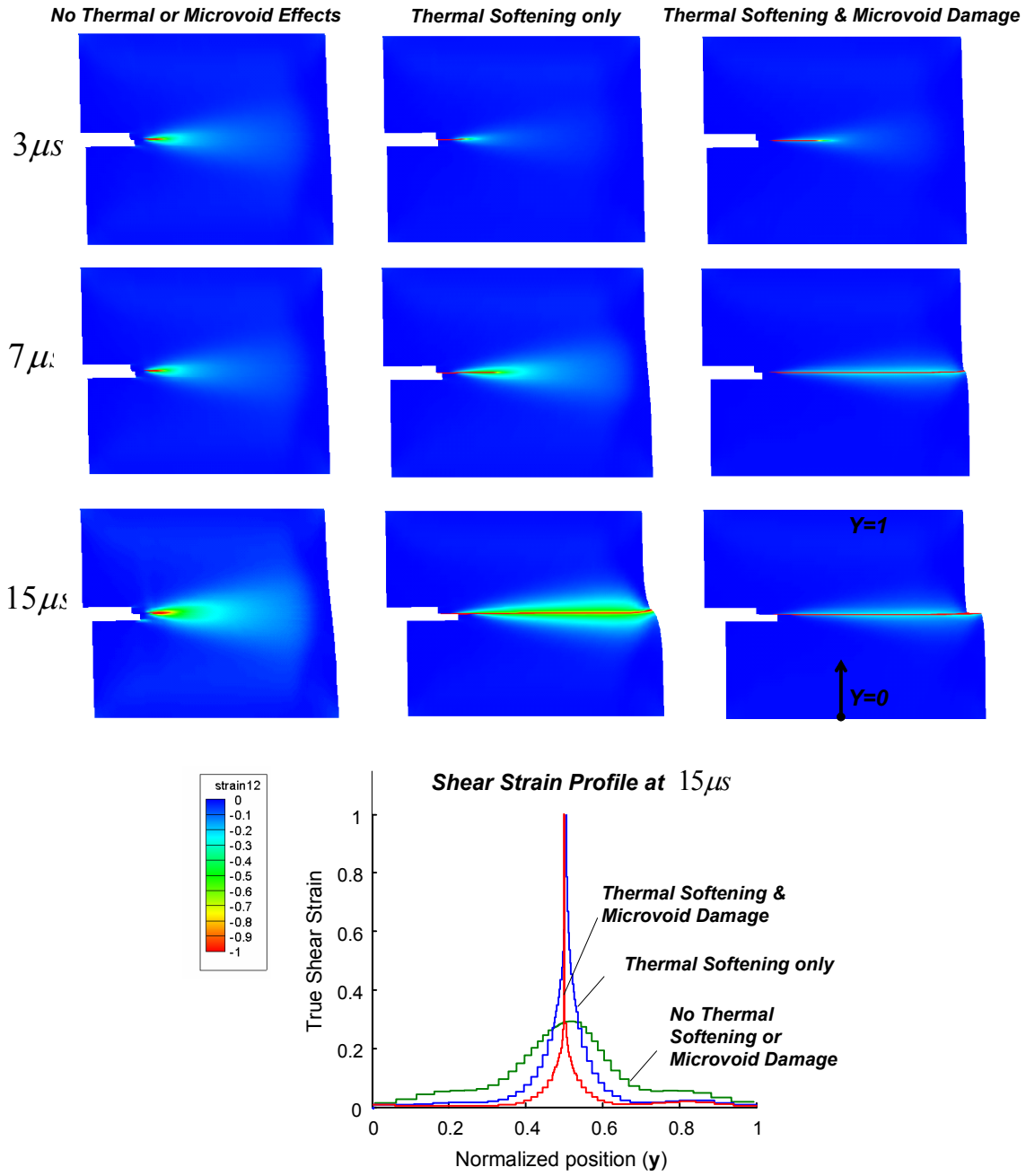

Figure 8.2. Thermal softening leads to a thermal shear instability. The addition of microvoiding acts to hasten the onset of a shear instability; the time for homogeneous deformation is reduced.

The shear strain across a section is plotted (Figure 8.2) for each case at 15 microseconds. From this plot it is clear that the terminal shear instability and subsequent strain localization occurs

first for Case (iii) at a shear strain of 0.25 which corresponds to the strain at microvoid nucleation. Case (ii) undergoes localization at a shear strain of 0.6 which is the strain at which thermal softening becomes grater than work (and rate) hardening and a thermally driven shear instability occurs. Terminal localization does not occur in Case (i). When microvoid damage is considered the shear band penetrates through the plate in approximately half the time (compared to when microvoiding is neglected). This emphasizes the importance of considering ***microvoid*** assisted adiabatic shear bands. Some other observations can be made about this simulation:

- When terminal localization occurs, the strain tends to localize spuriously in a single band of elements. It is likely that the post instability inhomogeneous deformation will be characterized by a length scale associated with the microvoids as described in Section 2.3.
- Even when only hardening is considered in Case (i), the deformation tends to localize giving rise to strong gradients. An extra hardening effect may be necessary to capture the effects of extra geometrically necessary dislocations associated with strong gradients in hardening alloys. This is discussed in Section 8.3.
- Thermal conductivity has not been considered in this simulation. The thermal conductivity effect will act to disperse the temperature rise over a wider area, possibly delaying the onset of a terminal shear instability or decreasing the severity of post instability strain localization (or both).

8.3 Hardening Length Scale

Inhomogeneous deformation is not limited to strain softening materials. For example in the process zone ahead of a crack tip deformation is extremely inhomogeneous. This gives rise to an increased number of geometrically necessary dislocations (GND's) resulting in increased work hardening (Gao et al. 1999) when small scale deformation occurs. In terms of the continuum constitutive response, (Gao et al. 1999) developed a flow stress relationship which accounts for the extra 'gradient' hardening at small scales:

$$\sigma = \sigma_0 \sqrt{\varepsilon^{2n} + l\eta} \tag{8.1}$$

where σ is the flow stress, σ_0 is the initial yield stress, ε is the plastic Mises strain, η is a scalar form of the strain gradient, n is the strain hardening exponent and l is the characteristic length scale of the deformation which induces extra hardening. The length scale effect in equation (8.1) is clear; as the gradient increases the amount of hardening increases.

The multiresolution approach developed in Chapter 5 is used here to demonstrate the effect of introducing a length scale into a continuum model of a work hardening material. Thermal softening and microvoid damage are neglected, resulting in a strain *hardening* BCJ constitutive relation (Table 8.1). A single microstress is used in the multiresolution governing equations (5.25) giving:

$$\begin{aligned} \left(\boldsymbol{\sigma} - \boldsymbol{\beta}^1\right) \bullet \nabla &= \mathbf{0} \quad \text{in} \quad \Omega \\ \nabla \bullet \overline{\boldsymbol{\beta}}^1 - \boldsymbol{\beta}^1 &= \mathbf{0} \quad \text{in} \quad \Omega \end{aligned} \tag{8.2}$$

and the microscale elastic constitutive response is given by equation (6.3), repeated here for clarity:

$$\overset{\nabla}{\boldsymbol{\beta}}^{1} = \mathbb{C}^{1} \bullet \left(\mathbf{L}^{1} - \mathbf{L} \right)^{e}$$
$$\overset{\nabla}{\overline{\boldsymbol{\beta}}}^{1} = \overline{\mathbb{C}}^{1} \bullet \left(\mathbf{L}^{1} \overset{\leftarrow}{\nabla} \right)^{e} \tag{8.3}$$

The microscale elastic tensors $\mathbb{C}^{1}$ and $\overline{\mathbb{C}}^{1}$ are defined according to equation (6.10) which is also repeated here:

$$\mathbb{C}^{1} = \mathbf{C}_{m}$$
$$\overline{\mathbb{C}}^{1} = \frac{\left(l^{h} \right)^{2}}{12} \mathbf{C}_{m} \otimes \mathbf{I} \tag{8.4}$$

The embedded length scale l^{h} is related to the scale over which inhomogeneous deformation occurs. In the case of a hardening material it is assumed here that the inhomogeneous deformation extends over the mean dislocation path length which is given by the alloy grain size. For the current steel alloy examined here a value of $l^{h} \sim 100 \mu m$ is reasonable for the grain size. The microstructural elastic tensor $\mathbf{C}_{m}$ is considered to be isotropic and equal to the alloy's elastic tensor i.e. a Young's modulus of $200 GPa$ and Poisson's rate of 0.29 are used.

A conventional continuum simulation is also compared, in which no length scale effect is present. The resulting plastic strain contours are compared in (Figure 8.3); the shear strain across a section is also plotted for each case.

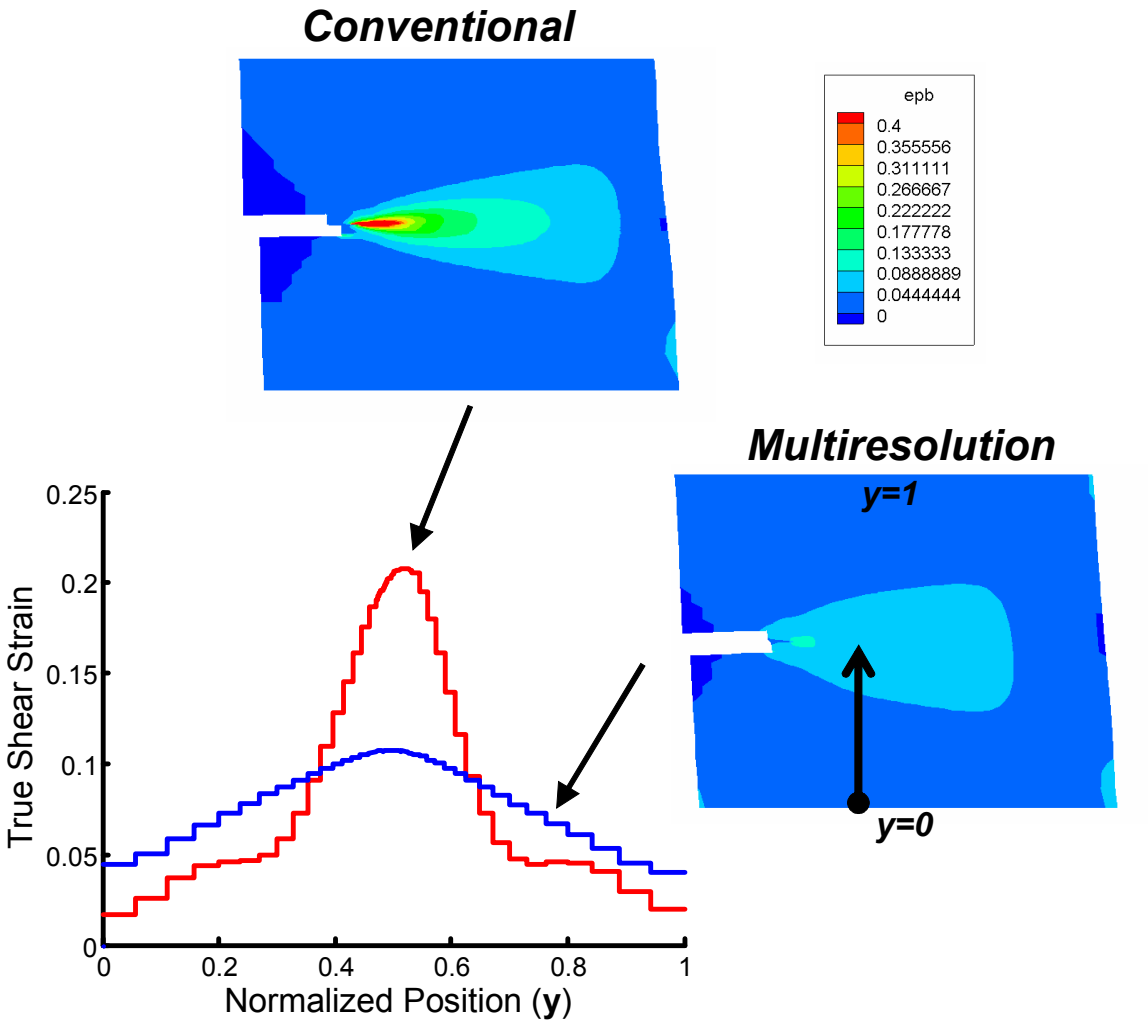

Figure 8.3. The addition of a hardening length scale in the model acts to reduce gradients during the work hardening stage of deformation. This is similar to introducing extra work hardening at small scales. Distances are normalized by the plate height i.e. y=1 corresponds to 4 mm as shown.

When the conventional continuum approach is used, the deformation localizes ahead of the pre-notch due to the geometrical stress concentrating effect. The strain gradients become quite high in this region. When the multiresolution approach is used, the deformation becomes more diffuse over the length scale associated with the embedded length l^h. The couple stress in the multiresolution formulation act to resist local strain gradients. This has the same effect as

increasing the work hardening, equation (8.1). More details can be found in (McVeigh et al. 2006a).

8.4 Void Assisted ASB with Two Length Scales

In this Section, the multiresolution approach is again used. Both microvoid damage and thermal softening are considered. The purpose of this section is to compare analysis techniques i.e. multiresolution versus conventional continuum and adiabatic versus fully couple thermal analysis. The problem is described in Section 8.4.1. Different analyses approaches are compared in Section 8.4.2. The shear band velocity is discussed in Section 8.4.3. A further length scale parameter l^v is introduced. This parameter becomes active when the material is softening i.e. in the post-shear instability regime of deformation. The value of this parameter is given by the length scale of strain localization observed in alloys which fail by micro-voiding which is often observed to be on the order of the microvoid spacing.

8.4.1 Problem Description

The length scales considered in the multiresolution analysis are related to:

- the grain size, l^h as discussed in Section 8.3.
- the microvoid spacing, l^v.

The hardening length scale l^h is given here by $l^h = 100\mu m$. The length scale of the post-instability localizing deformation l^v is given by $l^v = 20\mu m$ i.e. on the order of the precipitate

spacing. This length scale is used here to characterize the post-instability softening response of the alloy. The reduced multiresolution model described in Section 5.5 is used here for efficiency:

$$\begin{aligned} \left(\boldsymbol{\sigma}-\boldsymbol{\beta}^{ms}\right)\bullet\nabla &= 0 \quad \text{in} \quad \Omega \\ \nabla\bullet\bar{\boldsymbol{\beta}}^{ms}-\boldsymbol{\beta}^{ms} &= 0 \quad \text{in} \quad \Omega \end{aligned} \tag{8.5}$$

where the microstress constitutive relationship is given by equation (5.28):

$$\begin{aligned} \overset{\nabla}{\boldsymbol{\beta}}^{ms} &= \mathbb{C}^{ms}\bullet\left(\mathbf{L}^{ms}-\mathbf{L}\right)^{e} \\ \overset{\nabla}{\bar{\boldsymbol{\beta}}}^{ms} &= \bar{\mathbb{C}}^{ms}\bullet\left(\mathbf{L}^{ms}\tilde{\nabla}\right)^{e} \end{aligned} \tag{8.6}$$

The elastic tensors are given by equation (5.32):

$$\begin{aligned} \mathbb{C}^{ms} &= \mathbf{C}_{m} \\ \bar{\mathbb{C}}^{ms} &= \frac{\left(l^{ms}\right)^{2}}{12}\,\mathbf{C}_{m}\otimes\mathbf{I} \end{aligned} \tag{8.7}$$

The microstructural elastic tensor $\mathbf{C}_m$ is considered to be isotropic and equal to the alloy's elastic tensor i.e. a Young's modulus of $200GPa$ and Poisson's rate of 0.29 are used. There are two possible active length scales at any material point; l^h is active during hardening (before the shear instability), l^v is active during softening (after the shear instability). The shear instability occurs due to microvoid nucleation (Table 8.2) i.e. a microstructural instability event. Hence the microvoid nucleation strain $\varepsilon_{\mathcal{N}}$ determines when the material begins to soften and the active length scale switches from l^h to l^v as shown in (Figure 8.1):

$$\begin{aligned} l^{ms} &= l^{h} = 100\mu m \quad \text{when} \quad \varepsilon < \varepsilon_{\mathcal{N}} \\ l^{ms} &= l^{v} = 20\mu m \quad \text{when} \quad \varepsilon \geq \varepsilon_{\mathcal{N}} \end{aligned} \tag{8.8}$$

The effects of thermal conductance (compared to adiabatic) are also examined. When thermal conductance is considered, the predicted temperature rise is generally lower and more diffuse as

described in Section 2.3. This delays the terminal shear instability and widens the post-instability localization length scale.

Four combinations of thermal and mechanical analyses are examined in this Section:

- Conventional continuum (no length scale) with adiabatic temperature rise
- Conventional continuum (no length scale) with thermal conductance
- Multiresolution continuum (two length scales) with adiabatic temperature rise
- Multiresolution continuum (two length scales) with thermal conductance

8.4.2 Comparison of Analysis Methods

In (Figure 8.4) the plastic strain contours resulting from the four analyses are shown at $20\mu s$. The plastic strain across a section in the 'y' direction is also plotted. Two immediate observations can be made:

- the multiresolution analysis captures the micromechanical length scales associated with hardening and softening (compare the adiabatic cases)
- the fully coupled thermal-mechanical analysis results in a wider shear band (compare the conventional continuum case)

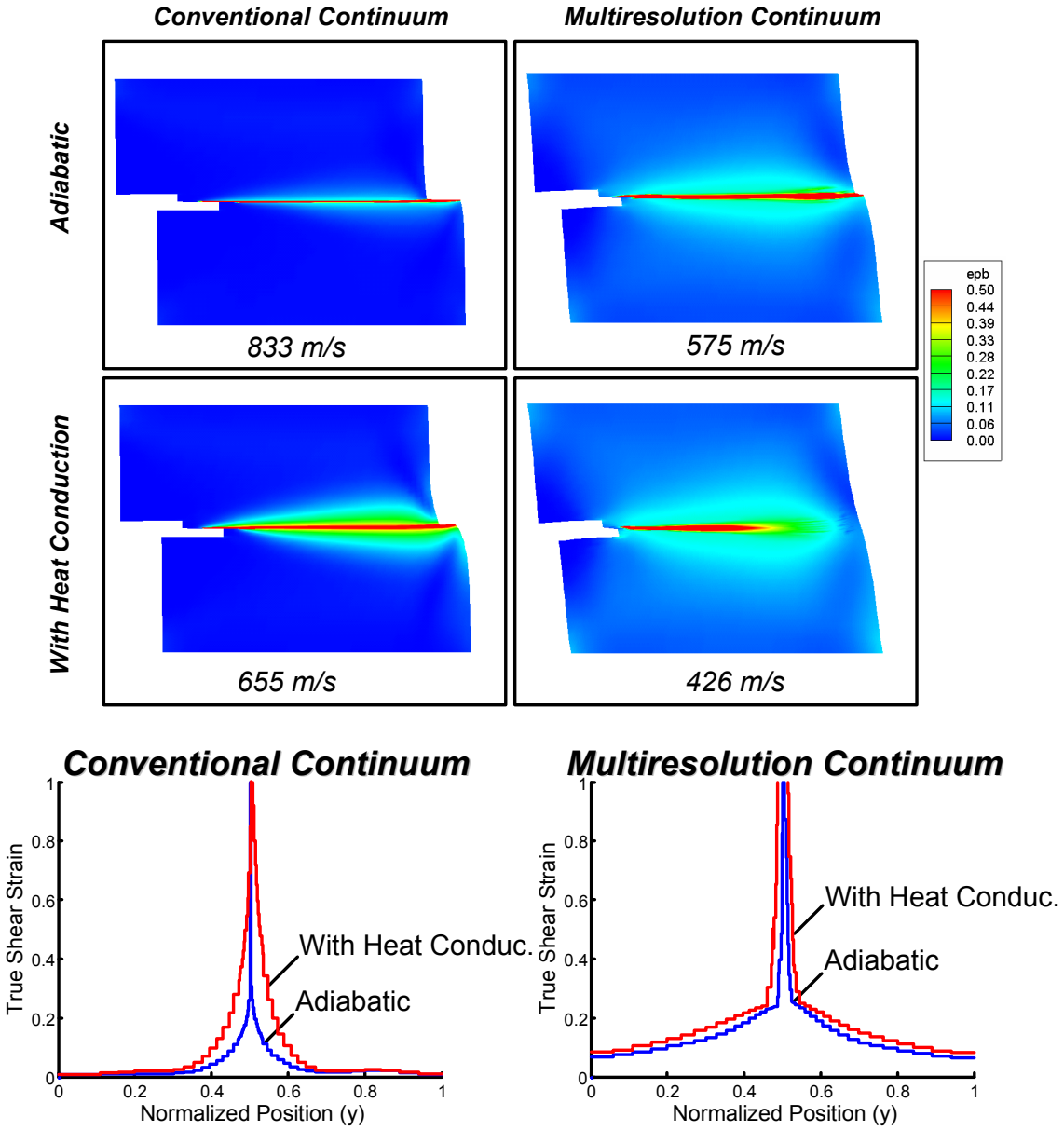

Figure 8.4. Heat conduction acts to widen the shear band, whether a conventional or multiresolution continuum approach is used. The multiresolution continuum analysis captures the diffuse homogeneous deformation and the post-instability inhomogeneous length scale.

When the multiresolution formulation is used in (Figure 8.4), the deformation ahead of the shear band is relatively homogeneous due to the embedded hardening length scale. This is consistent with physical shear band formation which is characterized by "*high external strain…and extreme*

internal strain" (Wright 2002). For example in (Figure 8.5) the high external strain field at the periphery of the localized shear band in a cold rolled steel can be observed.

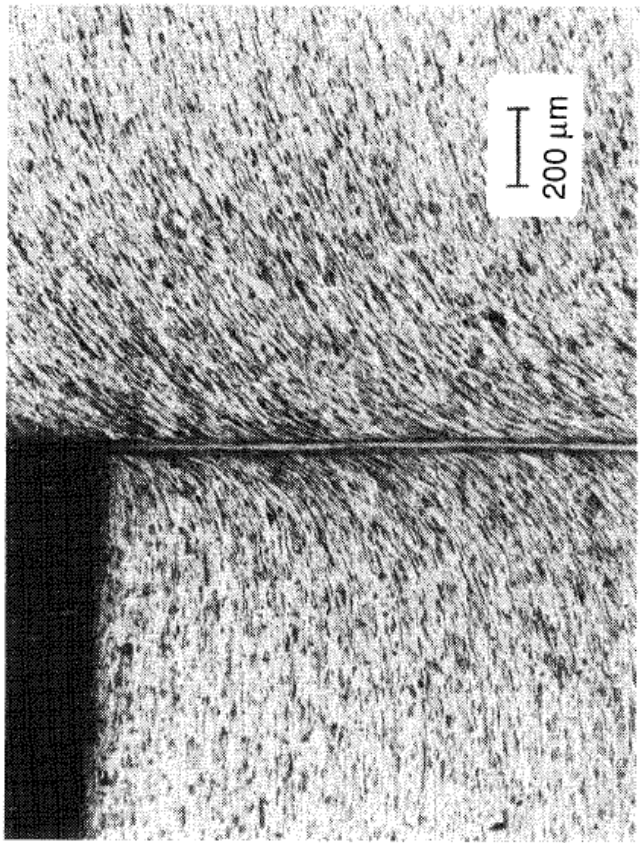

Figure 8.5. Shear bands usually exhibit an external region of high shear strain in addition to the shear band itself (Rogers 1983)

The mesh is plotted in (Figure 8.6) (at 24 microseconds) for each simulation. Two observations can be made:

- Conventional Continuum: The unphysical nature of strain localization predicted by the conventional continuum analyses can clearly be observed on the left most meshes. When a fully coupled simulation is used, the heat conduction delays the shear instability, however the post instability deformation still localizes unphysically in a single element.

- Multiresolution Continuum: The post-instability localization occurs at the length scale l^v. When the heat conduction is considered the post-instability localization is more diffuse – the conductance acts to widen the shear band.

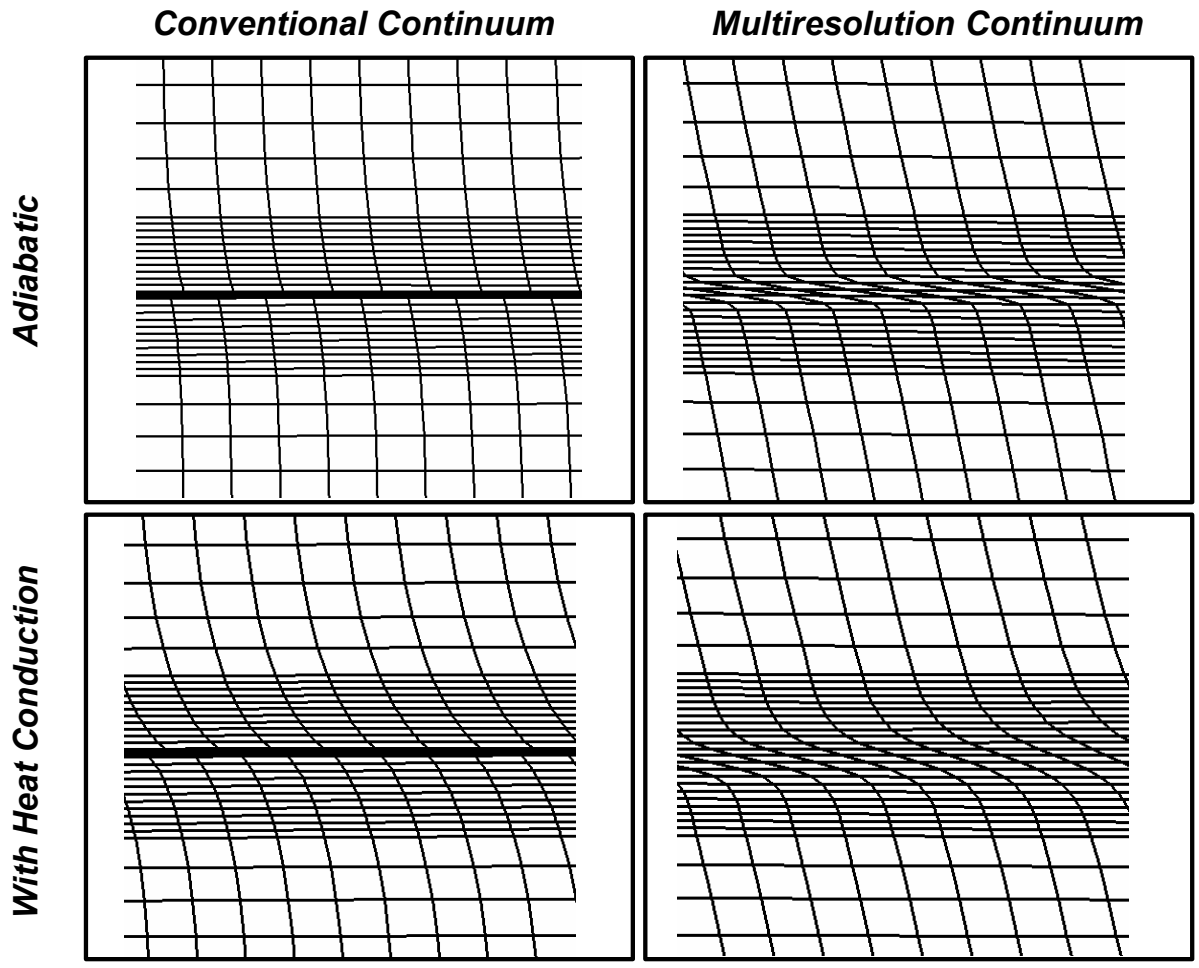

Figure 8.6. The conventional continuum analysis results in severe mesh dependency regardless of whether or not thermal conductance is included. The multiresolution analysis regularizes the post instability deformation over a physical scale, related to the microvoiding.

8.4.3 Shear Band Velocity

The distance traveled by the shear band is plotted in (Figure 8.7) for each of the four analyses performed in Section 8.4.2, (Figure 8.4). An element is considered to be part of the shear band when the Mises stress drops to 50% of the initial yield stress due to damage and thermal softening.

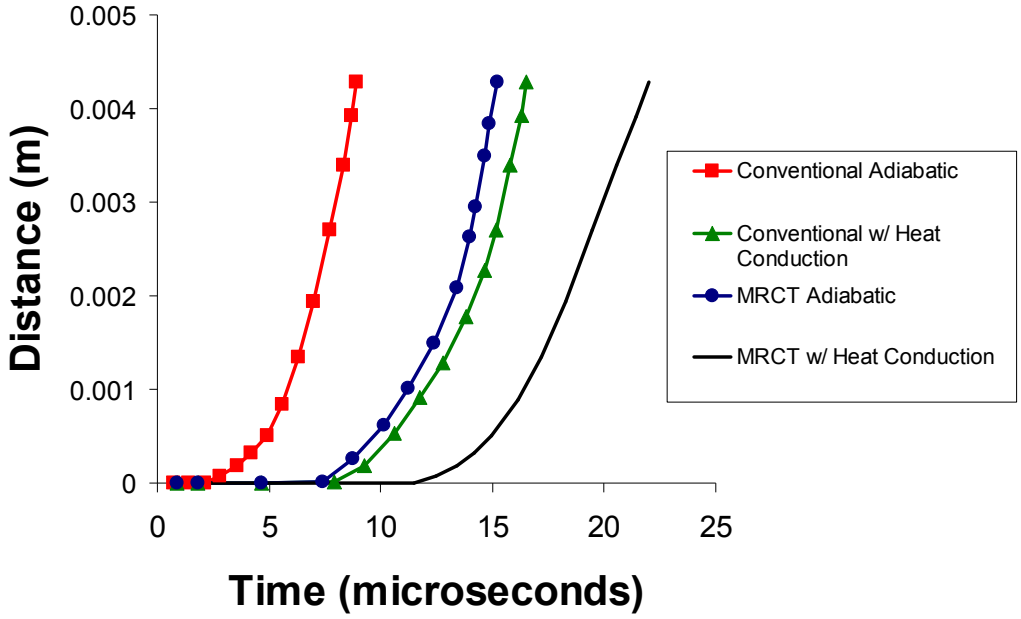

Figure 8.7. The shear band speed is greatest for the conventional continuum with adiabatic temperature rise. The slowest shear band is predicted by the MRCT analysis with heat conduction. (Medyanik et al. 2005) predicted a curve approximately half way between the Conventional Adiabatic and MRCT Adiabatic cases.

As expected the adiabatic conventional continuum case produces the fastest shear bands. Deformation is more localized even during the work hardening stage of deformation in front of the shear band and thermal softening is much more rapid due to the adiabatic temperature rise. Both of these effects accelerate the onset of shear instability. Once the instability occurs, the

deformation localizes within a single element band. The multiresolution (MRCT) approach with heat conduction predicts the slowest velocity; the embedded length scale gives rise to less diffuse deformation and the thermal conductance decreases the peak temperature. Both lead to a delay in the shear instability.

The average speed of the fully coupled multiresolution shear band propagation is 416m/s; this is similar to the velocity predicted by (Medyanik et al. 2005) for the same geometry, material and loading conditions. In their work, they switched from a solid to a fluid model when a rate and temperature criterion was satisfied – this causes the shear stresses to collapse. Here, the combined effects of thermal softening and microvoid damage are sufficient to replicate a rapid shear stress collapse within the resulting shear band, and a fluid model is not required to model the subsequent shear band propagation.

8.5 Design Considerations

The ability to predict adiabatic shear band behavior in alloys in terms of the underlying microstructural parameters has obvious advantages in terms of materials design for ballistic impact. Here we examine the changes in shear band velocity in terms of the constitutive parameters such that $v_{ASB} = v_{ASB}\left(\sigma^S, C_1, \vartheta_m, l^h, l^v, \mathcal{M}^*\right)$. Shear band velocity is assumed to be a good measure of resistance to adiabatic shear band formation and propagation. The key parameters which are varied are:

- precipitate particle interfacial strength σ^S, equation (8.5)
- initial yield strength C_1, equation (3.11)

- melt temperature ϑ_m, equation (3.11)
- length scale of hardening i.e. grain size l^h, equation (8.8)
- length scale of post-instability softening i.e. microvoid spacing l^v, equation (8.8)
- initial concentration/number density of precipitates $\mathcal{N}^*$, equation (8.4)

8.5.1 Precipitate Interfacial Strength σ^S

Increasing the precipitate particle interfacial strength σ^S increases the mean strain for nucleation ε_N according to Table 8.2. This delays the shear instability and results in a slower shear band as shown in (Figure 8.8). It is notable that when the interfacial strength is very large (>2GPa) the precipitates do not debond. However a shear instability will still occur due to thermal softening.

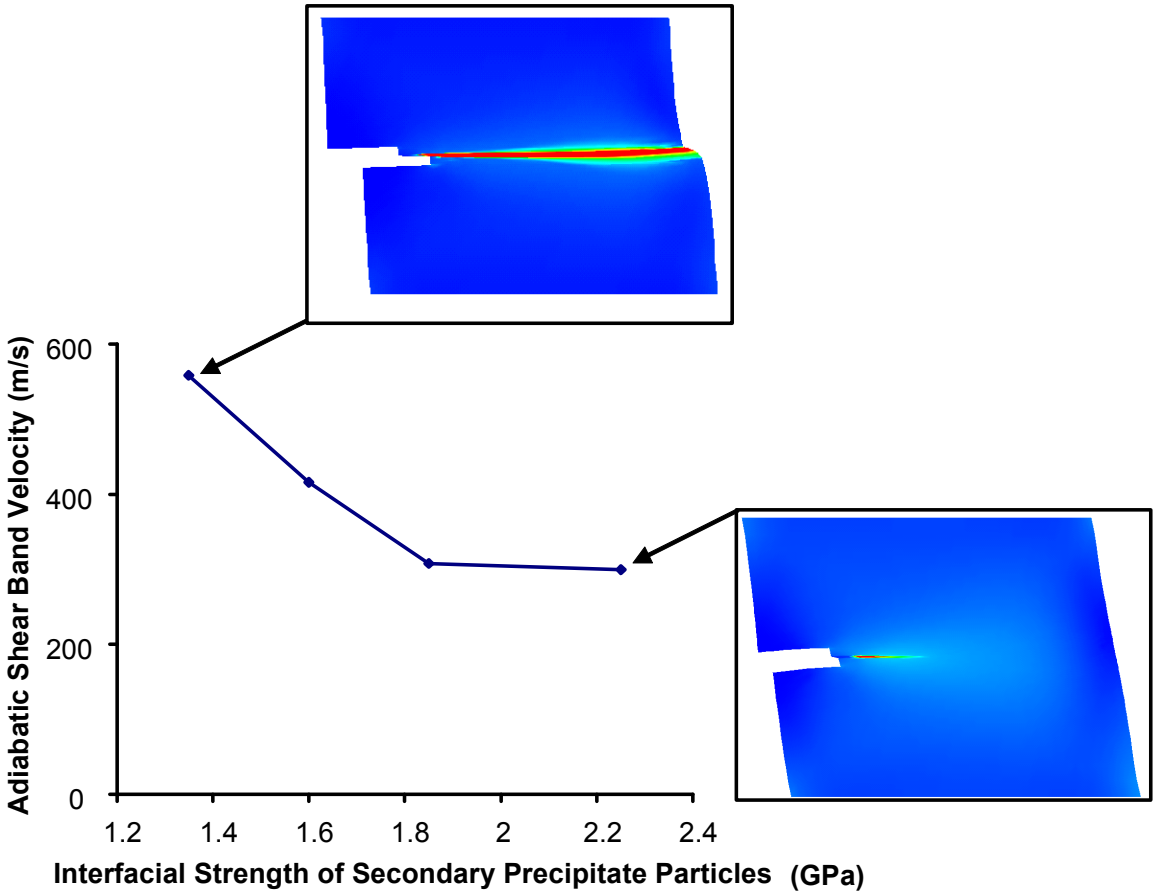

Figure 8.8. ASB velocity decreases with increasing precipitate interfacial strength

8.5.2 Initial Yield Stress C_1

The initial rate and temperature independent yield stress C_1, equation (3.11) is varied from 700-1200 MPa as shown in (Figure 8.9). The general trend shows that the shear band velocity increases with yield stress. This is consistent with (Medyanik et al. 2005) who showed that shear bands propagated much faster in steel than in copper (steel has a much higher yield stress than copper).

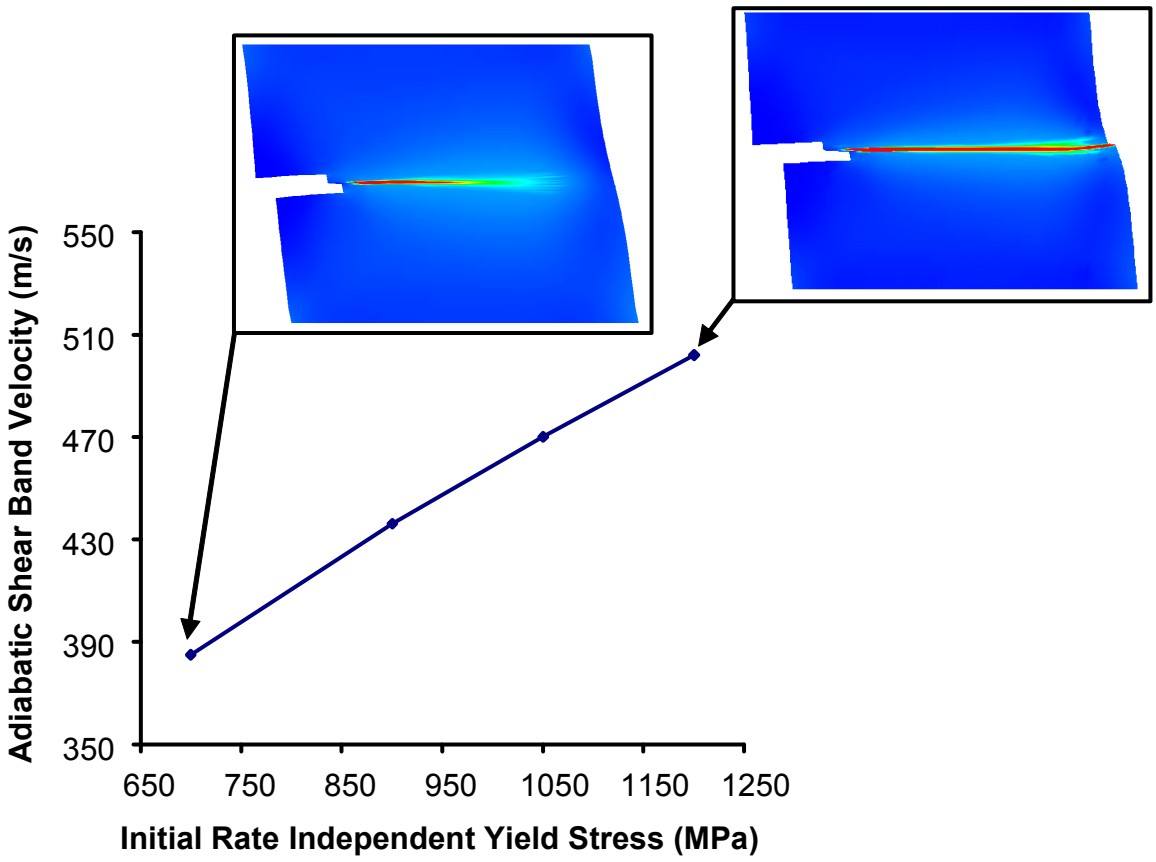

Figure 8.9. ASB velocity increases with initial yield stress

8.5.3 Thermal Softening ϑ_m

The effect of thermal softening is investigated by varying the melting temperature ϑ_m. This effectively scales the thermal softening function ϑ^* defined in equation (3.11) i.e. decreasing the melting temperature ϑ_m magnifies the thermal softening effect. As expected the model predicts increasing shear band velocity as melt temperature decreases (extra thermal softening is predicted), due to the extra thermal softening effect as shown in (Figure 8.10)

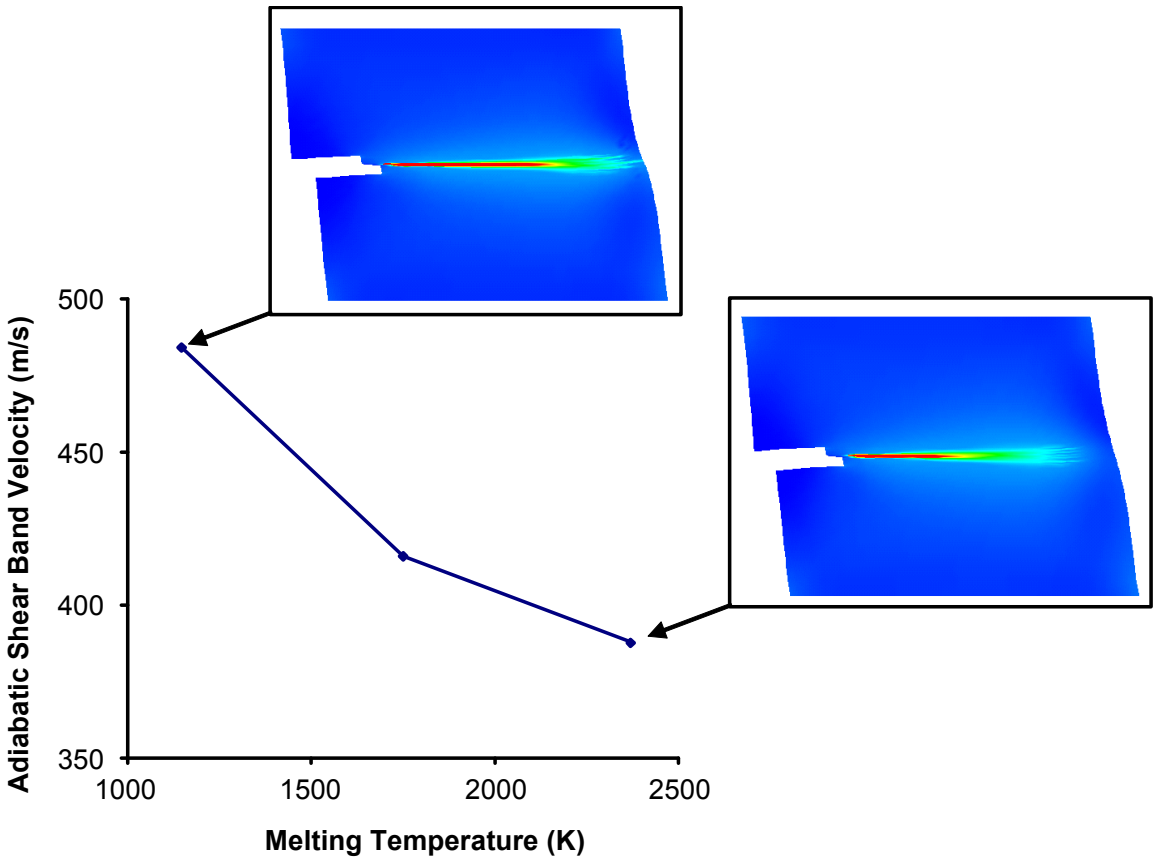

Figure 8.10. ABS velocity decreases with melting temperature

8.5.4 Length Scale of Hardening l^h

The hardening length scale l^h is varied from 100 to 25 microns as shown in (Figure 8.11). Larger values of l^h result in a more diffuse, homogenous strain field ahead of the shear band as shown in (Figure 8.3). This reduces the peak strain and stress, reducing thermal softening and delaying microvoid nucleation. Hence the shear instability is also delayed resulting in a lower shear band velocity.

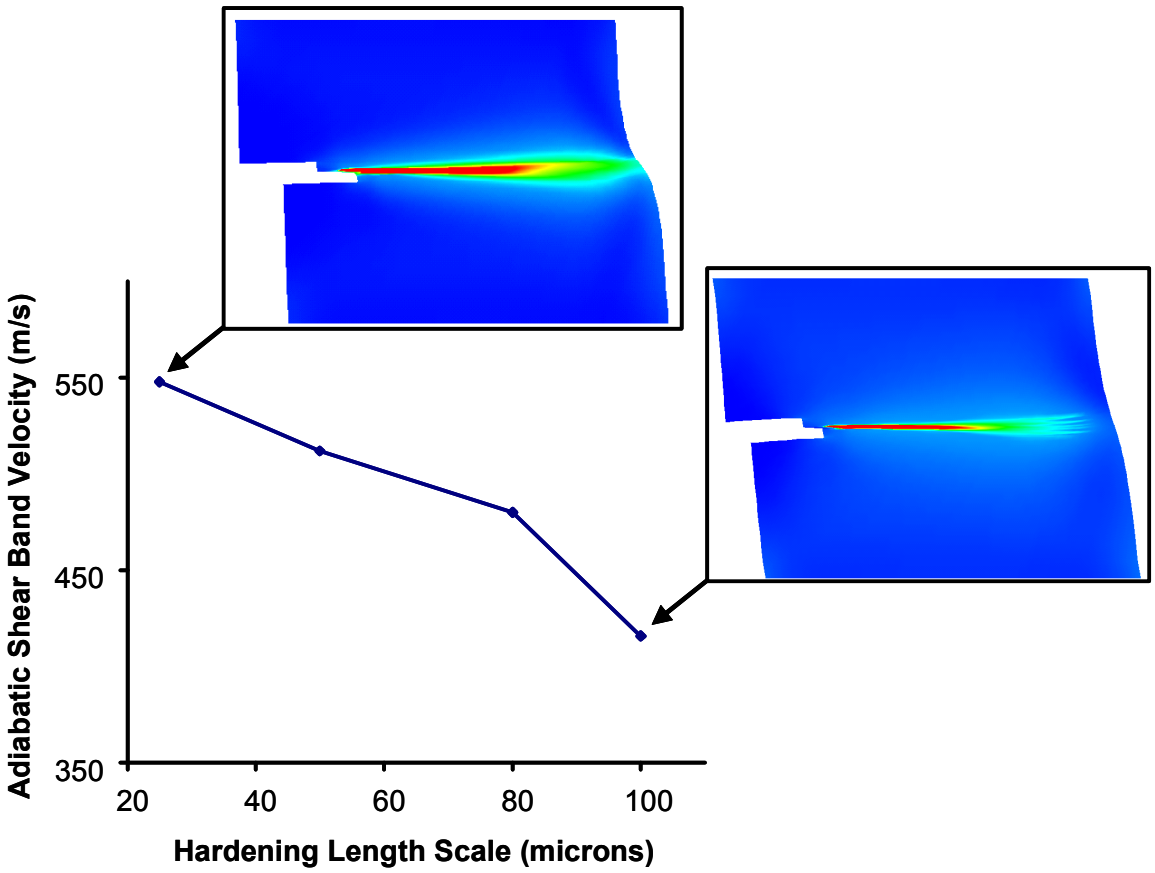

Figure 8.11. ASB velocity decreases with the hardening length scale

8.5.5 Length Scale of Microvoiding l^v

The length scale associated with microvoiding l^v is varied from 20 microns to 30 microns as shown in (Figure 8.12). Smaller values of l^v result in more localized post-instability deformation. The more localized plasticity results in greater thermal softening within the shear band which leads to a more rapid stress drop and hence faster shear band propagation.

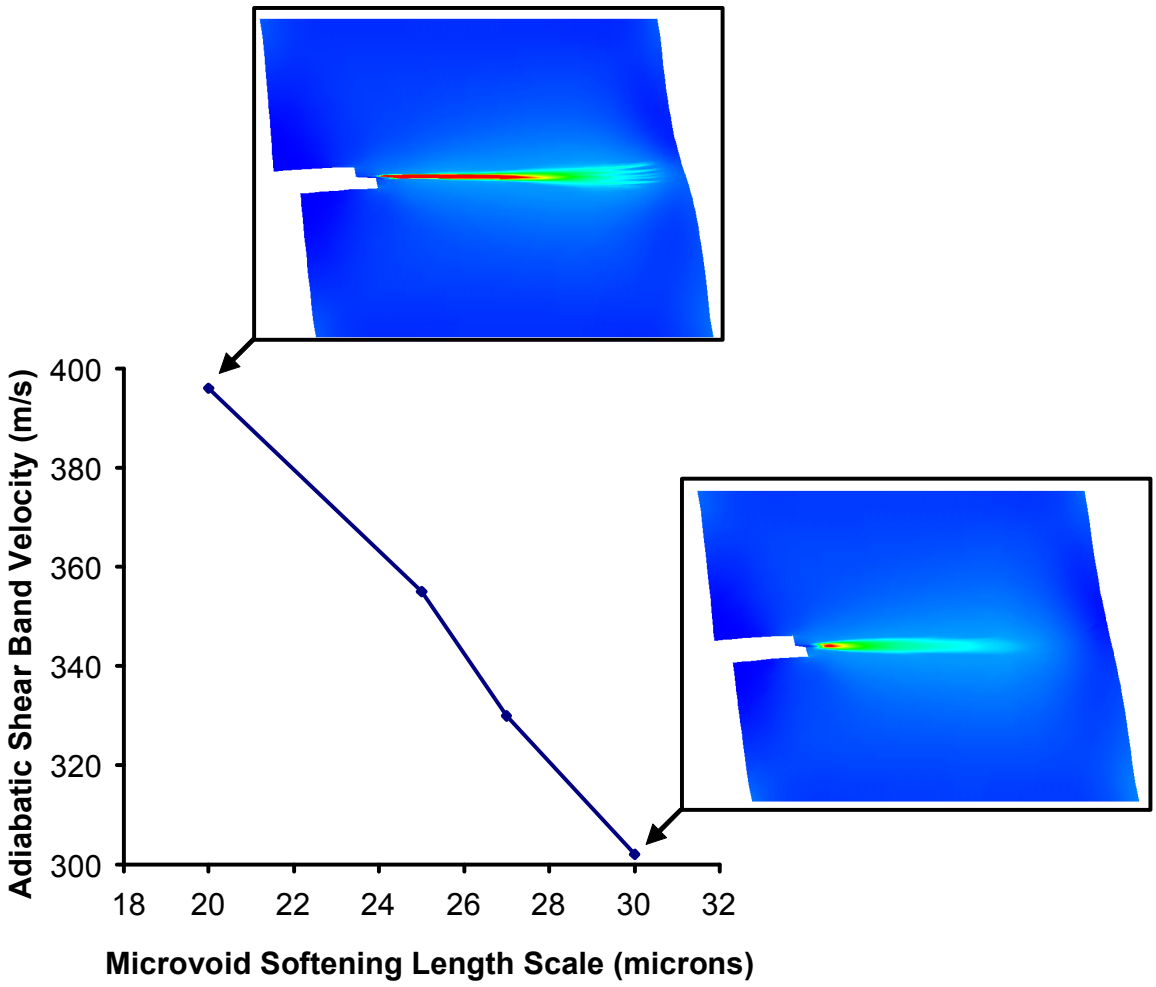

Figure 8.12. ASB velocity decreases with increasing post-instability softening length scale

8.5.6 Number Density of Precipitates $\mathcal{N}^*$

The number density of precipitates determines the magnitude of the microvoid porosity effect (-see Table 8.2). At larger values of $\mathcal{N}^*$ the stress collapse in the shear band is more rapid due to the higher porosity rate (Table 8.2). This leads to greater shear band velocities when more precipitates are present as shown in (Figure 8.13). The number of precipitates is varied here independently of precipitate/microvoid spacing (which is related to l^v) or precipitate size (which is not explicitly accounted for in the model).

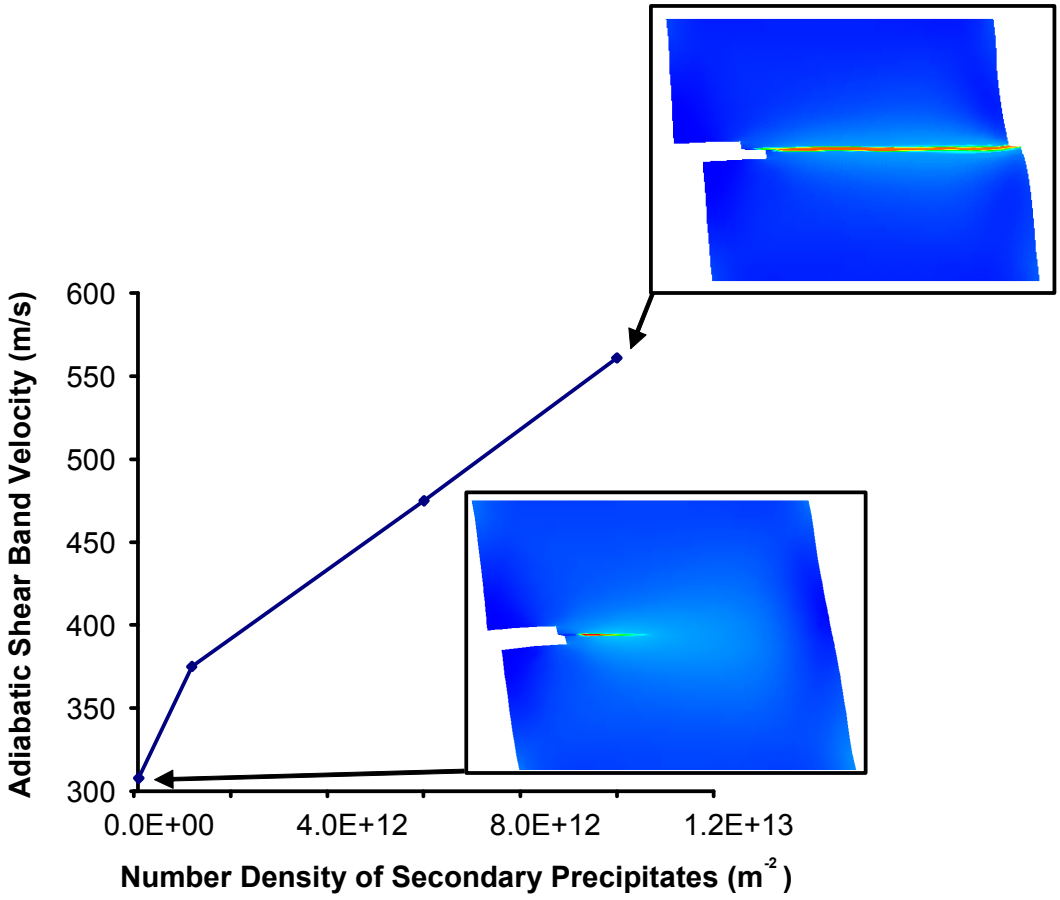

Figure 8.13. ASB velocity increases with increasing precipitate number density

8.6 Conclusion

The relationship between shear band speed v_{ASB} and microstructure and environmental conditions $\sigma^S, C_1, \vartheta_m, l^h, l^v, \mathcal{N}^*$ has been examined for a steel alloy using a multiresolution continuum theory. The velocity of the shear band is related to (a) how quickly a shear instability initiates and (b) the nature of the post-instability localization. Increasing interfacial strength σ^S is predicted to reduce shear band speed; however even at very high interfacial strengths thermal effects alone still initiate a shear band. Reducing the thermal softening (increasing ϑ_m) or the number density of precipitates $\mathcal{N}^*$ also leads to a slower shear band. The reduction in strength which would accompany a reduction in the number of precipitates $\mathcal{N}^*$ is not accounted for in the model. However a reduction in initial yield stress C_1 has been shown to reduce the shear band speed. Increasing the length scale of hardening l^h reduces the shear band velocity, presumably because the deformation is more diffuse, which delays microvoid nucleation and thermal softening. Increasing the length scale associated with post-instability localization l^v also leads to a reduction in shear band speed. This spreads out the post instability localizing strain over a more diffuse region, slowing the shear band.

9 Conclusions and Future Direction

The goal of this thesis was to develop a general material modeling approach which links material properties/component performance to evolving microstructure. In particular a method was sought which could retain the heterogeneous microstructure length scale effects within the context of a homogenized continuum.

9.1 Conclusions

An overview of current material modeling approaches including conventional continuum theory, higher order continuum and continuum-discrete coupling was been given in Chapter 1. The multiscale nature of two interesting materials (cemented carbide and a steel alloy) was discussed in Chapter 2. The form of the constitutive models used in this thesis were then outlined in detail in Chapter 3 in order to lay the ground work for building a hierarchical constitutive model of a cemented carbide (WC-Co composite) in Chapter 4. This hierarchical constitutive model incorporated the key microstructural–property relationships including the effects of temperature, strain rate, brittle damage and ductile damage, cobalt grain size and volume fraction. However when applied within a conventional continuum based numerical fracture toughness simulator, the predicted fracture toughness was lower than experimentally observed values.

This discrepancy was not due to the constitutive model – the problem lies in the conventional continuum (finite element) analysis used to model the crack growth. Traditional finite element analysis is notorious for it inability to predict size effects which occur when the wavelength of

deformation approaches the microstructural length scale. The only length scale present in the model relates to the size of the finite element mesh discretisation used. The strain field ahead of the crack tip subsequently localizes within a single band of elements.

However in the direct numerical simulations, where the discrete microstructural feature are modeled explicitly, the strain field ahead of a crack is observed to be spread out over several characteristic length scales which are directly related to the microstructural features. This multiscale inhomogeneous plastic deformation blunts the crack tip, leading to increased energy absorption by the material as the crack prorogates. Unfortunately this multiscale crack tip blunting cannot be replicated in the conventional continuum based fracture toughness simulator used in Chapter 4.

In Chapter 5 a multiresolution continuum analysis approach is developed which can be used to replicate microstructure length scale effects within the context of a higher order gradient enhanced continuum. In particular

- Extra ‘microstress’ and ‘microstress couple’ continuum fields were introduced into the continuum partial differential governing equations which capture the evolving scale of inhomogeneous deformation in a continuum simulation.
- This theory was developed from the standpoint of RVE cell modeling, giving a natural and systematic framework to develop ‘microstress’ and ‘microstress couple’ constitutive relations from computational RVE models as described in Chapter 6.
- The characteristic length scale of inhomogeneous deformation as linked to microstructural transition or instability events.

- A simplified single microstress approach, with a variable length scale parameter, was developed which leads to huge saving in computational cost.

The multiresolution approach was employed in Chapter 7 to model crack growth and to predict the fracture toughness of a cemented carbide. The predicted fracture toughness values were much greater than those predicted using the conventional continuum approach in Chapter 4. The multiresolution continuum analysis predicted inhomogeneous deformation ahead of the propagating crack tip at scales which were directly linked to the underlying microstructural features; in particular the deformation was initially dispersed over the cobalt grain scale, directly capturing the well known grain size effect in cemented carbides.

In Chapter 8 the multiresolution model was successfully applied to modeling the initiation and propagation of adiabatic shear bands in a steel alloy. A hardening length scale was introduced to capture the extra work hardening which occurs at small scales. When microvoid nucleation was predicted the length scale transitioned to a smaller scale which defined the size of the resulting shear band. Thermal shear band widening effects were also captured by coupling the multiresolution mechanical simulation to the conventional continuum energy equation. A parametric study was employed to gauge the effect of each of the underlying microstructural parameters on shear band velocity. Both the microstructural parameters and embedded length scales were shown to influence the timing of the terminal shear instability (initiation) and the subsequent propagation velocity of the shear band.

9.2 Future Directions

Constitutive Modeling

The multiresolution theory developed in this thesis is based on an extension of RVE averaging theory. As such it is quite natural to derive the necessary constitutive relations (stress, microstress and microstress couple) directly from RVE cell modeling. However in order to become a useful material modeling tool, empirical data should be used to either

- validate the numerically determined constitutive relations (developed from RVE simulations) or
- to directly formulate experimentally based microstress (and microstress couple) constitutive relationships.

In particular, the necking section of a tensile test specimen contains enough information to define the length scale of failure in alloys. Micro-bending experiments may be useful in determining the extra hardening which occurs at small scales. This could be used to calibrate the hardening length scale which operates during the work hardening stage of deformation.

Variable Length Scale Microstress Couple

The idea of using a single variable length scale microstress couple has been introduced in this thesis. This is in contrast to previous work (Vernerey 2006; Vernerey et al. 2007a; b) were a microstress and microstress couple is introduced for each characteristic length scale of inhomogeneous deformation. The variable length scale microstress introduced here acts as a moment with a lever arm which changes length as the microstructure evolves. In particular it changes length at each microstructural instability/transition point.

In this case a simple elastic constitutive relationship is used for the microstress and (variable length scale) microstress couple.

In order to develop a fully elastic-plastic constitutive relationship, an averaging volume must be defined which contracts or expands with the evolving characteristic scale of the inhomogeneous deformation. A method should be developed to construct such an averaging volume, which automatically senses the scale of inhomogeneous deformation (from the strain gradient field) and changes size accordingly. The shape of the averaging volume may also be variable in order to capture directional anisotropic effects.

Bibliography

ABAQUS, I. (2004). *Version 5 Documentation*.

Aifantis, E. C. (1992). "On the role of gradients in the localization of deformation and fracture." *Int. J. Eng. Sci.*, 30(1279–1299).

Anand, L., Kim, K. H., and Shawki, T. G. (1987). "Onset of Shear Localization in Viscoplastic Solids." *Journal for the Mechanics and Physics of Solids*, 37, 407-429.

Asaro, R. J. (1983a). "Crystal plasticity " *J. Appl. Mech.* , 50 921–934.

Asaro, R. J. (1983b). "Micromechanics of crystals and polycrystals." *Adv. App. Mech.*, 23, 1–115.

Asaro, R. J., and Rice, J. R. (1977). "Strain Localization in Ductile Single Crystals." *Journal for the Mechanics and Physics of Solids*, 25, 309.

Ashbee, K. H. G. (1967). "Intersecting stacking faults in face-centered cubic lattices." *Acta Metall.*, 15, 1129-1131.

Auriault, J. L. (1991). "Is an equivalent macroscopic description possible?" *International Journal of Science and Engineering*, 29(7), 785-795.

Bammann, D. J., Chiesa, M. L., Horstemeyer, M. F., and Weingarten, L. I. (1993). "Failure in Ductile Materials Using the Finite Element Method." In: *Structural Crashworthiness and Failure*, N. J. a. T. Weirzbicki, ed., Elsevier Applied Science, 1-54.

Bammann, D. J., Chiesa, M. L., and Johnson, G. C. (1996). "Modeling Large Deformation anf Failure in Manufacturing Processes." In: *Theoretical and Applied Mechanics*, T. Tatsumi, E. Watanabe, and T. Kambe, eds., Elsevier Applied Science, New York, 359-376.

Bammann, D. J., Chiesa, M. L., McDonald, A., Kawahara, W. A., Dike, J. J., and Revelli, V. D. (1990). "Prediction of ductile failure in metal structures." *American Society of Mechanical Engineers, Applied Mechanics Division*, 107 7-12.

Bazant, Z. P., and Belytschko, T. (1987). "Strain-softening continuum damage: localization and size effect." *Constitutive Laws of Engineering Materials: Theory and Applications* 11 - 33.

Belytschko, T., Liu, W. K., and Moran, B. (2000). *Nonlinear Finite Elements for Continua and Structures*, John Wiley and Sons.

Beran, M. (1968). "Statistical Continuum Theories." In: *Monographs in Statistical Physics and Thermodynamics*, Interscience Publishers, New York.

Borrego, A., Fernandez, R., del Carmen Cristina, M., Ibanez, J., and Gonzalez-Doncel, G. (2002). "Influence of extrusion temperature on the microstructure and the texture of 6061Al-15 vol.% SiCw PM composites." *Composites Science and Technology*, 62, 731-742.

Brand, A. J., Kalz, S., and Kopp, R. (1996). "Microstructural simulation in hot rolling of aluminium alloys." *Computational Materials Science*, 7, 242-246.

Brekelmans, W. (1993). "Nonlocal formulation of the evolution of damage in a one dimensional conguration." *International Journal of Solids and Structures* 30(11), 1503-1512.

Bruzzi, M. S., McHugh, P. E., O'Rourke, F., and Linder, T. (2001). "Micromechanical modelling of the static and cyclic loading of an Al 2124 – SiC MMC." *Int. J. Plasticity*, 17(4), 565-599.

Busso, E. P., Lei, Y., O'Dowd, N. P., and Webster, G. A. (1998). *ASME J. Engng. Mater. Technol.* , 120 328–337.

Chu, C. C., and Needleman, A. (1980). *Journal of Engineering Materials Technology*, 102, 249.

Connolly, P., and McHugh, P. E. (1999). "Fracture modelling of WC-Co hardmetals using crystal plasticity theory and the Gurson model." *Fatigue and Fracture of Engineering Materials and Structures*, 22(1), 77-86.

Cosserat, E., and Cosserat, F. (1909). *Theorie des corps deformables.* , A Hermann et Fils, Paris.

Courtney, T. H. (2000). *Mechanical Behavior of Solids*, McGraw Hill, Boston

Cowie, J. G., Azrin, M., and Olson, G. B. (1989). "Microvoid formation during shear deformation of ultrahigh strength steels." *Metallurgical Transactions A (Physical Metallurgy and Materials Science)*, 20A(1), 143-153.

Cuitino, A. M., and Ortiz, M. (1996). "Ductile Fracture by Vacancy Condensation in F.C.C. Single Crystals." *Acta Mater.*, 44(2), 427-436.

De Borst, R., and Muhlhaus, H. B. (Year). "Continuum models for discontinuous media." *International RILEM:ESIS Conference*, E+FN Spon London UK, Noordwijk, The Netherlands, 601-618.

De Borst, R., Sluys, L., Muhlhaus, H. B., and Pamin, J. (1993). "Fundamental issues in finite element analyses of localization of deformation." *Engineering Computations*(10), 99-121.

Domkin, K. (2005). "Constitutive Models based on Dislocation Density," Lulea University of Technology.

Engqvist, H., Jacobson, S., and Axen, N. (2002). "A Model for Hardness of Cemented Carbides." *Wear*, 252, 384.

Fischmeister, H. F., Schmauder, S., and Sigl, L. S. (1988). "Finite Element Modeling of Crack propagation in WC-Cohard Metals." *Mater. Sci. Eng. A*, 105/106, 305-311.

Fleck, N. A., and Hutchinson, J. W. (1997). "Strain gradient plasticity." *Adv. Appl. Mech.*, 33, 295–361.

Gao, H., Huang, Y., Nix, W. D., and Hutchinson, J. W. (1999). "Mechanism-based strain gradient plasticity-theory." *Journal of the Mechanics and Physics of Solids*, 47, 1239–1263.

German, R. M. (1985). "The Contiguity of Liquid Phase Sintered Microstructures." *Metall. Trans. A*, 16A, 1247.

Ghosh, S., Lee, K., and Raghavan, P. (2001). "A multi-level computational model for multi-scale damage analysis in composite and porous materials." *Int. J. Solids Structures*, 38, 2335–2385.

Gurland, J. (1988). "New Scientific Approaches to Development of Tool Materials." *Int. Mater. Rev.*, 33(3), 151

Gurson, A. L. (1977). "Continuum theory of ductile rupture by void nucleation and growth: Part I-yield criteria and flow rules for porous ductile media." *J. Engng Mater. Tech*, 99, 2–15.

Hao, S., Liu, W. K., Moran, B., Vernerey, F., and Olson, G. B. (2004). "Multi-scale constitutive model and computational framework for the design of ultra-high strength, high toughness steels." *Computer Methods in Applied Mechanics and Engineering* 193((17-20)), 1865-1908.

Hao, S., Moran, B., Liu, W. K., and Olson, G. B. (2003). "A Hierarchical Multi-Physics Constitutive Model for Steels Design." *Journal of Computer-Aided Materials Design*, 10 99–142.

Herrmann, L. R. (1983). "Hybrid and mixed finite element methods." In: *Mixed finite elements for couple-stress analysis*, S. N. Atluri, R. H. Gallagher, and O. C. Zienkiewicz, eds., John Wiley & Sons Ltd., 1-17.

Hill, R. (1963). "Elastic properties of reinforced solids: some theoretical principles." *Journal of the Mechanics and Physics of Solids*, 11, 357-372.

Hill, R. (1966). "Generalized Constitutive Relations for incremental Deformation of Metal Crystals by Multislip." *Journal for the Mechanics and Physics of Solids*, 14, 95.

Hill, R., and Rice, J. R. (1972). "Constitutive Analysis of Elastic-Plastic Crystals at Arbitrary Strain." *Journal for the Mechanics and Physics of Solids*, 20, 401.

Hilleborg, A., Modeer, M., and Petersson, P. E. (1976). "Analysis of Crack Formation and Crack Growth in Concrete by Means of Fracture Mechanics and Finite Elements." *Cement and Concrete Research*, 6, 773–782.

Hom, C. L., McMeeking, R. M., and 1989. (1989). *Journal of the Mechanics and Physics of Solids* 37(3), 395-415.

Horstemeyer, M. F., Lathrop, J., Gokhale, A. M., and Dighe, M. (2000a). "Modeling stress state dependent damage evolution in a cast Al-Si-Mg aluminum alloy." *Theoretical and Applied Fracture Mechanics* 33 31-47.

Horstemeyer, M. F., Matalanis, M. M., Sieber, A. M., and Botos, M. L. (2000b). "Micromechanical finite element calculations of temperature and void configuration effects on void growth and coalescence." *International Journal of Plasticity*, 16, 979-1015.

Horstemeyer, M. F., Ramaswamy, S., and Negrete, M. (2003). "Using a micromechanical finite element parametric study to motivate a phenomenological macroscale model for void/crack nucleation in aluminium with a hard second phase." *Mechanics of Materials*, 35, 675-687.

Huang, Y. (1991). "A User-Material Subroutine Incorporating Single Crystal Plasticity in teh Abaqus Finite Element Program." *Division of Applied Sciences, Harvard University, Cambridge, MA*, 02138.

Inframat.com. (Dec 4th 2006). "Description of Tungsten Carbide Technology – Superfine Tungsten Carbide for Bulk Hardmetal Applications." <http://www.inframat.com/wcdetail.htm> (Dec 4th, 2006).

itia.org.uk. (2006). "Cemented Carbides." <http://www.itia.org.uk/Default.asp?Page=53> (4th Dec, 2006).

Johnson, G. R., and Cook, W. H. (1985). "Fracture characteristics of three metals subjected to various strains, strain rates, temperatures and pressures." *Eng. Fract. Mech.*, 21(1), 31-48.

Kadowaki, H., and Liu, W. K. (2004). "Bridging multi-scale method for localization problems." *Computer Methods in Applied Mechanics and Engineering*, 193, 3267–3302.

Kadowaki, H., and Liu, W. K. (2005). "A multiscale approach for the micropolar continuum model." *Computer modeling in Engineering and Science*, 7, 269–282

Kanninen, M. F., and Popelar, C. H. (1985). In: *In Advanced Fracture mechanics*, O. E. Series, ed., Oxford.

Karhausen, K. F., and Roters, F. (2002). "Development and application of constitutive equations for multiple-stand hot rolling of Al-alloys." *Journal of Materials Processing Technology* 123, 155-166.

Karpov, E. G., Wagner, G. J., and Liu, W. K. (2005). "A Green's function approach to deriving non-reflecting boundary conditions in molecular dynamics simulations." *International Journal of Numerical Methods and Engineering*, 62(1250–1262).

Kim, C.-S. (2004). "Microstructural-Mechanical Property Relationships in WC-Co composites," Carnegie Mellon University.

Knap, J., and Ortiz, M. (2001). "An analysis of the quasicontinuum method." *Journal of the Mechanics and Physics of Solids*, 49, 1899–1923.

Kouznetsova, V., Geers, M. G. D., and Brekelmans, W. A. M. (2002). "Multi-scale constitutive modelling of heterogeneous materials with a gradient-enhanced computational homogenization scheme." *Int. J. Numer. Meth. Engrg.*, 54, 1235-1260.

Lee, H. C., and Gurland, J. (1978). "Hardness and Deformation of Cemented Tungsten Carbide." *Mater. Sci. Eng.*, 33, 125.

Li, S., Liu, W. K., Qian, D., Guduru, R., and Rosakis, A. J. (2001). "Dynamic Shear Band Propagation and Micro-Structure of Adiabatic Shear Band." *Computer Methods in Applied Mechanics and Engineering*, 191(1-2), 73-92.

Li, S., Liu, W. K., Rosakis, A. J., Belytschko, T., and Hao, W. (2002). "Mesh-free Galerkin simulations of dynamic shear band propagation and failure mode transition." *International Journal of Solids and Structures*, 39, 1213-1240.

Li., S., Liu, W. K., Rosakis, A. J., Belytschko, T., and Hao, W. (2002). "Mesh-free Galerkin simulations of dynamic shear band propagation and failure mode transition." *International Journal of Solids and Structures*, 39, 1213-1240.

Liu, W. K., Karpov, E. G., Zhang, S., and Park, H. S. (2004). "An introduction to computational nanomechanics and materials." *Computer Methods in Applied Mechanics and Engineering*, 193(17-20), 1529-1578.

Liu, W. K., and McVeigh, C. (2007). "Predictive Multiscale Theory for Design of Heterogeneous Materials." *Computational Mechanics* Submitted.

Ljungberg, A. B., Chatfield, C., Hehenberger, M., and Sundstrom, B. (Year). *International Conference on Science of Hard Materials*, 725.

Marchand, A., and Duffy, J. (1988). "An Experimental Study of the Formation Process of Adiabatic Shear Bands in a Structural Steel." *Journal for the Mechanics and Physics of Solids*, 36, 251-283.

McClintock, F. A. (1968). "A Criterion for Ductile Fracture by Growth of Holes." *Journal of Applied Mechanics*, 35, 363.

McHugh, P. E., Asaro, R. J., and Shih, C. F. (1993). "Computational modelling of metal-matrix composite materials-I. Isothermal deformation patterns in ideal microstructures." *Acta Metall. Mater.*, 41(5), 1461-1476.

McHugh, P. E., and Connolly, P. (2003). "Micromechanical Modelling of Ductile Crack Growth in the Binder Phase of WC-Co." *Computational Materials Science*, 27, 423-436.

McHugh, P. E., and Mohrmann, R. (1997). "Modelling of creep in a Ni base superalloy using single crystal plasticity." *Comput. Mater. Sci. Eng.*, 9, 134-140.

McVeigh, C., Vernerey, F., Liu, W. K., and Brinson, L. C. (2006a). "Multiresolution analysis for material design." *Computer Methods in Applied Mechanics and Engineering*, 195(37-40), 5053-5076.

McVeigh, C., Vernerey, F., Liu, W. K., Moran, B., and Olson, G. B. (2006b). "An Interactive Microvoid Shear Localization Mechanism in High Strength Steels " *Journal for the Mechanics and Physics of Solids* 55(2), 225-244.

Medyanik, S. N., Liu, W. K., and Li., S. (2005). "On criteria for dynamic adiabatic shear band propagation. ." *Journal of the Mechanics and Physics of Solids*, 55(7), 1439-1461.

memsnet.org. (2006a). "Material: Stainless steel, bulk." <http://www.memsnet.org/material/stainlesssteelbulk/> (Dec 4th, 2006).

memsnet.org. (2006b). "Material: Tungsten Carbide (WC), bulk." <http://www.memsnet.org/material/tungstencarbidewcbulk/> (Dec 4th, 2006).

Mesarovic, S. D., and Padbidri, J. (2005). "Minimal kinematic boundary conditions for simulations of disordered microstructures." *Philosophical Magazine*, 85(1), 65-78.

Michel, J. C., Moulinec, H., and Suquet, P. (1999). "Effective properties of composite materials with periodic microstructure: a computational approach." *Comput. Methods Appl. Mech. Engrg.*, 172, 109-143.

Mindlin, R. D. (1964). "Micro-structure in linear elasticity." *Arch. Ration. Mech. Anal*, 16, 15-78.

Mura, T. (1987). *Micromechanics of Defects in Solids*, Dordrecht.

Murray, M. J., and Smith, D. C. (1973). "Stress induced cavitation in cobalt bonded tungsten carbide." *Journal of Materials Science*, 8, 1706-1710.

Needleman, A. (1988). "Material rate dependence and mesh sensitivity in localization problems." *Computer Methods in Applied Mechanics and Engineering* 67, 69-85.

Nemat-Nasser, S., and Hori, M. (1993). *Micromechanics] Overall Properties of Heterogeneous Materials*, Elsevier Science Publishers.

Olson, G. B. "Northwestern University." *Dept. of Materials Science*.

Park, H. S., Karpov, E. G., and Liu, W. K. (2004). "A Temperature Equation for Coupled Atomistic/Continuum Simulations." *Computer Methods in Applied Mechanics and Engineering*, 193, 1713-1732.

Park, H. S., Karpov, E. G., Liu, W. K., and Klein, P. A. (2005). "The Bridging Scale for Two-Dimensional Atomistic/Continuum Coupling." *Philosophical Magazine 2005*, 85(1), 79-113.

Peerlings, R. H. J., and Fleck, N. A. (2001). "Numerical analysis of strain gradient effects in periodic media. ." *J. Phys. IV*, 11, 153–160.

Pickens, J. R., and Gurland, J. (1978). "The Fracture Toughness of WC-Co Alloys Measured on Single-edge Notched Beam Specimens Precracked by Electron Discharge Machining." *Mater. Sci. Eng.*, 33, 135.

Pijaudier-Cabot, G., and Bazant, Z. P. (1987). "Nonlocal damage theory." *Journal of Engineering Mechanics ASCE*, 113, 1512–1533.

Poech, M. H., Fischmeister, H. F., and Spiegler, R. (1991). "Assessment of the In-Situ properties of the cobalt phase in WC-Co hard metals." *Journal of Hard Materials*, 2(3/4), 197-205.

Qian, D., and Gondhalekar, R. H. (2004). "A virtual atom cluster approach to the mechanics of nanostructures." *International Journal for multiscale computational engineering*, 2(2), 277-289.

Qian, D., Wagner, G. J., Ruoff, R. S., Yu, M. F., and Liu, W. K. (2002). "Mechanics of Carbon Nanotubes." *Applied Mechanics Reviews*, 55(2), 495-533.

Quinn, D. F., Connolly, P. J., Howe, M. A., and McHugh, P. E. (1997). "Simulation of void growth in WC-Co hardmetals using crystal plasticity theory." *International Journal of Mechanical Sciences*, 39(2), 173-183.

Ranjan, K. (1983). "Stacking fault strengthening in low stacking fault energy alloys." *Scripta Metall*, 17, 101-104.

Ravichandran, K. S. (1994). "Fracture Toughness of Two Phase WC-Co Cermets." *Acta Metall. Mater.*, 42(1), 143.

Rice, J. R. (1971). "Inelastic Constitutive Relations for Solids: An Internal Variable Theory and its Application to Metal Plasticity." *Journal for the Mechanics and Physics of Solids*, 19, 433.

Rice, J. R., and Johnson, M. A. (1970). In: *Inelastic Behavior of Solids*, M. F. Kanninen, W. F. Adler, A. R. Rosenfield, and R. I. Jaffee, eds., McGraw-Hill, New York.

Roebuck, B., Almond, E., and Cottenden, A. M. (1984). "The influence of composition, phase transformation and varying the relative FCC and HCP phase contents on the properties of Co-WC alloys." *Matls Sci Engng*, 66, 179-194.

Rogers, H. C. (Year). "Adiabatic Shearing - General Natuer and Material Aspects." *Material Behavior Under High Stress and Ultrahigh Loading rates*, 29th Sagamore Conference, 101-118.

Rolshoven, S., and Jirasek, M. (2002). "Nonlocal Formulations of Softening Plasticity." In: *WCCM V Fifth World Congress on Computational Mechanics*, Vienna, Austria.

Sellars, C. M., and Zhu, Q. (2000). "Microstructural modeling of aluminium alloys during thermomechanical processing." *Materials Science and Engineering A*, 280, 1-7.

Shi, Y. W., and Barnby, J. T. (1984). "Void nucleation during tensile deformation of a C-Mn structural steel." *International Journal of Fracture*, 25, 143-151.

Sigl, L. S., and Exner, H. E. (1987). "Experimental Study of the Mechanics of Fracture in WC-Co Alloys." *Metallurgical Transactions*, 18A, 1299-1308.

Sigl, L. S., and Fischmeister, H. F. (1988). "On the Fracture Toughness of Cemented Carbides." *Acta Metall.*, 36(4), 887.

Sluys, L., and De Borst, R. (1992). "Wave propagation and localization in a rate dependent cracked medium model formulation and one dimensional examples." *International Journal of Solids and Structures*, 29(23), 2945-2958.

Socrate, S. (1995). "Mechanics of microvoid nucleation and growth in high-strength metastable austenitic steels."

Sokolov, L. D., Gladkikh, A. N., Skudnov, V. A., and Solenov, V. M. (1969). "Mechanical Properties of Cobalt at Different Temperatures and Deforamtion Rates." *Translated from Metallovedenie i Termicheskaya Obrabotka Metallov*, 8, 37-39.

Spiegler, R., and Fischmeister, H. F. (1992). "Prediction of crack paths in WC-Co alloys." *Acta. Metall. Mater.*, 40(7), 1653.

Sutton, M. A., yang, B., Reynolds, A. P., and Taylor, R. (2002). "Microstructural studies of friction welds in 2024-T3 aluminum." *Materials Science and Engineering A*, 323, 160-166.

Tang, S., Hou, T. Y., and Liu, W. K. (2006). "A Mathematical Framework of the Bridging Scale Method." *International Journal for Numerical Methods in Engineering*, 65, 1688-1713.

Toupin, R. (1962). "Elastic materials with couple stresses." *Archives of Rational Mechanics and Analysis*, 11, 385-414.

Triantafyllidis, N., and Bardenhagen, S. (1996). "The influence of scale size on the stability of periodic solids and the role of associated higher order gradient continuum models." *J. Mech. Phys. Solids*, 44(11), 1891-1928.

Tvergaard, V., and Needleman, A. (1981). "Influence of Voids on Shear Band Instabilities under Plane Strain Conditions." *International Journal of Fracture*, 17, 389-407.

Tvergaard, V., and Needleman, A. (1995). "Effects of non-local damage in porous plastic solids." *International Journal of Solids and Structures*, 32(8/9), 1063-1077.

Underwood, E. (1970). *Quantitative Stereology*, Addison-Wesly, Inc., New York.

Vernerey, F. (2006). "Multi-scale Mechanics of Microstructured Materials," Northwestern University, Evanston.

Vernerey, F., Liu, W. K., and Moran, B. (2007a). "A Micromorphic Model for the Multiple Scale Failure of Heterogeneous Materials." *J. Mech. Phys. Solids.*, under revision.

Vernerey, F., Liu, W. K., and Moran, B. (2007b). "Multi-scale Micromorphic Theory for Hierarchical Materials." *J. Mech. Phys. Solids*, doi:10.1016/j.jmps.2007.04.008

Vijayaraju, K., Dwarakadasa, E. S., and Panchapagesan, T. S. (1986). "Role of vacancies in the ductile fracture of commercially pure aluminium." *Journal of Materials Science Letters*, 1000-1002.

Vosbeek, P. (1994). "A micromechanical approach to deformation and failure of discrete media," Eindhoven University of Technology, Eindhoven.

Wagner, G. J., Karpov, E. G., and Liu, W. K. (2004). "Molecular Dynamics Boundary Conditions for Regular Crystal Lattices." *Computer Method in Applied Mechanics and Engineering*, 193(17-20), 1579-1601.

Wagner, G. J., and Liu, W. K. (2001). "Hierarchical enrichment for bridging scales and mesh-free boundary conditions." *International Journal for Numerical Methods in Engineering*, 50, 507–524.

Wagner, G. J., and Liu, W. K. (2003). "Coupling of atomistic and continuum simulations using a bridging scale decomposition." *Journal of Computational Physics*, 190, 249–274.

Wang, P. T., Geertruyden, W. H. V., and Misiolek, W. Z. (Year). "1st International Symposium on Metallurgical Modeling for Aluminum Alloys." *Materials Solutions Conference*, 199-208.

Wang, W., Sluys, L., and De Borst, R. (1996). "Interaction between material length scale and imperfection size for localisation phenomena in viscoplastic media." *European Journal of Mechanics A:Solids*, 15(3), 447-464.

Wright, T. W. (2002). *The Physics and Mathematics of Adiabatic Shear Bands*, Cambridge University Press, Cambridge.

Xia, Z. C., and Hutchinson, J. W. (1996). "Crack tip fields in strain gradient plasticity." *J. Mech. Phys. Solids*, 44(10), 1621–1648.

Zbib, H. M., and Aifantis, E. C. (2003). "Size effects and length scales in gradient plasticity and dislocation dynamics." *Scripta Materialia*, 48(2), 155-160.

Appendices

A1 Periodic Displacement Boundary Conditions

Throughout this thesis periodic boundary conditions are used as described in Section 3.1.1 and in equation (3.3). The method for applying periodic boundary conditions is described here. Consider four points on the RVE surface as shown in (Figure A.1) The following linear constraints are applied:

$$\begin{aligned} u_1\left(\frac{l}{2}, x_2\right) - u_1\left(-\frac{l}{2}, x_2\right) &= d_1 \\ u_2\left(x_1, \frac{l}{2}\right) - u_2\left(x_1, -\frac{l}{2}\right) &= d_2 \\ u_1\left(x_1, \frac{l}{2}\right) - u_1\left(x_1, -\frac{l}{2}\right) &= d_3 \\ u_2\left(\frac{l}{2}, x_2\right) - u_2\left(-\frac{l}{2}, x_2\right) &= d_4 \end{aligned} \qquad \text{(A1)}$$

The values of d_1, d_2, d_3 and d_4 are applied displacements which define the average true strains in the ε_{11}, ε_{22}, ε_{12} and ε_{21} directions respectively as:

$$\begin{aligned} \varepsilon_{11} &= \log\left(1 + \frac{d_1}{l}\right) \\ \varepsilon_{22} &= \log\left(1 + \frac{d_2}{l}\right) \\ \varepsilon_{12} &= \log\left(1 + \frac{d_3}{l}\right) \\ \varepsilon_{21} &= \log\left(1 + \frac{d_4}{l}\right) \end{aligned} \qquad \text{(A2)}$$

Hence only four displacements are required to define the average strain state in each direction, in 2D. In finite element software packages, the displacements d_1, d_2, d_3 and d_4 are generally applied at a dummy node with four degrees of freedom. The surface displacements can then be constrained to the dummy node via equation (A1). A useful result of this application approach is that the tractions on the dummy node t_1, t_2, t_3 and t_4 can be used to compute the average Cauchy stress associated with the RVE:

$$\begin{aligned} \sigma_{11} &= \frac{t_1}{l + d_2} \\ \sigma_{22} &= \frac{t_2}{l + d_1} \\ \sigma_{12} &= \frac{t_3}{l + d_1} \\ \sigma_{21} &= \frac{t_4}{l + d_2} \end{aligned} \tag{A3}$$

Application of Periodic Boundary Conditions

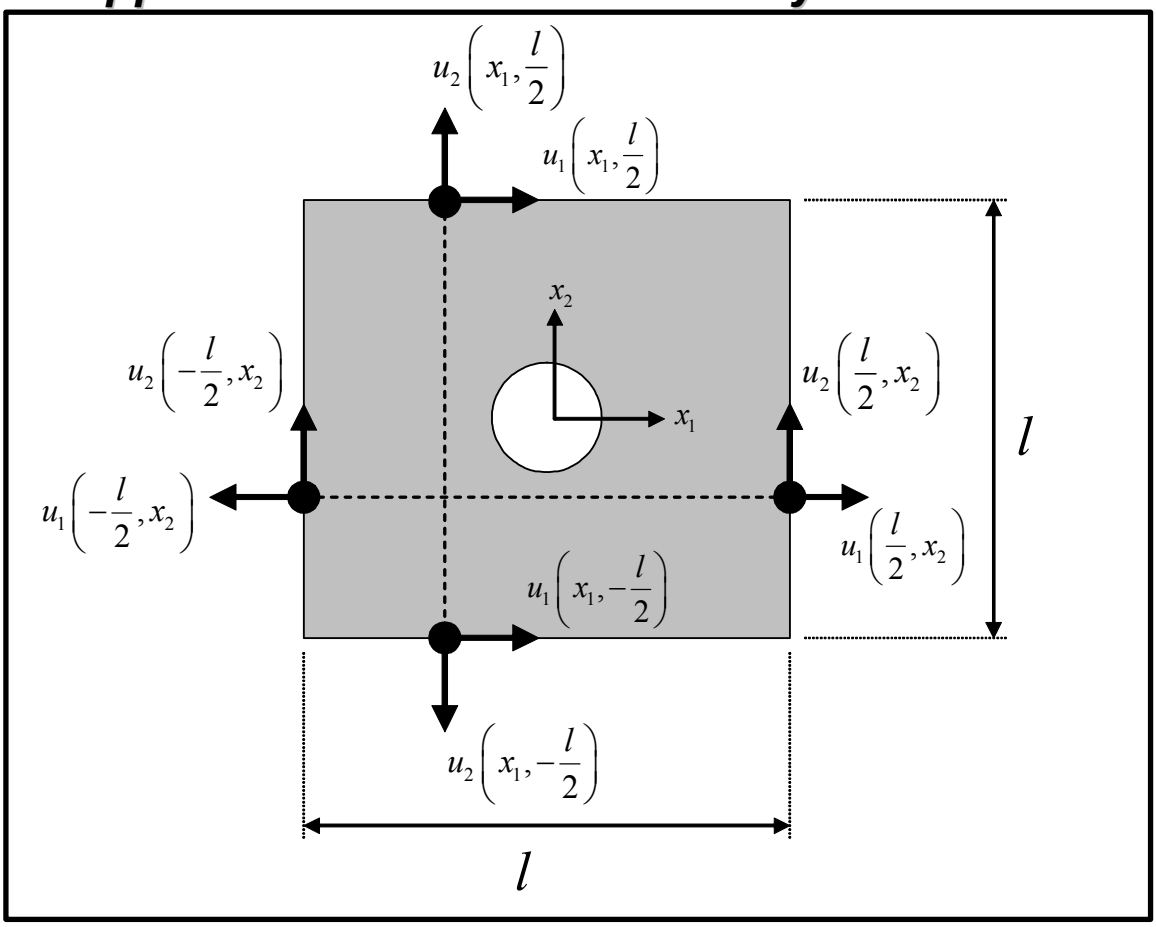

Dummy Node

Applied Displacement d_1, d_2, d_3, d_4

Resulting Traction t_1, t_2, t_3, t_4

Figure A.1. Periodic Boundary Conditions

A2 Constant Triaxiality

Triaxiality is treated as a parameter in the constitutive relations used throughout this thesis. The goal is to perform computational RVE modeling while maintaining a constant average state of triaxiality. In the method used here, the stress ratio $R = \frac{\sigma_{11}}{\sigma_{22}}$ is kept constant. This ratio is related to the stress triaxiality through the following equation:

$$T = \frac{1}{\sqrt{3}} \frac{R+1}{1-R} \tag{A4}$$

The method relies on a feedback loop as shown in (Figure A.2). The approach is summarized as follows:

- The periodic boundary conditions described in Appendix A.1 are applied
- A spring of stiffness K is attached to the dummy node
- An average strain ε_{22} is applied by displacing one end of the spring by $\bar{d}_2$ (- the other end of the spring naturally tries to follow, inducing a displacement d_2)
- The corresponding stress σ_{22} is computed via the spring at the dummy node
- A pressure is applied to ensure the stress ratio $\frac{\sigma_{11}}{\sigma_{22}}$ is constant, equal to R

This sub-routine is called at the end of every time step.

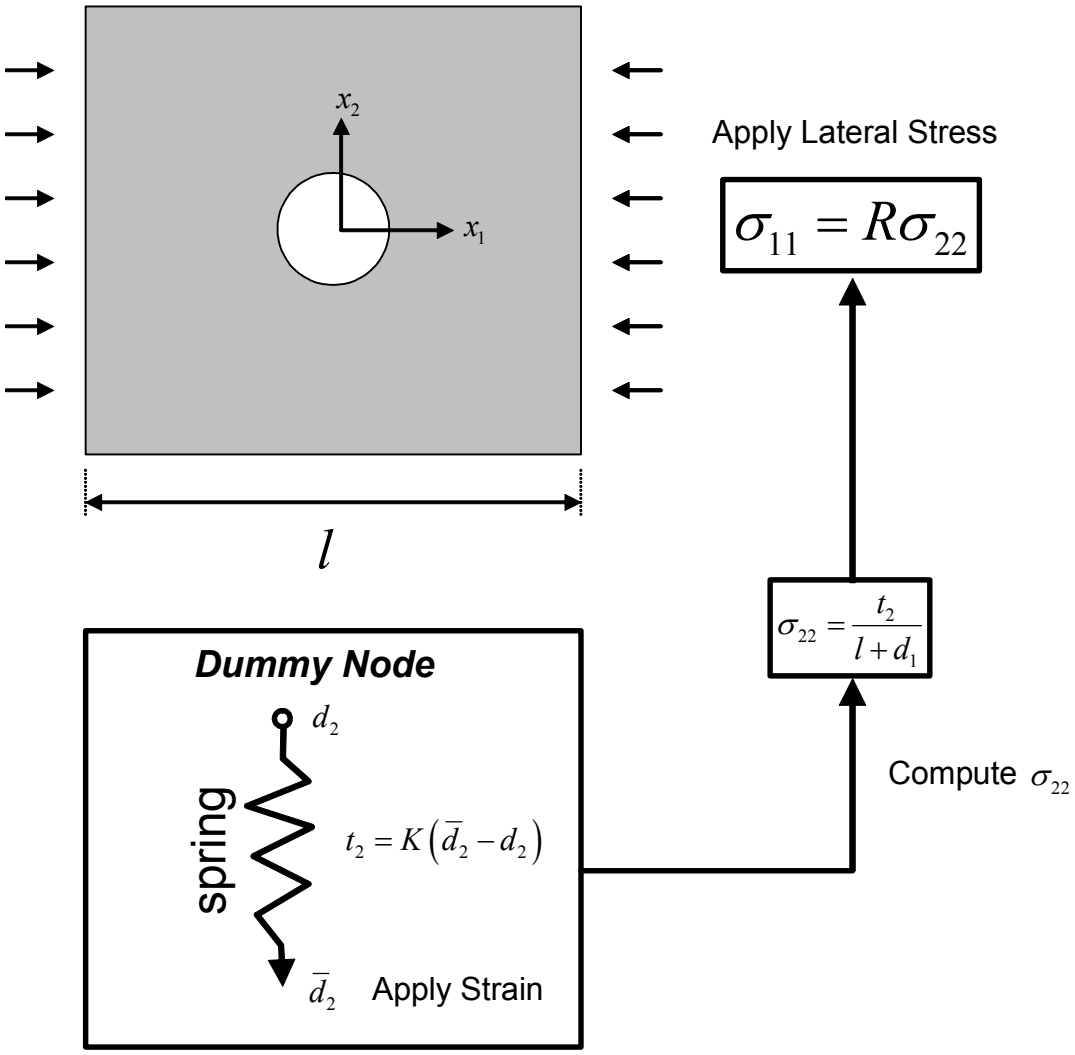

Figure A.2. Constant Triaxiality Loop

A3 Calibrating the BCJ Model to Known Material Response

The BCJ internal state variable model is general enough to be extended to include many physical phenomena including grain growth, recrystalization, phase changes, dislocation densities, etc. However each requires the addition of extra material parameters and constants. In the BCJ model described in this thesis, the constants which must be determined are given in Table 3.1.

Constants such as the grain size d, density ρ, specific heat c_{pt}, inelastic heat fraction h_c, initial temperature θ_0 and melt temperature θ_m are self explanatory. The goal of this Section is to describe the process of calibrating the plastic flow constants to known material response. Known material response usually means the experimentally recorded response. However here the BCJ constants are calibrated to the predefined crystal plasticity model as shown in (Figure A.3). The concept is exactly the same as calibrating to experiment. The experiment here is replaced by the cobalt alloy crystal plasticity model summarized in Table (4.1). Calibration is performed in a simplified one dimensional analysis, similar to a uniaxial compression experiment.

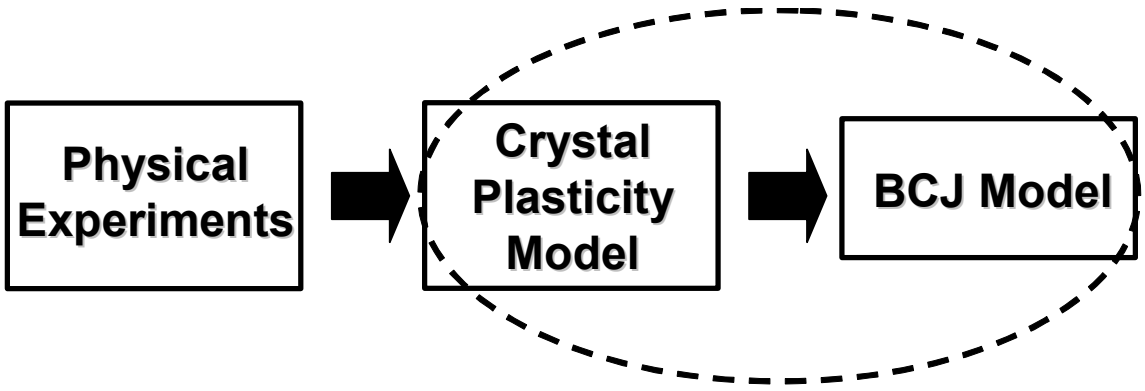

Figure A.3. BCJ model is fitted to the crystal plasticity model

The 1D flow rule for the BCJ model is described by equations (3.23) and (3.24). Neglecting damage the flow stress is written as:

$$\sigma = Y(\vartheta) + \mathrm{V}\sinh^{-1}\left[\frac{\dot{\varepsilon}}{\mathrm{f}}\right] + \kappa = 0 \qquad \text{(A5)}$$

The parameters f, V and $Y(\vartheta)$ are determined in Section A3.1-A3.3. The hardening and recovery parameters related to the isotropic hardening stress κ are determined in Section A3.4.

A3.1 Transition Strain Rate f

The transition strain rate f describes the strain rate at which rate hardening becomes important, in terms of initial yield. It is determined here by plotting the initial yield stress against strain rate (predicted by the crystal plasticity model). The strain rate at which rate effects become important, f, is approximately $f = 2\times10^{-5}s^{-1}$.

A3.2 Magnitude of Rate Dependency V

Referring to equation (A5) the rate dependent initial yield stress is given by $Y(\vartheta) + \mathrm{V}\sinh^{-1}\left[\frac{\dot{\varepsilon}}{\mathrm{f}}\right]$ which is called Y_{rate} here for convenience. If the strain rate $\dot{\varepsilon}$ is much greater than the transition strain rate f, this can be approximated as:

$$Y_{rate} = Y(\vartheta) + \mathrm{V}\sinh^{-1}\left[\frac{\dot{\varepsilon}}{\mathrm{f}}\right] \approx Y(\vartheta) + \mathrm{V}\ln(2\dot{\varepsilon}) \qquad \text{(A6)}$$

The change in initial yield stress with respect to the strain rate $\dot{\varepsilon}$ is given by:

$$\frac{\partial Y_{rate}}{\partial \ln(\dot{\varepsilon})} = \mathrm{V} \tag{A7}$$

This can be approximated by:

$$\mathrm{V} = \frac{\partial Y_{rate}}{\partial \ln(\dot{\varepsilon})} = \frac{Y_{rate}(\dot{\varepsilon}_2) - Y_{rate}(\dot{\varepsilon}_1)}{\ln(\dot{\varepsilon}_2) - \ln(\dot{\varepsilon}_1)} \tag{A8}$$

where $\dot{\varepsilon}_2$ and $\dot{\varepsilon}_1$ are two different loading rates. The rate dependency of initial yield, V , is computed via equation (A8) as $V = \mathrm{C}_5 = 69MPa$.

A3.3 Rate Independent Yield $Y(\vartheta)$

The temperature dependence of the initial rate independent yield stress $Y(\vartheta)$ is given by equation (3.11):

$$Y(\vartheta) = \mathrm{C}_1\left[1 - \left(\frac{\vartheta - \vartheta_0}{\vartheta_{mp} - \vartheta_0}\right)^t\right] + \mathrm{C}_2 d^{-1/2} \tag{A9}$$

This is determined by using different temperatures at under rate loading, and keeping the grain size d constant. The initial yield stress is determined at two different temperatures ϑ_1 and ϑ_2 . This gives two equations:

$$\begin{aligned} Y(\vartheta_1) &= \mathrm{C}_1\left[1 - \left(\frac{\vartheta_1 - \vartheta_0}{\vartheta_{mp} - \vartheta_0}\right)^t\right] + \mathrm{C}_2 d^{-1/2} \\ Y(\vartheta_2) &= \mathrm{C}_1\left[1 - \left(\frac{\vartheta_2 - \vartheta_0}{\vartheta_{mp} - \vartheta_0}\right)^t\right] + \mathrm{C}_2 d^{-1/2} \end{aligned} \tag{A10}$$

with two unknowns C_1 and t. Values of $C_1 = 750MPa$ and $t = 1$ found from the crystal plasticity simulations. The same procedure can be applied to determine the grain size constant C_2. Now the temperature is held constant and the simulations are repeated using two different grain sizes d_1 and d_2. This leaves two equations:

$$\begin{aligned} Y(d_1) &= C_1\left[1-\left(\frac{\vartheta-\vartheta_0}{\vartheta_{mp}-\vartheta_0}\right)^t\right]+C_2 d_1^{-1/2} \\ Y(d_2) &= C_1\left[1-\left(\frac{\vartheta-\vartheta_0}{\vartheta_{mp}-\vartheta_0}\right)^t\right]+C_2 d_2^{-1/2} \end{aligned} \tag{A11}$$

which can be subtracted giving:

$$C_2 = \frac{Y(d_1)-Y(d_2)}{d_1^{-1/2}-d_2^{-1/2}} \tag{A12}$$

The value for C_2 determined from the crystal plasticity model is 3.35×10^5

A3.4 Hardening and Recovery Moduli

According to equation (3.12), the hardening $H(\vartheta)$ and recovery $R_d(\vartheta), R_s(\vartheta)$ moduli must be determined to complete the expression for the isotropic hardening stress κ. These expressions are defined in equation (3.13) and repeated here:

$$\begin{aligned} H(\vartheta) &= C_3\vartheta + C_4 \\ R_d(\vartheta) &= C_5\exp\left(-\frac{C_6}{\vartheta}\right) \\ R_s(\vartheta) &= C_7\exp\left(-\frac{C_8}{\vartheta}\right) \end{aligned} \tag{A13}$$

The hardening modulus is estimated as the initial slope of the stress-strain curve at two different temperatures, ϑ_1 and ϑ_2 giving two equations:

$$\begin{aligned} H\left(\vartheta_1\right) &= \mathrm{C}_3\vartheta_1 + \mathrm{C}_4 \\ H\left(\vartheta_2\right) &= \mathrm{C}_3\vartheta_2 + \mathrm{C}_4 \end{aligned} \tag{A14}$$

and two unknowns C_3, and C_4. Values of $\mathrm{C}_3 = -69 MPaK^{-1}$ and $\mathrm{C}_4 = 31 GPa$ are determined from the crystal plasticity model.

In order to determine the recovery moduli R_d and R_s, it is necessary to integrate the flow rule, equation (3.22), giving:

$$\sigma = Y_{rate} + \sqrt{\frac{H\dot{\varepsilon}}{R_d\dot{\varepsilon} + R_s}} \tanh\left(\sqrt{\frac{H\left(R_d\dot{\varepsilon} + R_s\right)}{\dot{\varepsilon}}}\varepsilon\right) \tag{A15}$$

This equation allows one to examine the difference between dynamic and static recovery in the case of uniaxial stress at a constant true strain rate. At large values of strain ε, the stress saturates (reaches an asymptote) at a stress of:

$$\sigma_{sat} = Y_{rate} + \sqrt{\frac{H\dot{\varepsilon}}{R_d\dot{\varepsilon} + R_s}} \tag{A16}$$

At a particular temperature ϑ it is possible to compute the recovery moduli R_s and R_d in terms of the variation of saturation stress σ_{sat} with strain rate $\dot{\varepsilon}$:

$$\begin{aligned} R_d &= \frac{H\dot{\varepsilon}_1\left(\sigma_{sat}\left(\dot{\varepsilon}_2\right) - Y_{rate}\left(\dot{\varepsilon}_2\right)\right)^2 - H\dot{\varepsilon}_2\left(\sigma_{sat}\left(\dot{\varepsilon}_1\right) - Y_{rate}\left(\dot{\varepsilon}_1\right)\right)^2}{\left(\dot{\varepsilon}_1 - \dot{\varepsilon}_2\right)\left(\sigma_{sat}\left(\dot{\varepsilon}_1\right) - Y_{rate}\left(\dot{\varepsilon}_1\right)\right)^2\left(\sigma_{sat}\left(\dot{\varepsilon}_2\right) - Y_{rate}\left(\dot{\varepsilon}_2\right)\right)^2} \\ R_s &= \frac{H\dot{\varepsilon}_1\dot{\varepsilon}_2\left(\sigma_{sat}\left(\dot{\varepsilon}_2\right) - Y_{rate}\left(\dot{\varepsilon}_2\right)\right)^2 - \left(\sigma_{sat}\left(\dot{\varepsilon}_1\right) - Y_{rate}\left(\dot{\varepsilon}_1\right)\right)^2}{\left(\dot{\varepsilon}_2 - \dot{\varepsilon}_1\right)\left(\sigma_{sat}\left(\dot{\varepsilon}_1\right) - Y_{rate}\left(\dot{\varepsilon}_1\right)\right)^2\left(\sigma_{sat}\left(\dot{\varepsilon}_2\right) - Y_{rate}\left(\dot{\varepsilon}_2\right)\right)^2} \end{aligned} \tag{A17}$$

where $\dot{\varepsilon}_2$ and $\dot{\varepsilon}_2$ are two different strain rates.

The values of the recovery moduli R_s and R_d can then be recomputed using the same formulae at a different temperature. When the value of each modulus is known at two different temperatures, the temperature dependence in equation (A13) can be computed. The values determined from the crystal plasticity model are $C_5 = 1.674 \times 10^{-6}$, $C_6 = 0$, $C_7 = 0.02$ and $C_8 = -1877K$. The values $C_1 - C_8$, V and f are summarized in Table 4.3.

A4 Microvoid Assisted Adiabatic Shear Bands

As described in Chapter 2, microvoid nucleation has been identified as a terminal shear localization mechanism in quasi-static and dynamic loading of high strength steels by (Cowie et al. 1989) and in (McVeigh et al. 2006); the physics of void assisted adiabatic shear band formation has been described by (Wright 2002). Microvoid nucleation, growth and coalescence are incorporated in the BCJ model, equation (3.9), and used in Chapter 8 to model adiabatic void assisted shear band formation and propagation. A brief overview of the continuum treatment of nucleation, growth and coalescence of voids in shear is now given, followed by one dimensional void assisted adiabatic shear band simulation examples.

A4.1 Microvoid Evolution in a Steel Alloy

Porosity is considered to arise in the alloy due to void nucleation and growth at these precipitate sites. The precipitates nucleate microvoids by debonding with the surrounding alloy matrix. In a continuum sense, the average porosity at a material point is the product of the average number of voids per unit volume η and the average volume of a void v plus any additional void growth effect arising from coalescence ϕ_{coal}. This is originally given as equation (3.17):

$$\phi = \eta v + \phi_{coal} \tag{A18}$$

Expressions for these terms are developed here for a steel alloy.

A4.2 Nucleation

The rate of change of the number of nucleated voids per unit volume η is a simple rate equation, in terms of the plastic deformation rate, equation (3.15):

$$\dot{\eta} = \mathcal{N} \left\| \mathbf{D}_p \right\| \tag{A19}$$

Nucleation rate $\dot{\eta}$ is considered to be normally distributed about a mean value of nucleation strain $\varepsilon_{\mathcal{N}}$. The nucleation parameter $\mathcal{N}$ is therefore defined as follows, in terms of the number of precipitates per unit volume $\mathcal{N}^*$, the accumulated plastic strain ε^p, the mean value of strain at which nucleation occurs $\varepsilon_{\mathcal{N}}$ and the standard deviation of nucleation s_n about the mean:

$$\mathcal{N} = \frac{\mathcal{N}^*}{s_{\mathcal{N}} \left(2\pi\right)^{0.5}} \exp\left\{ -\frac{1}{2} \left(\frac{\varepsilon^p - \varepsilon_{\mathcal{N}}}{s_{\mathcal{N}}} \right)^2 \right\} \tag{A20}$$

Assuming spherical precipitates which are 50nm in radius and a volume fraction of 0.2%, the number density of voids is approximately $\mathcal{N}^* = 2.55 \times 10^{12} m^{-2}$.

(Vernerey 2006) performed computational cell models of a debonding precipitate in high strength steel and proposed an expression relating the strain at nucleation $\varepsilon_{\mathcal{N}}$ to the interfacial strength σ^S of a precipitate particle and the first invariant of the stress I_1:

$$\varepsilon_{\mathcal{N}} = \left(F_1 + F_1 \sigma^S \right) \left(1 - \frac{I_1}{3\sigma^S} \right) \tag{A21}$$

A4.3 Growth

Following the work of (Horstemeyer et al. 2000), the well known McClintock (McClintock 1968) form of void growth is chosen to represent the growing void radius in terms of the initial void radius r_0, the plastic strain ε^p and the first and second stress invariants I_1 and J_2:

$$r = r_0 \exp\left(\mathcal{G}\sqrt{3/2}\,\varepsilon^p\right)$$
$$\mathcal{G} = \frac{\sqrt{3}}{2(1-n)}\sinh\left(\frac{\sqrt{3}}{2}(1-n)\left(\frac{2I_1}{3\sqrt{J_2}}+\frac{1}{3}\right)\right) \qquad \text{(A22)}$$

The McClintock void growth parameter n has a value of 0.3. The evolving void area (2D) is computed as:

$$v = \pi r^2 \qquad \text{(A23)}$$

A4.4 Coalescence

These porosity evolution equations are particularly useful for capturing nucleation and growth of voids under high triaxiality loading; however void evolution under shear loading is not well documented. (McVeigh et al. 2006) used computational cell models to show that void growth and coalescence both contributed to failure in alloys over a range of triaxialities, even shear. Under pure shear loading conditions, nucleated voids, which subsequently undergo minimal hydrostatic growth, were observed to elongate and coalesce causing ductile rupture. The void growth observed in shear was similar to the growth of a Mode II crack i.e. a flat void which undergoes rapid increases in surface area but little or no increase in void volume as shown in (Figure A.4) for a 2d example and in (Figure A.5) for a 3d example. In these example, the

coalescence of neighboring microvoid ‘tails’ coincided with a terminal shear instability in the average stress-strain response.

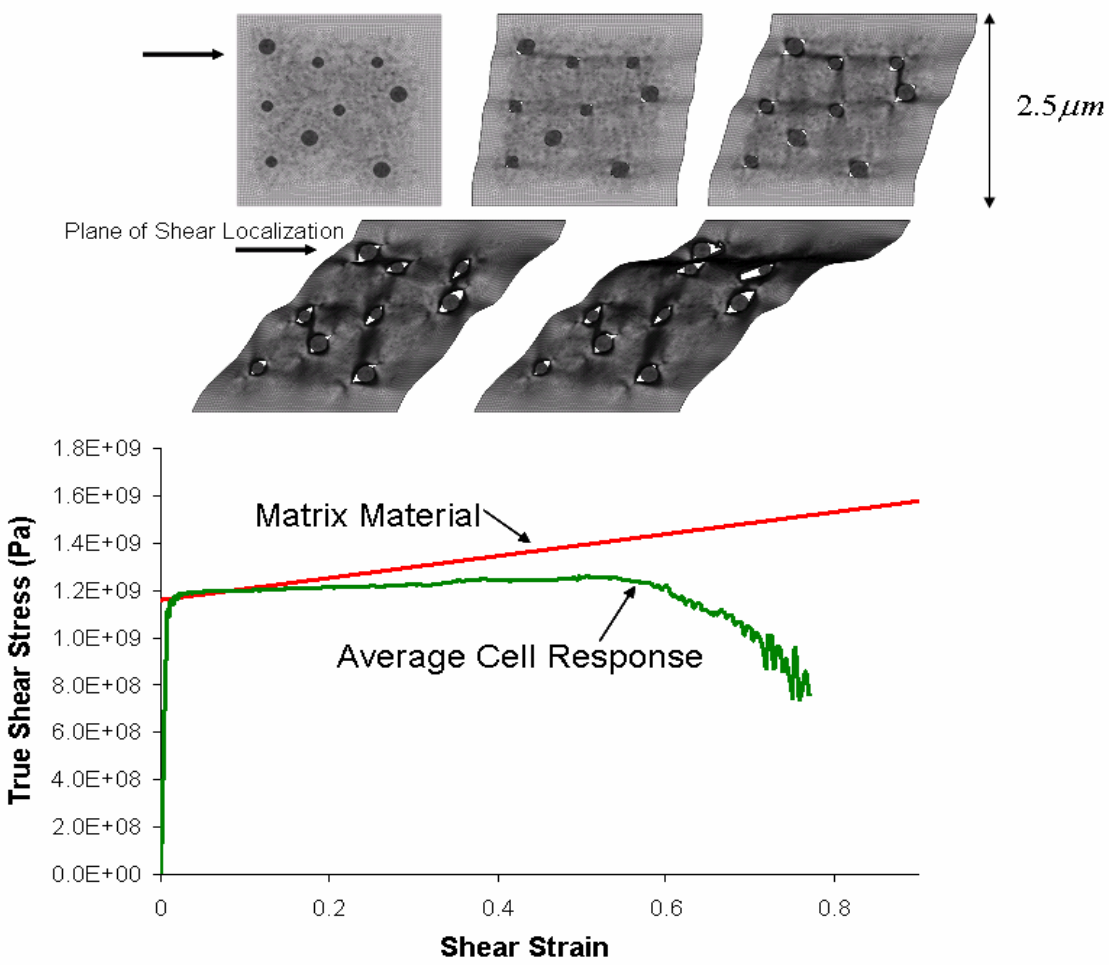

Figure A.4. A shear instability occurs in steel alloy due to shear driven void nucleation and coalescence

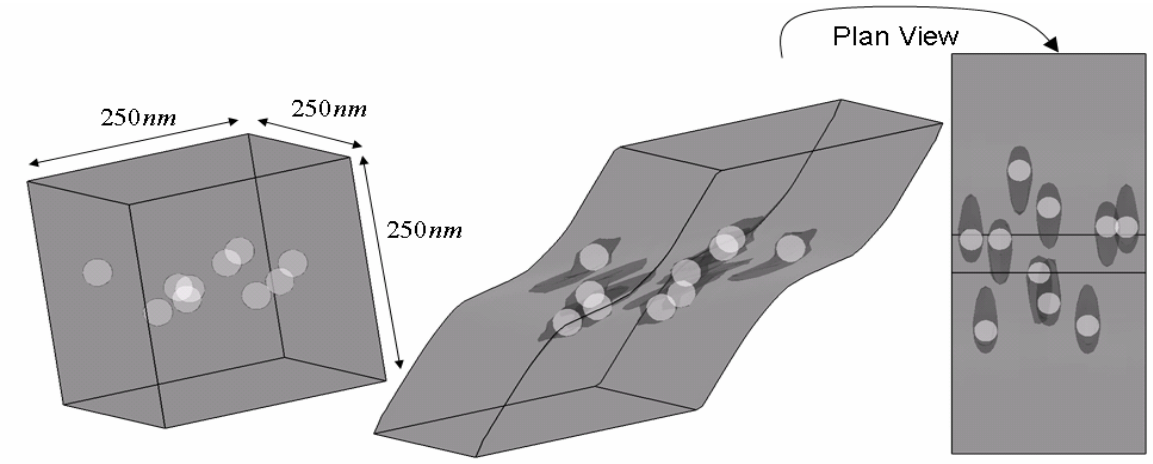

Figure A.5. Void tails grow in shear loading

These computational cell models were used to develop an expression for predicting the onset of coalescence over a range of triaxialities as depicted in (Figure A.6).

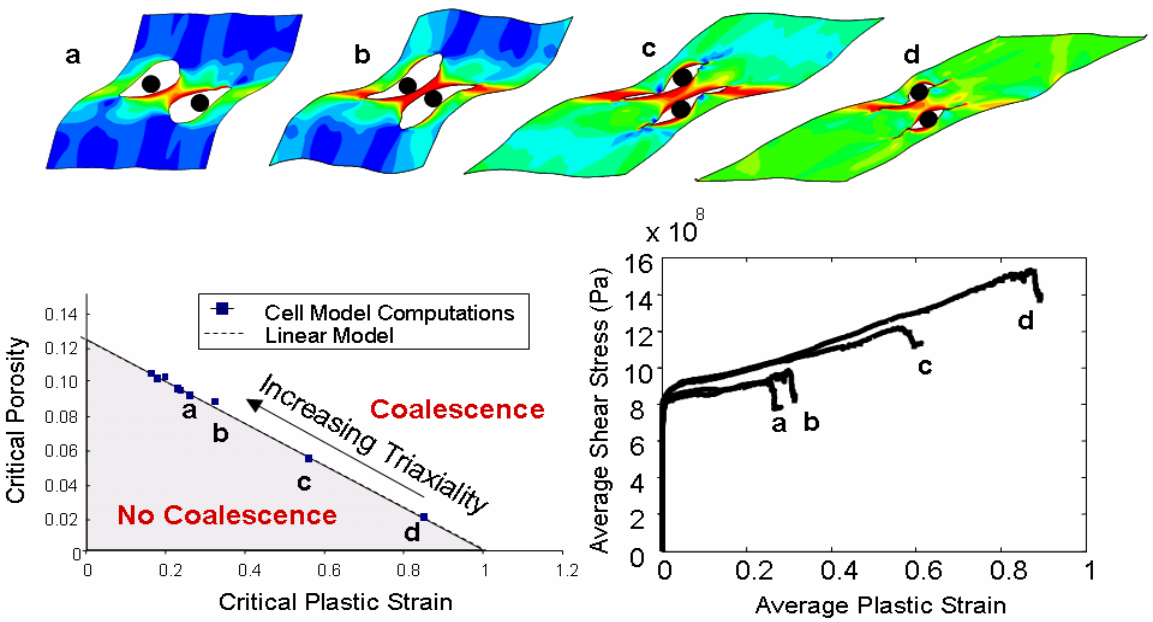

Figure A.6. Coalescence occurs due to shearing and void growth

Simple cell models containing particles were loaded under different triaxialities (a)-(d). It was observed that the plastic instability strain decreased with increasing triaxiality (lower right curve). This plastic instability strain is interpreted as the critical plastic strain for void coalescence. The critical strain is plotted against the critical porosity (at plastic instability) on the lower left curve. This curve defines the critical strain and porosity state when microvoid coalescence occurs, over a range of triaxialities.

At high triaxiality (naturally accompanied by high porosity ϕ) coalescence may occur at quite low plastic strains ε^p. At low triaxiality (indicated by low porosity ϕ) coalescence still occurs if the plastic strain ε^p is sufficiently large; this is the shear driven coalescence range. The following coalescence criterion was derived from the lower left curve in (Figure A.6):

$$\phi + \mathrm{F}_3\varepsilon^p + \mathrm{F}_4 > 0 \qquad \text{(A24)}$$

When this expression is satisfied the coalescence term ϕ_{coal} in equation (A18) begins to grow

$$\dot{\phi}_{coal} = \mathcal{C}\left\|\mathbf{D}_p\right\| \qquad \text{(A25)}$$

Here the parameter $\mathcal{C}$ determines the magnitude of the coalescence effect; a value of 1 has been used by (Vernerey 2006) and (McVeigh et al. 2006). The damage parameters are summarized in Table 8.2.

A5 Thermal Adiabatic Shear Bands

A simple one dimensional problem is used to illustrate the main features of adiabatic shear band formation in a high strength alloy. A brief description of the phenomena which have an effect on shear banding is offered in A5.1. A simple 1D simulation is performed in Section A5.2 to illustrate concepts such as stress collapse in the shear band. The effects of rate hardening and thermal softening are described in Section A5.3. The effect of heat conductance is described in Section A5.4. The effect of microvoiding is described in Section A5.5 within the context of a multiresolution formulation.

A5.1 Description of Shear Band Controlling Factors

In general, shear band formation is controlled by a number of factors, both in terms of the material constitutive behavior and the geometry and loading conditions:

- Temperature effect on flow stress
- Thermal conductivity
- Rate hardening
- Work hardening and dislocation recovery (both are temperature dependent)
- Microvoid damage nucleation and accumulation
- Initial perturbation (existence of a pre-notch)
- Length scale of deformation during hardening – '*smaller is stronger*'
- Length scale of deformation during post-instability material softening
- Applied loading rate

Unless otherwise stated, the BCJ parameters in Table A1 are used in the 1D analysis to follow in Sections A5.2-A5.5. No strain hardening or recovery is considered, however strain rate hardening and thermal softening are accounted for. Under quasi static loading the predicted response is perfectly plastic (when no damage is considered). Microvoid damage, considered in Section A5.5 and A5.6, is explained in Appendix A4 and the parameters are given in Table 8.2.

BCJ Parameters used in ASB Analysis					
Parameter		***Value***	***Parameter***		***Value***
Initial Temperature	θ_0	$297K$	Isotropic Static Recovery Modulus	C_7	–
Melt Temperature	θ_m	$1750K$		C_8	–
Thermal Softening Exponent	t	1.03	Kinematic Hardening Modulus	C_9	–
Reference Strain Rate	f	$1s^{-1}$		C_{10}	–
Magnitude of Rate Effect	V	$16MPa$	Kinematic Dynamic Recovery Modulus	C_{11}	–
Initial Yield Stress	C_1	$792MPa$		C_{12}	–
Hall-Petch Effect	C_2	–	Kinematic Static Recovery Modulus	C_{13}	–
Isotropic Hardening Modulus	C_3	–		C_{14}	–
	C_4	–	Specific Heat	c_{pt}	500
Isotropic Dynamic Recovery Modulus	C_5	–	Density	ρ	$8000kgm^{-3}$
	C_6	–	Heat Fraction	h_c	0.9

Table A1 BCJ parameters used in 1D ASB problems

Velocity boundary conditions of 0.5m/s are applied at either end of a 100 micron wide one dimensional specimen giving a nominal strain rate of $5000s^{-1}$. The domain is meshed with 51 finite elements unless otherwise stated. Only the shear components of stress and strain are considered. A small perturbation is made to the rate independent initial yield stress $Y(\vartheta)$, equation (3.11), within the center-most finite element, ensuring that a shear band will initiate at the center of the specimen. Although not focused on here, the magnitude of the initial perturbation has a significant effect on the subsequent localization behavior during adiabatic shear band formation. Here the perturbation is a reduction of 0.1%.

A5.2 Adiabatic Shear Band Simulation (1D)

A conventional finite element continuum approach, equation (1.5), with adiabatic temperature rise, equation (3.21), is used to model the 1D problem. In (Figure A.7) the shear strain rate, mises stress and temperature within the initially weakened element are plotted with time. After approximately $7\mu s$ the destabilizing effect of the plastic dissipation induced temperature rise overcomes the stabilizing rate hardening effect and an adiabatic shear band forms very rapidly, as evidenced by the drastically increased shear rate, decreasing stress and increasing temperature. Over a period of a few microseconds, the strain rate within the shear band increases one hundred fold and the temperature rises several hundred degrees resulting in a rapid stress collapse.

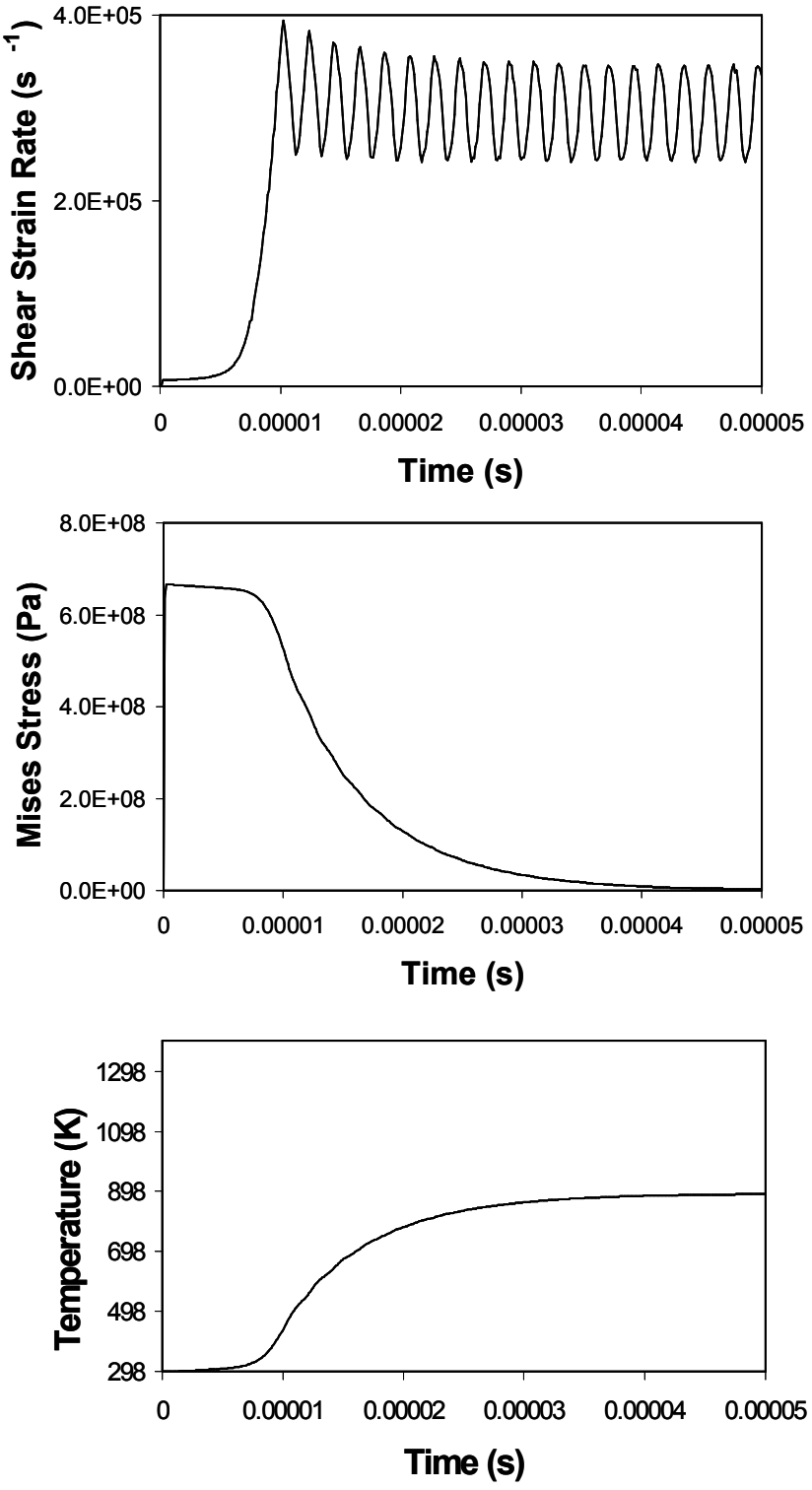

Figure A.7. Shear strain rate increases rapidly, stress collapses and temperature increases rapidly in an adiabatic shear band

The resulting post instability strain profile at $t = 20\mu s$ is shown in (Figure A.8). As shown, the shear band is limited to a single element. The mesh dependency of the results is immediately obvious when the simulation is repeated with a different mesh discretisation; 13, 25 and 51 elements are used in (Figure A.8).

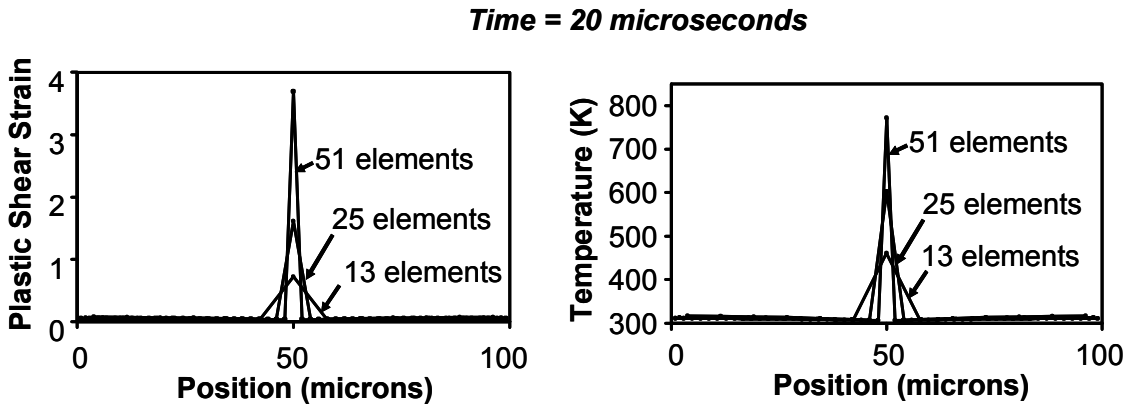

Figure A.8. The shear band width is mesh dependent in an adiabatic analysis

A5.3 Rate Hardening & Thermal Softening Effect (1D)

The adiabatic simulation is repeated. Different rate hardening parameters V, equation (3.9), and melting temperatures ϑ_m, equation (3.11), are used to gauge the effect of rate hardening and thermal softening on shear band initiation (Figure A.9). The evolution of Mises stress within the resulting shear band is plotted with time for each case.

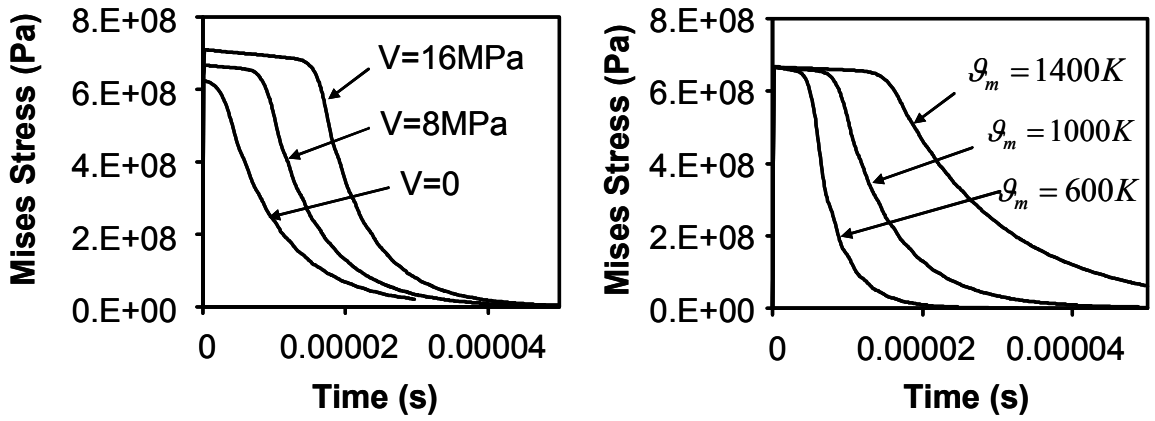

Figure A.9. Strain rate hardening delays shear band initiation. Thermal softening hastens shear band formation

When a rate independent material is modeled, $V = 0$ in (Figure A.9), shear band formation occurs immediately upon yielding (left curve). Increasing the rate hardening to $V = 16MPa$ delays terminal localization substantially. An interesting observation is that the material undergoes a period of stable thermal softening before a terminal localization occurs, due to the stabilizing rate hardening effect. This is consistent with experimental observations where terminal shear band formation occurs somewhat after shear instability is recorded (Wright 2002). The thermal softening effect is also illustrated in (Figure A.9), by arbitrarily increasing the melting temperature ϑ_m in the thermal softening expression, equation (3.11). Decreasing the thermal softening effect (increased ϑ_m) delays the onset and severity of terminal shear localization; stress collapse associated with shear band formation occurs later and is less severe.

A5.4 Heat Conduction Effects (1D)

The effect of heat conduction on shear band initiation is considered here; a fully coupled thermal-mechanical analysis is performed. Three values of conductance are chosen; $k = 200 Wm^{-1}K^{-1}$, $k = 100 Wm^{-1}K^{-1}$ and $k = 50 Wm^{-1}K^{-1}$. The plastic strain rate within the perturbed central element is plotted with time in (Figure A.10). Increasing conductivity has a two-fold effect

- it reduces the peak temperature and delays the onset of localization as shown in (Figure A.10).
- a more diffuse localization occurs - wider shear bands and lower peak strains

Although the localization is regularized to a certain degree, a significant dependency on the mesh discretisation remains; peak strains and temperatures within the shear band still vary substantially depending on the numerical discretisation used.

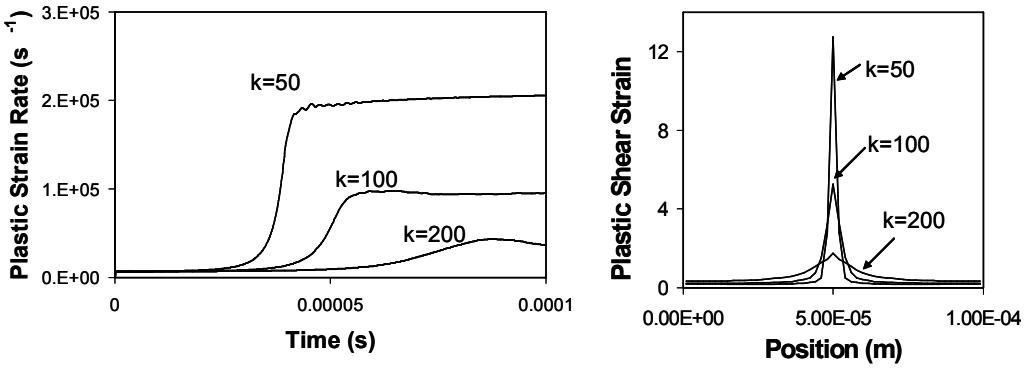

Figure A.10. Thermal conductance delays shear band formation and widens the shear band.

A5.5 Microvoid Assisted ASB with Length Scale

A mechanical length scale l^v is now embedded in the continuum model through the multiresolution continuum model developed in Chapter 5, equation (5.25):

$$\begin{aligned} \left(\sigma - \beta^1\right) \bullet \nabla = 0 \quad \text{in} \quad \Omega \\ \nabla \bullet \bar{\beta}^1 - \beta^1 = 0 \quad \text{in} \quad \Omega \end{aligned} \tag{0.1}$$

A simple linear elastic constitutive response is used to model the microstress β^1 and microstress couple $\bar{\beta}^1$:

$$\begin{aligned} \beta &= E\left(\varepsilon^1 - \varepsilon\right) \\ \bar{\beta} &= E\left(l^v\right)^2 \nabla \varepsilon^1 \end{aligned} \tag{A26}$$

where E is the elastic modulus of a steel alloy i.e. $E = 200GPa$. The length scale l^v is given as 25 microns.

101 equally sized elements are used to model the domain in order to resolve the shear band width. An adiabatic formulation is used first; in (Figure A.11) the resulting shear band width is related to the embedded length scale, l^v. The final strain profile and temperature at $t = 30\mu s$ are also plotted.

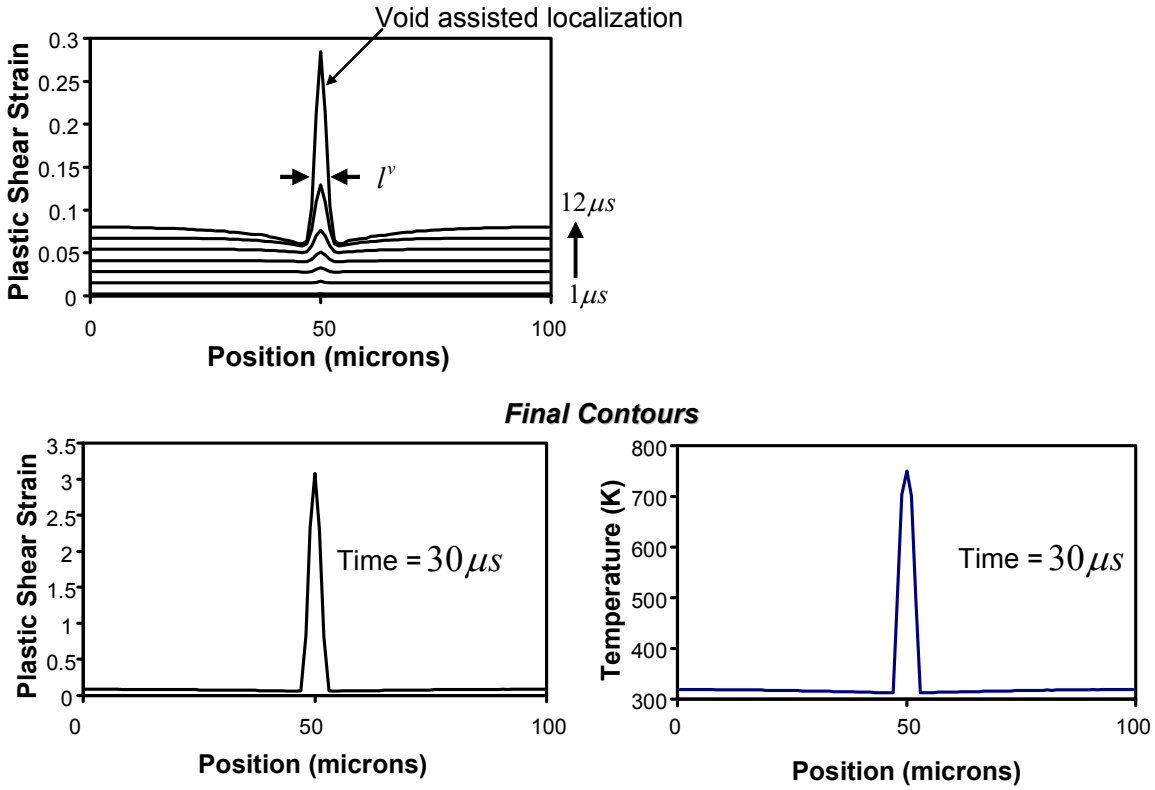

Figure A.11. The multiresolution analysis can be used to capture the localization length scale

The multiresolution 1d simulation is repeated, now couple to a thermal analysis i.e. thermal conductance is considered. The thermal conductance acts to widen the shear band as shown in (Figure A.12), over an area related to the conductance and written as l^{th} here. This widening effect can be observed by comparing the adiabatic and fully coupled approaches: (Figure A.11) and (Figure A.12).

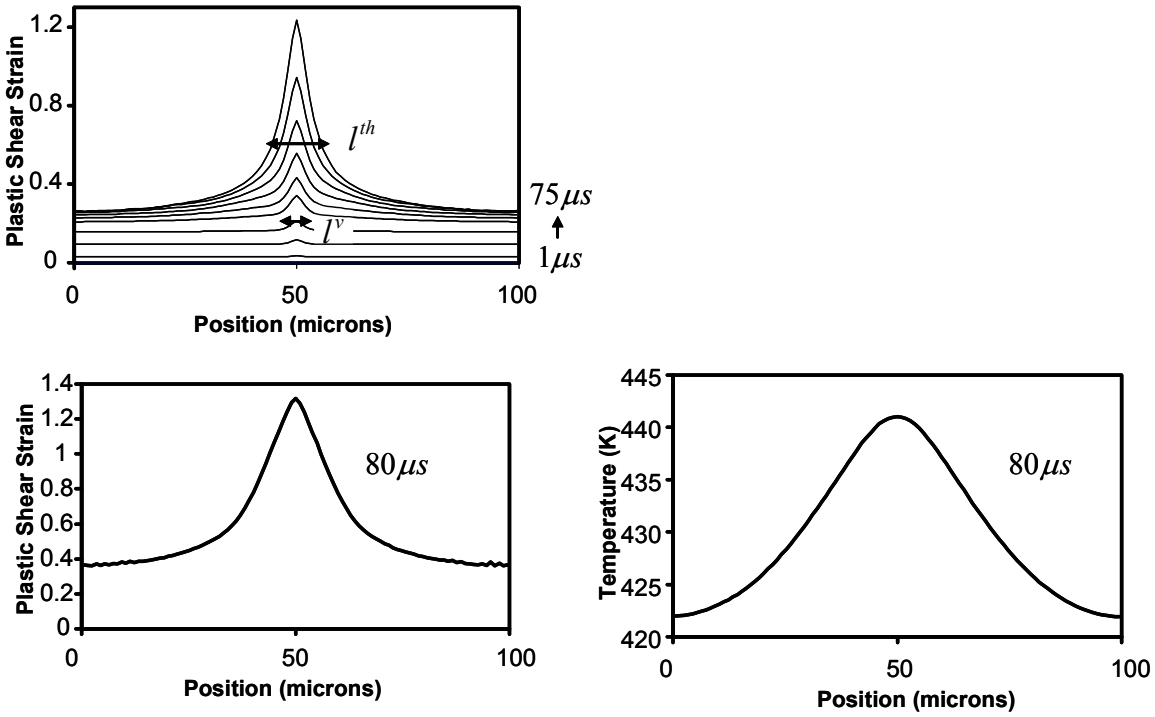

Figure A.12. Thermal conductance widens the localization band

A6 Multiresolution vs Lagrange Multiplier Formulations

The multiresolution continuum theory developed in Chapter 5 is compared to a Lagrange multiplier approach used by several authors previously (Herrmann 1983; Kouznetsova et al. 2002; Xia and Hutchinson 1996). Higher order strain gradient theories generally require special interpolation function is the numerical implementation scheme because the second gradient of displacement must be computed. (Herrmann 1983; Kouznetsova et al. 2002; Xia and Hutchinson 1996) have each avoided using higher order interpolation functions by using a Lagrange Multiplier approach which is discussed here. The resulting expressions for internal power density, external power density and hence the final governing equations are similar in form to the multiresolution formulation derived in Chapter 5. However subtle differences exist, particularly in the interpretation of the Lagrange Multiplier term which corresponds to the multiresolution microstress. The Lagrange Multiplier approach is developed here and compared to the multiresolution approach.

A6.1 Lagrange Multiplier Approach: Internal and External Virtual Power

Consider the strain gradient formulation shown in equation (5.7). To avoid having to compute the second gradient of an unknown solution variable, a second unknown independent variable (a second order tensor field $\mathbf{L}'$) is introduced in the virtual internal power expression of the gradient continuum. The unknown field $\mathbf{L}'$ is kinematically constrained to the original velocity gradient $\mathbf{L}$ by a Lagrange multiplier $\boldsymbol{\lambda}$, earning it the name "relaxed" velocity gradient. Because $\mathbf{L}$ and $\mathbf{L}'$ are equal, the original second gradient of velocity $\mathbf{G}$ should be equal to the newly introduced tensor $\mathbf{G}'$ which is the gradient of $\mathbf{L}'$, symmetrized on the first and last indices:

$$G'_{ijk} = \frac{1}{2}\left(\nabla_i L'_{jk} + \nabla_k L'_{ji}\right) \tag{A27}$$

Furthermore, a second Lagrange multiplier $\boldsymbol{\mu}$ is introduced to constrain the *relaxed* velocity gradient on the surface, $\mathbf{L}'_S$, to the original velocity gradient on the surface $\nabla^s \mathbf{v}$, where ∇^S is the surface gradient defined by $\nabla^S = \left(\mathbf{I} - \mathbf{NN}\right)\bullet\nabla$ (see equation (5.7)). The surface Lagrange multiplier $\boldsymbol{\mu}$ is considered to be a double traction tensor.

The virtual internal power expression is rewritten as:

$$\delta P_{int} = \int_\Omega \boldsymbol{\sigma} : \delta\mathbf{L} + \delta\left(\boldsymbol{\lambda} : \left(\mathbf{L}' - \mathbf{L}\right)\right) + \overline{\boldsymbol{\beta}} \vdots \delta\mathbf{G}' d\Omega - \int_S \boldsymbol{\mu} : \left(\delta\mathbf{L}'_S - \delta\left(\nabla^S \mathbf{v}\right)\right) dS \tag{A28}$$

The external virtual power expression is given by:

$$\delta P_{ext} = \int_\Omega \mathbf{b}\bullet\delta\mathbf{v} d\Omega + \int_S \mathbf{t}\bullet\delta\mathbf{v} + \mathbf{R}\bullet\delta\mathbf{L}' dS \tag{A29}$$

where $\mathbf{R}$ is a double traction tensor related to the double traction vector $\mathbf{r}$ used in the gradient formulation, equation (5.6), by:

$$\mathbf{R} = \mathbf{rN} = \mathbf{N}\bullet\overline{\boldsymbol{\sigma}}\bullet\mathbf{NN} \tag{A30}$$

On examination of the external and internal virtual power expressions, only the first gradient of each unknown field i.e. $\mathbf{G}'$ and $\mathbf{L}$ is required in the formulation and C^0 shape functions are sufficient.

A6.2 Derivation of the Governing Equations and Boundary Conditions

Assuming that the Lagrange multiplier $\boldsymbol{\lambda}$ is sufficient to kinematically constrain $\mathbf{L}'$ to $\mathbf{L}$ within the homogenized body Ω, it is possible to reasonable to neglect the surface Lagrange multiplier $\boldsymbol{\mu}$; the resulting equilibrium equations are:

$$\begin{aligned}
&\nabla\bullet\left(\boldsymbol{\sigma}-\boldsymbol{\lambda}\right)+\mathbf{b}=0 \quad \text{in} \quad \Omega \\
&\nabla\bullet\bar{\boldsymbol{\beta}}-\boldsymbol{\lambda}=0 \quad \text{in} \quad \Omega \\
&\mathbf{L}'-\mathbf{L}=0 \quad \text{in} \quad \Omega \\
&\mathbf{t}-\mathbf{N}\bullet\left(\boldsymbol{\sigma}-\boldsymbol{\lambda}\right)=0 \quad \text{on} \quad S \\
&\mathbf{R}=\mathbf{r}\mathbf{N}=\mathbf{N}\bullet\bar{\boldsymbol{\beta}}:\left(\mathbf{N}\mathbf{N}\right) \quad \text{on} \quad S
\end{aligned} \tag{A31}$$

The multiresolution governing equations (5.25) are repeated here for ease of comparison:

$$\begin{aligned}
&\nabla\bullet\left(\boldsymbol{\sigma}-\sum_{n=1}^{N}\boldsymbol{\beta}^{n}\right)+\mathbf{b}=\mathbf{0} \quad \text{in} \quad \Omega \\
&\nabla\bullet\bar{\boldsymbol{\beta}}^{n}-\boldsymbol{\beta}^{n}+\mathbf{B}^{n}=\mathbf{0} \quad \text{in} \quad \Omega \\
&\mathbf{t}-\mathbf{N}\bullet\left(\boldsymbol{\sigma}-\sum_{n=1}^{N}\boldsymbol{\beta}^{n}\right)=\mathbf{0} \quad \text{on} \quad S \\
&\mathbf{R}^{n}=\mathbf{r}^{n}\mathbf{N}=\mathbf{N}\bullet\bar{\boldsymbol{\beta}}^{n}:\left(\mathbf{N}\mathbf{N}\right) \quad \text{on} \quad S
\end{aligned} \tag{A32}$$

It is clear that when $N=1$, the two approaches are almost identical. One clear distinction is that the multiresolution approach contains various microstresses which act N scales. Also, the multiresolution formulation does not explicitly tie the strain fields at each scale as the Lagrange Multiplier approach does i.e. $\mathbf{L}'-\mathbf{L}=0$ in equation (A31).

Furthermore, the Lagrange multiplier $\boldsymbol{\lambda}$ is a numerical tool which is used in an arbitrary way to constrain the dummy field $\mathbf{L}'$ to the velocity gradient $\mathbf{L}$. There is no clear relationship between the Lagrange Multiplier $\boldsymbol{\lambda}$ and the couple stress $\bar{\boldsymbol{\beta}}$ in equation (A31). On the other hand the

multiresolution microstress $\boldsymbol{\beta}^n$ has a clear physical meaning – it is the average resistance to inhomogeneous deformation at scale n. Also, the relationship between the multiresolution microstress $\boldsymbol{\beta}^n$ and the couple microstress $\overline{\boldsymbol{\beta}}$ is defined in equation (5.22). Both formulations decompose to the conventional continuum equilibrium equation $\nabla \bullet \boldsymbol{\sigma} + \mathbf{b} = 0$ when the Lagrange Multiplier $\boldsymbol{\lambda}$ or Microstress $\boldsymbol{\beta}^n$ is set to zero.

A7 Previous Analytical and Empirical Models of WC-Co

An over view of previously reported hardness and toughness models are reported for cemented carbides.

Hardness

The simplest models for hardness consider individual contributions from the carbide phase and the cobalt binder phase. Lee and Gurland's model (Lee and Gurland 1978) is based on a 'continuous carbide volume fraction' which involves the volume fraction of carbide and the carbide contiguity. They proposed the following empirical equation for composite hardness:

$$H = H_{WC} f_{WC} C_{WC} + H_{Co}\left(1 - f_{WC} C_{WC}\right) \tag{A32}$$

where H_{WC} and H_{Co} are the hardness of tungsten carbide and cobalt respectively. Enqvist et al. (2002) proposed a model in which hardness decays exponentially with the cobalt grain size, d:

$$H = \left(H_{WC} - H_{Co}\right)\exp^{\frac{d}{k}} + H_{Co} \tag{A33}$$

where k is the empirically measured hardening range factor.

Toughness

Fracture toughness models are usually based on the strain energy release rate, G. The critical strain energy release rate G_{IC} is a material parameter which describes when a crack will cause fracture and is related to the critical stress intensity factor K_{IC} (for plain strain fracture):

$$K_{IC} = \sqrt{\frac{G_{IC} E}{\left(1 - \nu^2\right)}} \tag{A34}$$

Pickens and Gurland (1978) described a simple model in which the critical strain energy release rate is linearly related to the cobalt grain size d and yield strength σ_y:

$$G_{IC} = \alpha d \sigma_y \tag{A35}$$

where α is the linear coefficient. The yield strength is related to the hardness which may be computed from Lee and Gurland's hardness model above.

Sigl and Fischmeister (1988) presented a complex model in which cracks are assumed to progress through the cobalt binder (Co), binder/carbide interfaces (Co-WC), the carbide (WC) or carbide/carbide interfaces (WC-WC). The total strain energy release rate is based on the release rates of the four possible paths:

$$G_{IC} = \left(r_{Co} A_{Co} + r_{Co-WC} A_{Co-WC} \right) \sigma_f + \left(A_{WC} + A_{WC-WC} \right) G_{IC}^{'} \tag{A36}$$

The area fractions of each crack path $A_{Co}, A_{Co-WC}, A_{WC}, A_{WC-WC}$ are calculated using empirical relations. The distances r_{Co} and r_{Co-WC} are the average sizes of the binder plastic zone within the cobalt binder and at the cobalt binder/carbide interface. The flow stress in the binder is given by σ_f and the fracture energy of the carbide and carbide/carbide boundaries is given by $G_{IC}^{'}$.

Ravichandran (1994) developed a simpler model in which the strain energy release rate is a summation of the fracture energy of the brittle carbide phase $f_{WC} G_{IC}^{'}$ and fracture resistance of ductile binder phase $f_{Co} \sigma_f d\chi$:

$$G_{IC} = f_{WC} G_{IC}^{'} + f_{Co} \sigma_f d\chi \tag{A37}$$

where $G_{IC}^{'}$ is the fracture energy of carbide phase, σ_f is the bulk flow stress of the binder, and χ is a rupture parameter associated with the cobalt binder. Each of these models has been compared to experimentally obtained hardness and fracture toughness values for various cemented carbides; none of the models performed well.